Title
Defining regulation of prostate cancer initiation, progression, and resistance to androgen receptor blockade

Author
Crowell, Preston Drake

Publication Date
2022

Peer reviewed|Thesis/dissertation

UNIVERSITY OF CALIFORNIA

Los Angeles

Defining regulation of prostate cancer initiation, progression, and resistance to androgen receptor blockade

A dissertation submitted in partial satisfaction of the requirements for the degree Doctor of Philosophy in Molecular Biology

by

Preston Drake Crowell

2022

ABSTRACT OF THE DISSERTATION

Defining regulation of prostate cancer initiation, progression, and resistance to androgen receptor blockade

by

Preston Drake Crowell

Doctor of Philosophy in Molecular Biology
University of California, Los Angeles, 2022
Professor Andrew S. Goldstein, Chair

Prostate cancer is the leading cause of cancer-related death in non-smoking males. Key factors that contribute to prostate mortality include high incidence and poor survival after recurrence. Delineating mechanisms of prostate cancer initiation, progression, and therapy resistance is required to reduce mortality from the disease. Aging is the largest risk factor for prostate cancer initiation, yet age-related changes to the cell types that can initiate prostate cancer are poorly defined. Cells that survive treatment enable prostate cancer progression and therapy resistance, in many cases, by transitioning from therapy-responsive to therapy-resistant lineages. However, how lineage identity is regulated in the prostate is not fully understood. Furthermore, uncovering vulnerabilities of cells that survive treatment remains an area of active research. In this dissertation, I explore the effects of aging on the cell types of the prostate and identify an age-related expansion of progenitor-enriched prostate epithelial cells as one mechanism by which aging could increase prostate cancer incidence. In addition, I define metabolic regulation of lineage transitions, which enable therapy resistance, and identify targetable treatment-induced metabolic vulnerabilities. These findings yield new strategies to prevent prostate cancer initiation and reduce death from resistant disease.

The dissertation of Preston Drake Crowell is approved.

Orian Shirihai

Heather Christofk

Brigitte Gomperts

Matthew Rettig

Andrew Goldstein, Committee Chair

University of California, Los Angeles,

2022

This dissertation is dedicated to my grandfather, Arnold Shaw, whose dream of pursuing a Ph.D. in Biology was sadly derailed

I would also like to dedicate this dissertation to my parents, Rick and Dana Crowell

Table of Contents

List of figures

Chapter 1: Introduction

Chapter 2: Expansion of luminal progenitor cells in the aging mouse and human prostate

Acknowledgements

School never came easy for me until I stumbled upon biology in high school. Suddenly, I looked forward to something other than hanging ten while surfing. My passion for biology was solidified during my freshman year of college at UCLA after taking the prerequisite course for the biomedical research minor taught by Dr. Ira Clark. By the summer after my freshman year, I had joined the biomedical research minor and been placed into the laboratory of Dr. John Colicelli. My undergraduate research experience was extraordinary. Cloning reminded me of the logic puzzles that I loved as a kid and the feeling of contributing to the ever-expanding pool of scientific knowledge was remarkable. I would like to thank both Dr. Clark and Dr. Colicelli for helping clarify my desire to pursue a career in science and providing great mentorship during my undergraduate years.

I would like to thank my thesis advisor and mentor Dr. Andrew Goldstein. Andrew taught me how to apply my creativity to complex scientific questions. Andrew's emphasis on written and oral scientific communication significantly improved my communication skills. Furthermore, Andrew fostered a collaborative environment and did not fear challenging conversations. I credit Andrew for much of my growth not only as a scientist but also as a person. I would also like to thank my thesis committee, Dr. Orian Shirihai, Dr. Heather Christofk, Dr. Brigitte Gomperts, and Dr. Matthew Rettig for their scientific feedback and continued guidance as I embark on the next stage of my career.

I would like to thank all members of the Goldstein lab both past and present for their support and friendship. I would like to extend a special thank you to Jenna Giafaglione. I

cannot use words to describe how supportive Jenna has been over the years. Jenna has been my most ardent supporter and my life has been greatly enriched by knowing her. I look forward to making more wonderful memories together. I would also like to thank our lab manager Dr. Takao Hashimoto and my undergraduate researchers Nicholas Nunley, Amelie Delcourt, Jonathan Fox, Kylie Heering and Johnny Diaz for their strong work ethic and dedication to our research program. Thank you to our collaborators including Anthony Jones, Dr. Ajit Divakaruni, Anton Petcherski, Michaela Veliova, Dr. Orian Shirihai, Dr. Heather Christofk and Dr. Douglas Strand. Thank you to my friends outside the lab including Buddy Howe, Matthew Knox, Tyler Carroll, Cliff Hansen, Otis Sistrunk, Terry Prettyman, Jason Khatra, Nik Bergum, and Anthony Jones.

Finally, I would like to thank my parents, Rick and Dana Crowell, for tolerating me for 28 years. Even though I did not seem the smartest growing up, my parents never put limits on what they thought I could achieve. They taught me strong worth ethic, responsibility, resiliency, and core values. They have provided me with unconditional love and support my entire life and I love them dearly in return. I would also like to thank my brother, Trevor Crowell, for his support and friendship. Thank you to my grandparents, Arnold and Shelley Shaw, and Charles and Doris Crowell.

Chapter 2 was originally published in Cell Reports. Preston D. Crowell, Jonathan J. Fox, Takao Hashimoto, Johnny A. Diaz, Hector I. Navarro, Gervaise H. Henry, Blake A. Feldmar, Matthew G. Lowe, Alejandro J. Garcia, Ye E. Wu, Dipti P. Sajed, Douglas W. Strand & Andrew S. Goldstein. 2019. Expansion of Luminal Progenitor Cells in the Aging

Mouse and Human Prostate. Cell Reports volume 28, pages 1499-1510 (2019). It is accessible with the DOI:10.1016/j.celrep.2019.07.007. J.J.F. was supported by a scholarship from the UCLA Minor in Biomedical Research and the Silva Endowment as part of the Undergraduate Research Scholars Program at UCLA. P.D.C. and M.G.L. were supported by the Ruth L. Kirschstein National Research Service Award GM007185. H.I.N. is supported by the Eugene V. Cota-Robles Fellowship. J.A.D. was supported by the National Institute of General Medical Sciences of the NIH (R25GM055052 awarded to T. Hasson) and the Saul Martinez Scholarship. A.S.G. is supported by the Spitzer Family Foundation Fund and the Gill Endowment. This work was supported by the American Cancer Society (RSG-17-068-01-TBG), Department of Defense (W81XWH-13-1-0470), Margaret E. Early Medical Research Trust, STOP CANCER, NIH/NCI (P50CA092131/UCLA SPORE in Prostate Cancer), UCLA Eli and Edythe Broad Center of Regenerative Medicine and Stem Cell Research Rose Hills Foundation Innovator Grant, and support from UCLA's Jonsson Comprehensive Cancer Center, Broad Stem Cell Research Center, Clinical and Translational Science Institute, and Institute of Urologic Oncology. D.W.S. is supported by the NIH/NIDDK (R01 DK115477).

Chapter 3 was originally published in the American Journal of Clinical and Experimental Urology. Preston D. Crowell, Jenna M. Giafaglione, Takao Hashimoto & Andrew S. Goldstein. 2020. Distinct cell-types in the prostate share an aging signature suggestive of metabolic reprogramming. Am J Clin Exp Urol volume 8(4), pages 140-151 (2020). It is accessible with the PMID:32929410. This work was supported by the American Cancer Society (RSG-17-068-01-TBG), NIH/NCI (R01CA2371- 91), Rose Hills Foundation, Gill

endowment dedicated to cancer research and the Spitzer Family Foundation Fund, as well as support from UCLA's Jonsson Comprehensive Cancer Center, Broad Stem Cell Research Center, Clinical and Translational Science Institute, and Institute of Urologic Oncology. PDC and JMG were supported by a Ruth L. Kirschstein National Research Service Award GM007185.

Chapter 4 is currently in preparation for submission. It reflects work performed by Jenna M. Giafaglione, Preston D. Crowell, Amelie M.L. Delcourt, Takao Hashimoto, Daniel Ha, Elsa Tika, Nicholas M. Nunley, Leigh Ellis, Cedric Blanpain & Andrew S. Goldstein.

Chapter 5 is currently in peer review. The preprint manuscript is available on BioRxiv. Preston D. Crowell, Jenna M. Giafaglione, Anthony E. Jones, Nicholas M. Nunley, Takao Hashimoto, Amelie M.L. Delcourt, Anton Petcherski, Matthew J. Bernard, Rong Rong Huang, Jin-Yih Low, Nedas Matulionis, Xiangnan Guan, Nora M. Navone, Joshi J. Alumkal, Michael C. Haffner, Huihui Ye, Amina Zoubeidi, Heather R. Christofk, Orian S. Shirihai, Ajit S. Divakaruni & Andrew S. Goldstein. Androgen receptor inhibition induces metabolic reprogramming and increased reliance on oxidative mitochondrial metabolism in prostate cancer. 2022. It is accessible with the DOI: 10.1101/2022.05.31.494200. P.D.C. and J.M.G. acknowledge the support of the UCLA Eli and Edythe Broad Center of Regenerative Medicine and Stem Cell Research Training Program. P.D.C. is also supported by the NIH grants TL1 DK132768 and U2C DK129496. A.E.J. is supported by the UCLA Tumor Cell Biology Training Grant (NIH T32CA009056). A.S.G. is supported by the National Cancer Institute of the National Institutes of Health under Award Number

R01CA237191. The content is solely the responsibility of the authors and does not necessarily represent the official views of the National Institutes of Health. A.M.L.D. is supported by NCI/NIH supplement related to R01CA237191. A.S.G. is also supported by American Cancer Society award RSG-17-068-01-TBG, the UCLA Eli and Edythe Broad Center of Regenerative Medicine and Stem Cell Research Rose Hills Foundation Innovator Grant, the UCLA Jonsson Comprehensive Cancer Center and Eli and Edythe Broad Center of Regenerative Medicine and Stem Cell Research Ablon Scholars Program, the National Center for Advancing Translational Sciences UCLA CTSI Grant UL1TR001881, STOP CANCER, and the UCLA Institute of Urologic Oncology. A.S.G., A.S.D. and O.S.S. are supported by the UCLA Prostate Cancer Specialized Programs of Research Excellence (SPORE) NCI P50 CA092131. J.J.A is supported by the National Cancer Institute award R01CA251245, the Pacific Northwest Prostate Cancer Specialized Programs of Research Excellence (SPORE) NCI P50 CA097186, the NCI Drug Resistance and Sensitivity Network NCI P50 CA186786-07S1, and the Department of Defense Idea Award (W81XWH-20-1-0405). M.C.H. is supported by the U.S. Department of Defense Prostate Cancer Research Program (W81XWH-20-1-0111, W81XWH-21-1-0229) and Grant 2021184 from the Doris Duke Charitable Foundation. N.M.N. is supported by NCI U01 CA224044-03.

VITA

EDUCATION:

University of California, Los Angeles **2016**
B.S., Molecular, Cell, and Developmental Biology

PUBLICATIONS:

Crowell P.D., Giafaglione J.M., Jones A.E., Nunley N.M., Hashimoto, T., Delcourt A.M.L., Petcherski A., Bernard M.J., Huang R., Low J., et al. (2022). **Androgen receptor inhibition induces metabolic reprogramming and increased reliance on oxidative mitochondrial metabolism in prostate cancer**. *BioRχiv*. doi: https://doi.org/10.1101/2022.05.31.494200.

Freeland J., **Crowell P.D.**, Giafaglione J.M., Boutros P.C., Goldstein A.S. (2021). **Aging of the progenitor cells that initiate prostate cancer**. *Cancer Letters*. *515*, 28-35.

Crowell, P.D., Giafaglione, J.M., Hashimoto, T., Goldstein, A.S. (2020). **Distinct cell-types in the prostate share an aging signature suggestive of metabolic reprogramming**. Am J Clin Exp Urol. 8(4):140-151.

Crowell, P.D., Giafaglione, J.M., Hashimoto, T., Diaz, J.A., Goldstein, A.S. (2019). **Evaluating the Differentiation Capacity of Mouse Prostate Epithelial Cell Using Organoid Culture**. JoVE 153, e60223.

Crowell, P.D., Fox, J.J., Hashimoto, T., Diaz, J.A., Navarro, H.I., Henry, G.H., Feldmar, B.A., Lowe, M.G., Garcia, A.J., Wu, Y.E., et al. (2019). **Expansion of Luminal Progenitor Cells in the Aging Mouse and Human Prostate**. Cell Rep. *28*, 1499-1510.

Mottahedeh, J., Haffner, M.C., Grogan, T.R., Hashimoto, T., **Crowell, P.D.**, Beltran, H., Sboner, A., Bareja, R., Esopi, D., Isaacs, W.B., et al. (2018). **CD38 is methylated in prostate cancer and regulates extracellular NAD+**. Cancer Metab. *6*, 13.

Crowell, P.D., and Goldstein, A.S. (2017). **Functional evidence that progenitor cells near sites of inflammation are precursors for aggressive prostate cancer**. Mol. Cell. Oncol. *4*, 1–2.

PRESENTATIONS:

Crowell PD. (2021) **Oxidative metabolism sustains prostate cancer cells after AR inhibition**. Molecular, Cell & Developmental Biology Departmental Retreat, Santa Monica, CA. (TALK)

Crowell PD. (2021) **Defining metabolic vulnerabilities of castration-resistant prostate cancer cells**. Cell and Molecular Biology Training Program: 3rd Year Talk, Los Angeles, CA. (TALK)

Crowell PD. (2020) **Expansion of Luminal Progenitor Cells in the Aging Mouse and Human Prostate**. **University of California**, Los Angeles, 2020 Annual Stem Cell Symposium, Los Angeles, CA. (POSTER)

Crowell PD. (2019) **Expansion of Luminal Progenitor Cells in the Aging Mouse and Human Prostate**. Society for Basic Urologic Research Annual Meeting, New Orleans, LA. (POSTER)

Crowell PD. (2019) **Defining the role of metabolic signaling in regulation of lineage identity in normal prostate and castration-resistant prostate cancer**. Mito Super Group Series, Los Angeles, CA. (TALK)

Crowell PD. (2019) **Defining metabolic regulation of lineage plasticity in castration-resistant prostate cancer**. Molecular Biology Interdepartmental Program Student Seminar Series, Los Angeles, CA. (TALK)

Crowell PD. (2019) **Age-related expansion of luminal progenitor cells maintains old mouse prostate**. University of California, Los Angeles, 2019 Annual Stem Cell Symposium, Los Angeles, CA. (POSTER)

Crowell PD. (2018) **Defining the role of metabolism in prostate progenitor cell differentiation**. Cell Symposia: Metabolites as Signaling Molecules, Seattle, WA. (POSTER)

Crowell PD. (2018) **Defining the role of metabolism in prostate progenitor cell differentiation**. Plenary Session: University of California, Los Angeles, Molecular, Cell & Developmental Biology Departmental Retreat, Lake Arrowhead, CA. (TALK)

Crowell PD. (2018) **Basal and Luminal Cells Isolated from Mouse Prostate Generate and Utilize Pyruvate Differently**. University of California, Los Angeles, 2018 Annual Molecular Biology Institute Retreat, Ventura Beach, CA. (POSTER)

Crowell PD. (2018) **Metabolic Profiles Correlate with Progenitor Activity and Cancer Initiation in Prostate Epithelial Cells**. University of California, Los Angeles, 2018 Annual Stem Cell Symposium, Los Angeles, CA. (POSTER)

Crowell PD. (2018) **Metabolic Profiles Correlate with Progenitor Activity and Cancer Initiation in Prostate Epithelial Cells**. Keystone Tumor Metabolism Conference, Snowbird Resort, UT. (POSTER)

Crowell PD. (2017) **Characterizing the Metabolism of the Basal and Luminal Cells of the Prostate Epithelium**. University of California, Los Angeles, Molecular, Cell & Developmental Biology Departmental Retreat, Lake Arrowhead, CA. (POSTER)

AWARDS:

UCLA KUH-ART Fellowship Award (T32) **2021-2022**

Rose Hills Foundation – Broad Stem Cell Research Center Predoctoral Fellowship **2020-2021**

Ruth L. Kirschtein National Research Service Award (T32) **2018-2020**

Chapter 1: Introduction

The prostate gland and cell types

The prostate is a gland that represents one component of the male reproductive system. Located between the bladder and the penis and encapsulating the urethra, the prostate secretes seminal fluid, which contributes to semen (Figure 1) [1]. The muscles that surround the prostate prevent urine from entering the urethra during ejaculation and ensure that semen is forcefully expelled outward. The prostate gland contains stromal cells and epithelial cells (Figure 2) [2]. The epithelium is comprised of basal and luminal cells and rare neuroendocrine cells[2]. The luminal cells are the secretory cells and reside adjacent to the lumen of the gland[2]. Basal cells, which line the basement membrane of the gland, are encapsulated by the stroma, which contains fibroblasts and smooth muscle cells[2]. Lineage tracing studies have revealed that basal and luminal cells are predominately self-sustained by distinct progenitors under normal physiological conditions; however, basal progenitor cells have the capacity to form luminal cells during development, tissue regeneration, inflammation, and prostate cancer initiation[3-8]. Basal and luminal prostate epithelial cells can be efficiently isolated and separated by fluorescence-activated cell sorting, which enables *ex vivo* functional characterization of each lineage[9,10].

Prostate cancer initiation

Prostate cancer is among the most commonly diagnosed forms of cancer in the world. In 2022, more than 268,490 men in the United States will be diagnosed with prostate cancer[11]. Its most common form, prostate adenocarcinoma, affects the prostate glands and is characterized by expansion of malignant luminal cells and loss of basal cells. Due to the histology of the disease, prostate cancer was hypothesized to originate from luminal

cells. However, lineage tracing studies in the mouse and *in vivo* transformation assays using oncogene-transduced human prostate epithelial cells have identified both basal and luminal prostate epithelial cells as cells-of-origin for prostate cancer[3,6,9,12-16]. Basal- and luminal-derived prostate cancers cannot be distinguished as basal to luminal differentiation precedes prostate cancer initiation from basal cells[9,17]. Uncontrolled luminal proliferation in prostate cancer is driven by aberrant activity from the androgen receptor (AR), an intracellular ligand-dependent steroid hormone receptor that functions as a transcription factor and regulates the growth of the prostate. Mechanisms of aberrant AR activity include increased production of its ligand, dihydrotestosterone, AR mutation, AR amplification, and the expression of constitutively active AR splice variants[18,19]. Strategies to target aberrant AR activity to treat prostate cancer will be covered in the *prostate cancer progression and treatment resistance* section of the introduction.

Among the greatest risk factors for prostate cancer initiation are aging and chronic inflammation[20-23]. Inflammation-associated luminal cells in the human prostate exhibit morphological changes known as proliferative inflammatory atrophy (PIA), characterized by an atrophic appearance, an imbalance between proliferation and apoptosis, and increased oxidative stress[24,25]. We have shown that PIA-like human luminal cells can be isolated by low CD38 expression ($CD38^{lo}$) and are progenitor-enriched and exhibit greater susceptibility to transformation than other luminal subsets[16]. These findings further implicate chronic inflammation in prostate cancer initiation. Delineating mechanisms of prostate cancer initiation may reveal approaches to reduce prostate cancer incidence, yet surprisingly, the effects of aging on prostate epithelial cells are poorly defined.

Aging and progenitor activity

Aging is associated with the functional decline of cells, tissues, and organs, and increased risk for various diseases[26]. Aging promotes epigenetic changes that reduce the regenerative potential of hematopoietic stem cells[27]. In addition, aging is associated with atrophy of muscles, brain, eyes, and thymus, consistent with a decline in progenitor activity in these tissues[28-33]. In many contexts, age-related tissue atrophy and progenitor cell dysfunction has been attributed to chronic inflammation, as proinflammatory cytokines have been shown to inhibit stem/progenitor regeneration[34,35]. However, we have shown that inflammation-associated $CD38^{lo}$ luminal cells in the human prostate are progenitor-enriched, and prostatic aging is associated with growth-related diseases, rather than atrophy[23]. Therefore, the prostate exhibits a distinct response to aging from other tissues, yet the effects of aging on the gene expression and progenitor activity of prostate epithelial cells have not been established.

In chapter 2, I discuss our group's effort to define the effects of aging on prostate epithelial cells. We found that the *ex vivo* progenitor activity of mouse prostate epithelial cells is retained during aging. Using RNA sequencing and flow cytometry, we identified a progenitor-enriched subset of luminal cells, marked by Trop2, that has since been validated via single cell RNA sequencing by several groups[36-38]. Trop2+ luminal cells are robustly expanded in the aged mouse prostate and exhibit transcriptional similarity to $CD38^{lo}$ human luminal progenitor cells. Importantly, we found that human luminal progenitor cells are expanded during aging, suggesting that age-related luminal

progenitor cell expansion is conserved across species. It was recently reported that tumors originating from mouse Trop2+ luminal cells after PTEN deletion develop faster than tumors derived from other luminal subsets[36]. In addition, we have shown that, unlike other subsets, progenitor-enriched human luminal cells can initiate human prostate cancer in response to oncogenic transformation[16]. Therefore, aging expands the pool of cells with greater susceptibility to transformation. It is unclear whether aging-associated immune cell infiltration influences luminal progenitor cell expansion. Future work will seek to identify key regulators of age-related luminal progenitor cell expansion as interfering with luminal progenitor cell expansion may reduce prostate cancer incidence.

Aging and metabolic reprogramming

Metabolic reprogramming occurs during aging in various tissues and can contribute to cancer initiation[39]. In chapter 3, I describe our work thus far to define age related changes to prostate metabolism. We transcriptionally profiled stromal, basal, Trop2+ luminal, and Trop2- luminal cells isolated from mouse prostate. Motif analysis revealed upregulated hypoxia-related signaling in old prostate cell types. We identified glutathione and antioxidant response as commonly enriched across all aged prostatic lineages. Our findings suggest that a common age-related metabolic signature may be shared by distinct cell types in the old prostate. More work is necessary to define functional changes to metabolism in aged cell types using profiling and nutrient tracing approaches. As chronic inflammation is common in the aged prostate and increases susceptibility to prostatic disease, it is critical to understand whether inflammation-induced changes to the microenvironment influence the metabolism of aged prostate cell types[20-22]. Upregulation

of glutathione and antioxidant response genes could reflect a cellular response to inflammation-induced oxidative stress[40]. Future work will seek to understand how immune cell infiltration alters prostate epithelial metabolism and whether aging- and/or inflammation-induced metabolic features increase susceptibility to prostatic disease.

Prostate cancer progression and treatment resistance

Prostate cancer is the leading cause of cancer-related death in non-smoking males in the United States[11]. In 2022, an estimated 34,500 men in the United States will die from prostate cancer[11]. Localized or regional prostate cancer has a 5-year survival rate of greater than 99 percent and is typically treated with surgery and/or radiation therapy[11]. The overwhelming majority of prostate cancer mortality occurs from metastatic disease, which has a 5-year survival rate of only 31 percent[11]. Prostate cancer progression from localized to advanced metastatic disease is driven by aberrant androgen receptor activity (Figure 3). Accordingly, patients that develop metastatic prostate cancer are treated with androgen deprivation therapies (ADTs), which reduce AR activity by interfering with the production of circulating androgens, alone or in combination with chemotherapy[41]. Prostate cancer that responds to ADT is termed castration-sensitive prostate cancer and prostate cancer that recurs after ADT is termed castration-resistant prostate cancer (CRPC) [42]. As AR activity remains critical for the survival and growth of the majority of CRPC cells, CRPC is treated with androgen-receptor pathway inhibitors (ARPIs), including enzalutamide[43]. These drugs bind to the ligand binding domain of AR to prevent ligand binding-induced AR activation[43]. Although ARPIs are initially effective, prolonged ARPI treatment invariably leads to treatment resistance[44]. One mechanism of treatment

resistance of particular interest is lineage plasticity, which describes the transition from an AR-dependent luminal-like lineage to an AR-indifferent lineage that contains basal and/or neuroendocrine features[44-46]. As most prostate cancer mortality occurs from treatment-resistant disease, identifying approaches to prevent, interfere with and/or reverse treatment-resistance is of utmost importance.

Metabolic regulation of cell fate

Cellular identity is defined and maintained by the epigenome and metabolism has emerged as a key upstream regulator of the epigenome in recent years (Figure 4) [47]. Metabolites such as SAM and alpha-ketoglutarate are important substrates and cofactors respectively for chromatin-modifying enzymes[48-50]. Furthermore, select metabolic enzymes facilitate site-specific substrate production for acetylation and methylation reactions[51,52]. Through these mechanisms, metabolic signaling has been shown to regulate the differentiation of pluripotent stem cells as well as adult progenitor cells including intestinal and hair follicle stem cells[53-55]. In an effort to better understand lineage plasticity in prostate cancer, several groups have characterized epigenetic changes associated with lineage transitions and identified key epigenetic regulators[45,56,57]. However, defining upstream metabolic regulation of lineage identity in the prostate has been challenging due in part to a poor understanding of prostate epithelial cell type-specific metabolic features. Understanding metabolic regulation of luminal cell identity could inform new approaches to prevent or reverse lineage plasticity in advanced metastatic prostate cancer.

In chapter 4, I describe our group's investigation of metabolic regulation of prostate epithelial lineage identity. We developed an approach to perform metabolic profiling and nutrient tracing on basal and luminal prostate epithelial cell isolated from mouse prostate and identified cell type-specific metabolic features. We validated organoid culture as an *ex vivo* model of basal to luminal differentiation and found that luminal differentiation in prostate organoids is associated with a metabolic shift toward increased glucose oxidation. These data were corroborated *in vivo* using lineage tracing approaches coupled with RNA sequencing. Using genetic and pharmacological approaches, we identified the mitochondrial pyruvate carrier (MPC) as a key regulator of prostate luminal identity in both benign and prostate cancer cells. As observed with MPC inhibition, both lactate supplementation and inhibition of lactate efflux reduced basal to luminal differentiation in prostate organoids, suggesting that intracellular lactate accumulation may mediate inhibition of luminal differentiation. Our results provide the first evidence that distinct prostate epithelial cell types exhibit unique metabolic features and that metabolism can regulate prostate epithelial lineage identity. Future studies will seek to identify how to accelerate luminal differentiation using metabolic drugs as restoring the luminal identity of treatment-resistant cells may sensitize these cells to existing AR inhibitors.

Therapy-induced metabolic reprogramming in cancer

Metabolic reprogramming is not merely associated with cancer initiation and progression, but also occurs after treatment where it can interfere with treatment-induced apoptosis and contribute to treatment resistance[58]. For example, increased glutamine metabolism

and glutathione biosynthesis reduce apoptosis by protecting cancer cells from chemotherapy-induced oxidative stress[59,60]. In addition, a hyperfused mitochondrial phenotype has been observed in triple negative breast cancer cells that survive chemotherapy and enables chemotherapy resistance in gynecological cancers[61,62]. In pancreatic cancer, glutaminase inhibition sensitizes chemo-resistant KRAS-mutant pancreatic cancer cells to chemotherapy[63]. These data support combining standard-of-care treatments with drugs that interfere with treatment-induced metabolic rewiring.

Metabolic reprogramming occurs during prostate cancer initiation and progression and several studies suggest that metabolic pathways can be targeted in prostate cancer to reduce tumor growth[64-71]. For example, inhibition of lipogenesis or glutamine metabolism have been shown to antagonize CRPC[64,71]. CAMKK2 inhibition disrupts autophagy and thereby impairs both CSPC and CRPC growth[69,70]. Furthermore, serine biosynthesis and lactate export have been targeted to impair tumor growth in neuroendocrine prostate cancer models[65,67]. Surprisingly, the effect of AR blockade on the metabolic signaling of prostate cancer cells has not been comprehensively defined. Furthermore, whether altered metabolism in the cells that survive AR inhibition can be targeted to delay or prevent prostate cancer progression is poorly understood.

In chapter 5, I detail our group's effort to define how AR blockade alters prostate cancer cell metabolism. Using transcriptomics, metabolomics, and bioenergetics approaches, we found that AR inhibition maintains oxidative mitochondrial metabolism and reduces glycolytic activity and capacity, through hexokinase II downregulation and decreased

MYC activity. Elongation of mitochondria via reduced Drp1-driven mitochondrial fission supports cellular fitness after AR blockade. Furthermore, AR inhibition sensitizes prostate cancer cells to complex I inhibitors in several models, suggesting that AR blockade promotes increased reliance on oxidative mitochondrial metabolism. Our findings identify altered metabolic signaling as a mechanism through which prostate cancer cells survive AR blockade and highlight the potential of therapies that target metabolic vulnerabilities in AR-inhibited cells. Future work will seek to identify the mechanism by which mitochondrial elongation supports cell fitness after AR blockade.

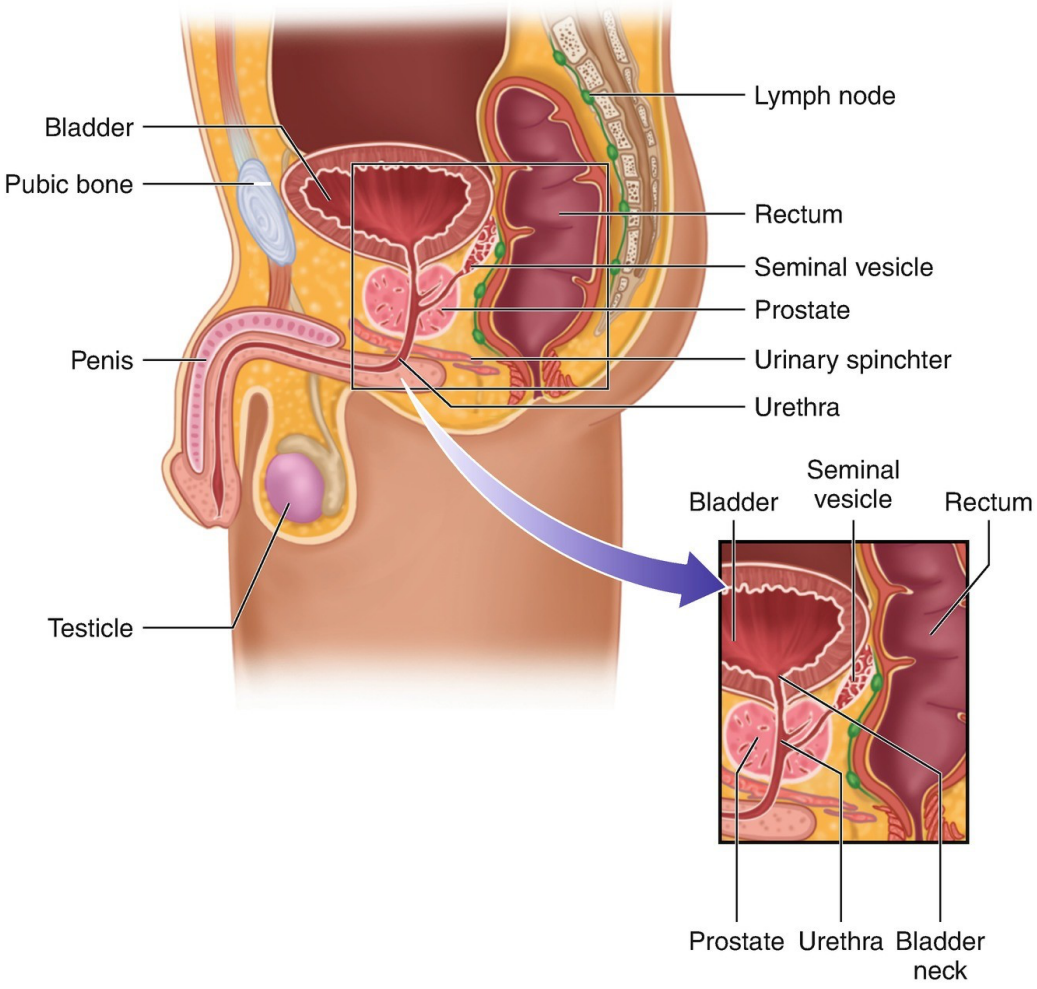

Figure 1. Visualization of prostate within pelvic region.

The prostate encapsulates the urethra, which while allows urine and semen from the bladder and secretory ducts respectively to travel out of the body. The prostate provides the fluid component of semen and the muscles that surround the prostate contract to expel semen outward during ejaculation.

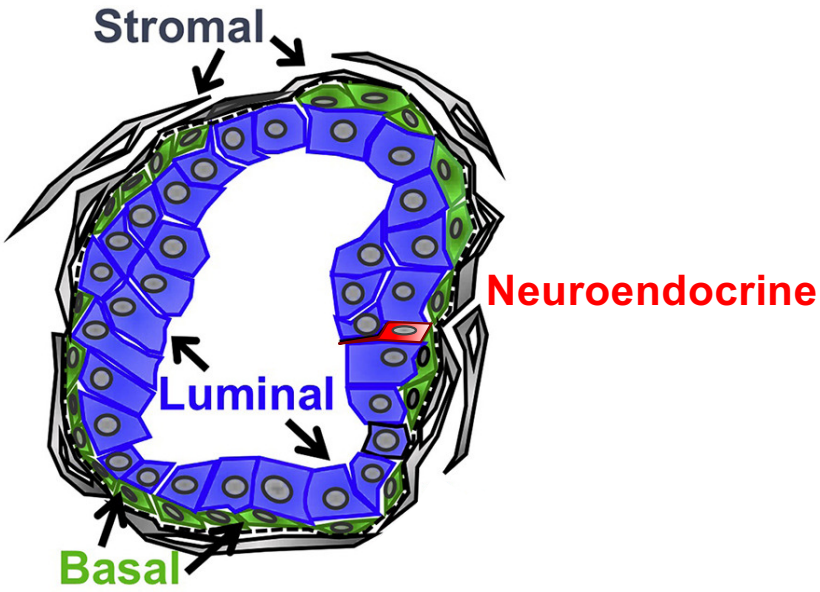

Figure 2. Schematic of the prostate gland.

The prostate gland is comprised of epithelial and stromal cells (grey). Within the prostate epithelium are basal (green), luminal (blue), and rare neuroendocrine (red) cells. The basement membrane is depicted by the dashed line.

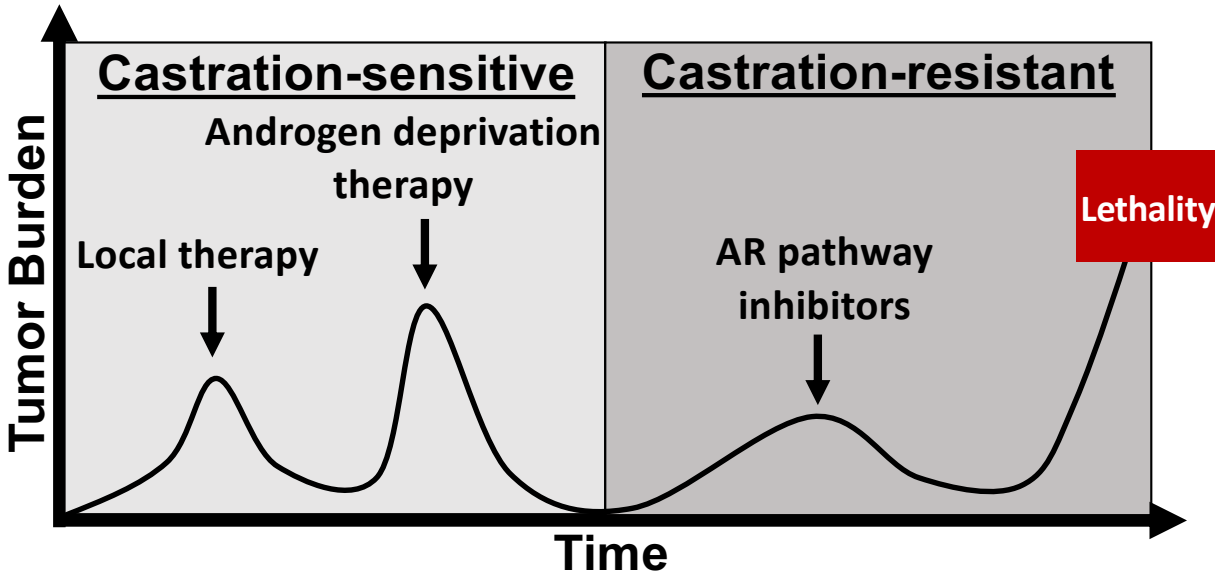

Figure 3. Prostate cancer progression and treatment.

Castration-sensitive prostate cancer that recurs after local therapy is treated with androgen deprivation therapy (ADT). Prostate cancer that recurs after ADT is termed castration-resistant prostate cancer and is treated with androgen receptor (AR) pathway inhibitors (APIs). Resistance to APIs contributes to the vast majority of prostate cancer lethality.

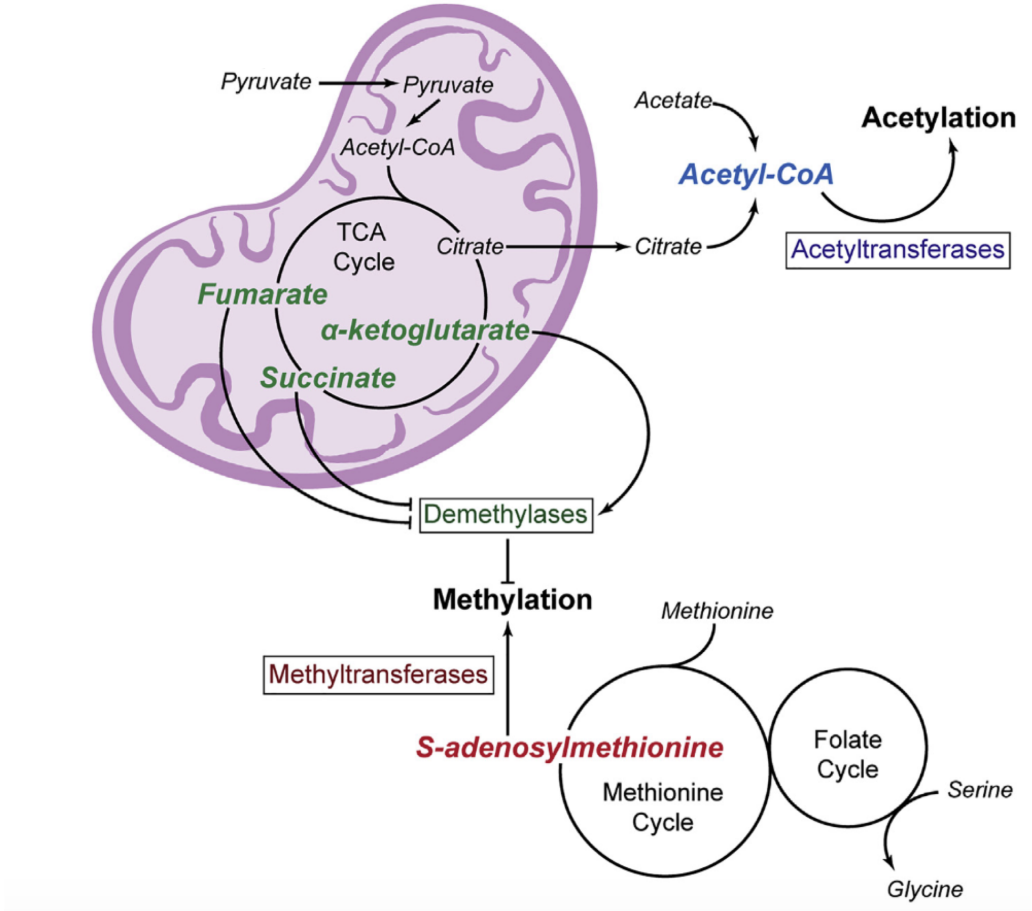

Figure 4. Metabolites as epigenetic regulators.

Metabolites facilitate epigenetic modifications. Acetyl CoA, generated from citrate or acetate, is the substrate for acetyltransferases for acetylation reactions. S-adenosylmethionine, generated from the methionine cycle, is the substrate for methylation reactions. α-ketoglutarate is a co-factor for demethylases and fumarate and succinate inhibit demethylase activity.

References

1. McCormick BJ, Raynor MC. The Prostate and Benign Prostatic Hyperplasia. In: Isaacson AJ, Bagla S, Raynor MC, Yu H, eds. *Prostatic Artery Embolization.* Cham: Springer International Publishing; 2020:1-9.
2. Aaron L, Franco OE, Hayward SW. Review of Prostate Anatomy and Embryology and the Etiology of Benign Prostatic Hyperplasia. *Urol Clin North Am.* 2016;43(3):279-288. PMC4968575
3. Choi N, Zhang B, Zhang L, Ittmann M, Xin L. Adult murine prostate basal and luminal cells are self-sustained lineages that can both serve as targets for prostate cancer initiation. *Cancer Cell.* 2012;21(2):253-265. PMC3285423
4. Ousset M, Van Keymeulen A, Bouvencourt G, Sharma N, Achouri Y, Simons BD, Blanpain C. Multipotent and unipotent progenitors contribute to prostate postnatal development. *Nat Cell Biol.* 2012;14(11):1131-1138.
5. Wang J, Zhu HH, Chu M, Liu Y, Zhang C, Liu G, Yang X, Yang R, Gao WQ. Symmetrical and asymmetrical division analysis provides evidence for a hierarchy of prostate epithelial cell lineages. *Nat Commun.* 2014;5:4758.
6. Wang ZA, Mitrofanova A, Bergren SK, Abate-Shen C, Cardiff RD, Califano A, Shen MM. Lineage analysis of basal epithelial cells reveals their unexpected plasticity and supports a cell-of-origin model for prostate cancer heterogeneity. *Nat Cell Biol.* 2013;15(3):274-283. PMC3743266
7. Kwon OJ, Zhang B, Zhang L, Xin L. High fat diet promotes prostatic basal-to-luminal differentiation and accelerates initiation of prostate epithelial hyperplasia originated from basal cells. *Stem Cell Res.* 2016;16(3):682-691.
8. Kwon OJ, Zhang L, Ittmann MM, Xin L. Prostatic inflammation enhances basal-to-luminal differentiation and accelerates initiation of prostate cancer with a basal cell origin. *Proc Natl Acad Sci U S A.* 2014;111(5):E592-600. PMC3918789
9. Goldstein AS, Huang J, Guo C, Garraway IP, Witte ON. Identification of a cell of origin for human prostate cancer. *Science.* 2010;329(5991):568-571. PMC2917982
10. Crowell PD, Fox JJ, Hashimoto T, Diaz JA, Navarro HI, Henry GH, Feldmar BA, Lowe MG, Garcia AJ, Wu YE, Sajed DP, Strand DW, Goldstein AS. Expansion of Luminal Progenitor Cells in the Aging Mouse and Human Prostate. *Cell Rep.* 2019;28(6):1499-1510 e1496. PMC6710009
11. Siegel RL, Miller KD, Fuchs HE, Jemal A. Cancer statistics, 2022. *CA Cancer J Clin.* 2022;72(1):7-33.
12. Lu TL, Huang YF, You LR, Chao NC, Su FY, Chang JL, Chen CM. Conditionally ablated Pten in prostate basal cells promotes basal-to-luminal differentiation and causes invasive prostate cancer in mice. *Am J Pathol.* 2013;182(3):975-991.
13. Wang ZA, Toivanen R, Bergren SK, Chambon P, Shen MM. Luminal cells are favored as the cell of origin for prostate cancer. *Cell Rep.* 2014;8(5):1339-1346. PMC4163115
14. Lawson DA, Zong Y, Memarzadeh S, Xin L, Huang J, Witte ON. Basal epithelial stem cells are efficient targets for prostate cancer initiation. *Proc Natl Acad Sci U S A.* 2010;107(6):2610-2615. PMC2823887

15. Taylor RA, Toivanen R, Frydenberg M, Pedersen J, Harewood L, Australian Prostate Cancer B, Collins AT, Maitland NJ, Risbridger GP. Human epithelial basal cells are cells of origin of prostate cancer, independent of CD133 status. *Stem Cells.* 2012;30(6):1087-1096.
16. Liu X, Grogan TR, Hieronymus H, Hashimoto T, Mottahedeh J, Cheng D, Zhang L, Huang K, Stoyanova T, Park JW, Shkhyan RO, Nowroozizadeh B, Rettig MB, Sawyers CL, Elashoff D, Horvath S, Huang J, Witte ON, Goldstein AS. Low CD38 Identifies Progenitor-like Inflammation-Associated Luminal Cells that Can Initiate Human Prostate Cancer and Predict Poor Outcome. *Cell Rep.* 2016;17(10):2596-2606. PMC5367888
17. Stoyanova T, Cooper AR, Drake JM, Liu X, Armstrong AJ, Pienta KJ, Zhang H, Kohn DB, Huang J, Witte ON, Goldstein AS. Prostate cancer originating in basal cells progresses to adenocarcinoma propagated by luminal-like cells. *Proc Natl Acad Sci U S A.* 2013;110(50):20111-20116. PMC3864278
18. Guo Z, Yang X, Sun F, Jiang R, Linn DE, Chen H, Chen H, Kong X, Melamed J, Tepper CG, Kung HJ, Brodie AM, Edwards J, Qiu Y. A novel androgen receptor splice variant is up-regulated during prostate cancer progression and promotes androgen depletion-resistant growth. *Cancer Res.* 2009;69(6):2305-2313. PMC2672822
19. Grasso CS, Wu YM, Robinson DR, Cao X, Dhanasekaran SM, Khan AP, Quist MJ, Jing X, Lonigro RJ, Brenner JC, Asangani IA, Ateeq B, Chun SY, Siddiqui J, Sam L, Anstett M, Mehra R, Prensner JR, Palanisamy N, Ryslik GA, Vandin F, Raphael BJ, Kunju LP, Rhodes DR, Pienta KJ, Chinnaiyan AM, Tomlins SA. The mutational landscape of lethal castration-resistant prostate cancer. *Nature.* 2012;487(7406):239-243. PMC3396711
20. Gurel B, Lucia MS, Thompson IM, Jr., Goodman PJ, Tangen CM, Kristal AR, Parnes HL, Hoque A, Lippman SM, Sutcliffe S, Peskoe SB, Drake CG, Nelson WG, De Marzo AM, Platz EA. Chronic inflammation in benign prostate tissue is associated with high-grade prostate cancer in the placebo arm of the prostate cancer prevention trial. *Cancer Epidemiol Biomarkers Prev.* 2014;23(5):847-856. PMC4012292
21. Sfanos KS, De Marzo AM. Prostate cancer and inflammation: the evidence. *Histopathology.* 2012;60(1):199-215. PMC4029103
22. Shafique K, Proctor MJ, McMillan DC, Qureshi K, Leung H, Morrison DS. Systemic inflammation and survival of patients with prostate cancer: evidence from the Glasgow Inflammation Outcome Study. *Prostate Cancer Prostatic Dis.* 2012;15(2):195-201.
23. Roehrborn CG. Benign prostatic hyperplasia: an overview. *Rev Urol.* 2005;7 Suppl 9:S3-S14. PMC1477638
24. De Marzo AM, Marchi VL, Epstein JI, Nelson WG. Proliferative inflammatory atrophy of the prostate: implications for prostatic carcinogenesis. *Am J Pathol.* 1999;155(6):1985-1992. PMC1866955
25. De Marzo AM, Platz EA, Sutcliffe S, Xu J, Gronberg H, Drake CG, Nakai Y, Isaacs WB, Nelson WG. Inflammation in prostate carcinogenesis. *Nat Rev Cancer.* 2007;7(4):256-269. PMC3552388

26. Lopez-Otin C, Blasco MA, Partridge L, Serrano M, Kroemer G. The hallmarks of aging. *Cell.* 2013;153(6):1194-1217. PMC3836174
27. de Haan G, Lazare SS. Aging of hematopoietic stem cells. *Blood.* 2018;131(5):479-487.
28. Baumgartner RN, Koehler KM, Gallagher D, Romero L, Heymsfield SB, Ross RR, Garry PJ, Lindeman RD. Epidemiology of sarcopenia among the elderly in New Mexico. *Am J Epidemiol.* 1998;147(8):755-763.
29. Klein R, Klein BE, Linton KL. Prevalence of age-related maculopathy. The Beaver Dam Eye Study. *Ophthalmology.* 1992;99(6):933-943.
30. Meier-Ruge W, Ulrich J, Bruhlmann M, Meier E. Age-related white matter atrophy in the human brain. *Ann N Y Acad Sci.* 1992;673:260-269.
31. Simpson JG, Gray ES, Beck JS. Age involution in the normal human adult thymus. *Clin Exp Immunol.* 1975;19(2):261-265. PMC1538100
32. Conboy IM, Conboy MJ, Smythe GM, Rando TA. Notch-mediated restoration of regenerative potential to aged muscle. *Science.* 2003;302(5650):1575-1577.
33. Molofsky AV, Slutsky SG, Joseph NM, He S, Pardal R, Krishnamurthy J, Sharpless NE, Morrison SJ. Increasing p16INK4a expression decreases forebrain progenitors and neurogenesis during ageing. *Nature.* 2006;443(7110):448-452. PMC2586960
34. Josephson AM, Bradaschia-Correa V, Lee S, Leclerc K, Patel KS, Muinos Lopez E, Litwa HP, Neibart SS, Kadiyala M, Wong MZ, Mizrahi MM, Yim NL, Ramme AJ, Egol KA, Leucht P. Age-related inflammation triggers skeletal stem/progenitor cell dysfunction. *Proc Natl Acad Sci U S A.* 2019;116(14):6995-7004. PMC6452701
35. de Gonzalo-Calvo D, Neitzert K, Fernandez M, Vega-Naredo I, Caballero B, Garcia-Macia M, Suarez FM, Rodriguez-Colunga MJ, Solano JJ, Coto-Montes A. Differential inflammatory responses in aging and disease: TNF-alpha and IL-6 as possible biomarkers. *Free Radic Biol Med.* 2010;49(5):733-737.
36. Guo W, Li L, He J, Liu Z, Han M, Li F, Xia X, Zhang X, Zhu Y, Wei Y, Li Y, Aji R, Dai H, Wei H, Li C, Chen Y, Chen L, Gao D. Single-cell transcriptomics identifies a distinct luminal progenitor cell type in distal prostate invagination tips. *Nat Genet.* 2020;52(9):908-918. PMC8383310
37. Crowley L, Cambuli F, Aparicio L, Shibata M, Robinson BD, Xuan S, Li W, Hibshoosh H, Loda M, Rabadan R, Shen MM. A single-cell atlas of the mouse and human prostate reveals heterogeneity and conservation of epithelial progenitors. *Elife.* 2020;9. PMC7529463
38. Karthaus WR, Hofree M, Choi D, Linton EL, Turkekul M, Bejnood A, Carver B, Gopalan A, Abida W, Laudone V, Biton M, Chaudhary O, Xu T, Masilionis I, Manova K, Mazutis L, Pe'er D, Regev A, Sawyers CL. Regenerative potential of prostate luminal cells revealed by single-cell analysis. *Science.* 2020;368(6490):497-505. PMC7313621
39. Ren R, Ocampo A, Liu GH, Izpisua Belmonte JC. Regulation of Stem Cell Aging by Metabolism and Epigenetics. *Cell Metab.* 2017;26(3):460-474.
40. Mittal M, Siddiqui MR, Tran K, Reddy SP, Malik AB. Reactive oxygen species in inflammation and tissue injury. *Antioxid Redox Signal.* 2014;20(7):1126-1167. PMC3929010

41. Sayegh N, Swami U, Agarwal N. Recent Advances in the Management of Metastatic Prostate Cancer. *JCO Oncol Pract.* 2022;18(1):45-55.
42. Nakazawa M, Paller C, Kyprianou N. Mechanisms of Therapeutic Resistance in Prostate Cancer. *Curr Oncol Rep.* 2017;19(2):13. PMC5812366
43. Tran C, Ouk S, Clegg NJ, Chen Y, Watson PA, Arora V, Wongvipat J, Smith-Jones PM, Yoo D, Kwon A, Wasielewska T, Welsbie D, Chen CD, Higano CS, Beer TM, Hung DT, Scher HI, Jung ME, Sawyers CL. Development of a second-generation antiandrogen for treatment of advanced prostate cancer. *Science.* 2009;324(5928):787-790. PMC2981508
44. Schmidt KT, Huitema ADR, Chau CH, Figg WD. Resistance to second-generation androgen receptor antagonists in prostate cancer. *Nat Rev Urol.* 2021;18(4):209-226.
45. Ku SY, Rosario S, Wang Y, Mu P, Seshadri M, Goodrich ZW, Goodrich MM, Labbe DP, Gomez EC, Wang J, Long HW, Xu B, Brown M, Loda M, Sawyers CL, Ellis L, Goodrich DW. Rb1 and Trp53 cooperate to suppress prostate cancer lineage plasticity, metastasis, and antiandrogen resistance. *Science.* 2017;355(6320):78-83. PMC5367887
46. Mu P, Zhang Z, Benelli M, Karthaus WR, Hoover E, Chen CC, Wongvipat J, Ku SY, Gao D, Cao Z, Shah N, Adams EJ, Abida W, Watson PA, Prandi D, Huang CH, de Stanchina E, Lowe SW, Ellis L, Beltran H, Rubin MA, Goodrich DW, Demichelis F, Sawyers CL. SOX2 promotes lineage plasticity and antiandrogen resistance in TP53- and RB1-deficient prostate cancer. *Science.* 2017;355(6320):84-88. PMC5247742
47. Campbell SL, Wellen KE. Metabolic Signaling to the Nucleus in Cancer. *Mol Cell.* 2018;71(3):398-408.
48. Carey BW, Finley LW, Cross JR, Allis CD, Thompson CB. Intracellular alpha-ketoglutarate maintains the pluripotency of embryonic stem cells. *Nature.* 2015;518(7539):413-416. PMC4336218
49. Mentch SJ, Mehrmohamadi M, Huang L, Liu X, Gupta D, Mattocks D, Gomez Padilla P, Ables G, Bamman MM, Thalacker-Mercer AE, Nichenametla SN, Locasale JW. Histone Methylation Dynamics and Gene Regulation Occur through the Sensing of One-Carbon Metabolism. *Cell Metab.* 2015;22(5):861-873. PMC4635069
50. Kinnaird A, Zhao S, Wellen KE, Michelakis ED. Metabolic control of epigenetics in cancer. *Nat Rev Cancer.* 2016;16(11):694-707.
51. Wellen KE, Hatzivassiliou G, Sachdeva UM, Bui TV, Cross JR, Thompson CB. ATP-citrate lyase links cellular metabolism to histone acetylation. *Science.* 2009;324(5930):1076-1080. PMC2746744
52. Mews P, Donahue G, Drake AM, Luczak V, Abel T, Berger SL. Acetyl-CoA synthetase regulates histone acetylation and hippocampal memory. *Nature.* 2017;546(7658):381-386. PMC5505514
53. TeSlaa T, Chaikovsky AC, Lipchina I, Escobar SL, Hochedlinger K, Huang J, Graeber TG, Braas D, Teitell MA. alpha-Ketoglutarate Accelerates the Initial Differentiation of Primed Human Pluripotent Stem Cells. *Cell Metab.* 2016;24(3):485-493. PMC5023506

54. Flores A, Schell J, Krall AS, Jelinek D, Miranda M, Grigorian M, Braas D, White AC, Zhou JL, Graham NA, Graeber T, Seth P, Evseenko D, Coller HA, Rutter J, Christofk HR, Lowry WE. Lactate dehydrogenase activity drives hair follicle stem cell activation. *Nat Cell Biol.* 2017;19(9):1017-1026. PMC5657543
55. van Gastel N, Stegen S, Eelen G, Schoors S, Carlier A, Daniels VW, Baryawno N, Przybylski D, Depypere M, Stiers PJ, Lambrechts D, Van Looveren R, Torrekens S, Sharda A, Agostinis P, Lambrechts D, Maes F, Swinnen JV, Geris L, Van Oosterwyck H, Thienpont B, Carmeliet P, Scadden DT, Carmeliet G. Lipid availability determines fate of skeletal progenitor cells via SOX9. *Nature.* 2020;579(7797):111-117. PMC7060079
56. Dardenne E, Beltran H, Benelli M, Gayvert K, Berger A, Puca L, Cyrta J, Sboner A, Noorzad Z, MacDonald T, Cheung C, Yuen KS, Gao D, Chen Y, Eilers M, Mosquera JM, Robinson BD, Elemento O, Rubin MA, Demichelis F, Rickman DS. N-Myc Induces an EZH2-Mediated Transcriptional Program Driving Neuroendocrine Prostate Cancer. *Cancer Cell.* 2016;30(4):563-577. PMC5540451
57. Davies A, Nouruzi S, Ganguli D, Namekawa T, Thaper D, Linder S, Karaoglanoglu F, Omur ME, Kim S, Kobelev M, Kumar S, Sivak O, Bostock C, Bishop J, Hoogstraat M, Talal A, Stelloo S, van der Poel H, Bergman AM, Ahmed M, Fazli L, Huang H, Tilley W, Goodrich D, Feng FY, Gleave M, He HH, Hach F, Zwart W, Beltran H, Selth L, Zoubeidi A. An androgen receptor switch underlies lineage infidelity in treatment-resistant prostate cancer. *Nat Cell Biol.* 2021;23(9):1023-1034. PMC9012003
58. Faubert B, Solmonson A, DeBerardinis RJ. Metabolic reprogramming and cancer progression. *Science.* 2020;368(6487). PMC7227780
59. Bansal A, Simon MC. Glutathione metabolism in cancer progression and treatment resistance. *J Cell Biol.* 2018;217(7):2291-2298. PMC6028537
60. Franco R, Cidlowski JA. Apoptosis and glutathione: beyond an antioxidant. *Cell Death Differ.* 2009;16(10):1303-1314.
61. Kong B, Tsuyoshi H, Orisaka M, Shieh DB, Yoshida Y, Tsang BK. Mitochondrial dynamics regulating chemoresistance in gynecological cancers. *Ann N Y Acad Sci.* 2015;1350:1-16.
62. Baek ML, Lee J, Pendleton KE, Berner MJ, Goff EB, Tan L, Martinez SA, Wang T, Meyer MD, Lim B, Barrish JP, Porter W, Lorenzi PL, Echeverria GV. Mitochondrial structure and function adaptation in residual triple negative breast cancer cells surviving chemotherapy treatment. *bioRxiv.* 2022:2022.2002.2025.481996.
63. Mukhopadhyay S, Goswami D, Adiseshaiah PP, Burgan W, Yi M, Guerin TM, Kozlov SV, Nissley DV, McCormick F. Undermining Glutaminolysis Bolsters Chemotherapy While NRF2 Promotes Chemoresistance in KRAS-Driven Pancreatic Cancers. *Cancer Res.* 2020;80(8):1630-1643. PMC7185043
64. Zadra G, Ribeiro CF, Chetta P, Ho Y, Cacciatore S, Gao X, Syamala S, Bango C, Photopoulos C, Huang Y, Tyekucheva S, Bastos DC, Tchaicha J, Lawney B, Uo T, D'Anello L, Csibi A, Kalekar R, Larimer B, Ellis L, Butler LM, Morrissey C, McGovern K, Palombella VJ, Kutok JL, Mahmood U, Bosari S, Adams J, Peluso S, Dehm SM, Plymate SR, Loda M. Inhibition of de novo lipogenesis targets androgen receptor signaling in castration-resistant prostate cancer. *Proc Natl Acad Sci U S A.* 2019;116(2):631-640. PMC6329966

65. Reina-Campos M, Linares JF, Duran A, Cordes T, L'Hermitte A, Badur MG, Bhangoo MS, Thorson PK, Richards A, Rooslid T, Garcia-Olmo DC, Nam-Cha SY, Salinas-Sanchez AS, Eng K, Beltran H, Scott DA, Metallo CM, Moscat J, Diaz-Meco MT. Increased Serine and One-Carbon Pathway Metabolism by PKClambda/iota Deficiency Promotes Neuroendocrine Prostate Cancer. *Cancer Cell.* 2019;35(3):385-400 e389. PMC6424636
66. Bader DA, Hartig SM, Putluri V, Foley C, Hamilton MP, Smith EA, Saha PK, Panigrahi A, Walker C, Zong L, Martini-Stoica H, Chen R, Rajapakshe K, Coarfa C, Sreekumar A, Mitsiades N, Bankson JA, Ittmann MM, O'Malley BW, Putluri N, McGuire SE. Mitochondrial pyruvate import is a metabolic vulnerability in androgen receptor-driven prostate cancer. *Nat Metab.* 2019;1(1):70-85. PMC6563330
67. Choi SYC, Ettinger SL, Lin D, Xue H, Ci X, Nabavi N, Bell RH, Mo F, Gout PW, Fleshner NE, Gleave ME, Collins CC, Wang Y. Targeting MCT4 to reduce lactic acid secretion and glycolysis for treatment of neuroendocrine prostate cancer. *Cancer Med.* 2018. PMC6051138
68. Zhang J, Mao S, Guo Y, Wu Y, Yao X, Huang Y. Inhibition of GLS suppresses proliferation and promotes apoptosis in prostate cancer. *Biosci Rep.* 2019;39(6). PMC6591571
69. Lin C, Blessing AM, Pulliam TL, Shi Y, Wilkenfeld SR, Han JJ, Murray MM, Pham AH, Duong K, Brun SN, Shaw RJ, Ittmann MM, Frigo DE. Inhibition of CAMKK2 impairs autophagy and castration-resistant prostate cancer via suppression of AMPK-ULK1 signaling. *Oncogene.* 2021;40(9):1690-1705. PMC7935762
70. Massie CE, Lynch A, Ramos-Montoya A, Boren J, Stark R, Fazli L, Warren A, Scott H, Madhu B, Sharma N, Bon H, Zecchini V, Smith DM, Denicola GM, Mathews N, Osborne M, Hadfield J, Macarthur S, Adryan B, Lyons SK, Brindle KM, Griffiths J, Gleave ME, Rennie PS, Neal DE, Mills IG. The androgen receptor fuels prostate cancer by regulating central metabolism and biosynthesis. *EMBO J.* 2011;30(13):2719-2733. PMC3155295
71. Xu L, Yin Y, Li Y, Chen X, Chang Y, Zhang H, Liu J, Beasley J, McCaw P, Zhang H, Young S, Groth J, Wang Q, Locasale JW, Gao X, Tang DG, Dong X, He Y, George D, Hu H, Huang J. A glutaminase isoform switch drives therapeutic resistance and disease progression of prostate cancer. *Proc Natl Acad Sci U S A.* 2021;118(13). PMC8020804

Chapter 2: Expansion of luminal progenitor cells in the aging mouse and human prostate

Article

Cell Reports

Expansion of Luminal Progenitor Cells in the Aging Mouse and Human Prostate

Graphical Abstract

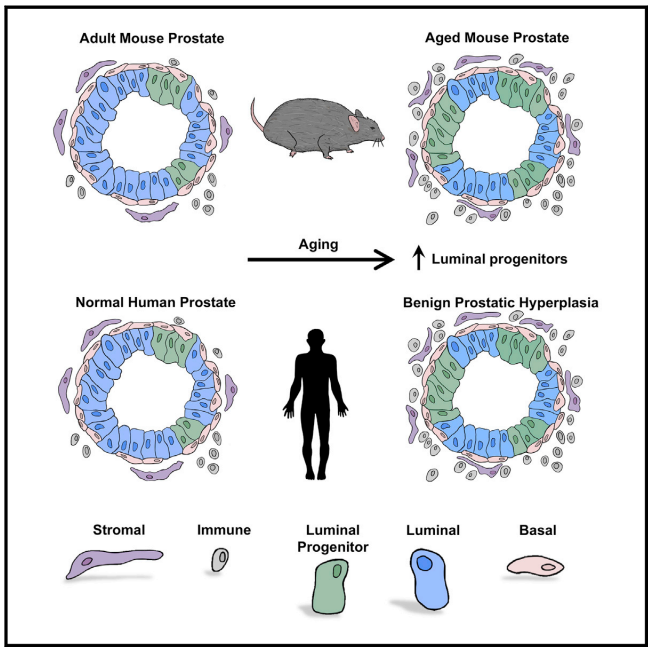

Authors

Preston D. Crowell, Jonathan J. Fox, Takao Hashimoto, ..., Dipti P. Sajed, Douglas W. Strand, Andrew S. Goldstein

Correspondence

agoldstein@mednet.ucla.edu

In Brief

Aging is a significant risk factor for BPH and prostate cancer, but how aging increases disease risk in the prostate remains poorly defined. Crowell et al. show that progenitor-enriched luminal cells are expanded with aging in the mouse and human prostate, and may contribute to BPH.

Highlights

- Organoid-forming capacity is maintained in old mouse prostate epithelial cells
- Identification of Trop2^{+} luminal cells as a progenitor-enriched subset
- Trop2^{+} luminal progenitor cells are expanded in the aging mouse prostate
- Increase in PSCA^{+} luminal progenitor cells in aging human prostate and BPH

Crowell et al., 2019, Cell Reports *28*, 1499–1510
August 6, 2019
https://doi.org/10.1016/j.celrep.2019.07.007

CellPress

Cell Reports
Article

Expansion of Luminal Progenitor Cells in the Aging Mouse and Human Prostate

Preston D. Crowell,[1,12] Jonathan J. Fox,[2,12] Takao Hashimoto,[2] Johnny A. Diaz,[2] Héctor I. Navarro,[1] Gervaise H. Henry,[3] Blake A. Feldmar,[2] Matthew G. Lowe,[1] Alejandro J. Garcia,[4] Ye E. Wu,[5,6] Dipti P. Sajed,[7] Douglas W. Strand,[3] and Andrew S. Goldstein[2,8,9,10,11,13,*]

[1]Molecular Biology Interdepartmental Program, University of California, Los Angeles, Los Angeles, CA 90095, USA
[2]Department of Molecular, Cell, and Developmental Biology, University of California, Los Angeles, Los Angeles, CA 90095, USA
[3]Department of Urology, UT Southwestern Medical Center, Dallas, TX 75390, USA
[4]Division of Hematology-Oncology, Department of Medicine, David Geffen School of Medicine, University of California, Los Angeles, Los Angeles, CA 90095, USA
[5]Department of Biological Chemistry, David Geffen School of Medicine, University of California, Los Angeles, Los Angeles, CA 90095, USA
[6]Department of Neurobiology, David Geffen School of Medicine, University of California, Los Angeles, Los Angeles, CA 90095, USA
[7]Department of Pathology and Laboratory Medicine, David Geffen School of Medicine, University of California, Los Angeles, Los Angeles, CA 90095, USA
[8]Department of Urology, David Geffen School of Medicine, University of California, Los Angeles, Los Angeles, CA 90095, USA
[9]Eli and Edythe Broad Center of Regenerative Medicine and Stem Cell Research, University of California, Los Angeles, Los Angeles, CA 90095, USA
[10]Jonsson Comprehensive Cancer Center, University of California, Los Angeles, Los Angeles, CA 90095, USA
[11]Molecular Biology Institute, University of California, Los Angeles, Los Angeles, CA 90095, USA
[12]These authors contributed equally
[13]Lead Contact
*Correspondence: agoldstein@mednet.ucla.edu
https://doi.org/10.1016/j.celrep.2019.07.007

SUMMARY

Aging is associated with loss of tissue mass and a decline in adult stem cell function in many tissues. In contrast, aging in the prostate is associated with growth-related diseases including benign prostatic hyperplasia (BPH). Surprisingly, the effects of aging on prostate epithelial cells have not been established. Here we find that organoid-forming progenitor activity of mouse prostate basal and luminal cells is maintained with age. This is caused by an age-related expansion of progenitor-like luminal cells that share features with human prostate luminal progenitor cells. The increase in luminal progenitor cells may contribute to greater risk for growth-related disease in the aging prostate. Importantly, we demonstrate expansion of human luminal progenitor cells in BPH. In summary, we define a Trop2^{+} luminal progenitor subset and identify an age-related shift in the luminal compartment of the mouse and human prostate epithelium.

INTRODUCTION

As living organisms age, they experience changes that result in the functional decline of their cells, tissues, and organs, increasing risk for a range of diseases (López-Otín et al., 2013). Many aspects of the aging process are thought to contribute to disease, such as aberrant signaling pathways, defects in autophagy, and shortening of telomeres (Niccoli and Partridge, 2012). Aging is associated with a loss of tissue mass, structural integrity, and regenerative potential (van Deursen, 2014), which may be caused by defects in tissue stem and progenitor cells. Age-related atrophy of muscles, brain, eyes, and thymus has been well documented (Baumgartner et al., 1998; Klein et al., 1992; Meier-Ruge et al., 1992; Simpson et al., 1975), consistent with a decline in progenitor activity in many of these tissues (Conboy et al., 2003; Molofsky et al., 2006). In contrast, the prostate gland has been shown to undergo expansion with age. Prevalence of benign prostatic hyperplasia (BPH), characterized by enlargement of the prostate, increases with age (Roehrborn, 2005). However, the link between age and progenitor capacity in the prostate has not been well defined.

Previous observations in old mice have identified age-related changes in the prostate microenvironment, including stromal disorganization and increased inflammation (Bianchi-Frias et al., 2010). We have previously identified a population of progenitor-like luminal cells in the human prostate that are expanded in regions adjacent to chronic inflammation (Liu et al., 2016). These CD38^{low} luminal progenitor cells express prostate stem cell antigen (PSCA) and exhibit an inflammatory signature. Whether the aging mouse prostate similarly contains a phenotypically distinct subset of progenitor-like luminal cells has not been established.

In this study, we performed transcriptional and functional characterization of epithelial cells from 3-month-old and 24-month-old mice. We found that prostate basal and luminal cells from old mice surprisingly maintain their progenitor activity. Luminal cells from old mice exhibit increased expression of progenitor markers including *Trop2* and *Psca*. Mechanistically, this is driven by an age-related increase in a distinct Trop2^{+} luminal progenitor subset capable of generating large organoids.

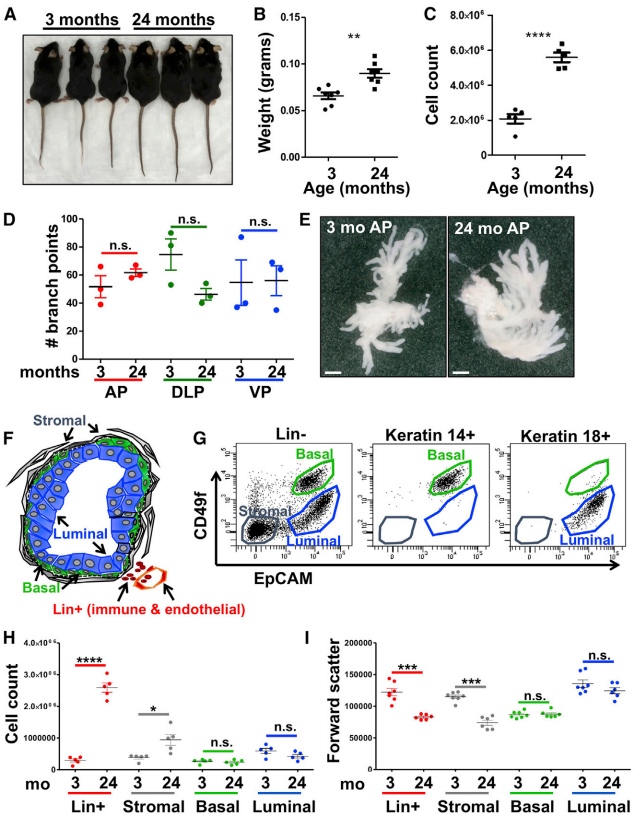

Figure 1. Characterization of Adult and Old Mouse Prostates

(A) Representative images of adult (3-month-old) and old (24-month-old) mice.

(B) Weights of prostates isolated from adult and old mice.

(C) Number of dissociated cells per prostate from each age.

(D) Quantification of the number of branch points in the anterior prostate (AP), dorso-lateral prostate (DLP), and ventral prostate (VP) lobes isolated from adult and old mice.

(E) Representative images of branching in AP lobe of adult and old prostate. Scale bars, 1 mm.

(F) Illustration of the normal mouse prostate gland, including basal cells (green), luminal cells (blue), stromal cells (gray), and Lin$^+$ immune and endothelial cells (red). Basement membrane is shown as a dotted line.

(G) Fluorescence-activated cell sorting (FACS) of whole mouse prostate using surface antibodies (CD49f and EpCAM) and intracellular staining to identify basal and luminal populations. Left: gated on total Lin$^-$ cells. Center: gated on K14$^+$ basal cells. Right: gated on K18$^+$ luminal cells.

(H and I) Quantification of the number (H) and forward scatter (I) of Lin$^+$, stromal, basal, and luminal cells in mouse prostates at 3 and 24 months of age. Data represent mean ± SEM of five to seven biological replicates.

Lin, lineage (CD31, CD45, Ter119); Mo, months of age. $^*p < 0.05$, $^{**}p < 0.01$, $^{***}p < 0.001$, $^{****}p < 0.0001$. n.s. = not significant, $p \geq 0.05$.

See also Figure S1.

In human prostate tissues, we found an increase in PSCA$^+$ luminal cells associated with age and BPH. Defining the cell types that maintain the prostate with age may shed light on the mechanisms promoting BPH.

RESULTS

Isolation of Prostate Epithelial Cells from Young Adult and Old Mice

We aged C57BL/6 (B6) male mice to 24 months and compared their prostates with post-pubertal 3-month-old young adult mice, hereafter referred to as adult (Figure 1A). Old mouse prostates are heavier than adult prostates (Figure 1B) and contain significantly greater numbers of cells per prostate (Figure 1C). We hypothesized that increased cell number may be caused by increased branching during aging. However, quantification of the number of branch points per lobe (anterior, dorso-lateral, and ventral) did not reveal any statistically significant differences between adult and old prostates (Figures 1D and 1E).

At the histological level, old prostates did not demonstrate features of prostate adenocarcinoma. However, rare age-related phenotypes were observed. In adult mice, prostatic acini are lined by a cuboidal to columnar epithelium with simple papillary infoldings and uniform nuclei (Figure S1A). In one lobe of an old prostate, acini were observed with a proliferation of the epithelium showing architectural disorganization and increased atypia in the form of nuclear pleomorphism, features of mouse prostatic intraepithelial neoplasia (PIN) (Ittmann et al., 2013) (Figure S1B). We also observed a single instance of a prostatic lobe with a markedly cellular mesenchymal proliferation infiltrating the space between benign prostatic glands, indicative of malignant sarcomatous features (Figure S1C).

To determine which cell types are responsible for the increased cell number in old prostates, we utilized fluorescence-activated cell sorting (FACS) to distinguish basal, luminal, stromal, and Lin$^+$ cells (expressing immune and endothelial markers) from adult and old prostates (Figures 1F and 1G). After depleting Lin$^+$ (CD31, CD45, Ter119) cells, we identified basal and luminal cells based on differential expression of CD49f and epithelial cell adhesion molecules (EpCAM). Intracellular flow

cytometry for basal (K14, K5) and luminal (K18, K8) keratins confirmed successful fractionation of basal and luminal cells within the CD49f^{hi} EpCAM^{+} and CD49f^{lo} EpCAM^{+} gates, respectively (Figures 1G, S1D, and S1E). Stromal cells, including cells expressing Desmin, were isolated within the Lin^{-} CD49f^{-} EpCAM^{-} fraction (Figures 1G and S1F).

We observed a dramatic increase in the number of Lin^{+} cells with age (Figure 1H), consistent with a 3- to 4-fold increase in the proportion of CD45^{+} cells in old prostates (Figure S1G). We also noted a minor increase in the number of stromal cells in old prostates (Figure 1H). No significant change in the number of basal or luminal epithelial cells was observed. We quantified forward scatter, a feature of FACS that is associated with cell size, from each population of cells. Interestingly, both Lin^{+} and stromal cells exhibited a significant decrease in forward scatter levels with age, whereas no significant difference was found in epithelial subsets (Figure 1I). These findings suggest age-related changes in the prostate microenvironment, consistent with a previous report (Bianchi-Frias et al., 2010).

Mass Cytometry Reveals an Age-Related Increase in Prostate-Infiltrating Lymphocytes

Using mass cytometry (cytometry by time-of-flight [CyTOF]) to comprehensively phenotype immune cells, we stained single-cell suspensions of total mouse prostate with a panel of metal-tagged antibodies against cell surface markers (Figure 2A; Table S1). To confirm that CyTOF can accurately detect immune cell populations in the prostate, we compared immune-competent B6 mice and immune-deficient NOD-SCID-IL-R2γ^{null} (NSG) mice that lack T cells, B cells, and natural killer (NK) cells, but still have myeloid cells (Ito et al., 2012). B6 mice were found to have cells staining positive for T cell (CD3, CD4, and CD8), B cell (CD19), and myeloid (CD11b and F4/80) markers (Figure S2A). In contrast, NSG mice stained positively for markers of myeloid cells, but not lymphocytes (Figures S2A–S2C).

We performed CyTOF on FACS-isolated Lin^{+} cells from adult and old mouse prostate tissue using the markers CD11c, Ly6C, CD19, CD8, CD25, CD27, B220, CD4, F4/80, CD11b, CD138, CD3, CD117, and FCER1A. To examine age-related changes to the gross immune cell composition of the mouse prostate, we classified CD45^{+} cells into three major groups. Cells expressing CD3 were classified as T cells. Cells expressing CD19 or B220 were classified as B cells. Cells expressing at least one of the markers, CD11b, CD11c, F4/80, and Ly6C, were classified as myeloid cells. NK and myeloid cells were difficult to separate based on the markers used, so we chose to group them together for this analysis. Although myeloid/NK cells were found to be dominant in both the adult and old mouse prostate immune compartments, T and B cells significantly increased with age as a proportion of CD45^{+} cells (Figure 2B).

We used t-Stochastic Neighbor Embedding (t-SNE) to visualize high-dimensional CyTOF data on a two-dimensional scatterplot, where cells with similar expression of surface markers are grouped closer together (Mair et al., 2016). Visualizing the resulting t-SNE plot as a heatmap of marker expression, the T cells and B cells are separated from cells expressing myeloid markers (Figure 2C). Consistent with age-related changes in the proportion of major immune lineages (Figure 2B), T and B cell regions identified in the t-SNE plot appeared more dense in the old mouse prostate (Figure 2D). These results are also consistent with age-related changes in Lin^{+} cell size (Figure 1I), because prostate-infiltrating lymphocytes exhibit lower levels of forward scatter than myeloid cells (Figure S2D).

Old Luminal Cells Generate Larger Organoids

Having characterized age-related changes to the prostate microenvironment, we sought to evaluate the effects of aging on prostate epithelial cells. We quantified the percentage of Ki67^{+} epithelial cells in the mouse prostate by flow cytometry, and found increased proliferation rates in basal cells compared with luminal cells (Figure S3A). Although proliferation rates did not change with age in the basal population, old luminal cells exhibited a significant increase in proliferation rates (Figure S3A). We next utilized the prostate organoid assay (Karthaus et al., 2014) to measure age-related changes in epithelial progenitor activity. We isolated basal and luminal cells from adult and old mice, and measured primary organoid formation, organoid size, and self-renewal capacity upon re-plating into secondary organoid culture. Within the basal cells, no significant age-related differences were observed based on primary organoid-forming capacity (Figure 3A), organoid size (diameter) (Figure 3B), and self-renewal (Figure 3C). Luminal cells from adult and old mice had no significant difference in primary organoid-forming capacity (Figure 3D). Organoids derived from aged luminal cells were larger on average (Figure 3E) and contained a significantly greater proportion of large (>400-μm diameter) organoids than those derived from adult luminal cells (Figure S3B). No significant differences in self-renewal capacity were observed upon re-plating into secondary organoid culture (Figure 3F).

Confocal microscopy was performed to evaluate markers of each lineage in organoids derived from adult and old basal and luminal cells. Basal-derived organoids from both adult and old mice contained multi-layered epithelium with outer layers expressing high levels of the basal marker p63 surrounding inner layers expressing high levels of the luminal marker K8 (Figure 3G). Luminal-derived organoids from both adult and old mice generally contained a single layer of cells with high expression of K8 and low-to-undetectable levels of p63 (Figure 3H). Western blots confirmed expression of basal and luminal markers in organoids derived from each cell type and age, indicative of multipotency (Figures S3C and S3D), as has been reported for adult basal and luminal cells (Chua et al., 2014; Karthaus et al., 2014).

Aging Is Associated with a Luminal Progenitor Signature

To gain insight into age-related changes associated with increased luminal organoid size, we performed gene expression analysis using RNA sequencing (RNA-seq) on epithelial cells isolated from adult and old mouse prostates. Principal component analysis of RNA-seq expression indicated that each cell type and age clusters independently, with principal component (PC) #1 separating basal from luminal cells and PC #2 distinguishing adult from old epithelial cells (Figure 4A). Within each cell type, significant gene expression changes were determined based

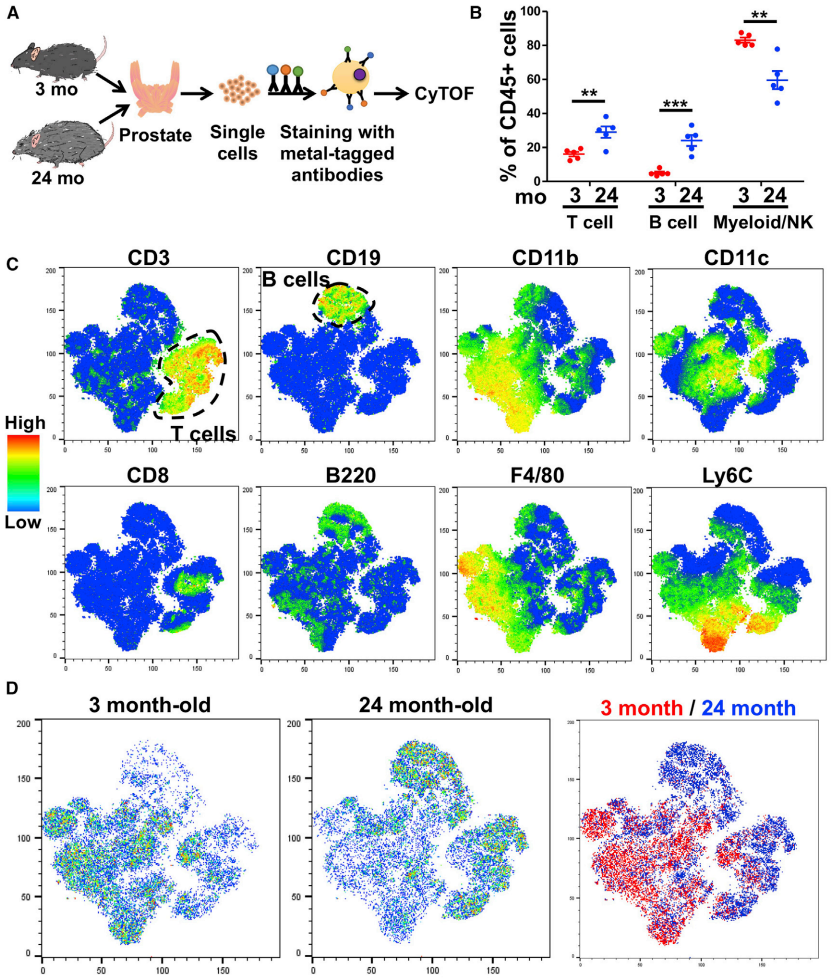

Figure 2. Mass Cytometry Reveals an Age-Related Increase in Prostate-Infiltrating Lymphocytes

(A) Workflow for mass cytometry (CyTOF) experiments in mouse. Prostates are removed, dissociated to single cells, stained with metal-tagged antibodies, and run on a mass cytometer.

(B) Frequencies of major immune cell populations in the prostates of adult and old B6 mice detected using CyTOF.

(C and D) t-SNE plots generated by clustering immune cells from adult and old mouse prostates based on expression of 14 surface markers detected with CyTOF.

(C) Heatmaps of t-SNE plot showing expression of eight selected markers, with scale on left. T cell and B cell regions are denoted by dotted line.

(D) t-SNE plots showing equal numbers of immune cells for adult (left), old (center), and both (right).

Data represent mean ± SEM of 5 biological replicates. $^{**}p < 0.01$, $^{***}p < 0.001$.

See also Figure S2.

on greater than 1.5-fold differential expression between adult and old, using a cutoff of false discovery rate (FDR) <0.1. Interestingly, 10 genes were significantly upregulated in both basal and luminal cells from old mice (Figure S4A), including several metabolic genes (*Cyp2f2*, *Hmox1*, *Urah*). Fourteen genes were found to be significantly downregulated in both basal and

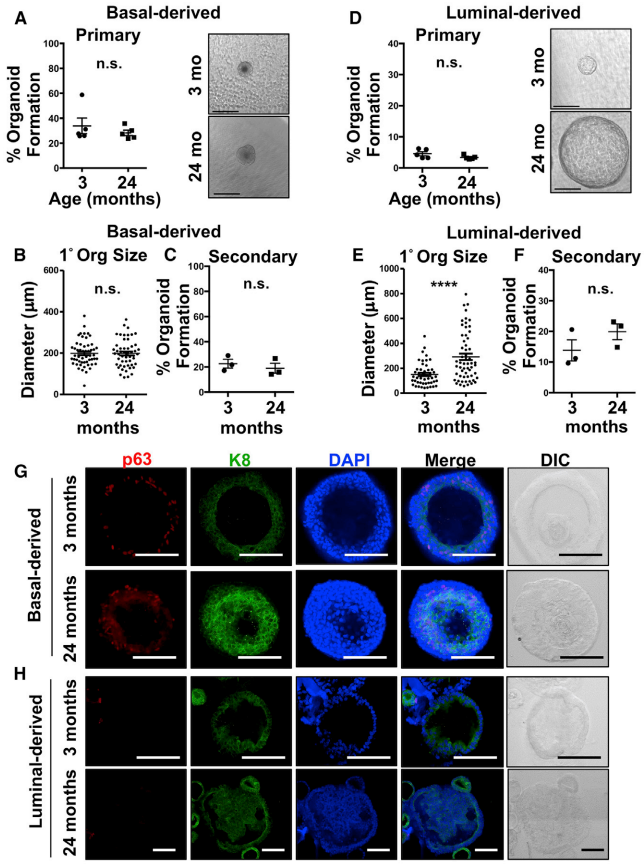

Figure 3. Epithelial Progenitor Activity Is Maintained in Old Mouse Prostate

(A) Primary organoid formation of sorted basal cells, shown as percentage of basal cells from 3- and 24-month-old mouse prostates that form organoids, with representative images shown on the right. Scale bars, 250 μm.

(B) Quantification of diameter of basal-derived primary organoids from 3- and 24-month-old mice.

(C) Percentage of single cells dissociated from primary basal-derived organoids that can generate secondary organoids.

(D) As in (A), with luminal cells from 3- and 24-month-old mouse prostates. Scale bars, 250 μm.

(E) As in (B), measuring organoids derived from luminal cells.

(F) As in (C), with organoids derived from luminal cells.

(G and H) Representative immunofluorescent and differential interference contrast (DIC) images of basal-derived (G) and luminal-derived (H) organoids from adult and old mice. Staining for p63 (red), K8 (Keratin 8, green), and DAPI (blue) individually and merged. Scale bars, 100 μm. Note: old luminal group is zoomed out to include large organoid. Data represent mean ± SEM of three to five biological replicates.

****$p < 0.0001$. n.s., not significant, $p \geq 0.05$. Mo, months of age.

See also Figure S3.

luminal cells from old mice compared with adult mice (Figure S4B), including several genes related to the extracellular matrix (*Col1a1*, *Col1a2*, *Col3a1*, *Sparc*). Reduced expression of collagen genes in old epithelial cells is consistent with a previous report (Bianchi-Frias et al., 2010).

Gene Ontology analysis was performed on gene sets significantly upregulated in each cell type and age, demonstrating that adult basal cells were enriched in terms related to cell adhesion and migration (Figure S4C), whereas the old basal cell signature was associated with ribosome biogenesis (Figure S4D). Within the luminal cells, the adult signature was enriched in male sex differentiation and gonad development (Figure S4E). Several gene ontology terms of interest were enriched in old luminal cells including cell motility and migration, angiogenesis, and inflammatory response (Figure S4F).

A similar signature was previously demonstrated in CD38^{low} luminal progenitor cells in the human prostate (Liu et al., 2016), suggesting that aged mouse prostate luminal cells may share features with human luminal progenitor cells. Several markers of human prostate luminal progenitors, including elevated *Bcl2*, *Cd74*, *Pigr*, and *Psca* and low *Cd38*, are associated with aged mouse prostate luminal cells (Figure 4B). Gene set enrichment analysis was used to demonstrate that the aged mouse prostate luminal signature significantly overlaps with the CD38^{low} luminal progenitor signature (Figure 4C).

Elevated Expression of Trop2 in Old Luminal Cells

Old luminal cells were found to express elevated transcript levels of several stem and progenitor cell markers including *Cd44*, *Itga2*, and *Tacstd2* (*Trop2*) (Figure 4B). We performed flow cytometry to measure mean fluorescence intensity (MFI) of Trop2 expression on basal and luminal cells from adult and old mouse prostates. Although Trop2 expression does not change with age on basal cells, old luminal cells express significantly higher levels of Trop2 than adult luminal cells (Figures 4D–4F).

Mechanistically, we wondered whether progenitor genes including *Trop2* are elevated uniformly in old luminal cells

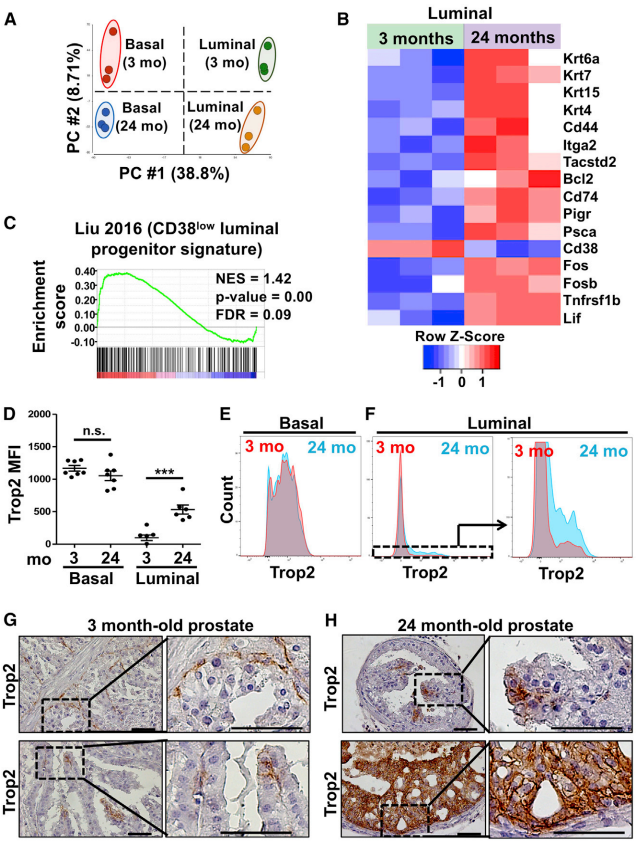

Figure 4. Increased Trop2 Expression in Luminal Cells from Old Mouse Prostate

(A) Principal component analysis of RNA sequencing data for basal and luminal cells from 3- and 24-month-old mice with three biological replicates per age.

(B) Heatmap of selected differentially expressed genes from RNA sequencing of luminal cells from 3- and 24-month-old mice with three biological replicates per age.

(C) Gene set enrichment analysis comparing 24-month-old mouse luminal cell signature with human CD38^{low} luminal cell signature, showing normalized enrichment score (NES) and false discovery rate (FDR).

(D) Trop2 mean fluorescence intensity (MFI) measured by flow cytometry in basal and luminal cells isolated from 3- and 24-month-old prostates with five to seven biological replicates per age. Data represent mean ± SEM.

(E and F) Histogram of Trop2 expression in basal cells (E) and luminal cells (F) from 3- and 24-month-old mice measured by flow cytometry.

(F) Boxed region on left is expanded in the right panel.

(G and H) Immunohistochemical analysis of representative prostate glands from adult (G) and old (H) mice stained for Trop2. Scale bars, 50 μm.

***p < 0.001. n.s. = not significant, p ≥ 0.05. Mo = months of age.

See also Figures S4 and S5.

or whether there is an age-related expansion of a pre-existing progenitor-like luminal population. By flow cytometry, a subset of luminal cells from both adult and old prostates appeared to express elevated levels of Trop2 (Figure 4F). We utilized immunohistochemistry to evaluate Trop2 expression in adult and old prostate tissue. Trop2 expression was observed on the vast majority of basal cells (Figures 4G and 4H), as well as on proximally located luminal cells in both adult and old prostates, as we have previously reported (Goldstein et al., 2008). In distal regions of adult and old prostates, we observed Trop2-expressing luminal cells in ridges protruding into the lumen of ducts (Figures 4G and 4H), where distally located label-retaining luminal cells were reported to reside (Tsujimura et al., 2002). In old prostates, Trop2-expressing luminal cells were also observed in rare regions with epithelial hyperplasia (Figures 4H and S5).

Trop2 Expression Defines a Subset of Large Organoid-Forming Luminal Progenitor Cells

Using FACS, we isolated a subpopulation of Trop2$^+$ luminal cells from preparations of dissociated adult prostate comprising approximately 5%–6% of total CD49f^{lo} EpCAM$^+$ luminal cells. Trop2$^+$ and Trop2$^-$ luminal cells express comparable levels of the luminal marker K18 and low or absent expression of basal markers K5 and K14 (Figures S6A–S6C). Interestingly, the Trop2$^+$ fraction exhibited a greater proportion of Ki67$^+$ cells (Figure 5A), suggesting that Trop2$^+$ and Trop2$^-$ subsets may be functionally distinct. Upon plating both luminal subpopulations from adult prostate into the organoid-forming assay, we found that Trop2$^+$ luminal cells were capable of forming organoids at a higher rate (Figure 5B). Furthermore, organoids derived from Trop2$^+$ luminal cells were considerably larger than organoids derived from Trop2$^-$ luminal cells (Figure 5C). Both Trop2$^+$ and Trop2$^-$ luminal cells generated organoids containing one or two layers of cells with high expression of K8, whereas Trop2$^+$ luminal-derived organoids tended to express higher levels of p63 than Trop2$^-$ luminal-derived organoids (Figures 5D and 5E). These differences in functional capacity suggest that Trop2$^+$ luminal cells represent a progenitor-enriched subpopulation from the adult prostate.

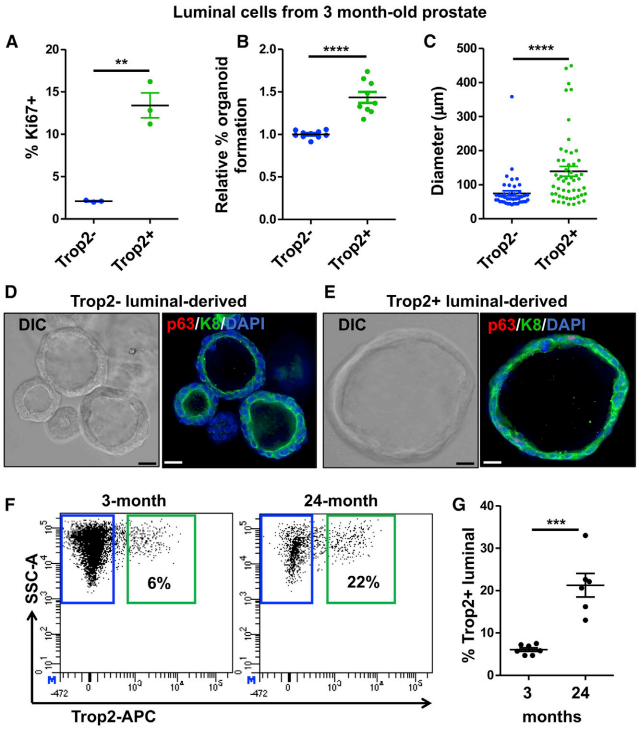

Figure 5. Trop2$^+$ Luminal Cells Represent a Progenitor-Enriched Subpopulation that Is Expanded with Age

(A) Percentage of Ki67$^+$ cells within the Trop2$^-$ and Trop2$^+$ luminal fractions from adult mice measured using intracellular flow cytometry with three biological replicates.

(B) Relative percent organoid formation of Trop2$^-$ and Trop2$^+$ luminal cells isolated from adult mouse prostate, normalized to Trop2$^-$ luminal cells from each replicate experiment.

(C) Quantification of diameter of luminal-derived primary organoids from Trop2$^-$ and Trop2$^+$ luminal cells from adult mice.

(D and E) Representative differential interference contrast (DIC, left) and immunofluorescent images (right) of Trop2$^-$ luminal-derived (D) and Trop2$^+$ luminal-derived (E) organoids stained for p63 (red), K8 (green), and DAPI (blue). Three small organoids derived from Trop2$^-$ luminal cells are shown in (D). Scale bars, 20 μm.

(F) Representative flow cytometry plots illustrating the percentage of luminal cells that stain positively for Trop2 in adult and old mouse prostates. SSC-A, side scatter.

(G) The percentage of luminal cells that express Trop2 as measured by flow cytometry with six to seven biological replicates per age. Data represent mean ± SEM.

**p < 0.01, ***p < 0.001, ****p < 0.0001.

See also Figure S6.

Age-Related Expansion of Trop2$^+$ Luminal Progenitor Cells

The mean percentage of Trop2$^+$ luminal cells increased from 6% in adult to 21% in old prostates (Figures 5F and 5G), indicating a significant age-related expansion of this subpopulation. Similar fractions of Trop2$^+$ and Trop2$^-$ luminal cells were observed when comparing total dissociated cells and DAPI-negative viable cells (Figures S6D and S6E), ruling out the possibility that the expanded Trop2$^+$ fraction in old prostates is a result of preferential survival during dissociation.

To determine whether luminal subsets defined by Trop2 expression retain their gene signature with age, we performed RNA-seq on Trop2$^+$ and Trop2$^-$ luminal cells from adult and old mice. When comparing genes that were greater than 1.5-fold enriched in Trop2$^+$ luminal cells with a p value <0.05 and FDR < 0.1, we identified 1,121 genes in the adult and 1,252 genes in the old prostate associated with a Trop2$^+$ luminal signature. Importantly, the majority of these genes were shared by both adult (66%) and old (59%) Trop2$^+$ luminal cells (Figure 6A), suggesting an age-related maintenance of the core Trop2$^+$ progenitor signature. Interestingly, the Trop2$^+$ luminal signature includes *Psca* (Figures 6B and 6C), a marker of human prostate luminal progenitor cells (Liu et al., 2016) that was recently shown to define a distinct luminal subset in prostate tissues from healthy human donors (Henry et al., 2018). CD44, a marker of stem and progenitor cells in several epithelial tissues including prostate (Garraway et al., 2010), was also found in the Trop2$^+$ signature and validated at the protein level by flow cytometry (Figures 6D and 6E).

Similar analysis of genes enriched in Trop2$^-$ luminal cells revealed considerable overlap between adult (61%) and old (41%) prostates (Figure 6A). The degree of overlap within Trop2$^-$ luminal cells was lower than that of Trop2$^+$ luminal cells, which may reflect increased responsiveness to age-related signals from the microenvironment. Alternatively, the Trop2$^-$ luminal subset may contain a greater degree of heterogeneity that has yet to be defined.

Trop2$^+$ Luminal Cells Maintain Progenitor Activity with Age

We evaluated the functional capacity of Trop2$^+$ and Trop2$^-$ luminal cells from both adult and old mice to determine the effect of age on progenitor capacity within each phenotypically defined subset. Both adult and old Trop2$^+$ luminal cells form organoids at similar rates and generate structures of similar size (Figures 6F–6H), indicating an age-related maintenance of the progenitor activity from this subpopulation. In contrast, Trop2$^-$ luminal cells from old prostates have a diminished

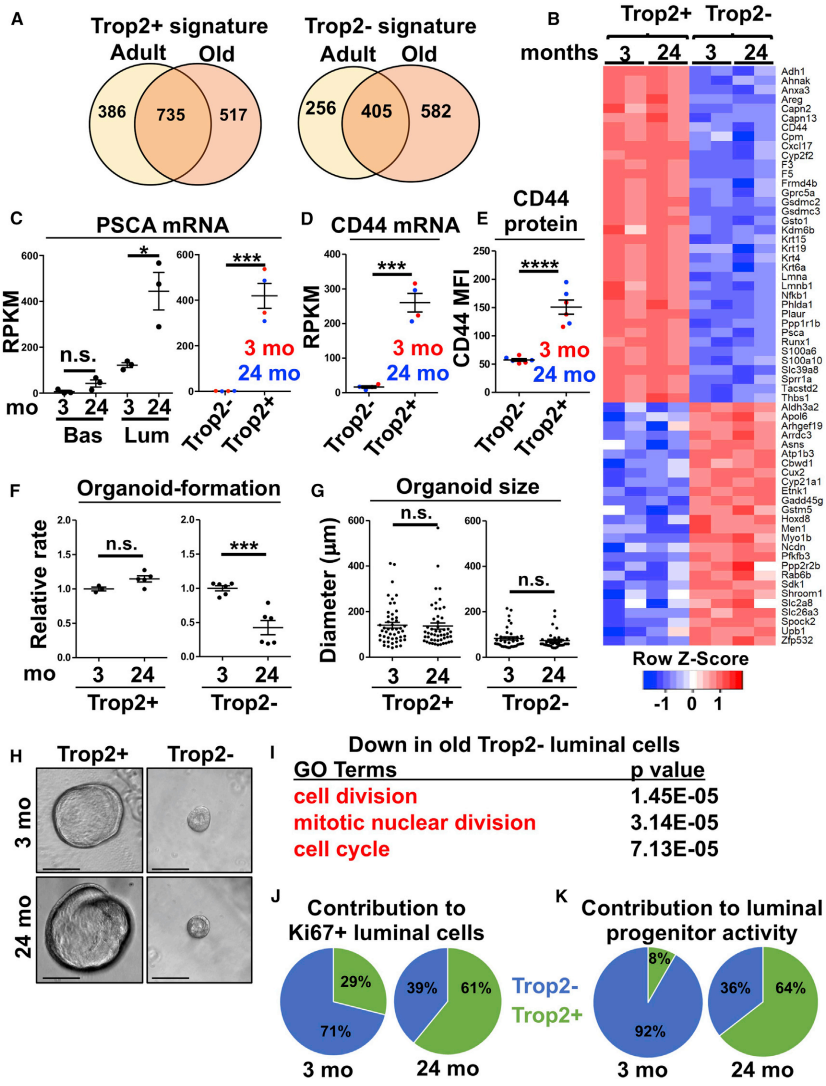

Figure 6. Trop2^{+} Luminal Signature and Progenitor Activity Are Maintained with Age

(A) Venn diagram shows the number of genes that are significantly upregulated in Trop2^{+} luminal cells (left) or Trop2^{-} luminal cells (right) from adult and old mouse prostate.

(B) Heatmap showing representative genes in the Trop2^{+} and Trop2^{-} luminal signatures, with biological replicates of each subset from adult and old mice.

(C) *Psca* mRNA in basal and luminal cells (left) and Trop2^{+} and Trop2^{-} luminal cells (right) shown as reads per kilobase of transcript per million mapped reads (RPKM).

(D) As in (C), with expression of *Cd44* in Trop2^{+} and Trop2^{-} luminal cells.

(E) Mean fluorescence intensity (MFI) of CD44 in Trop2^{+} and Trop2^{-} luminal cells from adult and old mice measured with flow cytometry.

(legend continued on next page)

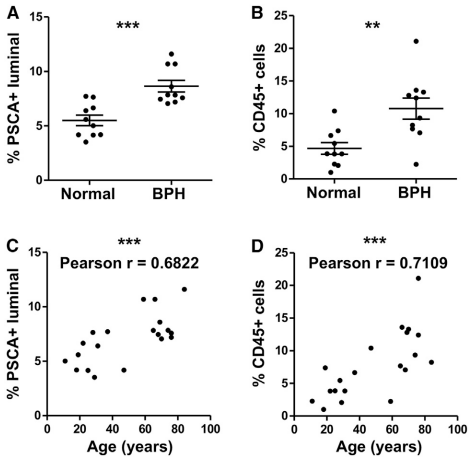

Figure 7. Human PSCA$^+$ Luminal Cells and Inflammatory Cells Expand in Aging and BPH

(A) The percentage of luminal (CD45$^-$ EpCAM$^+$ PDPN$^-$ CD26$^{low/+}$) cells that express PSCA in dissociated human prostate preparations from 10 men with BPH and 10 organ donors.

(B) As in (A), but measuring the percentage of total dissociated human prostate cells expressing CD45 as measured by flow cytometry. Data represent mean ± SEM.

(C) Plots show correlation between the percentage of luminal cells that express PSCA and patient age.

(D) Plots show correlation between the percentage of prostate cells that express CD45 and patient age.

**p < 0.01, ***p < 0.001.

capacity to form organoids with a trend toward reduced organoid size (Figures 6F–6H). The reduced organoid-forming activity of old Trop2- luminal cells correlates with a decline in gene expression associated with gene ontology terms cell division, mitotic nuclear division, and cell cycle (Figure 6I).

We multiplied the percentage of luminal cells that are Trop2$^+$ or Trop2$^-$ by the proliferative index (% Ki67$^+$) within each luminal subset to determine the contribution of each subset to total proliferating luminal cells in the mouse prostate. Whereas the majority of proliferating luminal cells in the adult prostate are Trop2$^-$, the majority of proliferating luminal cells in the old prostate express Trop2 (Figure 6J). We quantified the contribution of Trop2$^+$ and Trop2$^-$ cells to total luminal progenitor activity by multiplying the percentage of Trop2$^+$ or Trop2$^-$ luminal cells by the rate of organoid formation for each subset. Whereas 8% of luminal organoids in the young prostate are generated by Trop2$^+$ cells, 64% of luminal organoids in the old prostate arise from Trop2$^+$ progenitor cells (Figure 6K), representing a dramatic age-related shift in the luminal compartment.

Human PSCA$^+$ Luminal Cells and Inflammatory Cells Expand in Aging and BPH

Having demonstrated a significant overlap in gene expression between Trop2$^+$ luminal cells and human luminal progenitor cells, we asked whether luminal progenitor cells are expanded with age in human prostate. Using PSCA as a marker of human prostate luminal progenitor cells (Liu et al., 2016), we evaluated the frequency of PSCA$^+$ luminal cells (Henry et al., 2018) in human prostate tissues from young healthy men and older men with BPH. We observed a significant increase in the percentage of PSCA$^+$ luminal cells in prostates from men with BPH compared with normal prostates from organ donors (Figure 7A). Interestingly, we also found a significant increase in the proportion of CD45$^+$ immune cells in BPH compared with normal prostates (Figure 7B). Both PSCA$^+$ luminal cells and CD45$^+$ immune cells are positively correlated with age in the human prostate (Figures 7C and 7D).

DISCUSSION

Aging is thought to play an important role in the development of BPH and prostate cancer. In this study, we examined the progenitor capacity of the prostate epithelium and found that basal and luminal cells from old mice maintain their organoid-forming activity. Luminal cells from old mice exhibit a progenitor-like signature and generate larger organoids than young adult luminal cells (Figures 3E, 4B, and 4C). We set out to determine whether luminal cells gain progenitor features with age or whether there is an age-related expansion of a pre-existing luminal progenitor subset. We found that Trop2 expression defines a unique subset of luminal cells in the adult prostate that generate large organoids (Figures 4F, 5B, and 5C). The Trop2$^+$ luminal fraction is dramatically expanded with age and contributes to the vast majority of luminal progenitor activity in old mouse prostate (Figures 5F, 5G, and 6K). The age-related expansion of progenitor-like luminal cells was also found in the human prostate in men with BPH (Figure 7A), suggesting that luminal progenitor cells may play a functional role in the disease. In addition to an age-related expansion of luminal progenitor cells, we also found an age-related increase in inflammatory cells in both mouse and human prostates (Figures 7C and 7D). Although mice are not known to develop BPH, our

(F) Relative percent organoid formation of Trop2$^-$ and Trop2$^+$ luminal cells isolated from adult and old prostate, normalized to adult prostate from each replicate experiment.

(G) Quantification of diameter of luminal-derived primary organoids from Trop2$^-$ and Trop2$^+$ luminal cells from adult and old mice. Data represent mean ± SEM.

(H) Representative images of organoids derived from adult and old Trop2$^+$ and Trop2$^-$ luminal cells. Scale bars, 100 μm.

(I) Gene ontology terms of gene sets downregulated in old compared with adult Trop2$^-$ luminal cells.

(J and K) Pie charts representing the contribution of Trop2$^-$ luminal (blue) and Trop2$^+$ luminal (green) cells to total proliferating (Ki67$^+$) luminal cells (J) and total luminal organoid formation (K). Relative rates of proliferation (J) or organoid formation (K) for Trop2$^+$ and Trop2$^-$ luminal cells were multiplied by the percentage of total luminal cells with a Trop2$^+$ or Trop2$^-$ phenotype, and represented as the ratio of total luminal proliferation or organoid formation from each subset.

*p < 0.05, ***p < 0.001, ****p < 0.0001. n.s. = not significant, p ≥ 0.05. Mo = months of age.

results suggest that further study of mouse prostate aging may reveal mechanisms relevant to BPH.

It remains unclear what mechanisms are responsible for the age-related expansion of Trop2$^+$ luminal cells in the mouse prostate. Basal cells exhibit higher proliferation rates than luminal cells at both 3 and 24 months of age (Figure S3A), consistent with results in the human prostate (Moad et al., 2017). Within the luminal compartment, we observed significantly greater proliferation from the Trop2$^+$ subset in adult mice (Figure 5A). Whether proliferating Trop2$^+$ luminal cells undergo self-renewing divisions or give rise to Trop2$^-$ luminal cells has not been established. An age-related expansion of Trop2$^+$ luminal cells may result from a sustained proliferative advantage within this subset throughout life. Trop2$^+$ luminal cells may also be derived from other epithelial populations, such as basal cells or Trop2$^-$ luminal cells. Lineage tracing will be necessary to distinguish these possibilities.

One possibility is that systemic or local signals originating outside of the epithelium may contribute to the age-related expansion of Trop2$^+$ luminal cells. Given that old mice are heavier than adult mice and contain a greater amount of adipose tissue, we hypothesized that increased body fat in adult mice may replicate the aging phenotype. However, we did not observe an expansion of Trop2$^+$ luminal cells in adult mice fed a high-fat diet for 3 months (Figures S7A–S7F), suggesting that increased body fat in old mice is not likely to drive the luminal progenitor expansion. Changes in hormone levels may play a role in the expansion of Trop2$^+$ luminal cells, as we have previously demonstrated a dramatic increase in Trop2$^+$ luminal cells in the castrated mouse prostate (Goldstein et al., 2008). It remains unclear whether the increase in Trop2$^+$ luminal cells in the castrated prostate arises out of an expansion of pre-existing Trop2$^+$ luminal cells or through the increased expression of Trop2 in castration-resistant luminal cells. Additional studies will be required to define the cues that drive an age-related expansion of luminal progenitor cells.

The age-related expansion of luminal progenitor cells may also increase the risk for prostate cancer initiation. Using a variety of *in vivo* approaches with mouse and human prostate tissue, we and others have established that progenitor cells within both the basal and the luminal layers are capable of initiating prostate cancer in response to genetic alterations (Choi et al., 2012; Goldstein et al., 2008, 2010; Kwon et al., 2014; Lawson et al., 2010; Lu et al., 2013; Park et al., 2016; Stoyanova et al., 2013; Wang et al., 2009, 2013). Therefore, as luminal progenitor cells expand with age in the prostate, the pool of potential target cells for transformation likely expands as well. Future work will be aimed at determining whether aged prostate epithelial cells are more susceptible to oncogenic transformation.

STAR★METHODS

Detailed methods are provided in the online version of this paper and include the following:

- KEY RESOURCES TABLE
- LEAD CONTACT AND MATERIALS AVAILABILITY
- EXPERIMENTAL MODEL AND SUBJECT DETAILS
  - Animal Work
  - Collection of Mouse Prostate Tissue
  - Collection of Human Prostate Tissue
- METHOD DETAILS
  - Quantification of Branch Points
  - Mouse Prostate Dissociation to Single Cells
  - Human Prostate Processing
  - Staining and Sorting Cells from Mouse Prostate
  - Intracellular Flow Cytometry
  - Organoid Culture and Assays
  - Immunoblot Analysis
  - Immunohistochemistry
  - Antibodies for Mass Cytometry
  - Cell Surface Staining for Mass Cytometry
  - Mass Cytometry
  - RNaseq
- QUANTIFICATION AND STATISTICAL ANALYSIS
  - RNaseq Analysis
  - CyTOF Clustering
  - Statistical Analysis
- DATA AND CODE AVAILABILITY

SUPPLEMENTAL INFORMATION

Supplemental Information can be found online at https://doi.org/10.1016/j.celrep.2019.07.007.

ACKNOWLEDGMENTS

We thank the families of organ donors at the Southwest Transplant Alliance for their commitment to basic science research. Special thanks to Donghui Cheng for cell sorting, Jack Mottahedeh for mouse work, Tom Carmichael and Stacey Gallegos for aged mice, Enca Montecino-Rodriguez and Ken Dorshkind for high-fat-diet mice, and Miriam Guemes for CyTOF sample acquisition. Mass cytometry was performed in the UCLA Jonsson Comprehensive Cancer Center (JCCC) and Center for AIDS Research Flow Cytometry Core Facility that is supported by NIH awards P30 CA016042 and 5P30 AI028697. The purchase of the Helios/CyTOF mass cytometer that was used in this work was, in part, supported by funds provided by the James B. Pendleton Charitable Trust. J.J.F. is supported by a scholarship from the UCLA Minor in Biomedical Research and the Silva Endowment as part of the Undergraduate Research Scholars Program at UCLA. P.D.C. and M.G.L. are supported by the Ruth L. Kirschstein National Research Service Award GM007185. H.I.N. is supported by the Eugene V. Cota-Robles Fellowship. J.A.D. is supported by the National Institute of General Medical Sciences of the NIH (R25GM055052 awarded to T. Hasson) and the Saul Martinez Scholarship. A.S.G. is supported by the Spitzer Family Foundation Fund and the Gill Endowment. This work was supported by the American Cancer Society (RSG-17-068-01-TBG), Department of Defense (W81XWH-13-1-0470), Margaret E. Early Medical Research Trust, STOP CANCER, NIH/NCI (P50CA092131/UCLA SPORE in Prostate Cancer), UCLA Eli and Edythe Broad Center of Regenerative Medicine and Stem Cell Research Rose Hills Foundation Innovator Grant, and support from UCLA's Jonsson Comprehensive Cancer Center, Broad Stem Cell Research Center, Clinical and Translational Science Institute, and Institute of Urologic Oncology. D.W.S. is supported by the NIH/NIDDK (R01 DK115477). We thank UCLA's Technology Center for Genomics and Bioinformatics, Translational Pathology Core Laboratories, and UCLA's Institute for Quantitative and Computational Biology. The anti-alpha-tubulin monoclonal antibody (12G10) was obtained from the Developmental Studies Hybridoma Bank, created by the NICHD of the NIH and maintained at the University of Iowa, Department of Biology, Iowa City, IA.

AUTHOR CONTRIBUTIONS

P.D.C., J.J.F., T.H., J.A.D., H.I.N., B.A.F., and M.G.L. conducted the experiments. P.D.C., J.J.F., and A.S.G. designed the experiments. P.D.C., J.J.F., and A.S.G. wrote and edited the manuscript. Y.E.W. performed bioinformatics analyses and wrote part of the manuscript. A.J.G. assisted with CyTOF samples and wrote part of the manuscript. D.P.S. provided pathology expertise and wrote part of the manuscript. G.H.H. and D.W.S. performed human prostate experiments and wrote part of the manuscript. A.S.G. procured funding and supervised the experiments.

DECLARATION OF INTERESTS

The authors declare no competing interests.

Received: November 14, 2018
Revised: March 29, 2019
Accepted: June 28, 2019
Published: August 6, 2019

REFERENCES

Baumgartner, R.N., Koehler, K.M., Gallagher, D., Romero, L., Heymsfield, S.B., Ross, R.R., Garry, P.J., and Lindeman, R.D. (1998). Epidemiology of sarcopenia among the elderly in New Mexico. Am. J. Epidemiol. *147*, 755–763.

Bianchi-Frias, D., Vakar-Lopez, F., Coleman, I.M., Plymate, S.R., Reed, M.J., and Nelson, P.S. (2010). The effects of aging on the molecular and cellular composition of the prostate microenvironment. PLoS ONE *5*, e12501.

Choi, N., Zhang, B., Zhang, L., Ittmann, M., and Xin, L. (2012). Adult murine prostate basal and luminal cells are self-sustained lineages that can both serve as targets for prostate cancer initiation. Cancer Cell *21*, 253–265.

Chua, C.W., Shibata, M., Lei, M., Toivanen, R., Barlow, L.J., Bergren, S.K., Badani, K.K., McKiernan, J.M., Benson, M.C., Hibshoosh, H., and Shen, M.M. (2014). Single luminal epithelial progenitors can generate prostate organoids in culture. Nat. Cell Biol. *16*, 951–961, 1–4.

Conboy, I.M., Conboy, M.J., Smythe, G.M., and Rando, T.A. (2003). Notch-mediated restoration of regenerative potential to aged muscle. Science *302*, 1575–1577.

Drost, J., Karthaus, W.R., Gao, D., Driehuis, E., Sawyers, C.L., Chen, Y., and Clevers, H. (2016). Organoid culture systems for prostate epithelial and cancer tissue. Nat. Protoc. *11*, 347–358.

Garraway, I.P., Sun, W., Tran, C.P., Perner, S., Zhang, B., Goldstein, A.S., Hahm, S.A., Haider, M., Head, C.S., Reiter, R.E., et al. (2010). Human prostate sphere-forming cells represent a subset of basal epithelial cells capable of glandular regeneration in vivo. Prostate *70*, 491–501.

Goldstein, A.S., Lawson, D.A., Cheng, D., Sun, W., Garraway, I.P., and Witte, O.N. (2008). Trop2 identifies a subpopulation of murine and human prostate basal cells with stem cell characteristics. Proc. Natl. Acad. Sci. USA *105*, 20882–20887.

Goldstein, A.S., Huang, J., Guo, C., Garraway, I.P., and Witte, O.N. (2010). Identification of a cell of origin for human prostate cancer. Science *329*, 568–571.

Henry, G.H., Malewska, A., Joseph, D.B., Malladi, V.S., Lee, J., Torrealba, J., Mauck, R.J., Gahan, J.C., Raj, G.V., Roehrborn, C.G., et al. (2018). A Cellular Anatomy of the Normal Adult Human Prostate and Prostatic Urethra. Cell Rep. *25*, 3530–3542.e5.

Huang, W., Sherman, B.T., and Lempicki, R.A. (2009). Systematic and integrative analysis of large gene lists using DAVID bioinformatics resources. Nat. Protoc. *4*, 44–57.

Ito, R., Takahashi, T., Katano, I., and Ito, M. (2012). Current advances in humanized mouse models. Cell. Mol. Immunol. *9*, 208–214.

Ittmann, M., Huang, J., Radaelli, E., Martin, P., Signoretti, S., Sullivan, R., Simons, B.W., Ward, J.M., Robinson, B.D., Chu, G.C., et al. (2013). Animal models of human prostate cancer: the consensus report of the New York meeting of the Mouse Models of Human Cancers Consortium Prostate Pathology Committee. Cancer Res. *73*, 2718–2736.

Karthaus, W.R., Iaquinta, P.J., Drost, J., Gracanin, A., van Boxtel, R., Wongvipat, J., Dowling, C.M., Gao, D., Begthel, H., Sachs, N., et al. (2014). Identification of multipotent luminal progenitor cells in human prostate organoid cultures. Cell *159*, 163–175.

Klein, R., Klein, B.E., and Linton, K.L. (1992). Prevalence of age-related maculopathy. The Beaver Dam Eye Study. Ophthalmology *99*, 933–943.

Kwon, O.J., Zhang, L., Ittmann, M.M., and Xin, L. (2014). Prostatic inflammation enhances basal-to-luminal differentiation and accelerates initiation of prostate cancer with a basal cell origin. Proc. Natl. Acad. Sci. USA *111*, E592–E600.

Lai, K.P., Yamashita, S., Vitkus, S., Shyr, C.R., Yeh, S., and Chang, C. (2012). Suppressed prostate epithelial development with impaired branching morphogenesis in mice lacking stromal fibromuscular androgen receptor. Mol. Endocrinol. *26*, 52–66.

Langmead, B., and Salzberg, S.L. (2012). Fast gapped-read alignment with Bowtie 2. Nat. Methods *9*, 357–359.

Lawson, D.A., Zong, Y., Memarzadeh, S., Xin, L., Huang, J., and Witte, O.N. (2010). Basal epithelial stem cells are efficient targets for prostate cancer initiation. Proc. Natl. Acad. Sci. USA *107*, 2610–2615.

Li, B., and Dewey, C.N. (2011). RSEM: accurate transcript quantification from RNA-Seq data with or without a reference genome. BMC Bioinformatics *12*, 323.

Liu, X., Grogan, T.R., Hieronymus, H., Hashimoto, T., Mottahedeh, J., Cheng, D., Zhang, L., Huang, K., Stoyanova, T., Park, J.W., et al. (2016). Low CD38 Identifies Progenitor-like Inflammation-Associated Luminal Cells that Can Initiate Human Prostate Cancer and Predict Poor Outcome. Cell Rep. *17*, 2596–2606.

López-Otín, C., Blasco, M.A., Partridge, L., Serrano, M., and Kroemer, G. (2013). The hallmarks of aging. Cell *153*, 1194–1217.

Lu, T.L., Huang, Y.F., You, L.R., Chao, N.C., Su, F.Y., Chang, J.L., and Chen, C.M. (2013). Conditionally ablated Pten in prostate basal cells promotes basal-to-luminal differentiation and causes invasive prostate cancer in mice. Am. J. Pathol. *182*, 975–991.

Mair, F., Hartmann, F.J., Mrdjen, D., Tosevski, V., Krieg, C., and Becher, B. (2016). The end of gating? An introduction to automated analysis of high dimensional cytometry data. Eur. J. Immunol. *46*, 34–43.

Meier-Ruge, W., Ulrich, J., Brühlmann, M., and Meier, E. (1992). Age-related white matter atrophy in the human brain. Ann. N Y Acad. Sci. *673*, 260–269.

Moad, M., Hannezo, E., Buczacki, S.J., Wilson, L., El-Sherif, A., Sims, D., Pickard, R., Wright, N.A., Williamson, S.C., Turnbull, D.M., et al. (2017). Multipotent Basal Stem Cells, Maintained in Localized Proximal Niches, Support Directed Long-Ranging Epithelial Flows in Human Prostates. Cell Rep. *20*, 1609–1622.

Molofsky, A.V., Slutsky, S.G., Joseph, N.M., He, S., Pardal, R., Krishnamurthy, J., Sharpless, N.E., and Morrison, S.J. (2006). Increasing p16INK4a expression decreases forebrain progenitors and neurogenesis during ageing. Nature *443*, 448–452.

Niccoli, T., and Partridge, L. (2012). Ageing as a risk factor for disease. Curr. Biol. *22*, R741–R752.

Park, J.W., Lee, J.K., Phillips, J.W., Huang, P., Cheng, D., Huang, J., and Witte, O.N. (2016). Prostate epithelial cell of origin determines cancer differentiation state in an organoid transformation assay. Proc. Natl. Acad. Sci. USA *113*, 4482–4487.

Robinson, M.D., McCarthy, D.J., and Smyth, G.K. (2010). edgeR: a Bioconductor package for differential expression analysis of digital gene expression data. Bioinformatics *26*, 139–140.

Roehrborn, C.G. (2005). Benign prostatic hyperplasia: an overview. Rev. Urol. *7* (*Suppl 9*), S3–S14.

Simpson, J.G., Gray, E.S., and Beck, J.S. (1975). Age involution in the normal human adult thymus. Clin. Exp. Immunol. *19*, 261–265.

Stoyanova, T., Cooper, A.R., Drake, J.M., Liu, X., Armstrong, A.J., Pienta, K.J., Zhang, H., Kohn, D.B., Huang, J., Witte, O.N., and Goldstein, A.S. (2013). Prostate cancer originating in basal cells progresses to adenocarcinoma propagated by luminal-like cells. Proc. Natl. Acad. Sci. USA *110*, 20111–20116.

Subramanian, A., Tamayo, P., Mootha, V.K., Mukherjee, S., Ebert, B.L., Gillette, M.A., Paulovich, A., Pomeroy, S.L., Golub, T.R., Lander, E.S., and Mesirov, J.P. (2005). Gene set enrichment analysis: a knowledge-based approach for interpreting genome-wide expression profiles. Proc. Natl. Acad. Sci. USA *102*, 15545–15550.

Tsujimura, A., Koikawa, Y., Salm, S., Takao, T., Coetzee, S., Moscatelli, D., Shapiro, E., Lepor, H., Sun, T.T., and Wilson, E.L. (2002). Proximal location of mouse prostate epithelial stem cells: a model of prostatic homeostasis. J. Cell Biol. *157*, 1257–1265.

van Deursen, J.M. (2014). The role of senescent cells in ageing. Nature *509*, 439–446.

Wang, X., Kruithof-de Julio, M., Economides, K.D., Walker, D., Yu, H., Halili, M.V., Hu, Y.P., Price, S.M., Abate-Shen, C., and Shen, M.M. (2009). A luminal epithelial stem cell that is a cell of origin for prostate cancer. Nature *461*, 495–500.

Wang, Z.A., Mitrofanova, A., Bergren, S.K., Abate-Shen, C., Cardiff, R.D., Califano, A., and Shen, M.M. (2013). Lineage analysis of basal epithelial cells reveals their unexpected plasticity and supports a cell-of-origin model for prostate cancer heterogeneity. Nat. Cell Biol. *15*, 274–283.

Young, M.D., Wakefield, M.J., Smyth, G.K., and Oshlack, A. (2010). Gene ontology analysis for RNA-seq: accounting for selection bias. Genome Biol. *11*, R14.

STAR★METHODS

KEY RESOURCES TABLE

REAGENT or RESOURCE	SOURCE	IDENTIFIER
Antibodies		
Rat anti-CD49f-PE	BioLegend	Cat#313612; RRID: AB_893373
Rat anti-EpCAM-APC/Cy7	BioLegend	Cat#118218; RRID: AB_2098648
Rat anti-CD31-FITC	BioLegend	Cat#102405; RRID: AB_312900
Rat anti-CD45-FITC	BioLegend	Cat#103107; RRID: AB_312972
Rat anti-Ter119-FITC	BioLegend	Cat#116205; RRID: AB_313706
Rat anti-ESAM-FITC	BioLegend	Cat#136205; RRID: AB_2044017
Goat anti-mouse TROP-2-APC	R & D Systems	Cat#FAB1122A; RRID: AB_2287133
Rat anti-CD44-FITC	BioLegend	Cat#103021; RRID: AB_493684
Rabbit anti-cytokeratin 5-Alexa Fluor 647	Abcam	Cat#ab193895; RRID: AB_2728796
Rabbit anti-cytokeratin 8-Alexa Fluor 488	Abcam	Cat#ab192467
Mouse anti-cytokeratin 14-FITC	Abcam	Cat#ab77684; RRID: AB_2265437
Mouse anti-cytokeratin 18-FITC	Abcam	Cat#ab52459; RRID: AB_869874
Rat anti-Ki67-FITC	BioLegend	Cat#652409; RRID: AB_2562140
Goat anti-mouse IgG-Alexa Fluor 488	Invitrogen	Cat#A28175; RRID: AB_2536161
Goat anti-rabbit IgG-Alexa Fluor 594	Invitrogen	Cat#A11012; RRID: AB_141359
Goat anti-rabbit IgG-Alexa Fluor 647	Invitrogen	Cat#A-21244; RRID: AB_141663
Goat anti-mouse IgG-Alexa Fluor 647	Invitrogen	Cat#A-21235; RRID: AB_141693
Goat anti-rabbit IgG, HRP-conjugated	Invitrogen	Cat#31463; RRID: AB_228333
Goat anti-mouse IgG, HRP-conjugated	Invitrogen	Cat#31430; RRID: AB_228307
Rabbit anti-goat IgG, HRP-conjugated	Invitrogen	Cat#31402; RRID: AB_228395
Rabbit anti-keratin 5	BioLegend	Cat#905504; RRID: AB_2616956
Goat anti-Tp63	R & D Systems	Cat#AF1916-SP; RRID: AB_2207174
Rabbit anti-p63	BioLegend	Cat#619002; RRID: AB_2207170
Goat anti-mouse TROP-2	R & D Systems	Cat# AF1122-SP; RRID: AB_2205662
Mouse anti-cytokeratin 8	Biolegend	Cat#904804; RRID: AB_2616821
Rabbit anti-Prom1	Abnova	Cat#PAB12663; RRID: AB_10554766
Rabbit anti-Ki67	Abcam	Cat#ab15580; RRID: AB_443209
Mouse anti-tubulin	DSHB	Cat#12G10; RRID: AB_1157911
TruStain fcX (rat anti-mouse CD16/32) Antibody	BioLegend	Cat#101319; RRID: AB_1574973
Anti-mouse CD45 (clone 30-F11)-89Y	DVS	Cat#3089005B; RRID: AB_2651152
Anti-mouse CD27 (clone LG.3A10)	BioLegend	Cat#124202; RRID: AB_1236456
Anti-mouse CD138 (clone 281-2)	BioLegend	Cat#142502; RRID: AB_10965646
Anti-mouse CD45R (clone RA3-6B2)-144Nd	DVS	Cat#3144011B
Anti-mouse CD4 (clone RM4-5)-145Nd	DVS	Cat#3145002B; RRID: AB_2687832
Anti-mouse F4/80 (clone BM8)-146Nd	DVS	Cat#3146008B
Anti-mouse CD45 (clone 30-F11)-147Sm	DVS	Cat#3147003B
Anti-mouse CD11b (clone M1/70)-148Nd	DVS	Cat#3148003B
Anti-mouse CD3e (clone 145-2C11)-152Sm	DVS	Cat#3152004B; RRID: AB_2687836
Anti-mouse CD25 (clone 3C7)	BioLegend	Cat#101913; RRID: AB_2562798
Anti-mouse Ly6C (clone HK1.4)-162Dy	DVS	Cat#3162014B
Anti-mouse CD19 (clone 6D5)-166Er	DVS	Cat#3166015B; RRID: AB_2687846
Anti-mouse CD8a (clone 53-6.7)-168Er	DVS	Cat#3168003B
Anti-mouse CD117 (clone 2B8)	BioLegend	Cat#105802; RRID: AB_313211

(*Continued on next page*)

Continued

REAGENT or RESOURCE	SOURCE	IDENTIFIER
Anti-mouse FcεR1a (clone MAR-1)-176Yb	DVS	Cat#3176006B
Anti-mouse CD11c (clone N418)-209Bi	DVS	Cat#3176006B
Anti-CD31 (clone WM59) BV421	BioLegend	Cat#303123; RRID: AB_2562179
Anti-CD26 (clone BA5b) APC	BioLegend	Cat#302709; RRID: AB_10913814
Anti-CD271 (clone ME20.4) PE	BioLegend	Cat#345105; RRID: AB_2282827
Anti-CD326 (clone EBA-1) BB515	BD	Cat#565398; RRID: AB_2728107
Anti-CD45 (clone HI30) PerCP/Cy5.5	Tonbo	Cat#65-0459; RRID: AB_2621897
Anti-CD200 (clone OX-104) BV711	BioLegend	Cat#329223; RRID: AB_2715824
Anti-PDPN (clone NC-08) PE	BioLegend	Cat#337004; RRID: AB_1595457
Rabbit anti-PSCA	Abcam	Cat#Ab64919; RRID: AB_1142338
Donkey anti-rabbit IgG BV421	DVS	Cat#406410; RRID: AB_10897810
Chemicals, Peptides, and Recombinant Proteins		
Collagenase type I	GIBCO	Cat#17-100-017
Deoxyribonuclease	Millipore Sigma	Cat#D4263-1VL
TrypLE express enzyme, no phenol red	GIBCO	Cat#12604-013
16% paraformaldehyde	Electron Microscopy Sciences	Cat#15710-S
Y-27632 dihydrochloride	Tocris Bioscience	Cat#1254
Saponin	Millipore Sigma	Cat#47036
Dispase	GIBCO	Cat#17105-041
Trypsin-EDTA	GIBCO	Cat#25300-054
Sodium azide	Millipore Sigma	Cat#S2271-100
Cell-ID intercalator-103Rh	Fluidigm	Cat#201103A
Cell-ID cisplatin	Fluidigm	Cat#201064
Cell-ID intercalator-Ir	Fluidigm	Cat#201192A
Maxpar® fix and perm buffer	Fluidigm	Cat#201067
Maxpar® cell staining buffer	Fluidigm	Cat#201068
EQ four element calibration beads	Fluidigm	Cat#201078
cOmplete protease inhibitor cocktail tablet	Roche	Cat#11697498001
Triton X-100	Thermo Fisher Scientific	Cat#BP151-100
A83-01	Tocris Bioscience	Cat#2939
Advanced DMEM/F-12	Thermo Fisher Scientific	Cat#12634010
B-27 Supplement (50x), Serum Free	Thermo Fisher Scientific	Cat#17504044
(DiHydro)testosterone (5α-Androstan-17β-ol-3-one)	Millipore Sigma	Cat#A-8380
GlutaMAX	Thermo Fisher Scientific	Cat#35050061
Matrigel GFR Membrane Matrix	Corning	Cat#CB-40230C
N-acetyl-L-cysteine	Millipore Sigma	Cat#A9165
Recombinant Human EGF, Animal-Free	PeproTech	Cat#AF-100-15
Recombinant Human Noggin	PeproTech	Cat#120-10C
Sucrose	Millipore Sigma	Cat#S0389-500G
4',6-diamidino-2-phenylindole (DAPI)	Thermo Fisher Scientific	Cat#D1306
Critical Commercial Assays		
Anti-Goat HRP-DAB Cell & Tissue Staining Kit	R & D Systems	Cat#CTS008; RRID: AB_10052005
Maxpar X8® multimetal labeling kit	Fluidigm	Cat#201300
RNeasy Mini Kit	QIAGEN	Cat#74104
KAPA stranded mRNA-seq kit	Roche	Cat#07962193001

(*Continued on next page*)

Continued

REAGENT or RESOURCE	SOURCE	IDENTIFIER
Deposited Data		
Raw and processed RNaseq data (Adult and Old)	This paper	GEO: GSE122367
Raw and processed RNaseq data (Trop2+ and Trop2-)	This paper	GEO: GSE128724
Experimental Models: Organisms/Strains		
Mouse: C57BL/6J	Jackson Laboratories	Cat#000664
Mouse: C57BL/6N	UCLA Department of Radiation Oncology Animal Core Facility	N/A
Mouse: NSG	Jackson Laboratories and the UCLA Department of Radiation Oncology Animal Core Facility	Cat#005557
Software and Algorithms		
Sequencing Analysis Viewer (SAV)	Illumina	https://support.illumina.com/sequencing/sequencing_software/sequencing_analysis_viewer_sav.html
bcl2fastq Conversion Software V2.17	Illumina	https://support.illumina.com/sequencing/sequencing_software/bcl2fastq-conversion-software.html
Bowtie2 V2.1.0	Langmead and Salzberg, 2012	http://bowtie-bio.sourceforge.net/bowtie2/index.shtml
RNA-seq by Expectation-Maximization (RSEM) V1.2.15	Li and Dewey, 2011	http://deweylab.github.io/RSEM/
Empirical Analysis of Digital Gene Expression Data in R (edgeR)	Robinson et al., 2010	https://bioconductor.org/packages/release/bioc/html/edgeR.html
GOseq	Young et al., 2010	https://bioconductor.org/packages/release/bioc/html/goseq.html
Gene Set Enrichment Analysis (GSEA)	Subramanian et al., 2005	https://www.broadinstitute.org/gsea
Maxpar Panel Designer	Fluidigm	http://www.dvssciences.com/paneldesigner/resources
FlowJo V10	FlowJo LLC	https://www.flowjo.com/
Prism V7	GraphPad	https://www.graphpad.com/scientific-software/prism/
Other		
58Y1	Test Diet	Cat#1810473
35mm micro-dish	Ibidi USA	Cat#50-305-806
NuPAGE 4-12% Bis-Tris Gel	Novex	Cat#NP0335BOX
PVDF membrane	Millipore Sigma	Cat#IPVH00010
Sonic dismembrator	Thermo Fisher Scientific	Cat#FB120

LEAD CONTACT AND MATERIALS AVAILABILITY

This study did not generate new unique reagents. Further information and requests for resources and reagents should be directed to and will be fulfilled by the Lead Contact, Andrew S. Goldstein (agoldstein@mednet.ucla.edu).

EXPERIMENTAL MODEL AND SUBJECT DETAILS

Animal Work

Immunocompetent male C57BL/6J and C57BL/6N mice (B6) and immunodeficient male NOD.Cg-*Prkdc*^{scid} *Il2rg*^{tm1Wjl}/SzJ (NSG) mice from Jackson Laboratories and the UCLA Department of Radiation Oncology's animal core facility were used in experiments. Mice were bred and maintained under the care of the UCLA Division of Laboratory Animal Medicine (DLAM), using approved protocols. For aging experiments, mice were purchased from Jackson Laboratories at 12 months of age and were maintained at UCLA until they reached 24 months of age. For high fat diet experiments, 4 week-old B6 mice were fed normal chow or high fat diet (58Y1, Test Diet) for 14 weeks.

Collection of Mouse Prostate Tissue

Male mice were euthanized using carbon dioxide asphyxiation, and the urogenital tract was removed and placed into RPMI 1640 (GIBCO) containing 10% fetal bovine serum (FBS) (Corning), 1x penicillin-streptomycin (GIBCO). Under a microscope, seminal vesicles, the bladder, the urethra, and fat were removed from the urogenital tract to isolate the prostate. Mouse prostates were weighed, and weights were recorded.

Collection of Human Prostate Tissue

Prostate specimens used in this study were obtained from 10, 18-47 year old male organ donors whose families were consented at the Southwest Transplant Alliance from March 2017 to April 2019 under IRB STU 112014-033. After transplantable organs were harvested, a cystoprostatectomy was performed and the specimen was transported to UT Southwestern Medical Center for processing. Ten aged prostate specimens were collected from patients undergoing simple prostatectomy at Clements University Hospital for lower urinary tract symptoms due to BPH from March 2018 to April 2019 under IRB STU 112014-033.

METHOD DETAILS

Quantification of Branch Points

Branch point of mouse prostate lobes was quantified as described (Lai et al., 2012) with modifications. Briefly, the mouse prostate lobes were dissected and digested with 10 mg/ml collagenase type I (GIBCO) in RPMI 1640 (GIBCO) with 10% fetal bovine serum (Corning) for 1 h at 37°C. The ductal structure was exposed with fine forceps and branching points were counted under a dissection microscope.

Mouse Prostate Dissociation to Single Cells

Using a razor blade, individual mouse prostates were mechanically dissociated in dissociation media comprised of RPMI 1640 (GIBCO) containing 10% fetal bovine serum (Corning), 1x penicillin-streptomycin (GIBCO), 1 mg/mL collagenase type I (GIBCO), 1 mg/ml dispase (GIBCO), 0.1 mg/mL deoxyribonuclease (GIBCO), and 10uM of the p160ROCK inhibitor Y-27632 dihydrochloride (Tocris Bioscience). When chunks were no longer visible, the samples were incubated at 37°C on a nutating platform for 1 - 1.5 h in 5 mL of dissociation media. After centrifugation, the pellet was washed with 1x phosphate buffered saline (PBS, GIBCO). The cell pellet was resuspended in 2.7 mL of 0.05% Trypsin-EDTA (GIBCO) and incubated at 37°C for 5 min. Trypsin was inactivated with 300 μL of dissociation media. Cells were further dissociated by pipetting with a P-1000 pipette and an 18G syringe. Cells were passed through a 100 μm cell strainer (Corning). Dissociated cells were counted using a hemocytometer.

Human Prostate Processing

Fresh tissue samples less than 24 h post-collection were transported in ice-cold saline and immediately processed in a 4 h enzymatic digestion into single cells at 37°C using 5 mg/ml collagenase type I (GIBCO), 10 μM ROCK inhibitor Y-27632 (Tocris Bioscience), 1nM DHT (Sigma), 1mg DNase I (GIBCO), and 1% antibiotic/antimycotic solution (100X, Corning) in HBSS. Single cells were filtered and cryopreserved in 90% FBS/10% DMSO. For experiments, vials were rapidly thawed, washed, and incubated with antibodies for flow cytometry as described (Henry et al., 2018). Viable human prostate cells were analyzed by fluorescence activated cell sorting in the UT Southwestern CRI Flow Cytometry Core on a BD FACSAria FUSION SORP flow cytometer and analyzed with FlowJo software as performed previously (Henry et al., 2018).

Staining and Sorting Cells from Mouse Prostate

Dissociated cells were stained with directly conjugated primary antibodies: rat anti-CD49f-PE (BioLegend), rat anti-CD326 (EpCAM)-APC/Cy7 (BioLegend), goat anti-Trop2-APC (R & D Systems), rat anti-CD31-FITC (BioLegend), rat anti-CD45-FITC (BioLegend), and rat anti-Ter119-FITC (BioLegend) for 20 min on ice. Rat anti-ESAM-FITC (BioLegend) was also added to the Lin panel for some experiments. Rat anti-CD44-FITC (BioLegend) was used for analysis. Cells were stained in media containing RPMI 1640 (GIBCO), 10% FBS (Corning), 1x penicillin-streptomycin (GIBCO), and 10uM of the p160ROCK inhibitor Y-27632 dihydrochloride (Tocris Bioscience). Sorting was performed on a BD FACS Aria II (BD Biosciences) and flow cytometry analysis was performed on a BD FACS Canto (BD Biosciences).

Intracellular Flow Cytometry

Dissociated cells from mouse prostate were stained with rat anti-CD49f-PE (BioLegend), rat anti-CD326 (EpCAM)-APC/Cy7 (BioLegend) and goat anti-Trop2-APC (R & D Systems) for 20 min on ice. Cells were washed with PBS and fixed in 1ml of 2% paraformaldehyde made from 16% paraformaldehyde (Electron Microscopy Sciences) in PBS for 15 min on ice. Cells were washed with PBS and permeabilized in 1ml of permeabilization buffer (0.1% Saponin (Sigma-Aldrich), 5% FBS (Corning) in PBS) for 15 min at room temperature in the dark. Cells were resuspended in 100 μL of permeabilization buffer and stained with either rabbit anti-cytokeratin 5-Alexa Fluor 647 (Abcam) and rabbit anti-cytokeratin 8-Alexa Fluor 488 (Abcam), mouse anti-cytokeratin 14-FITC (Abcam), mouse anti-cytokeratin 18-FITC (Abcam) or rat anti-Ki67-FITC (BioLegend) for 20 min at room temperature in the dark. Cells were washed and resuspended in permeabilization buffer for analysis on a BD FACS Canto (BD Biosciences).

Organoid Culture and Assays

Basal and luminal primary cells from mouse prostate were isolated by fluorescence activated cell sorting. Luminal cell populations were double-sorted to ensure high purity. Sorted cell populations were plated in a 24-well plate (Corning). Basal cells were plated at a density of 500 or 1000 cells/well, while luminal cells were plated at a density of 2500 or 5000 cells/well. Prostate organoids were cultured based on established protocols (Drost et al., 2016). For passaging, primary organoids were dissociated in 1mg/ml dispase (GIBCO) for 30 min to 1 h prior to treatment with 0.05% Trypsin-EDTA (GIBCO) and re-plating. Single organoids were imaged on a light microscope and organoid diameter was measured as a readout of organoid size. For confocal microscopy, dispase-treated organoids were fixed with 4% paraformaldehyde in PBS for 2 h at room temperature, and permeabilized by incubating in blocking solution (10% fetal bovine serum and 0.2% Triton X-100 (Fisher) in PBS) for 2 h. Whole-mount immunofluorescent staining of organoids was performed by incubating with primary antibodies in blocking solution overnight at 4°C, washing with PBS three times for two h each, incubating with secondary antibodies and 1 μg/ml 4',6-diamidino-2-phenylindole dihydrochloride (DAPI, Sigma) in blocking solution overnight at 4°C, and washing with PBS three times for two h each. Tissue clearing was done with sucrose series (15%, 30%, 45%, and 60% sucrose with 1% Triton X-100 (Fisher) in PBS, 2 h each), and the organoids were mounted on chambered coverslips (35 mm micro-dish, Ibidi USA). Confocal microscopy with Airyscan was performed with LSM 880 (Zeiss). Primary antibodies used were rabbit anti-p63 (BioLegend) and mouse anti-K8 (BioLegend). Secondary antibodies used were Alexa Fluor 488 goat anti-mouse IgG (Invitrogen) and Alexa Fluor 594 goat anti-rabbit IgG.

Immunoblot Analysis

Organoids were collected at day 7 and lysed in RIPA buffer (50mM Tris-HCl pH 8.0, 150mM NaCl, 1% NP-40, 0.5% Sodium Deoxycholate, 0.1% SDS) containing a cOmplete protease inhibitor cocktail tablet (Roche) and every sample was sonicated with sonic dismembrator (Fisher). Proteins were run on NuPAGE 4%–12% Bis-Tris Gel (Novex) and transferred onto PVDF membranes (Millipore Sigma) and probed with antibodies. Keratin 5 and tubulin were detected via fluorescence using goat anti-rabbit IgG-Alexa Fluor 647 (Invitrogen) or goat anti-mouse IgG-Alexa Fluor 647 (Invitrogen) and all others using HRP-conjugated antibodies against rabbit, mouse, or goat IgG (Invitrogen). Immunoblot antibodies: rabbit anti-keratin 5 (Biolegend), goat anti-Tp63 (R & D systems), mouse anti-cytokeratin 8 (Biolegend), rabbit anti-Prom1 (Abnova), mouse anti-tubulin (DSHB).

Immunohistochemistry

3-month-old and 24-month-old mouse prostate tissue was embedded in paraffin and sectioned at UCLA's Translational Pathology Core Laboratory. Sections were incubated at 60°C in a vacuum oven for 45-60 min. Slides were transferred into xylene (Fisher) 3 times, 100% alcohol (Decon Labs) 2 times, 95% ethanol 1 time and 70% ethanol 1 time, each for 3 min. Slides were transferred into PBS (GIBCO) for 5 min prior to epitope unmasking using a heat antigen retrieval step. Staining of sections was performed using the manufacturer's protocol for the Anti-Goat HRP-DAB Cell & Tissue Staining Kit (R & D Systems) with primary antibody goat anti-mouse Trop2 (R & D Systems) at a 10 μg/ml concentration. Hematoxylin and eosin staining was performed by UCLA's Translational Pathology Core Laboratories. Frozen sections were fixed with 4% paraformaldehyde in PBS for 5 min at room temperature, washed with PBS, and stained with primary antibodies and stained with the following secondary antibodies: goat anti-mouse IgG-Alexa Fluor 488 and goat anti-rabbit IgG-Alexa Fluor 594.

Antibodies for Mass Cytometry

Antibodies used for mass cytometry experiments were purchased pre-conjugated from the manufacturer (Fluidigm) or conjugated in-house using MaxPar X8® multimetal labeling kit (Fluidigm) according to manufacturer's protocol. Panels were checked for signal tolerance using the Maxpar Panel Designer (Fluidigm). Table S1 shows the antibodies used in the mouse panel.

Cell Surface Staining for Mass Cytometry

Cell staining buffer was prepared with 1x PBS (GIBCO) containing 5% bovine serum albumin (BSA) protease-free (Sigma-Aldrich) and 0.2% sodium azide (Sigma-Aldrich). From single-cell suspension into tubes, $1 \times 10^5 - 1.5 \times 10^5$ cells were aliquoted for the unstained control, and $3 \times 10^5 - 1.8 \times 10^6$ cells aliquoted used for the stained samples. For Live/Dead staining with rhodium, samples were centrifuged and resuspended at 1×10^6 cells/mL in cell staining buffer containing 1 μM Cell-ID Intercalator-103Rh (Fluidigm) and incubated at 37°C for 15 min. For Live/Dead staining with cisplatin, samples were centrifuged and resuspended at 1×10^7 cells/mL in cell staining buffer. Stock Cell-ID Cisplatin (Fluidigm) was added to samples for a final concentration of 5 μM, and samples were incubated for 5 min at room temperature. Live/Dead stain was quenched with 2mL cell staining buffer and centrifuged. After Live/Dead staining, the antibody cocktail prepared was diluted to 1 μL of each antibody per 50 μL per sample. Cells were resuspended in 45 μL cell staining buffer and 5 μL of 5 μg/mL TruStain fcX (anti-mouse CD16/32) Antibody (BioLegend). Samples were incubated at room temperature for 10 min, then 50 μL of the antibody cocktail was added. Samples were incubated with antibodies added at room temperature for 30 min then washed twice with cell staining buffer and resuspended in 1 mL Maxpar® Fix and Perm Buffer (Fluidigm) containing 125 nM Cell-ID Intercalator-Ir (Fluidigm). Samples were incubated for 12 – 48 h at 4°C. Samples were then washed a total of 3 times with cell staining buffer, 1x PBS (GIBCO), then MilliQ Water (Millipore). Samples were passed through a 40 μm strainer (Corning) between the PBS and MilliQ Water washes. After the final wash, cells were resuspended in a residual amount of MilliQ Water for mass cytometry.

Mass Cytometry

Mass cytometry was performed at the UCLA Jonsson Comprehensive Cancer Center (JCCC) and Center for AIDS Research Flow Cytometry Core Facility. Prior to sample introduction cell pellets were washed twice with Maxpar® cell staining buffer (Fluidigm), twice with MilliQ Water and resuspended in 10% EQ Four Element Calibration Beads (Fluidigm) containing natural abundance cerium (140/142Ce), europium (151/153Eu), holmium (165Ho), and lutetium (175/176Lu). Samples were acquired on a Helios® mass cytometer (Fluidigm) at an event rate of 300-500 events/second. Post-acquisition data was normalized using bead-based normalization in the CyTOF software.

RNaseq

RNA was extracted from the cells using the RNeasy Mini Kit (QIAGEN) following the manufactural instruction. Libraries for RNA-Seq were prepared with KAPA Stranded mRNA-Seq Kit (Roche). The workflow consists of mRNA enrichment, cDNA generation, and end repair to generate blunt ends, A-tailing, adaptor ligation and PCR amplification. Different adaptors were used for multiplexing samples in one lane. Sequencing was performed on Illumina HiSeq 3000 for 1x50 run.

QUANTIFICATION AND STATISTICAL ANALYSIS

RNaseq Analysis

Data quality check was done on Illumina Sequence Analysis Viewer (SAV). Demultiplexing was performed with Illumina Bcl2fastq2 v 2.17 program. The reads were first mapped to the latest UCSC transcript set using Bowtie2 version 2.1.0 (Langmead and Salzberg, 2012) and the gene expression level was estimated using RNA-seq by Expectation-Maximization (RSEM) v1.2.15 (Li and Dewey, 2011). TMM (trimmed mean of M values) was used to normalize the gene expression. Differentially expressed genes were identified using the Empirical Analysis of Digital Gene Expression Data in R (edgeR) program (Robinson et al., 2010). Genes showing altered expression with $p < 0.05$, FDR < 0.1 and more than 1.5 fold changes were considered differentially expressed. Gene ontology analysis was performed using the R package goseq (Young et al., 2010), with gene length corrected. Up- and downregulated genes were separately tested and all genes that were detected (read count > 0) in at least two samples were used as the background. Gene ontology terms with p value < 0.05 were considered statistically significant. Gene ontology analysis was also performed using DAVID Bioinformatics (Huang et al., 2009). Heatmap of candidate genes was generated using the heatmap.2 function in the R package gplots. Expression values were scaled for each row (gene). GSEA analysis was performed using the GSEA software (https://www.broadinstitute.org/gsea) (Subramanian et al., 2005). Normalized enrichment score and false discovery rate were calculated.

CyTOF Clustering

Manual gating for live $CD45^+$ singlets in each sample was performed in FlowJo V10 (FlowJo LLC). Each sample was given a unique Sample ID, then all samples were concatenated into a single .fcs file. On this file T-Distributed Stochastic Neighbor Embedding (t-SNE) in FlowJo V10 was performed on equal numbers of cells from 3- and 24-month-old mouse prostate using all surface markers besides CD45 and the following settings: Iterations, 3000; Perplexity, 50; Eta (learning rate), 4105. Heatmaps of marker expression were generated using the Color Map Axis function.

Statistical Analysis

Prism V7 (GraphPad) was used to generate graphs and perform statistical analysis. Correlations were determined by calculating the Pearson correlation coefficient *r*. Number of replicates, type of replicate, and type of error bars are listed in figure legends. Unless otherwise stated, two-tailed Student's t test assuming unequal variance was performed to determine statistical significance. $^*p < 0.05$, $^{**}p < 0.01$, $^{***}p < 0.001$, $^{****}p < 0.0001$.

DATA AND CODE AVAILABILITY

The data discussed in this publication have been deposited in NCBI's Gene Expression Omnibus and are accessible through GEO Series accession number GSE122367 and GSE128724.

Cell Reports, Volume *28*

Supplemental Information

Expansion of Luminal Progenitor Cells in the Aging Mouse and Human Prostate

Preston D. Crowell, Jonathan J. Fox, Takao Hashimoto, Johnny A. Diaz, Héctor I. Navarro, Gervaise H. Henry, Blake A. Feldmar, Matthew G. Lowe, Alejandro J. Garcia, Ye E. Wu, Dipti P. Sajed, Douglas W. Strand, and Andrew S. Goldstein

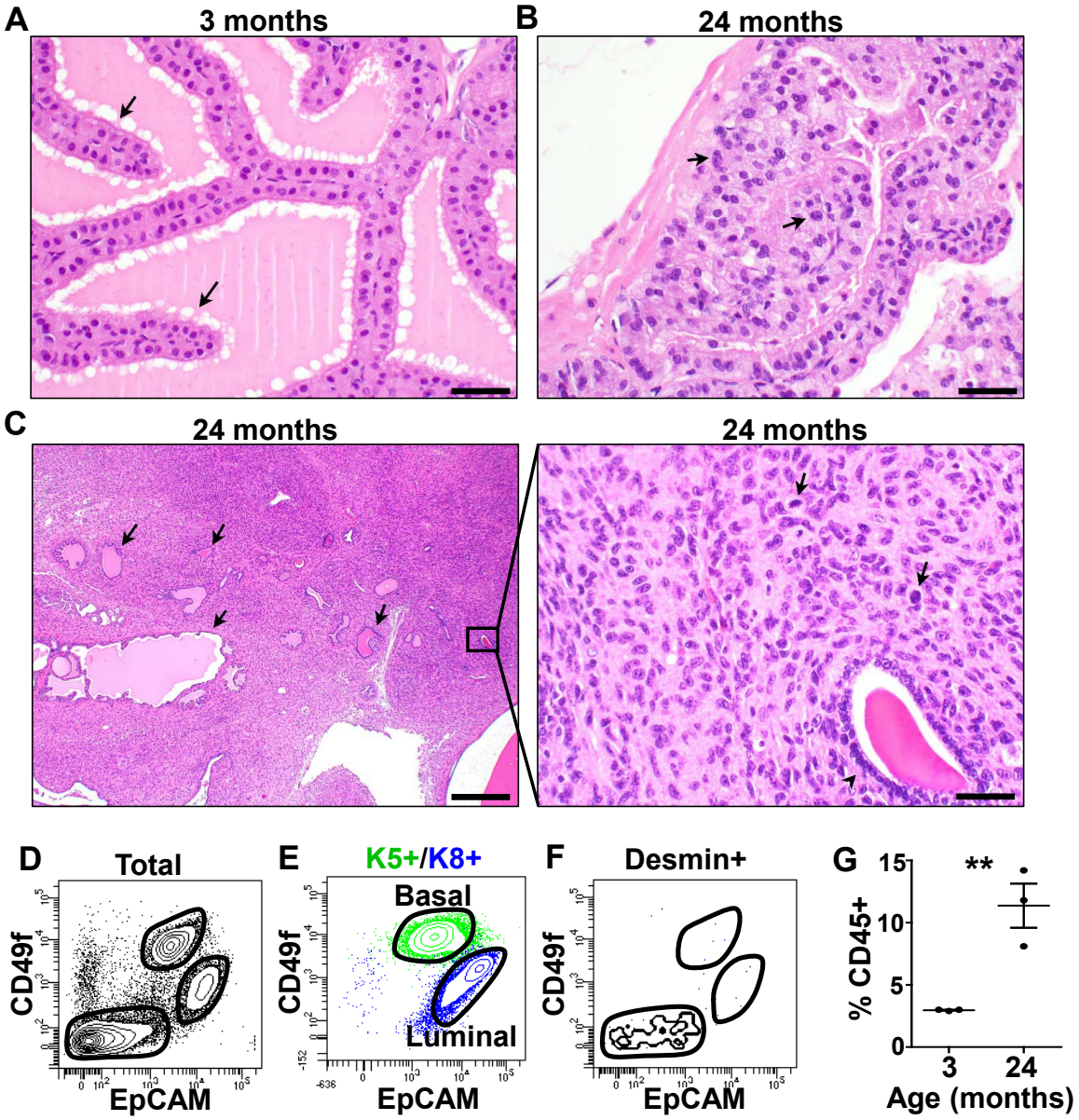

Supplemental figure 1, related to figure 1. Characterization of adult and old mouse prostates. (A-B) Representative epithelial glands from adult **(A)** and old **(B)** mouse prostate. Features of simple papillary infoldings and uniform nuclei are highlighted by arrows in A. PIN-like features of atypia in the form of nuclear pleomorphism are highlighted by arrows in B. Scale bars, 40 μm. **(C)** Rare instance of sarcomatous proliferation in the mesenchyme surrounding epithelial glands shown with arrows. Boxed region is magnified on right. Scale bars, 400 μm (left) and 40 μm (right). **(D)** Total dissociated cells stained for CD49f and EpCAM are shown with gates highlighting stromal, basal and luminal fractions. **(E)** CD49f and EpCAM staining gated on Keratin 8+ (K8+) luminal cells in blue and Keratin 5+ (K5+) basal cells in green. **(F)** CD49f and EpCAM staining gated on Desmin+ stromal cells. **(G)** Proportion of total dissociated cells staining for CD45 is shown for adult and old mouse prostate. Data +/- SEM for 3 biological replicates is shown.

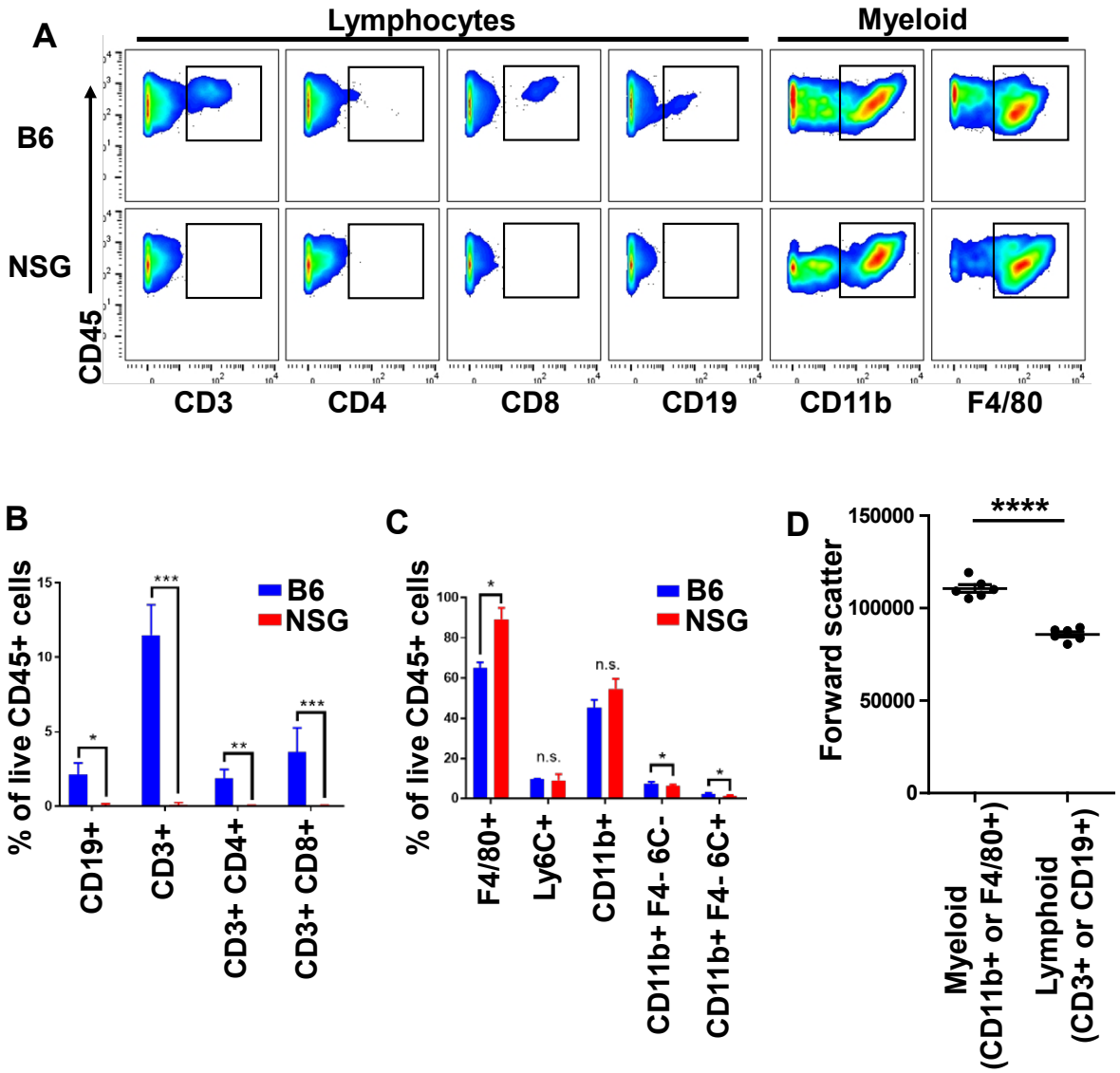

Supplemental figure 2, related to figure 2. Characterizing immune cells in B6 and NSG mice. (A) Mass cytometry analysis of immune cells in the prostates of B6 and NSG mice showing expression of surface markers. **(B-C)** Comparison of lymphocyte **(B)** and myeloid **(C)** marker frequencies in prostate immune cells of B6 and NSG mice detected using CyTOF. Abbreviations: F4, F4/80; 6C, Ly6C. **(D)** Forward scatter levels of myeloid cells and lymphocytes from adult mouse prostate measured with flow cytometry. Data represent mean +/- SEM of 6 biological replicates.

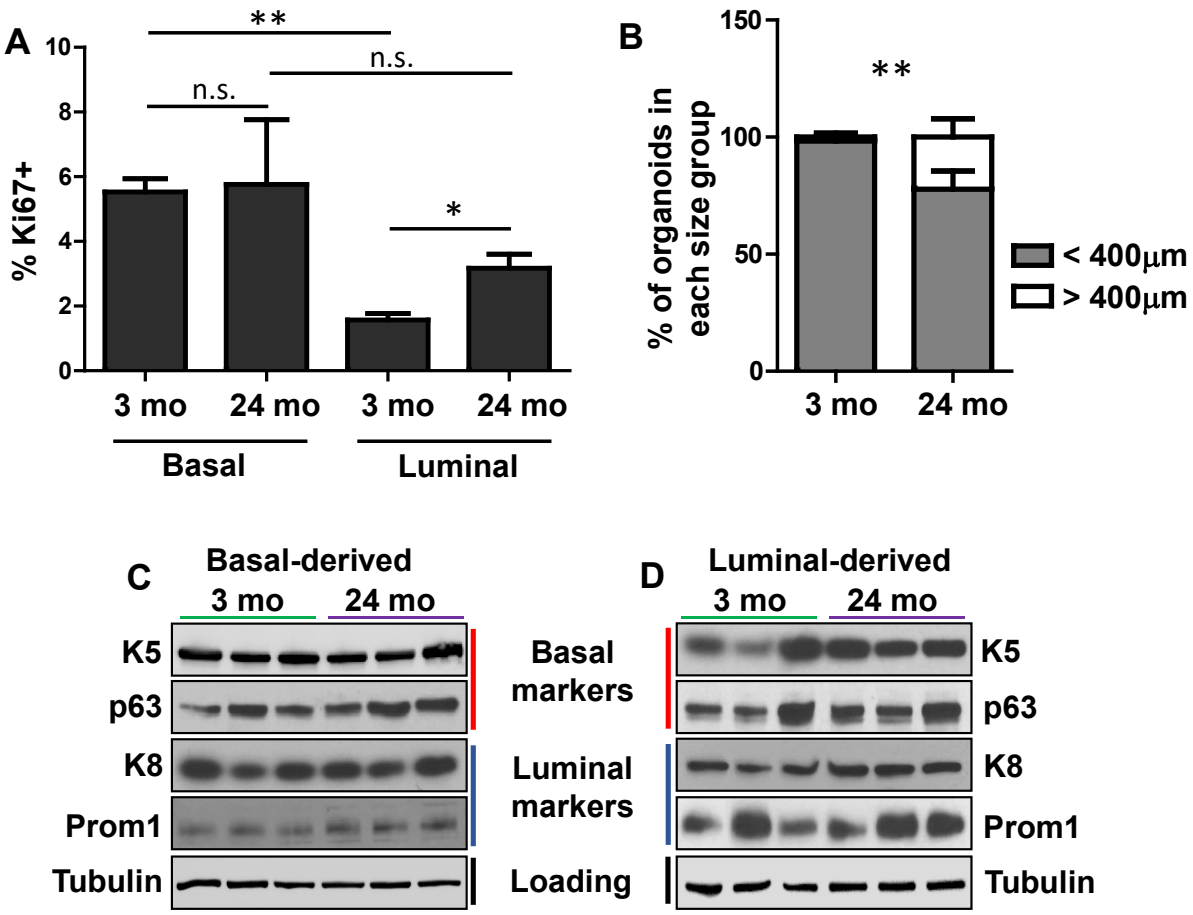

Supplemental figure 3, related to figure 3. Characterizing organoids derived from adult and old mouse prostate epithelial cells. (A) Percentage of Ki67+ cells within the basal and luminal fractions from adult and old mice measured using intracellular flow cytometry. Mean +/- SEM for 3 biological replicates is shown. **(B)** Quantification of organoids from each age classified into larger than or smaller than 400 μm in diameter. **(C-D)** Western blot analysis of basal-derived **(C)** and luminal-derived **(D)** organoids from 3- and 24-month-old mice. Staining for basal markers (K5 and p63), luminal markers (K8 and Prom1) and a loading control (Tubulin).

A

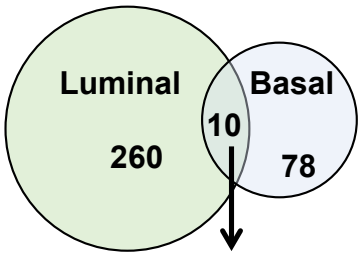

Arc, Cyp2f2, Egr1, Elfn1, Fam107b, Hmox1, Lrg1, Nabp1, Rasd1, Urah

B

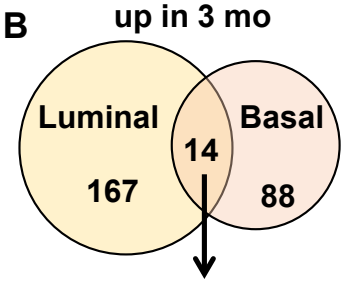

Col1a1, Col1a2, Col3a1, Cxcl14, Gata3, Gprc5b, Igfbp5, Lrrc75b, Rmnd5a, Scd2, Sirpa, Sparc, Tagln, Tnfrsf19

C

GO Terms up in 3 mo basal	p value
Extracellular matrix organization	9.78E-06
Cell migration	1.40E-05
Cell adhesion	1.40E-05
Localization of cell	2.26E-05

D

GO Terms up in 24 mo basal	p value
ncRNA metabolic process	2.47E-05
Ribosome biogenesis	2.47E-05
rRNA metabolic process	6.96E-05
Apoptotic process	0.00384

E

GO Terms up in 3 mo luminal	p value
Male sex differentiation	0.01408
Gonad development	0.02293
mammary gland development	0.03130

F

GO Terms up in 24 mo luminal	p value
Positive regulation of cell motility	1.12E-07
Positive regulation of cell migration	5.37E-07
Angiogenesis	7.01E-06
Inflammatory response	7.44E-06
Regulation of cell proliferation	7.44E-06
Vasculature development	9.31E-06
Defense response	1.11E-05
Immune system process	1.20E-05
Response to stimulus	1.43E-05

Supplemental figure 4, related to Figure 4. Gene expression profiles of basal and luminal cells isolated from adult and old mouse prostate. (A) Venn diagram shows the number of genes that are significantly upregulated in luminal cells, basal cells, or both in 24-month-old as compared to 3-month-old mouse prostate. Genes upregulated in both basal and luminal in 24-month-old are listed below. **(B)** As in A, showing the number of genes significantly upregulated in old mouse prostate epithelial cells, with overlapping genes listed. **(C-F)** Gene ontology analysis of gene sets upregulated in basal cells from 3-month-old mice **(C)**, basal cells from 24-month old mice **(D)**, luminal cells from 3-month-old mice **(E)** and luminal cells from 24-month-old mice **(F).**

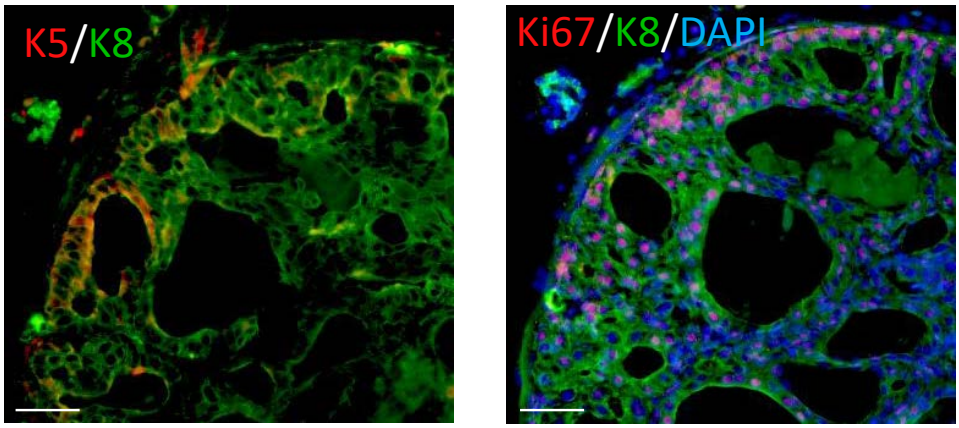

Supplemental figure 5, related to Figure 4. Characterization of hyperplastic region in old mouse prostate. Immunofluorescence of old mouse prostate epithelium demonstrating expression of basal (K5) and luminal (K8) markers as well as proliferation (Ki67) within hyperplastic region. Scale bars, 50 μm.

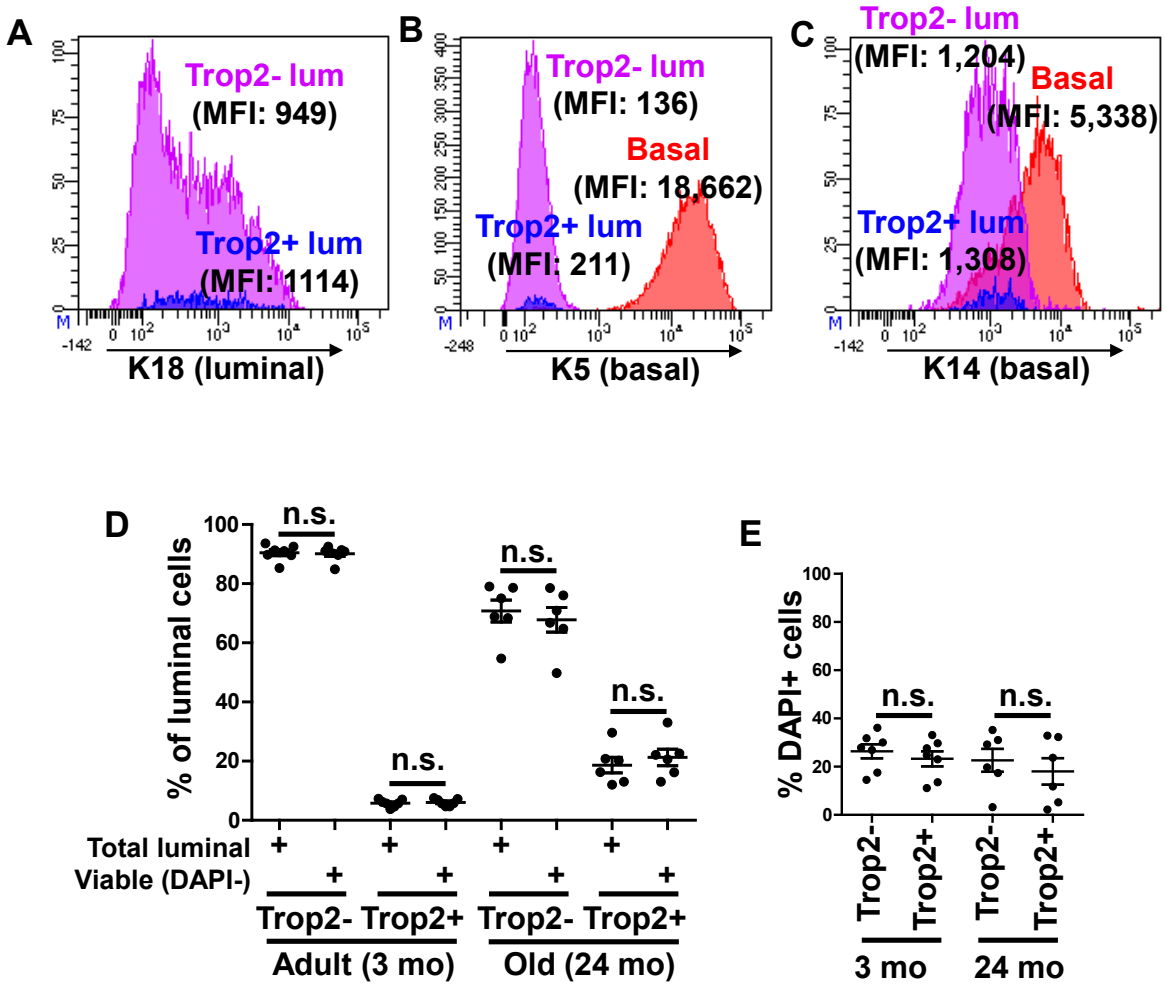

Supplemental figure 6, related to figure 5. Analysis of Trop2+ and Trop2- luminal cells from adult and old mouse prostate. (A-C) Intracellular flow cytometry for luminal (A) and basal (B-C) keratins within Trop2+ and Trop2- luminal cells. Mean fluorescence intensity values (MFI) are shown. **(D)** Quantification of the percentage of luminal cells with a Trop2- or Trop2+ phenotype from adult and old mouse prostate, comparing total luminal cells to DAPI-negative viable luminal cells. No statistically significant differences were observed within individual subsets when comparing total to viable cells. **(E)** Quantification of the percentage of DAPI+ non-viable luminal cells with a Trop2- or Trop2+ phenotype from adult and old mouse prostate.

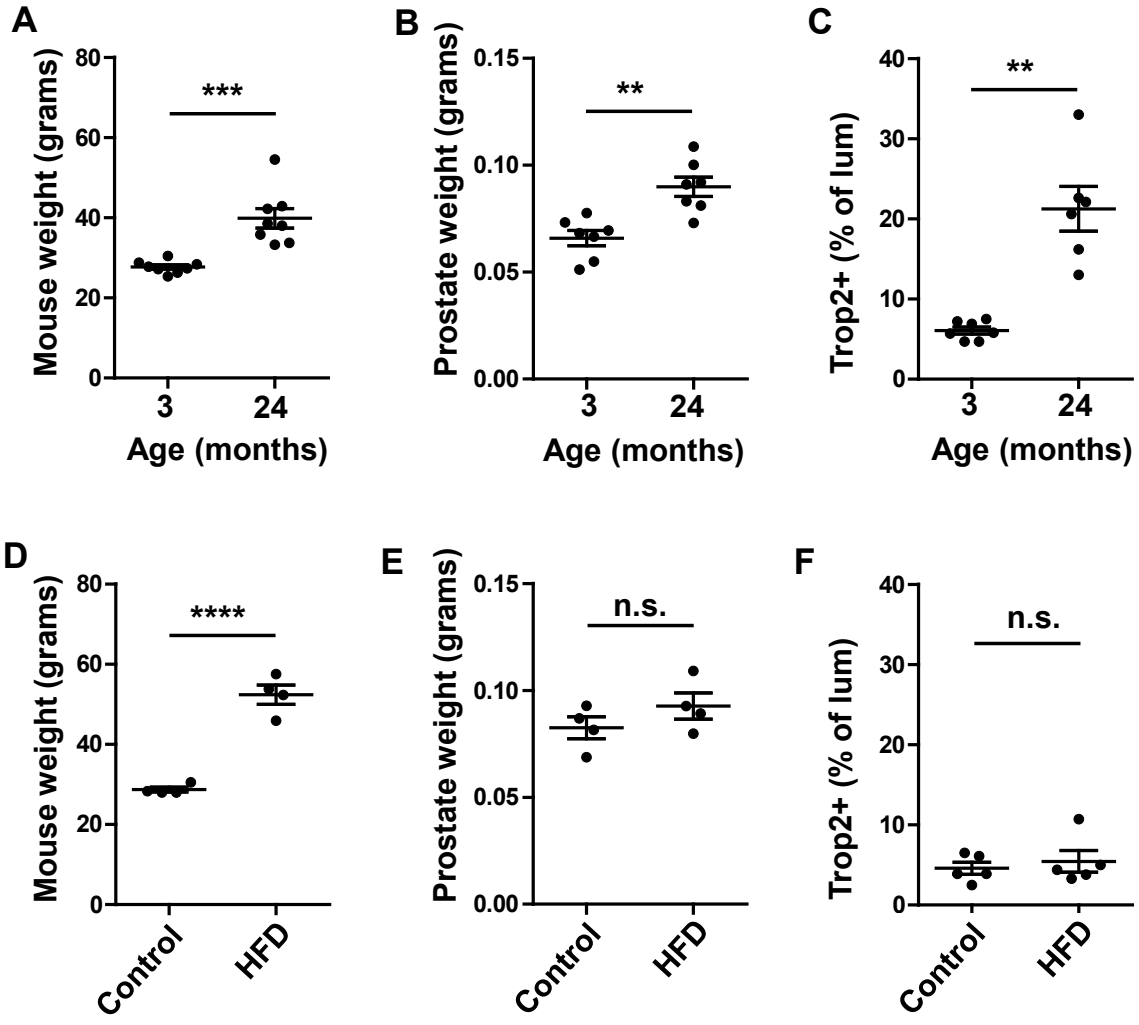

Supplemental figure 7. High fat diet treatment does not phenocopy aging in the mouse prostate. (A-C) Analysis of mouse weight **(A)**, prostate weight **(B)** and percentage of luminal cells that express Trop2 **(C)** from adult and old mice. Plot shown in B is identical to the plot shown in Figure 1B. **(D-F)** Analysis of mouse weight **(D)**, prostate weight **(E)** and percentage of luminal cells that express Trop2 **(F)** from adult mice treated with control or high fat diet (HFD) for 3 months. Data represent mean +/- SEM for 4-8 biological replicates.

Table S1. CyTOF Antibodies for Mouse Prostate Immune Cells. Related to STAR Methods.

Label	Target	Clone	Conjugation	Source
89Y	CD45	30-F11	Pre-conjugated	DVS
139La	CD27	LG.3A10	Maxpar Kit	BioLegend
141Pr	CD138	281-2	Maxpar Kit	BioLegend
144Nd	CD45R (B220)	RA3-6B2	Pre-conjugated	DVS
145Nd	CD4	RM4-5	Pre-conjugated	DVS
146Nd	F4/80	BM8	Pre-conjugated	DVS
147Sm	CD45	30-F11	Pre-conjugated	DVS
148Nd	CD11b	M1/70	Pre-conjugated	DVS
152Sm	CD3e	145-2C11	Pre-conjugated	DVS
155Gd	CD25	3C7	Maxpar Kit	BioLegend
162Dy	Ly6C	HK1.4	Pre-conjugated	DVS
166Er	CD19	6D5	Pre-conjugated	DVS
168Er	CD8a	53-6.7	Pre-conjugated	DVS
173Yb	CD117	2B8	Maxpar Kit	BioLegend
176Yb	FcεR1a	MAR-1	Pre-conjugated	DVS
209Bi	CD11c	N418	Pre-conjugated	DVS

Chapter 3: Distinct cell-types in the prostate share an aging signature suggestive of metabolic reprogramming

Am J Clin Exp Urol 2020;8(4):140-151
www.ajceu.us /ISSN:2330-1910/AJCEU0113153

Original Article

Distinct cell-types in the prostate share an aging signature suggestive of metabolic reprogramming

Preston D Crowell[1], Jenna M Giafaglione[1], Takao Hashimoto[2], Andrew S Goldstein[2,3,4,5,6]

[1]Molecular Biology Interdepartmental Program, University of California, Los Angeles, Los Angeles, CA, USA; [2]Department of Molecular, Cell, and Developmental Biology, University of California, Los Angeles, Los Angeles, CA, USA; [3]Department of Urology, David Geffen School of Medicine, University of California, Los Angeles, Los Angeles, CA, USA; [4]Eli and Edythe Broad Center of Regenerative Medicine and Stem Cell Research, University of California, Los Angeles, Los Angeles, CA, USA; [5]Jonsson Comprehensive Cancer Center, University of California, Los Angeles, Los Angeles, CA, USA; [6]Molecular Biology Institute, University of California, Los Angeles, Los Angeles, CA, USA

Received April 23, 2020; Accepted July 8, 2020; Epub August 15, 2020; Published August 30, 2020

Abstract: Age is a significant risk factor for disease of the prostate. However, the mechanisms by which age increases disease risk have not been well described. We previously reported age-related changes within the inflammatory and luminal compartments of the mouse prostate. Old mouse prostates exhibit an expansion of the population of Trop2+ luminal progenitor cells and a reduction in the frequency and functional capacity of Trop2- luminal cells, indicating that different cell-types have distinct responses to aging. Whether distinct cell-types in the prostate share a common signature of aging has not been established. We transcriptionally profiled four distinct cell-types in young adult and old mouse prostates: stromal, basal, Trop2+ luminal progenitor and Trop2- luminal cells. Motif analysis of genes upregulated in old prostate cell-types pointed to transcriptional regulators of inflammatory and hypoxia-related signaling. Glutathione metabolism and the antioxidant response emerged as a common signature of aging across prostatic lineages. Expression of genes implicated in mouse prostate aging, including the antioxidant response gene *Hmox1*, correlates with age of diagnosis in primary prostate tumors from the TCGA cohort. These findings reveal a common signature shared by distinct cell-types in the old prostate reflective of age-associated metabolic reprogramming.

Keywords: Prostate, stromal, basal, luminal, metabolism, inflammation, hypoxia

Introduction

Aging in the human prostate is strongly associated with histological changes including tissue enlargement, or benign prostatic hyperplasia (BPH), which occurs in 70% of men in their 70's [1]. Risk of prostate cancer also increases with age [2], and histological evidence of malignancy in the prostate is observed in 50% of men in their 70's [3]. As the percentage of men over 65 increases, understanding the fundamental changes that occur with age in the prostate will be essential to combat disease risk. However, the mechanisms by which age increases risk of BPH and prostate cancer is still poorly understood. Studies in rodents have begun to shed light on fundamental mechanisms of aging in the prostate.

The prostate is a cellular heterogeneous organ, with two epithelial layers consisting of basal and luminal cells, stromal cells, and an inflammatory component [4]. We and others have demonstrated a significant increase in prostate-infiltrating inflammatory cells in old mouse prostates, with a notable expansion in T and B-lymphocytes [5, 6]. In a recent study, we demonstrated a fundamental age-related shift within the luminal compartment, identifying Trop2+ luminal progenitor cells that are rare in young mouse prostate and expand in old prostates [5]. The age-related increase in inflammatory cells and luminal progenitor cells is observed not only in mouse prostate but also in non-cancerous human prostate, indicating that discoveries of prostatic aging in rodents can inform mechanisms of human prostate aging.

In several tissue systems, aging varies between cell-types. For example, an age-related increased frequency of megakaryocyte/erythrocyte progenitor cells and decreased frequency of common lymphoid progenitors indicates that not all cells in the blood system age equivalently [7]. This is true in the prostate, where basal cells and Trop2+ luminal cells maintain their organoid-forming activity with age, while Trop2- luminal cell-initiated organoid-forming capacity diminishes with age [5]. Despite functional differences between cell-types, we hypothesized that we might gain insight into prostatic aging by comparing age-related changes in gene expression profiles across distinct cell-types.

Inflammation is closely linked with tissue hypoxia, or low oxygen conditions, and oxidative stress [8]. Interestingly, hypoxia is associated with aging in the prostate [9], and increased glutathione, which protects cells against oxidative stress through scavenging of reactive oxygen species [10], has been observed in the old rat prostate [11]. Microdissection of stromal cells adjacent to prostatic glands in young and old mice revealed increased expression of inflammatory and oxidative stress-related genes [6], which may be caused by the inflammatory microenvironment in the aging prostate. We reasoned that shared signatures of aging across multiple distinct cell-types may reflect cellular responses to the local microenvironment.

Here we performed RNA-sequencing of stromal cells, basal cells, Trop2+ luminal progenitor cells and Trop2- luminal cells from 3-month-old and 24-month-old mouse prostates and evaluated age-related changes in gene expression profiles. Common signatures of aging were associated with inflammation and glutathione metabolism. Larger changes in metabolic gene expression were observed including alterations in genes that regulate glucose, lactate, glutamine, proline and lipid metabolism in old epithelial cell-types. Shared features of mouse prostate aging were associated with age of diagnosis in the TCGA primary prostate cancer cohort. These findings suggest that distinct prostate cell-types with distinct functional capacities share a common aging signature indicative of metabolic reprogramming as a response to the microenvironment.

Materials and methods

Animals

C57BL/6 mice were purchased from Jackson Laboratories and housed and maintained at UCLA by the Division of Laboratory Animal Medicine (DLAM) following approved protocols for animal care.

Mouse prostate dissociation and cell sorting

Prostates were collected from C57BL/6 mice aged to 3 or 24 months, dissociated to single cells, and stained with antibodies for Fluorescence Activated Cell Sorting as previously described [5, 12]. Stromal cells (Lin- EpCAM- CD49f-), basal cells (Lin- EpCAM+ CD49f^{hi}), Trop2+ luminal (Lin- EpCAM+ CD49f^{mid} Trop2+) and Trop2- luminal (Lin- EpCAM+ CD49f^{mid} Trop2-) were isolated on a FACSAria II cell sorter (BD Biosciences) as previously described [5].

RNA sequencing and analysis

RNA extraction from cells was carried out using the RNeasy Mini Kit (QIAGEN) following manufacturer's instructions. RNA-seq Libraries were prepared using KAPA Stranded mRNA-Seq Kit (Roche). The workflow was comprised of mRNA enrichment, cDNA generation, and end repair to generate blunt ends, A-tailing, adaptor ligation and PCR amplification. Different adaptors were used to multiplex samples in a single lane. Sequencing was performed on the Illumina HiSeq 3000 for 1x50 run. Data analysis was carried out as previously described [5] and sequencing data have been deposited in NCBI's Gene Expression Omnibus and can be accessed through GEO Series accession number GSE122367 and GSE128724. Principal component analysis was determined using iDEP [13] (http://bioinformatics.sdstate.edu/idep/). Gene set enrichment analysis (GSEA) was performed as described previously [14, 15] using GSEA 4.0.3 software and MSigDB hallmark gene sets. Motif analysis was performed using i-cisTarget [16, 17] (https://gbiomed.kuleuven.be/apps/lcb/i-cisTarget/). KEGG pathway and Gene Ontology analysis was performed using DAVID Bioinformatics [18, 19] (https://david.ncifcrf.gov/). TCGA primary prostate cancer data [20, 21] was accessed using the cBioPortal [22, 23] (https://www.cbioportal.org/). Tumors were stratified

based on age of diagnosis, and the bottom and top quartiles were compared for analysis of relative gene expression.

Results

Prostate stromal cells exhibit age-related transcriptional changes

In our previous analysis of aging prostates, we found an increase in the number of non-epithelial cells in 24-month-old prostates compared to 3-month-old young adult prostates, whereas the total number of basal and luminal cells did not significantly change with age [5]. Not only did we find a statistically significant increase in the number of Lin- EpCAM- CD49f- stromal cells in old mouse prostates, but we also found a significant decrease in stromal cell forward scatter, a measurement of Fluorescence Activated Cell Sorting (FACS) indicative of cell size. These findings suggest that aging is associated with multiple changes in the prostate stromal compartment. Here we set out to transcriptionally profile stromal cells from young adult and old mouse prostates using RNA-sequencing (RNA-seq) to gain further insight into age-related changes within the stromal compartment.

When we looked for genes that were increased or decreased at least 1.5-fold with a p-value < 0.05, we identified 1520 genes that changed significantly with age within the stromal compartment of the mouse prostate (**Figure 1A**). Out of 1520 genes, 1020 were elevated in old prostates, whereas only 500 were significantly downregulated with age. Gene set enrichment analysis showed a significant enrichment for hallmarks of inflammatory response and interferon signaling (**Figure 1B**). We performed gene ontology (GO) and pathway analysis (**Figures 1C**, **1D**, S1A, S1B) on significantly up- or downregulated genes. Immune-related GO terms and pathways were well represented in the aging signature (**Figures 1C**, S1A, S1B), consistent with age-related inflammation as we and others have previously described [5, 6]. We noted "response to drug" and "drug metabolism" as enriched pathways in old stromal cells (**Figures 1C**, S1A, S1B). In contrast, extracellular matrix (ECM) and adhesion-related terms and pathways were enriched in genes downregulated with age (**Figures 1D**, S1A, S1B), consistent with previous reports of reduced ECM stiffness in the aging prostate microenvironment [6, 24]. The most differentially expressed genes reflected these major pathways, including *Stc1*, an antioxidant response gene and inhibitor of inflammation [25], which was significantly elevated in old stromal cells (**Figure 1E**). The elastin gene (*Eln*), which encodes a protein critical for ECM elastic fibers [26], is the most significantly reduced gene in the old stromal compartment (**Figure 1E**).

We performed motif analysis on the 1020 genes elevated in old prostate stromal cells to identify candidate transcriptional regulators of the aging stromal signature. Motif analysis yielded the transcription factors Arnt, Irf3 and Egr2 (**Figure 1F**), suggesting that these transcription factors, or closely related family members with similar binding patterns, may be involved in promoting the aging stromal signature. We observed elevated mRNA expression of *Arnt2*, *Irf4*, *Egr1 and Egr2* in old prostate stromal cells (**Figures 1F**, S1C). Arnt2 forms a complex with Hif1a under conditions of low oxygen and activates hypoxia-regulated genes [27]. Irf4, Egr1 and Egr2 are associated with inflammation and immune function [28-30], while Egr family members may also be regulated by hypoxia [31]. These findings suggest that the aging stromal signature is likely to be influenced by the inflammatory microenvironment.

Prostate basal cells exhibit age-related transcriptional changes

We next looked into age-related changes in prostate basal cells, which sit adjacent to stromal cells in the gland. We previously demonstrated that the number and functional capacity of basal cells does not change significantly with age [5]. Using transcriptional profiling, we determined that 855 genes exhibited at least 1.5-fold differential gene expression between 3- and 24-month-old prostate basal cells. Similar numbers of genes were up (432) and downregulated (423) with age in the basal cell compartment (**Figure 2A**). Motif analysis on the 432 genes increased in old basal cells revealed enrichment for binding sites of Ets factors, Cebpb, and Egr1 (**Figure 2B**). Increased expression of *Egr1*, *Egr2* and *Elf3* in old basal cells (**Figures 2B**, **2C**, S2A) pointed to a potential role for these transcription factors in the aging basal cell signature.

Pathway analysis revealed enrichment for drug metabolism and glutathione metabolism in

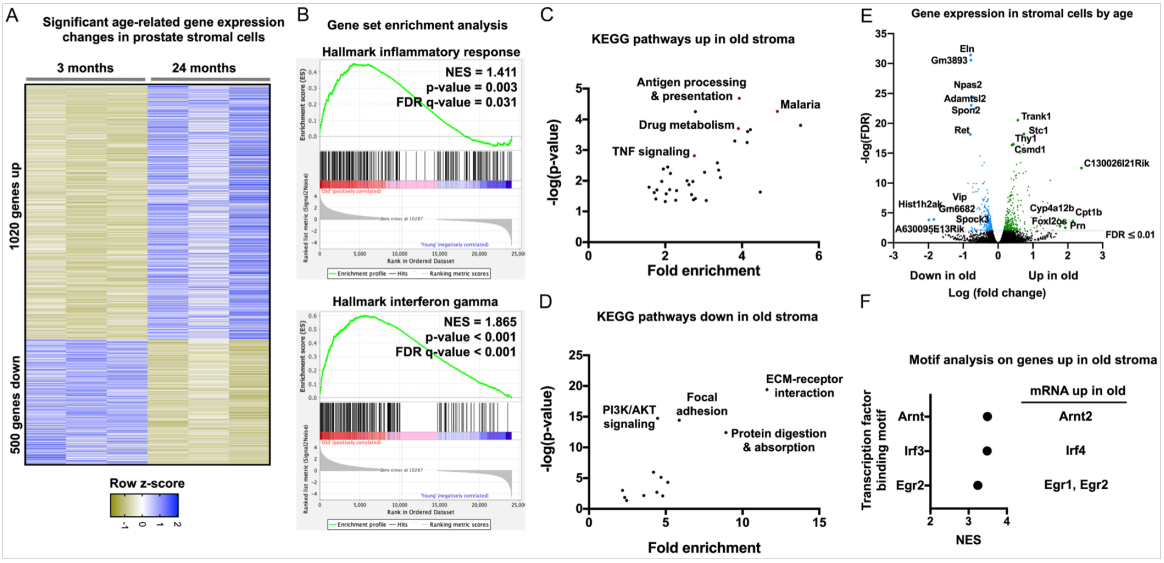

Figure 1. Age-related transcriptional changes in prostate stromal cells. (A) Heatmap of significantly differentially expressed genes in 3- and 24-month-old prostate stromal cells. Only genes greater than 1.5-fold enriched in either direction with a *p*-value < 0.05 are included. (B) Gene set enrichment analysis indicates significant enrichment for inflammatory response and interferon gamma hallmarks in the old prostate stromal signature. NES: normalized enrichment score. (C, D) KEGG pathway analysis reveals significantly enriched pathways in 24-month-old (C) or 3-month-old (D) stromal cell signatures. (E) Volcano plot reveals significantly altered genes based on -log (FDR) and log (fold change). FDR: false discovery rate. (F) Motif analysis reveals transcription factors with binding motif enrichment in the old prostate stromal signature. NES: normalized enrichment score.

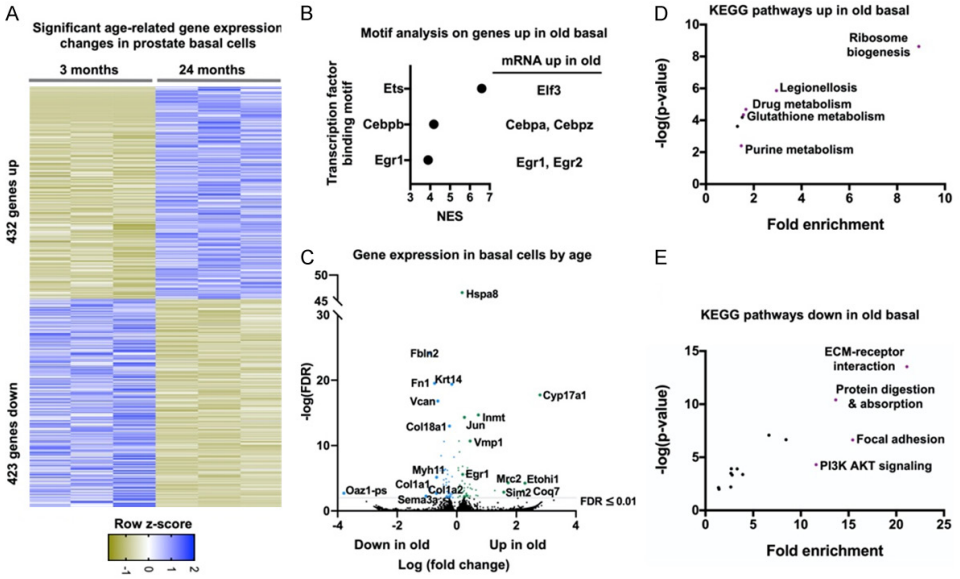

Figure 2. Age-related transcriptional changes in prostate basal cells. (A) Heatmap of significantly differentially expressed genes in 3- and 24-month-old prostate basal cells showing genes greater than 1.5-fold enriched in either direction with a *p*-value < 0.05. (B) Motif analysis reveals potential transcriptional regulators of the old prostate basal cell signature. NES: normalized enrichment score. (C) Volcano plot reveals significantly altered genes based on -log (FDR) and log (fold change). FDR: false discovery rate. (D, E) KEGG pathway analysis reveals significantly enriched pathways in 24-month-old (D) or 3-month-old (E) basal cell signatures.

aging basal cells (**Figures 2D**, S2B, S2C). Pathways downregulated in old basal cells included ECM interactions and adhesion (**Figures 2E**, S2B, S2C), with genes encoding ECM proteins including *Col1a1*, *Col1a2*, *Col18a1* and *Fn1* among the most significantly down with age (**Figure 2C**). Based on similarities in age-related pathway enrichment and potential transcriptional regulators in old stromal and basal cells, we set out to evaluate age-related signatures of additional cell subsets in the old mouse prostate.

Trop2+ luminal progenitor cells and Trop2- luminal cells share aging signatures

In our previous work, we identified Trop2 as a marker of luminal progenitor cells that generate large organoids and expand with age in the mouse prostate [5]. While Trop2+ luminal progenitor cells maintain their organoid-forming capacity with age, old Trop2- luminal cells exhibit reduced functional activity and reduced expression of cell cycle-related genes. We asked whether these two distinct luminal subsets with distinct functional responses to aging share common signatures of aging. Principal component analysis distinguished luminal subsets based on cell-type (PCA #1: Trop2+ vs Trop2-) and age (PCA #2: 3 months vs 24 months), suggesting that both luminal subsets share an aging signature (**Figure 3A**).

We evaluated genes that changed significantly with age in Trop2+ and Trop2- luminal cells (**Figure 3B**, **3C**) and performed GO analysis on significantly up and down-regulated genes (**Figures 3D**, **3E**, S3A-D). Both luminal populations in old prostates exhibited enrichment for terms associated with the immune response (**Figure 3D**, **3E**), consistent with increased inflammation in old prostates [5, 6]. GO analysis also revealed enrichment for glutathione metabolism and response to hypoxia in old luminal cells (**Figure 3A**, **3B**). ER unfolded protein response was among the common GO terms enriched for genes downregulated with age in the two luminal subsets (Figure S3C, S3D). Motif analysis of significantly upregulated genes in old Trop2+ and Trop2- luminal cells

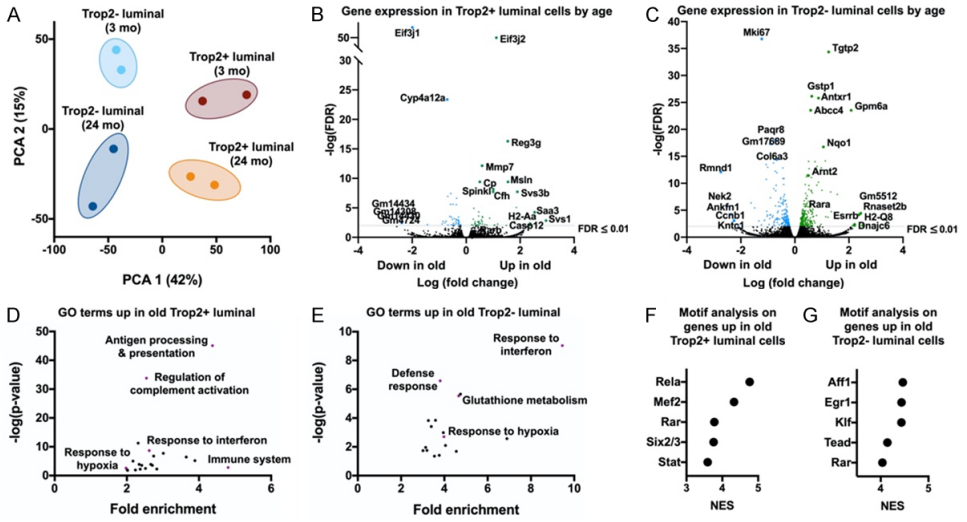

Figure 3. Age-related transcriptional changes in distinct luminal cell subsets. (A) Principal component analysis of gene signatures of Trop2+ and Trop2- luminal subsets from 3 and 24-month-old mouse prostates. (B, C) Volcano plots reveal significantly altered genes based on -log (FDR) and log (fold change) in Trop2+ (B) and Trop2- (C) luminal cells. FDR: false discovery rate. (D, E) Gene Ontology (GO) terms enriched in old Trop2+ (D) and Trop2- (E) luminal cell signatures. (F, G) Motif analysis reveals potential transcriptional regulators of the old Trop2+ (F) and Trop2- (G) luminal cell signatures. NES: normalized enrichment score.

revealed immune-related transcription factors and retinoic acid receptors (**Figure 3F**, **3G**). Elevated mRNA expression of retinoic acid receptor family members (*Rara*, *Rarb, Rarg*), and the previously described gene *Arnt2*, was also observed in old luminal cells (**Figures 3B**, **3C**, S3E, S3F). Retinoic acid receptors are upregulated in response to all-trans retinoic acid (ATRA) and have been associated with inflammation [32, 33] as well as protection from oxidative stress caused by hypoxia [34, 35]. These findings suggest that distinct luminal subsets share common features of aging, despite differences in age-related functional capacity.

Glutathione metabolism is a common feature of aging across distinct epithelial cell-types

We compared the genes significantly upregulated in old basal cells, old Trop2+ luminal cells, and old Trop2- luminal cells to identify common age-related changes (**Figures 4A**, S4A). Interestingly, 45% (217/484) of the genes upregulated in old Trop2+ luminal cells were shared with old basal cells, old Trop2- luminal cells, or with both. In contrast, 23% (201/888) of genes upregulated in old Trop2- luminal cells, and 23% (101/432) of genes upregulated in old basal cells were shared by other old epithelial cell-types. A total of 11 genes were found to be significantly upregulated in all three epithelial subsets (**Figure 4A**). This list included *Hmox1*, an antioxidant response gene, and *Gclc*, a regulator of glutathione synthesis (Figure S4A). Motif analysis of these common genes revealed a significant enrichment for the Mef2 family of transcription factors (Figure S4B). Mef2d has been shown to activate Nrf2 [36], a master regulator of the antioxidant response [37].

We evaluated age-related mRNA expression of metabolic genes and found consistently increased expression of many genes involved in glutathione metabolism in old epithelial cell-types (**Figure 4B-D**). We also observed increased expression of the glycolytic gene *Pkm*, the lactate transporter *Slc16a1* (which encodes Mct1), and *Pdk4 (*pyruvate dehydrogenase kinase 4) in old basal and Trop2+ luminal progenitor cells. Old Trop2+ and Trop2- luminal cells exhibited increased expression of the glycolytic gene *Pfkp* and lactate dehydrogenase b (*Ldhb*) (**Figure 4B-D**). Metabolic enzymes

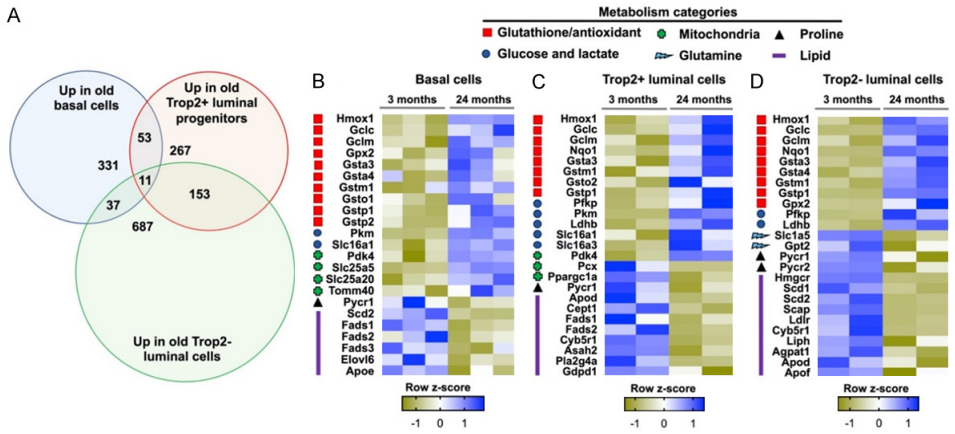

Figure 4. Shared aging signatures and metabolic genes across three distinct epithelial cell subsets. (A) Venn diagram comparing genes that are significantly upregulated in old epithelial cells. (B-D) Heatmaps reveal metabolic genes that are differentially expressed between 3- and 24-month-old basal cells (B), Trop2+ luminal cells (C) and Trop2- luminal cells (D).

involved in proline metabolism and lipid metabolism were consistently reduced in old epithelial cells (**Figure 4B-D**), consistent with GO analysis (Figure S3C). These results suggest that aging in prostate epithelial cells is likely associated with metabolic reprogramming beyond glutathione metabolism.

In contrast to old Trop2- luminal cells which exhibit reduced functional activity, both basal and Trop2+ luminal cells maintain their progenitor activity with age [5]. We further evaluated genes elevated in old basal and Trop2+ luminal cells to identify potential factors regulating the age-related maintenance of progenitor activity. Motif analysis revealed enrichment for Rela/Nfkb1 and Sox2 specifically for genes shared by basal and Trop2+ luminal cells, and these transcription factors were not significantly enriched in any other group (Figure S4B). Sox2 is an important regulator of self-renewal and stemness in many tissues [38, 39] and also plays a role in prostate cancer progression and antiandrogen-resistance [40, 41]. Importantly, *Sox2* and *Nfkb1* were both elevated in basal cells and in Trop2+ luminal cells at the mRNA level (Figure S4C, S4D).

Hmox1 and genes associated with aging in the mouse prostate correlate with age in human primary prostate cancer

We wondered whether transcriptional features of aging shared by distinct cell-types in the mouse prostate may also be observed in human prostate cancer. The Cancer Genome Atlas (TCGA) primary prostate cancer cohort contains nearly 500 cases of prostate cancer [20, 21], with age of diagnosis distributed over 4 decades (41 to 78 years). The antioxidant response gene [42] and Nrf2 target [43] *Hmox1* was correlated with age of diagnosis in a statistically significant manner (Figure S5). We evaluated mRNA expression of candidate genes in the lowest (41-56 years, 123 tumors) and highest (66-78 years, 124 tumors) quartiles from the TCGA cohort. In addition to *Hmox1*, we also observed increased mRNA expression of candidate regulators of the mouse prostate aging signature including *Rara*, *Egr2* and several interferon regulatory factors (*Irf1*, *Irf3*, *Irf4*, *Irf5*) in the upper quartile (**Figure 5A**). In contrast, lipid metabolism genes that are reduced in old mouse prostate cells (*Hmgcr*, *Scd*), and a regulator of the lipogenic program (*Srebf2*) [44], were also reduced in the upper quartile (**Figure 5A**). We evaluated the correlation between *Hmox1* mRNA and several age-related genes in the TCGA primary prostate cancer cohort and found positive correlations with *Egr2*, *Rara* and *Irf4* and negative correlations with *Hmgcr* and *Srebf2* (**Figure 5B**). These findings suggest an age-related signature in human primary prostate cancer associated with increased antioxidant response and inflammatory response genes and reduced lipid metabolism genes.

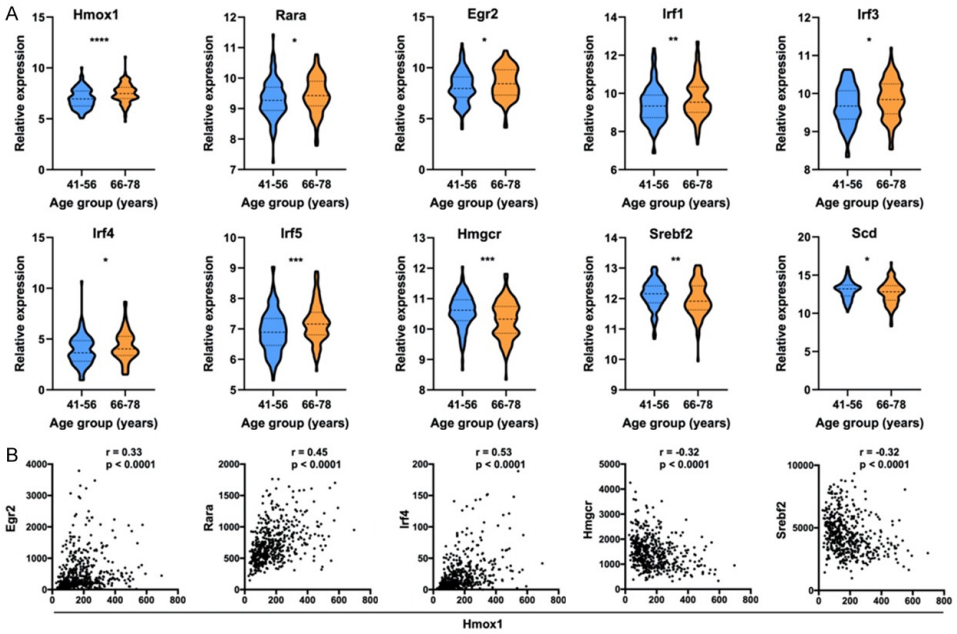

Figure 5. Genes associated with aging mouse prostate correlate with age in primary prostate cancer. A. Violin plots of mRNA expression in TCGA cohort of primary prostate cancer comparing the bottom and top quartiles by age of diagnosis. * P < 0.05, ** P < 0.01, *** P < 0.001, **** P < 0.0001. B. Plots revealing relative mRNA expression of Hmox1 with Egr2, Rar1, Irf4, Hmgcr and Srebf2 in TCGA primary prostate cancer specimens. Spearman correlation coefficients and *p*-values are shown. Note: 5-11 points with very high expression lie outside of the range of plots in order to better demonstrate correlations in B.

Discussion

Aging in the prostate is associated with an increase in inflammatory cell infiltration, most notably T and B lymphocytes which are relatively rare in the young adult prostate [5, 6]. How the old inflammatory microenvironment influences normal prostate stromal and epithelial cells has not been well described. We evaluated age-related changes to gene expression profiles in four distinct cell-types of the mouse prostate and identified a shared signature of aging. Stromal cells, basal cells, Trop2+ luminal progenitor cells, and Trop2- luminal cells exhibited age-related increases in inflammatory/immune-related and antioxidant/glutathione metabolism-related signatures. These results suggest that prostate stromal and epithelial cells are likely responding to a hypoxic inflammatory environment by increasing the antioxidant program. Some of the candidate transcriptional regulators of prostate aging signatures in multiple cell-types, including Arnt2, Egr1/2, Rara/b, may contribute to protecting old prostate cells from oxidative stress associated with an inflammatory and hypoxic environment. Future studies will be necessary to functionally evaluate the role of various transcriptional and metabolic regulators of prostate aging.

We previously reported age-related changes to the stromal compartment [5], based on an increase in the total number of stromal cells and a decrease in the forward scatter, a surrogate for cell size, in old mouse prostates. We now show significant age-related changes to the transcriptional profiles of isolated stromal cells. Transcriptional changes to the stromal compartment with age are consistent with a previous study that used laser capture microdissection to collect RNA from non-epithelial regions of the young and old mouse prostate [6]. The stromal subset used in our study is likely heterogeneous, containing fibroblasts and smooth muscle cells. One of the most sig-

nificant upregulated genes in old stromal cells is *Thy1* (CD90) (**Figure 1E**), which has recently been shown to mark a distinct subset of prostate stromal cells [45]. It is possible that a change in the proportion of subsets within the stromal compartment contributed to the age-related transcriptional changes observed here, similar to our previous report that age-related changes in the bulk luminal signature reflected an age-related increase in the proportion of Trop2+ luminal cells. By isolating out these distinct subsets and comparing their profiles from young and old mouse prostates, we can further understand signatures of aging.

In addition to increased glutathione metabolism in old prostate cells, we observed age-related changes in mRNA expression of metabolic genes encoding enzymes and transporters involved in glucose, lactate, glutamine and lipid metabolism. Age-related changes to the microenvironment, including inflammatory cytokines, hypoxia and nutrient availability, are capable of altering metabolic gene expression. Collectively, these results suggest a role for metabolic reprogramming in prostatic aging. Interestingly, gene expression patterns of aging in the mouse prostate were observed in primary prostate cancers from the TCGA cohort, with increased mRNA expression of antioxidant and inflammatory response genes and decreased expression of lipid metabolism genes in the oldest quartile by age. Age-related changes to the human prostate microenvironment may influence gene expression patterns of prostate cancer. Hypoxia is associated with increased genomic instability, mutations in p53, loss of Pten, and telomere shortening in localized prostate cancer [46]. This process is believed to occur through selective pressure on the tumor, whereby survival clones emerge when normal oxygen levels are restored. Whether hypoxia similarly exerts selective pressure on normal cells in the aging prostate has not been determined. Differential response to a hypoxic environment may provide one explanation for the increase in the proportion of Trop2+ luminal progenitor cells and the decrease in Trop2- luminal cells in the old mouse prostate.

In this study, we focused on age-related gene signatures shared by distinct cell-types, including basal and Trop2+ luminal cells that maintain progenitor activity with age as well as Trop2- luminal cells that exhibit functional decline with age. We reasoned that these analyses may also elucidate factors that enable basal and Trop2+ luminal cells to retain their functional capacity. Motif analysis of genes upregulated with age in basal and Trop2+ luminal cells revealed Sox2 and Nfkb1. Importantly, both *Sox2* and *Nfkb1* are expressed at higher levels (mRNA) in the populations that maintain progenitor activity with age as compared to Trop2- luminal cells. Whether these transcription factors contribute to the age-related maintenance of progenitor activity will need to be experimentally determined. Both basal and luminal progenitor cells are capable of responding to genetic alterations to initiate prostate cancer [47-51]. Therefore, understanding how they maintain their functional activity with age may yield new strategies to prevent prostate cancer initiation. In summary, we offer age-related signatures of distinct stromal and epithelial cell-types as a resource to gain new insight into mechanisms of aging and increased risk of disease in the prostate.

Acknowledgements

We thank Donghui Cheng for cell sorting and the UCLA Technology Center for Genomics & Bioinformatics for RNA sequencing. This work was supported by the American Cancer Society (RSG-17-068-01-TBG), NIH/NCI (R01CA2371-91), Rose Hills Foundation, Gill endowment dedicated to cancer research and the Spitzer Family Foundation Fund, as well as support from UCLA's Jonsson Comprehensive Cancer Center, Broad Stem Cell Research Center, Clinical and Translational Science Institute, and Institute of Urologic Oncology. PDC and JMG are supported by a Ruth L. Kirschstein National Research Service Award GM007185.

Disclosure of conflict of interest

None.

Address correspondence to: Dr. Andrew S Goldstein, Department of Molecular, Cell, and Developmental Biology, University of California, Los Angeles, 610 Charles E Young Drive South, Los Angeles, CA 90095, USA. Tel: 310-206-1402; Fax: 310-206-0356; E-mail: agoldstein@mednet.ucla.edu

References

[1] Platz EA, Smit E, Curhan GC, Nyberg LM and Giovannucci E. Prevalence of and racial/ethnic

variation in lower urinary tract symptoms and noncancer prostate surgery in U.S. men. Urology 2002; 59: 877-883.
[2] Stangelberger A, Waldert M and Djavan B. Prostate cancer in elderly men. Rev Urol 2008; 10: 111-119.
[3] Carter HB, Piantadosi S and Isaacs JT. Clinical evidence for and implications of the multistep development of prostate cancer. J Urol 1990; 143: 742-746.
[4] Strand DW and Goldstein AS. The many ways to make a luminal cell and a prostate cancer cell. Endocr Relat Cancer 2015; 22: T187-97.
[5] Crowell PD, Fox JJ, Hashimoto T, Diaz JA, Navarro HI, Henry GH, Feldmar BA, Lowe MG, Garcia AJ, Wu YE, Sajed DP, Strand DW and Goldstein AS. Expansion of luminal progenitor cells in the aging mouse and human prostate. Cell Rep 2019; 28: 1499-1510, e6.
[6] Bianchi-Frias D, Vakar-Lopez F, Coleman IM, Plymate SR, Reed MJ and Nelson PS. The effects of aging on the molecular and cellular composition of the prostate microenvironment. PLoS One 2010; 5: e12501.
[7] Rundberg Nilsson A, Soneji S, Adolfsson S, Bryder D and Pronk CJ. Human and murine hematopoietic stem cell aging is associated with functional impairments and intrinsic megakaryocytic/erythroid bias. PLoS One 2016; 11: e0158369.
[8] McGarry T, Biniecka M, Veale DJ and Fearon U. Hypoxia, oxidative stress and inflammation. Free Radic Biol Med 2018; 125: 15-24.
[9] Movsas B, Chapman JD, Greenberg RE, Hanlon AL, Horwitz EM, Pinover WH, Stobbe C and Hanks GE. Increasing levels of hypoxia in prostate carcinoma correlate significantly with increasing clinical stage and patient age: an Eppendorf pO(2) study. Cancer 2000; 89: 2018-2024.
[10] Ogunrinu TA and Sontheimer H. Hypoxia increases the dependence of glioma cells on glutathione. J Biol Chem 2010; 285: 37716-37724.
[11] Richie JP Jr, Das A, Calcagnotto AM, Aliaga CA and El-Bayoumy K. Age related changes in selenium and glutathione levels in different lobes of the rat prostate. Exp Gerontol 2012; 47: 223-228.
[12] Fox JJ, Navarro HI, Hashimoto T, Garcia AJ and Goldstein AS. Mass cytometry reveals species-specific differences and a new level of complexity for immune cells in the prostate. Am J Clin Exp Urol 2019; 7: 281-296.
[13] Ge SX, Son EW and Yao R. iDEP: an integrated web application for differential expression and pathway analysis of RNA-Seq data. BMC Bioinformatics 2018; 19: 534.
[14] Subramanian A, Tamayo P, Mootha VK, Mukherjee S, Ebert BL, Gillette MA, Paulovich A, Pomeroy SL, Golub TR, Lander ES and Mesirov JP. Gene set enrichment analysis: a knowledge-based approach for interpreting genome-wide expression profiles. Proc Natl Acad Sci U S A 2005; 102: 15545-15550.
[15] Mootha VK, Lindgren CM, Eriksson KF, Subramanian A, Sihag S, Lehar J, Puigserver P, Carlsson E, Ridderstrale M, Laurila E, Houstis N, Daly MJ, Patterson N, Mesirov JP, Golub TR, Tamayo P, Spiegelman B, Lander ES, Hirschhorn JN, Altshuler D and Groop LC. PGC-1alpha-responsive genes involved in oxidative phosphorylation are coordinately downregulated in human diabetes. Nat Genet 2003; 34: 267-273.
[16] Imrichova H, Hulselmans G, Atak ZK, Potier D and Aerts S. i-cisTarget 2015 update: generalized cis-regulatory enrichment analysis in human, mouse and fly. Nucleic Acids Res 2015; 43: W57-64.
[17] Herrmann C, Van de Sande B, Potier D and Aerts S. i-cisTarget: an integrative genomics method for the prediction of regulatory features and cis-regulatory modules. Nucleic Acids Res 2012; 40: e114.
[18] Huang da W, Sherman BT and Lempicki RA. Systematic and integrative analysis of large gene lists using DAVID bioinformatics resources. Nat Protoc 2009; 4: 44-57.
[19] Huang da W, Sherman BT and Lempicki RA. Bioinformatics enrichment tools: paths toward the comprehensive functional analysis of large gene lists. Nucleic Acids Res 2009; 37: 1-13.
[20] Cancer Genome Atlas Research Network. The molecular taxonomy of primary prostate cancer. Cell 2015; 163: 1011-1025.
[21] Liu J, Lichtenberg T, Hoadley KA, Poisson LM, Lazar AJ, Cherniack AD, Kovatich AJ, Benz CC, Levine DA, Lee AV, Omberg L, Wolf DM, Shriver CD, Thorsson V; Cancer Genome Atlas Research Network, Hu H. An integrated TCGA pan-cancer clinical data resource to drive high-quality survival outcome analytics. Cell 2018; 173: 400-416, e11.
[22] Cerami E, Gao J, Dogrusoz U, Gross BE, Sumer SO, Aksoy BA, Jacobsen A, Byrne CJ, Heuer ML, Larsson E, Antipin Y, Reva B, Goldberg AP, Sander C and Schultz N. The cBio cancer genomics portal: an open platform for exploring multidimensional cancer genomics data. Cancer Discov 2012; 2: 401-404.
[23] Gao J, Aksoy BA, Dogrusoz U, Dresdner G, Gross B, Sumer SO, Sun Y, Jacobsen A, Sinha R, Larsson E, Cerami E, Sander C and Schultz N. Integrative analysis of complex cancer genomics and clinical profiles using the cBioPortal. Sci Signal 2013; 6: pl1.
[24] Bianchi-Frias D, Damodarasamy M, Hernandez SA, Gil da Costa RM, Vakar-Lopez F, Coleman IM, Reed MJ and Nelson PS. The aged micro-

environment influences the tumorigenic potential of malignant prostate epithelial cells. Mol Cancer Res 2019; 17: 321-331.
[25] Tang SE, Wu CP, Wu SY, Peng CK, Perng WC, Kang BH, Chu SJ and Huang KL. Stanniocalcin-1 ameliorates lipopolysaccharide-induced pulmonary oxidative stress, inflammation, and apoptosis in mice. Free Radic Biol Med 2014; 71: 321-331.
[26] Halper J and Kjaer M. Basic components of connective tissues and extracellular matrix: elastin, fibrillin, fibulins, fibrinogen, fibronectin, laminin, tenascins and thrombospondins. Adv Exp Med Biol 2014; 802: 31-47.
[27] Maltepe E, Keith B, Arsham AM, Brorson JR and Simon MC. The role of ARNT2 in tumor angiogenesis and the neural response to hypoxia. Biochem Biophys Res Commun 2000; 273: 231-238.
[28] Nam S and Lim JS. Essential role of interferon regulatory factor 4 (IRF4) in immune cell development. Arch Pharm Res 2016; 39: 1548-1555.
[29] Gururajan M, Simmons A, Dasu T, Spear BT, Calulot C, Robertson DA, Wiest DL, Monroe JG and Bondada S. Early growth response genes regulate B cell development, proliferation, and immune response. J Immunol 2008; 181: 4590-4602.
[30] Miao T, Symonds ALJ, Singh R, Symonds JD, Ogbe A, Omodho B, Zhu B, Li S and Wang P. Egr2 and 3 control adaptive immune responses by temporally uncoupling expansion from T cell differentiation. J Exp Med 2017; 214: 1787-1808.
[31] Tamama K and Barbeau DJ. Early growth response genes signaling supports strong paracrine capability of mesenchymal stem cells. Stem Cells Int 2012; 2012: 428403.
[32] Pino-Lagos K, Guo Y and Noelle RJ. Retinoic acid: a key player in immunity. Biofactors 2010; 36: 430-436.
[33] Cao W, Chen W, Liang X, Zhou J, Wei C, Cui S and Liu J. All-trans-retinoic acid ameliorates the inflammation by inducing transforming growth factor beta 1 and interleukin 10 in mouse epididymitis. Am J Reprod Immunol 2014; 71: 312-321.
[34] Fernandez-Martinez AB, Jimenez MI, Hernandez IS, Garcia-Bermejo ML, Manzano VM, Fraile EA and de Lucio-Cazana FJ. Mutual regulation of hypoxic and retinoic acid related signalling in tubular proximal cells. Int J Biochem Cell Biol 2011; 43: 1198-1207.
[35] Jiang L, Qin Y, Lei F, Chen X and Zhou Z. Retinoic acid receptors alpha and gamma are involved in antioxidative protection in renal tubular epithelial cells injury induced by hypoxia/reoxygenation. Free Radic Res 2017; 51: 873-885.
[36] Nagar S, Noveral SM, Trudler D, Lopez KM, McKercher SR, Han X, Yates JR 3rd, Pina-Crespo JC, Nakanishi N, Satoh T, Okamoto SI and Lipton SA. MEF2D haploinsufficiency downregulates the NRF2 pathway and renders photoreceptors susceptible to light-induced oxidative stress. Proc Natl Acad Sci U S A 2017; 114: E4048-E4056.
[37] Nguyen T, Nioi P and Pickett CB. The Nrf2-antioxidant response element signaling pathway and its activation by oxidative stress. J Biol Chem 2009; 284: 13291-13295.
[38] Fong H, Hohenstein KA and Donovan PJ. Regulation of self-renewal and pluripotency by Sox2 in human embryonic stem cells. Stem Cells 2008; 26: 1931-1938.
[39] Avilion AA, Nicolis SK, Pevny LH, Perez L, Vivian N and Lovell-Badge R. Multipotent cell lineages in early mouse development depend on SOX2 function. Genes Dev 2003; 17: 126-140.
[40] Kregel S, Kiriluk KJ, Rosen AM, Cai Y, Reyes EE, Otto KB, Tom W, Paner GP, Szmulewitz RZ and Vander Griend DJ. Sox2 is an androgen receptor-repressed gene that promotes castration-resistant prostate cancer. PLoS One 2013; 8: e53701.
[41] Mu P, Zhang Z, Benelli M, Karthaus WR, Hoover E, Chen CC, Wongvipat J, Ku SY, Gao D, Cao Z, Shah N, Adams EJ, Abida W, Watson PA, Prandi D, Huang CH, de Stanchina E, Lowe SW, Ellis L, Beltran H, Rubin MA, Goodrich DW, Demichelis F and Sawyers CL. SOX2 promotes lineage plasticity and antiandrogen resistance in TP53- and RB1-deficient prostate cancer. Science 2017; 355: 84-88.
[42] Poss KD and Tonegawa S. Reduced stress defense in heme oxygenase 1-deficient cells. Proc Natl Acad Sci U S A 1997; 94: 10925-10930.
[43] Reichard JF, Motz GT and Puga A. Heme oxygenase-1 induction by NRF2 requires inactivation of the transcriptional repressor BACH1. Nucleic Acids Res 2007; 35: 7074-7086.
[44] Shao W and Espenshade PJ. Expanding roles for SREBP in metabolism. Cell Metab 2012; 16: 414-419.
[45] Kwon OJ, Zhang Y, Li Y, Wei X, Zhang L, Chen R, Creighton CJ and Xin L. Functional heterogeneity of mouse prostate stromal cells revealed by single-cell RNA-Seq. iScience 2019; 13: 328-338.
[46] Bhandari V, Hoey C, Liu LY, Lalonde E, Ray J, Livingstone J, Lesurf R, Shiah YJ, Vujcic T, Huang X, Espiritu SMG, Heisler LE, Yousif F, Huang V, Yamaguchi TN, Yao CQ, Sabelnykova VY, Fraser M, Chua MLK, van der Kwast T, Liu SK, Boutros PC and Bristow RG. Molecular landmarks of tumor hypoxia across cancer types. Nat Genet 2019; 51: 308-318.

[47] Goldstein AS, Huang J, Guo C, Garraway IP and Witte ON. Identification of a cell of origin for human prostate cancer. Science 2010; 329: 568-571.
[48] Liu X, Grogan TR, Hieronymus H, Hashimoto T, Mottahedeh J, Cheng D, Zhang L, Huang K, Stoyanova T, Park JW, Shkhyan RO, Nowroozizadeh B, Rettig MB, Sawyers CL, Elashoff D, Horvath S, Huang J, Witte ON and Goldstein AS. Low CD38 identifies progenitor-like inflammation-associated luminal cells that can initiate human prostate cancer and predict poor outcome. Cell Rep 2016; 17: 2596-2606.
[49] Stoyanova T, Cooper AR, Drake JM, Liu X, Armstrong AJ, Pienta KJ, Zhang H, Kohn DB, Huang J, Witte ON and Goldstein AS. Prostate cancer originating in basal cells progresses to adenocarcinoma propagated by luminal-like cells. Proc Natl Acad Sci U S A 2013; 110: 20111-20116.
[50] Choi N, Zhang B, Zhang L, Ittmann M and Xin L. Adult murine prostate basal and luminal cells are self-sustained lineages that can both serve as targets for prostate cancer initiation. Cancer Cell 2012; 21: 253-265.
[51] Wang ZA, Mitrofanova A, Bergren SK, Abate-Shen C, Cardiff RD, Califano A and Shen MM. Lineage analysis of basal epithelial cells reveals their unexpected plasticity and supports a cell-of-origin model for prostate cancer heterogeneity. Nat Cell Biol 2013; 15: 274-283.

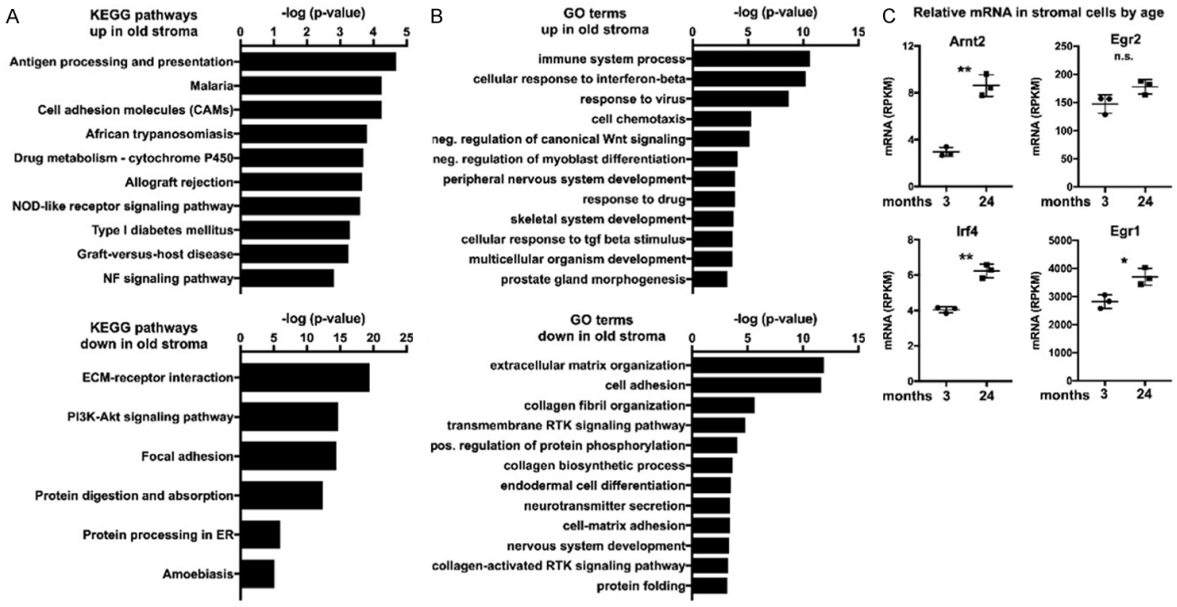

Figure S1. Related to **Figure 1**. A, B. KEGG pathways and Gene Ontology (GO) terms for genes significantly up or downregulated in old stromal cells. C. Relative mRNA expression (RPKM: reads per kilobase of transcript, per million mapped reads) in stromal cells from 3- and 24-month-old mouse prostate. * $P < 0.05$, ** $P < 0.01$, n.s. not significant.

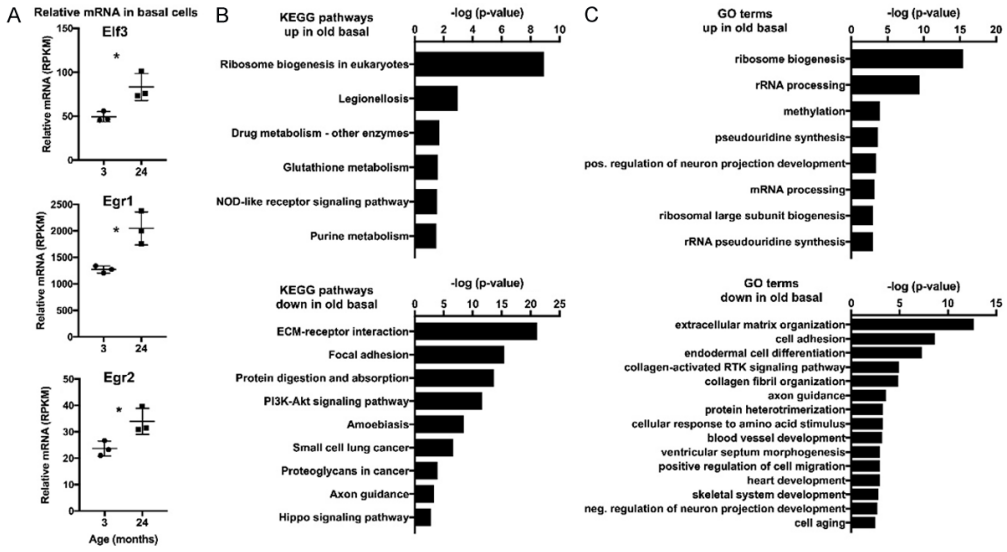

Figure S2. Related to **Figure 2**. A. Relative mRNA expression (RPKM: reads per kilobase of transcript, per million mapped reads) in basal cells from 3- and 24-month-old mouse prostate. * $P < 0.05$. B, C. KEGG pathways and Gene Ontology (GO) terms for genes significantly up or downregulated in old basal cells.

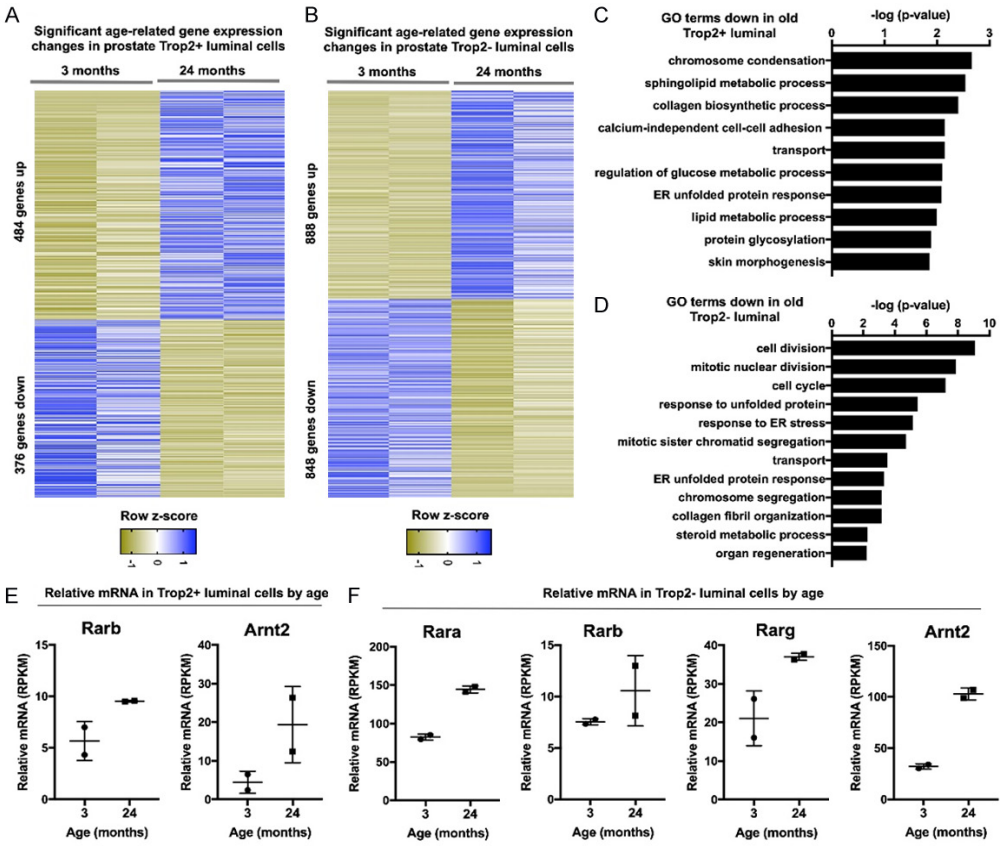

Figure S3. Related to **Figure 3**. (A, B) Heatmaps of significantly differentially expressed genes in 3- and 24-month-old Trop2+ luminal (A) and Trop2- luminal (B) cells. Only genes greater than 1.5-fold enriched in either direction with a *p*-value < 0.05 are included. (C, D) Gene Ontology (GO) terms for genes significantly downregulated in old Trop2+ luminal (C) and old Trop2- luminal (D) cells. (E, F) Relative mRNA expression (RPKM: reads per kilobase of transcript, per million mapped reads) in Trop2+ luminal (E) and Trop2- luminal (F) cells from 3- and 24-month-old mouse prostate.

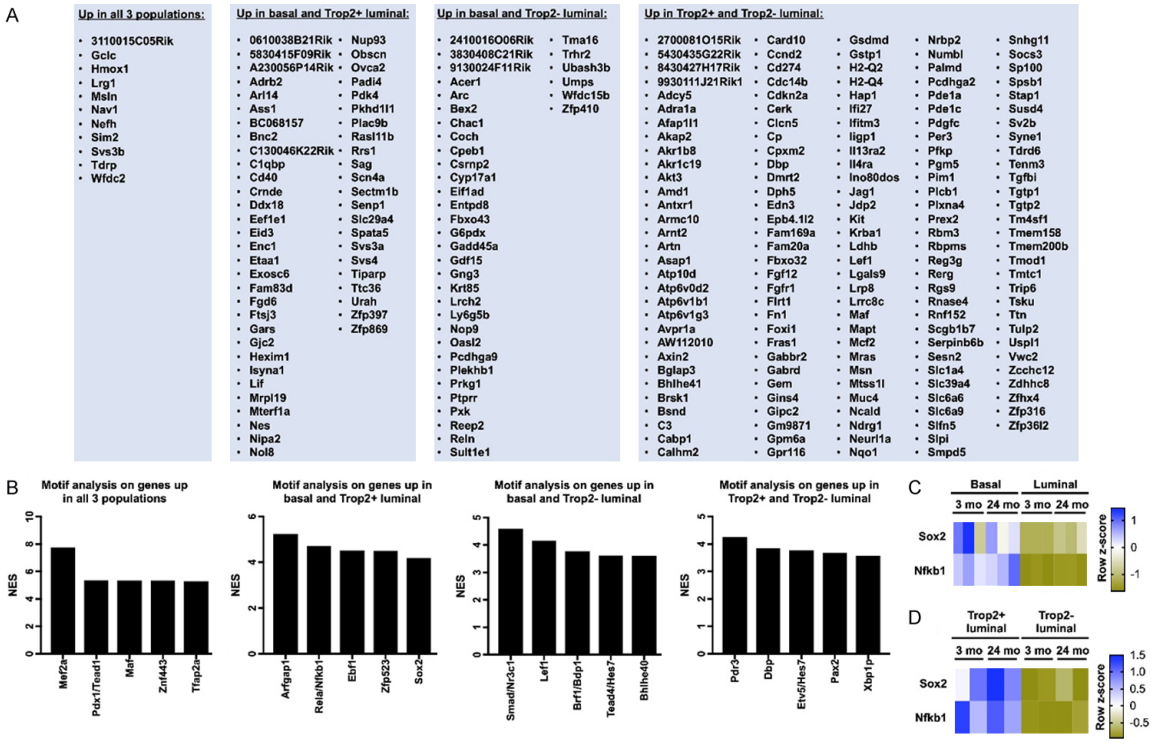

Figure S4. Related to **Figure 4**. (A) Lists of genes commonly upregulated in 2 or 3 cell-types in old mouse prostate. (B) Motif analysis of genes commonly upregulated in 2 or 3 cell-types in old mouse prostate. (C, D) Heatmaps reveal relative mRNA expression of Sox2 and Nfkb1. Regardless of mouse age, both genes are expressed at higher levels in basal cells compared to bulk luminal cells (C) and in Trop2+ luminal cells compared to Trop2- luminal cells (D).

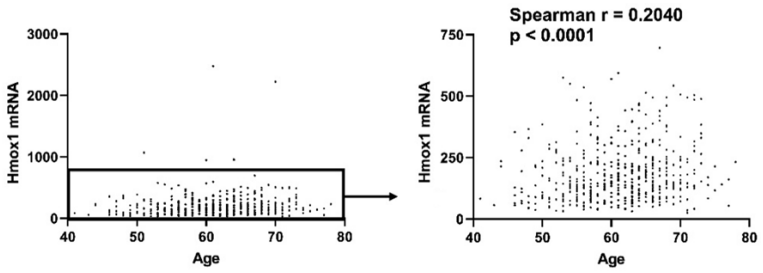

Figure S5. Related to **Figure 5**. Plot of relative Hmox1 mRNA expression and age of diagnosis in the TCGA primary prostate cancer cohort. Box on left is re-analyzed on the right to demonstrate correlation between Hmox1 mRNA and age. Spearman correlation coefficient and *p*-value are shown. 5 data points with Hmox1 mRNA > 750 are excluded from plot on the right.

Chapter 4: Reciprocal regulation of metabolism and prostate epithelial lineage identity

Title:
Reciprocal regulation of metabolism and prostate epithelial lineage identity

Authors:
Jenna M. Giafaglione, Preston D. Crowell, Amelie M.L. Delcourt, Takao Hashimoto, Daniel Ha, Elsa Tika, Nicholas M. Nunley, Leigh Ellis, Cedric Blanpain & Andrew S. Goldstein

Abstract:

Lineage transitions are a central feature of prostate development, tumorigenesis and treatment resistance. While epigenetic changes drive prostate lineage transitions, whether upstream metabolic signaling modulates prostate lineage identity remains unclear. Here, we develop an approach to perform metabolic profiling and nutrient tracing on primary prostate epithelial cells and demonstrate that basal and luminal cells exhibit distinct metabolic features. Furthermore, we show that basal to luminal differentiation *in vivo* and in three-dimensional *ex vivo* culture is accompanied by metabolic changes consistent with increased glucose oxidation. Using genetic and pharmacological approaches, we identify the mitochondrial pyruvate carrier (MPC) as a key regulator of prostate luminal identity. Lactate supplementation or inhibition of lactate efflux phenocopies the effect of MPC inhibition on lineage-specific gene expression in both benign and prostate cancer cells. These results indicate that distinct prostate epithelial cell types exhibit unique metabolic features and changes in metabolism can modulate prostate lineage.

Introduction:

The prostate epithelium contains basal and luminal cells as well as rare neuroendocrine cells. Lineage tracing studies have demonstrated that basal and luminal cells are

predominantly self-sustained by distinct progenitor populations under normal physiological conditions[1]. However, luminal differentiation from basal progenitors occurs during development[2, 3], tissue regeneration[4], inflammation[5] and prostate cancer initiation[1, 6]. Therefore, elucidating key regulators of prostate cell fate is of utmost importance. Recent work has implicated the epigenome in the establishment and maintenance of prostate epithelial identity. For example, deacetylation of KLF5 causes excess basal to luminal differentiation[7]. Furthermore, de-repression of the histone methyltransferase enhancer of zeste homolog 2 (EZH2) facilitates a loss of luminal identity and the activation of pluripotency networks[8–10]. Various mutations in FOXA1 alter chromatin accessibility to drive luminal, mesenchymal or neuroendocrine differentiation phenotypes[11, 12]. However, how upstream signaling contributes to the downstream epigenetic regulation of prostate lineage identity remains poorly understood.

Metabolism has emerged as a key upstream regulator of the epigenome. Most chromatin-modifying enzymes require intermediates of cellular metabolism as substrates or cofactors. For example, *S*-adenosylmethionine (SAM) is a substrate for histone and DNA methylation while a-ketoglutarate (a-KG) is a required cofactor for jumonji histone demethylases. Furthermore, MYC regulates acetyl-CoA generation for use in histone acetylation through ATP citrate lyase (ACLY) activity[13]. Through these mechanisms, metabolic rewiring can drive differentiation in a variety of tissues. Ascorbate regulates hematopoietic stem cell function and leukemogenesis, in part through Tet2-dependent DNA de-methylation[14]. Additionally, serine synthesis stimulates a-KG-dependent dioxygenases that remove repressive H3K27me3 to activate differentiation in epidermal

stem cells[15]. Chromatin-bound acetyl-CoA synthetase 2 (ACSS2) generates site-specific acetyl-CoA leading to increased histone acetylation and maintenance of neural function[16]. However, the interplay between metabolic signaling and lineage identity in the prostate remains to be elucidated due in part to a poor understanding of prostate epithelial cell type-specific metabolic features.

In this study, we developed an approach to perform metabolic profiling and heavy isotope nutrient tracing on primary prostate epithelial cells and discovered that basal and luminal cells have unique metabolic signatures. We utilized three-dimensional *ex vivo* culture as well as an *in vivo* lineage tracing model to illustrate that basal to luminal differentiation is associated with a metabolic shift towards increased pyruvate oxidation. We further establish the mitochondrial pyruvate carrier (MPC) as a key regulator of prostate luminal identity in both benign and prostate cancer cells. Pharmacological inhibition of mitochondrial pyruvate transport, or genetic deletion of *Mpc1* impairs basal to luminal differentiation. As observed with MPC inhibition, both lactate supplementation and inhibition of lactate efflux block luminal differentiation, suggesting that intracellular lactate accumulation mediates the effect on lineage identity. Taken together, our results indicate that (1) prostate epithelial cells have lineage-rooted metabolic features and (2) modulation of metabolism can govern prostate lineage transitions. In summary, our study establishes reciprocal regulation of prostate epithelial identity and metabolism.

Results:

Primary basal and luminal prostate cells have distinct metabolic features

To investigate the relationship between prostate epithelial cell type and metabolic identity, we used fluorescence-activated cell sorting (FACS) to isolate primary basal ($EpCAM^+$ $CD49f^{hi}$) and luminal ($EpCAM^+$ $CD49f^{lo}$) cells from adult mouse prostate and performed RNA sequencing, metabolic profiling and glucose tracing (Fig. 1a). Transcriptional analysis of canonical basal and luminal lineage markers validated successful isolation of the unique epithelial cell populations (Fig. S1a). Furthermore, gene set enrichment analysis (GSEA) demonstrated the *Smith et al* $CD49f^{high}$ basal and $CD49f^{low}$ luminal signatures[17] are enriched in their respective cell populations (Fig. S1b-c). 12 of the top 30 differentially expressed pathways identified by KEGG pathway analysis are metabolism-related (Fig. S1d). To better elucidate metabolic differences, we performed GSEA on all Hallmark, Reactome and KEGG metabolism gene sets and identified enrichment of *Myc* targets in basal cells and enrichment of pyruvate metabolism and oxidative phosphorylation in luminal cells (Fig. 1b). We also evaluated RNA abundance of key glycolytic and TCA cycle enzymes and transporters. Basal cells contain upregulation of several key glycolytic enzymes and transporters, including *Glut1*, *Mct1*, *Hk2* and *Pfkp*, while luminal cells contain upregulation of many key TCA cycle enzymes, such as *Pcx*, *Idh2*, *Sdha* and *Aco2* (Fig. 1c). The abundance of a subset of these enzymes and transporters was also validated at the protein-level in basal and luminal cells (Fig. S1e).

As transcriptomic analysis identified cell type-specific metabolic features, we sought to explore functional differences in metabolism. Therefore, we established an approach that enabled us to perform the first metabolic characterization of distinct prostate epithelial cell types using metabolic profiling and nutrient tracing. After FACS isolation, primary cells

were cultured overnight on plates coated with a 1/80 dilution of reduced-growth factor Matrigel in Advanced DMEM/F-12 to enhance cell attachment prior to metabolite extraction. Apoptosis analysis illustrated that adherent basal and luminal cells both exhibit greater than 80% viability after overnight culture (Fig. S1f), validating that metabolomics was performed on healthy cell populations. Metabolic profiling revealed basal cells have elevated levels of key glycolytic metabolites including F16BP, G3P, PEP, 3PG, F6P, F1P and G1P, while luminal cells have elevated levels of TCA cycle intermediates including isocitrate, aKG and succinate (Fig. 1d). We also performed glucose tracer analysis to evaluate differences in glucose utilization in basal and luminal cells. Previous studies established that zinc accumulation in the prostate epithelium inhibits aconitase activity to prevent citrate oxidation and promote citrate secretion[18, 19]. Interestingly, our [U-^{13}C]glucose tracing data revealed a significant reduction in incorporation of glucose-derived carbon from citrate to aconitate specifically in luminal cells (Fig. 1e), suggesting differential activity of the aconitase (ACO) enzyme between cell types. This metabolic wiring may enable luminal cells to perform their function to secret seminal fluid that contains high levels of citrate. Furthermore, [U-^{13}C]glucose tracer analysis illustrated that basal cells preferentially generate M2 citrate through pyruvate dehydrogenase (PDH) activity (Fig. 1f) while luminal cells preferentially generate M3 citrate through pyruvate carboxylase (PCX) activity (Fig. 1g). These data indicate that basal and luminal cells have both distinct metabolite abundance profiles and unique nutrient utilization patterns.

Having identified unique metabolic characteristics of basal and luminal cells in the mouse prostate, we asked whether cell type-specific metabolic features are conserved across

species. We utilized the *Zhang et al* dataset which contains RNA sequencing of benign prostatic basal and luminal epithelial populations from three human prostates to evaluate the expression of glycolytic and TCA cycle enzymes and transporters[20]. All the glycolytic enzymes and transporters evaluated, except HK2, were enriched in basal cells, while many TCA cycle enzymes were enriched in luminal cells (Fig. 1h). Taken together, our data provide the most comprehensive evidence to date that distinct prostate epithelial cell types contain unique metabolic features.

Basal to luminal differentiation is accompanied by metabolic reprogramming

Our transcriptomics and metabolomics data collectively indicate that cell type dictates metabolic phenotype. Therefore, we next evaluated a model of basal to luminal differentiation to investigate whether prostate epithelial lineage transitions are associated with metabolic reprogramming (Fig. 2a). Features of basal to luminal differentiation have been reported in prostate organoid culture; however, the kinetics of the induction of luminal marker expression were previously poorly defined[21]. We used Western blot and flow cytometry approaches to elucidate the kinetics of basal to luminal differentiation in basal-derived mouse prostate organoids. Western blot analysis revealed that basal-derived organoids initially express the basal marker p63ΔN and contain increased expression of the luminal marker cytokeratin 8 (KRT8) by day five in *ex vivo* culture (Fig. 2b). Using intracellular flow cytometry, we also tracked the induction of the luminal marker KRT8 at single-cell resolution and established that there is uniform upregulation of KRT8 that continues between days six and nine (Fig. S2a).

Using this *ex vivo* model of basal to luminal differentiation, we performed metabolic profiling and [U-^{13}C]glucose tracer analysis three, five and seven days after plating into organoid culture. Principal component analysis of both metabolic profiling data and glucose tracer analysis data illustrate that each timepoint clusters independently (Fig. S2b, 2c), indicative of metabolic reprogramming. Heatmap visualization also demonstrates that primary basal-derived organoids have distinct metabolite abundance profiles at days three, five and seven (Fig. 2Sc). [U-^{13}C]glucose tracer analysis revealed that incorporation of glucose-derived carbon into glycolytic metabolites does not significantly change across timepoints (Fig. 2d). In contrast, fractional contribution to TCA cycle intermediates increases significantly as basal-derived organoids acquire luminal features (Fig. 2e). Both fractional contribution to nucleotide intermediates and expression of the proliferation marker PCNA decrease between days five and seven (Fig. 2f, S2d). These data indicate that increased pyruvate oxidation is unlikely to be driven predominantly by organoid growth, but rather represents a shift in metabolism with luminal differentiation.

To investigate whether there is *in vivo* evidence of metabolic reprogramming during basal to luminal differentiation, we used a K5CreER/Rosa-tdTomato *in vivo* lineage tracing model to isolate multipotent basal cells and basal-derived luminal cells for RNA sequencing (Fig. 2g). Multipotent basal cells were isolated from postnatal mice (P10) based on having EpCAM^{+} Cd49f^{high} expression via FACS. As basal cells express tdTomato upon tamoxifen administration, basal-derived luminal cells can be isolated distinctly from luminal-derived luminal cells based on having tdTomato^{+} EpCAM^{+} Cd49f^{low}

expression. 15 of the top 30 differentially expressed pathways identified by KEGG pathway analysis are metabolism-related (Fig. S2e). Furthermore, GSEA revealed positive enrichment of KEGG oxidative phosphorylation in basal-derived luminal cells relative to multipotent basal cells (Fig. 2h). These data illustrate basal to luminal differentiation is associated with metabolic rewiring that includes a shift towards increased glucose oxidation.

Inhibition or knockout of the mitochondrial pyruvate carrier prevents basal to luminal differentiation

Having illustrated that basal to luminal differentiation is accompanied by metabolic reprogramming, we explored whether altering metabolism modulates prostate epithelial lineage identity. The mitochondrial pyruvate carrier (MPC) transports pyruvate from the cytosol to the mitochondria, where it can be oxidized to fuel the TCA cycle[22]. As basal to luminal differentiation is associated with increased pyruvate oxidation, we investigated how inhibiting the MPC with UK5099 alters differentiation. [U-^{13}C]glucose tracer analysis confirmed that UK5099 significantly reduced incorporation of glucose-derived carbon into TCA cycle intermediates in mouse basal-derived organoids, consistent with its on-target effect (Fig. 3a). To confirm that UK5099 does not alter basal-derived organoid viability, we showed that UK5099 does not influence the organoid-forming rate (Fig. 3b) or organoid size (Fig. 3c) of basal-derived organoids. We explored whether UK5099 is toxic to luminal cells and found that UK5099 does not modulate the organoid-forming rate (Fig. 3Sc) or the expression of proliferation and death markers (Fig. 3Sd) in luminal-derived organoids.

Next, we asked how UK5099 treatment alters luminal differentiation in basal-derived organoids. Remarkably, UK5099 treatment reduced the expression of the luminal markers androgen receptor (AR) and KRT8 and increased the expression of the basal marker p63ΔN (Fig. 3d). We evaluated KRT8 expression at single-cell resolution using intracellular flow cytometry and found uniform downregulation of KRT8 with UK5099 treatment (Fig. 3e-f). Furthermore, we established that UK5099 treatment reduces KRT8 expression in a dose-dependent manner without altering percent organoid formation (Fig. 3Sa-b). To verify that inhibition of luminal differentiation is due to the on-target effect of UK5099, we used a genetics approach to block pyruvate oxidation. Basal cells were isolated from *Mpc1*$^{fl/fl}$ mice, transduced with Cre recombinase and plated into organoid culture to establish *Mpc1* knockout (*Mpc1*-KO) organoids. [U-^{13}C]glucose tracer analysis revealed that *Mpc1*-KO organoids have reduced incorporation of glucose-derived carbon into TCA cycle intermediates (Fig. 3g). Western blot analysis demonstrated that *Mpc1*-KO, as observed with UK5099, blocks luminal differentiation in basal-derived organoids (Fig. 3h). In addition, GSEA revealed positive enrichment of the Cd49f^{low} luminal signature and negative enrichment of the Cd49f^{high} basal signature in vehicle-treated relative to UK5099-treated organoids (Fig. 3i, 3Se) and *Mpc1*-KO relative to control organoids (Fig. 3j, 3Sf).

To characterize how the MPC regulates lineage identity with better granularity, we performed single-cell RNA sequencing (scRNA-seq) on vehicle- and UK5099-treated organoids. Clustering analysis identified six distinct cell populations (Fig. 3k-l). Distinct

clusters were annotated based on relative expression of canonical lineage markers. MPC inhibition significantly decreased the percentage of cells identified as luminal and increased the percentage of cells identified as mesenchymal (Fig. 3m). Taken together, these data establish MPC as a key regulator prostate epithelial lineage identity.

MPC inhibition reduces luminal marker expression in prostate cancer

Having established the MPC as a key regulator of luminal differentiation in the benign prostate epithelium, we next asked whether MPC inhibition is antagonistic towards luminal identity in prostate cancer organoids. Basal cells were isolated from *Pten*$^{fl/fl}$ mice and *Pten*$^{fl/fl}$, *Rb1*$^{fl/fl}$ mice, transduced with Cre recombinase and plated into organoid culture to establish *Pten* single knockout (SKO) and *Pten*, *Rb1* double knockout (DKO) organoids. Western blot analysis validated successful knockout of *Pten* in SKO organoids and *Pten* and *Rb1* in DKO organoids (Fig. 4Sa). Furthermore, we found that SKO and DKO organoids were significantly larger in diameter than control wildtype organoids (Fig. 4Sb). Both SKO and DKO organoids have increased expression of canonical luminal markers while only DKO organoids have increased expression of canonical neuroendocrine markers relative to wildtype organoids (Fig. 4Sc). Similarly, SKO and DKO mouse prostates have increased expression of luminal markers while only DKO prostates have increased expression of neuroendocrine markers relative to wildtype prostates[8] (Fig. 4Sd). These data illustrate that SKO and DKO organoids retain lineage features observed in their respective primary tissues. We next used these models to investigate how MPC inhibition alters luminal differentiation in prostate cancer organoids. We found that UK5099 reduces expression of the luminal markers KRT8 and KRT18 in

both SKO and DKO organoids (Fig. 4a). RNA sequencing analysis also revealed that DKO organoids contain reduced expression of canonical luminal markers and increased expression of canonical basal markers with UK5099 treatment (Fig. 4b). Collectively, these data establish the MPC as a key regulator of lineage identity in prostate cancer organoids.

Discussion:

The role of metabolic signaling in regulation of prostate epithelial lineage identity is poorly defined. In this study, we used metabolic profiling approaches to identify prostate epithelial cell type-specific metabolic features. Basal cells are enriched for glycolysis whereas luminal cells contain greater TCA anaplerosis. In addition, basal to luminal differentiation in both *ex vivo* prostate organoid culture and *in vivo* lineage tracing models is associated with increased glucose oxidation. We found that MPC inhibition via genetic or pharmacological approaches reduces basal to luminal differentiation in basal-derived prostate organoids suggesting that MPC is a key regulator of lineage identity in the prostate. In data that is still in preparation, we found that MPC inhibition reduces luminal features in prostate cancer and that the effect of MPC inhibition on lineage identity is likely mediated through lactate accumulation. Our results uncover cell type-specific metabolic features in the prostate and implicate upstream metabolic signaling in regulation of prostate epithelial lineage identity.

Prostate cancer is the leading cause of cancer-related death in non-smoking men[23]. As treatment-resistant disease accounts for the vast majority of prostate cancer-related

deaths, identifying new strategies to prevent, interfere with and/or reverse treatment-resistance is critical to reduce prostate cancer mortality. At diagnosis, most prostate tumors are androgen-driven and rely on ligand-mediated androgen signaling to promote cell proliferation[24]. As follows, therapies targeting the androgen receptor (AR) signaling axis are initially effective and significantly extend patient survival[24]. Ultimately, however, resistance mechanisms drive disease progression and lethality[25]. Differentiation from an AR-dependent luminal lineage to an AR-indifferent lineage with basal and neuroendocrine features, termed lineage plasticity, is a common mechanism of resistance to androgen pathway inhibitors (APIs)[8, 26]. We have established that MPC inhibition reduces luminal differentiation. However, it remains unclear whether metabolic regulation of lineage identity can be exploited to promote the reacquisition of luminal features. Future studies will explore whether MPC overexpression or lactate dehydrogenase inhibition in non-luminal treatment-resistant prostate cancer organoids drives luminal differentiation and restores sensitivity to APIs.

References:

1. Choi, N., Zhang, B., Zhang, L., *et al.* Adult murine prostate basal and luminal cells are self-sustained lineages that can both serve as targets for prostate cancer initiation. *Cancer Cell*. **21** (2), 253–265, doi: 10.1016/j.ccr.2012.01.005 (2012).
2. Ousset, M., Keymeulen, A. Van, Bouvencourt, G., *et al.* Multipotent and unipotent progenitors contribute to prostate postnatal development. *Nature Cell Biology*. **14** (11), doi: 10.1038/ncb2600 (2012).
3. Wang, J., Zhu, H.H., Chu, M., *et al.* Symmetrical and asymmetrical division

analysis provides evidence for a hierarchy of prostate epithelial cell lineages. *Nature Communications*. **5** (4758), doi: 10.1038/ncomms5758 (2014).

4. Toivanen, R., Mohan, A., Shen, M.M. Basal progenitors contribute to repair of the prostate epithelium following induced luminal anoikis. *Stem Cell Reports*. **6** (5), 660–667, doi: 10.1016/j.stemcr.2016.03.007 (2016).
5. Kwon, O., Zhang, L., Ittmann, M.M., *et al.* Prostatic inflammation enhances basal-to-luminal differentiation and accelerates initiation of prostate cancer with a basal cell origin. *PNAS*. **5** (111), doi: 10.1073/pnas.1318157111 (2013).
6. Stoyanova, T., Cooper, A.R., Drake, J.M., *et al.* Prostate cancer originating in basal cells progresses to adenocarcinoma propagated by luminal-like cells. *PNAS*. **110** (50), 20111–20116, doi: 10.1073/pnas.1320565110 (2013).
7. Zhang, B., Ci, X., Tao, R., *et al.* Klf5 acetylation regulates luminal differentiation of basal progenitors in prostate development and regeneration. *Nature Communications*. **11** (1), doi: 10.1038/s41467-020-14737-8 (2020).
8. Ku, S.Y., Rosario, S., Wang, Y., *et al.* Rb1 and Trp53 cooperate to suppress prostate cancer lineage plasticity, metastasis, and antiandrogen resistance. *Science*. **355** (6320), 78–83, doi: 10.1126/science.aah4199 (2017).
9. Dardenne, E., Beltran, H., Benelli, M., *et al.* N-Myc induces an EZH2-mediated transcriptional program driving neuroendocrine prostate cancer. *Cancer Cell*. **30** (4), 563–577, doi: 10.1016/j.ccell.2016.09.005 (2016).
10. Berger, A., Beltran, H., Rickman, D.S., *et al.* N-Myc –mediated epigenetic reprogramming drives lineage plasticity in advanced prostate cancer. *Journal of Clinical Investigation*. **129** (9), 3924–3940, doi: 10.1172/JCI127961 (2019).

11. Adams, E.J., Karthaus, W.R., Hoover, E., *et al.* FOXA1 mutations alter pioneering activity, differentiation and prostate cancer phenotypes. *Nature*. **571** (7765), doi: 10.1038/s41586-019-1318-9 (2019).

12. Parolia, A., Cieslik, M., Chu, S., *et al.* Distinct structural classes of activating FOXA1 alterations in advanced prostate cancer. *Nature*. **571** (7765), doi: 10.1038/s41586-019-1347-4 (2019).

13. Morrish, F., Noonan, J., Perez-olsen, C., *et al.* Myc-dependent mitochondrial generation of acetyl-CoA contributes to fatty acid biosynthesis and histone ccetylation during cell cycle entry. *Journal of Biological Chemistry*. **285** (47), 36267–36274, doi: 10.1074/jbc.M110.141606 (2010).

14. Agathocleous, M., Meacham, C.E., Burgess, R.J., *et al.* Ascorbate regulates haematopoietic stem cell function and leukaemogenesis. *Nature*. **549** (7673), 476–481, doi: 10.1038/nature23876 (2017).

15. Baksh, S.C., Todorova, P.K., Gur-cohen, S., *et al.* Extracellular serine controls epidermal stem cell fate and tumour initiation. *Nature Cell Biology*. **22** (7), 779–790, doi: 10.1038/s41556-020-0525-9 (2020).

16. Mews, P., Donahue, G., Drake, A.M., *et al.* Acetyl-CoA synthetase regulates histone acetylation and hippocampal memory. *Nature*. **546** (7658), 381–386, doi: 10.1038/nature22405 (2017).

17. Smith, B.A., Sokolov, A., Uzunangelov, V., *et al.* A basal stem cell signature identifies aggressive prostate cancer phenotypes. *PNAS*. **112** (47), doi: 10.1073/pnas.1518007112 (2015).

18. Costello, L.C., Franklin, R.B. Aconitase activity, citrate oxidation, and zinc

inhibition in rat ventral prostate. *Enzyme*. **26** (6), 281–287, doi: 10.1159/000459195 (1981).

19. Costello, L.C., Liu, Y., Franklin, R.B., *et al.* Zinc inhibition of mitochondrial aconitase and its importance in citrate metabolism of prostate epithelial cells. *Journal of Biological Chemistry*. **272** (46), 28875–28881, doi: 10.1074/jbc.272.46.28875 (1997).
20. Zhang, D., Park, D., Zhong, Y., *et al.* Stem cell and neurogenic gene-expression profiles link prostate basal cells to aggressive prostate cancer. *Nature Communications*. **7** (10798), doi: 10.1038/ncomms10798 (2016).
21. Karthaus, W.R., Iaquinta, P.J., Drost, J., *et al.* Identification of multipotent luminal progenitor cells in human prostate organoid cultures. *Cell*. **159** (1), 163–175, doi: 10.1016/j.cell.2014.08.017 (2014).
22. Bricker, D.K., Taylor, E.B., Schell, J.C., *et al.* A mitochondrial pyruvate carrier required for pyruvate uptake in yeast, Drosophila, and humans. *Science*. **337** (6090), 96–101, doi: 10.1126/science.1218099 (2012).
23. Siegel, R.L. Cancer statistics. *American Cancer Society*. **72** (1), 7–33, doi: 10.3322/caac.21708 (2022).
24. Sayegh, N., Swami, U., Agarwal, N. Recent Advances in the Management of Metastatic Prostate Cancer. *JCO Oncol Pract*. **18** (1), doi: 10.1200/OP.21.00206 (2022).
25. Nakazawa, M., Paller, C., Kyprianou, N. Mechanisms of Therapeutic Resistance in Prostate Cancer. *Curr Oncol Rep*. **19** (2), doi: 10.1007/s11912-017-0568-7 (2017).

26. Mu, P., Zhang, Z., Benelli, M., *et al.* SOX2 promotes lineage plasticity and antiandrogen resistance in TP53- and RB1-deficient prostate cancer. *Science*. **88** (6320), 84–88, doi: 10.1126/science.aah4307 (2017).

27. Drost, J., Karthaus, W.R., Gao, D., *et al.* Organoid culture systems for prostate epithelial and cancer tissue. *Nature Protocols*. **11** (2), 347–358, doi: 10.1038/nprot.2016.006 (2016).

28. Crowell, P.D., Fox, J.J., Hashimoto, T., *et al.* Expansion of luminal progenitor cells in the aging mouse and human prostate. *Cell Reports*. **28** (6), 1499–1510, doi: 10.1016/j.celrep.2019.07.007 (2019).

29. Crowell, P.D., Giafaglione, J.M., Hashimoto, T., *et al.* Evaluating the differentiation capacity of mouse prostate epithelial cells using organoid culture. *Journal of Visualized Experiments*. **153**, 1–9, doi: 10.3791/60223 (2019).

Figure 1. Primary basal and luminal mouse prostate cells have distinct metabolic features

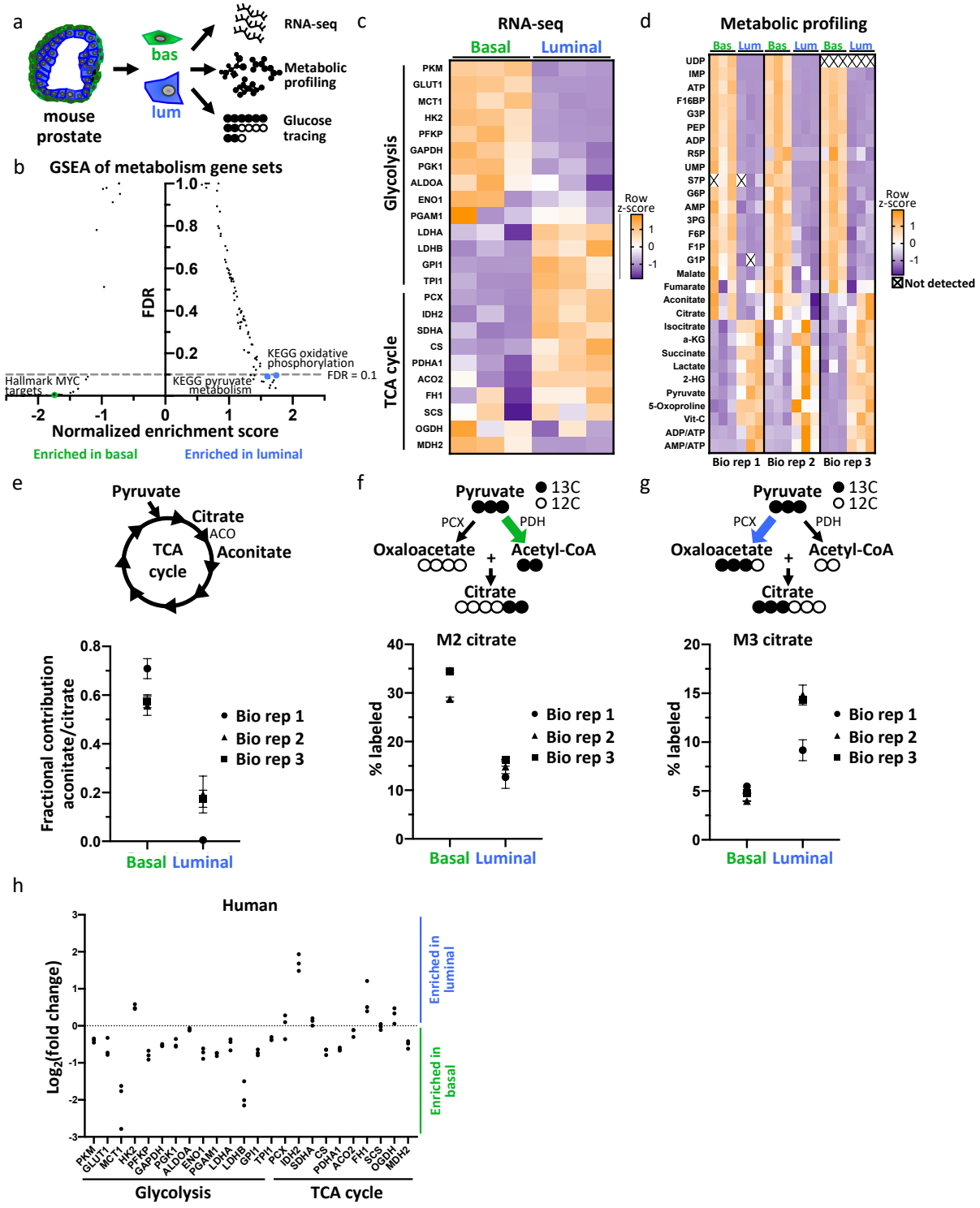

Figure 1. Primary basal and luminal mouse prostate cells have distinct metabolic features. (a) Schematic of RNA sequencing, metabolic profiling and glucose tracing performed on primary basal and luminal cells isolated from mouse prostate. (b) Gene set enrichment analysis of all KEGG, Hallmark, and Reacome metabolism gene sets in basal and luminal cells. (c) Heatmap of glycolytic and TCA cycle enzymes from RNA sequencing of three biological replicates of basal and luminal cells. (d) Heatmap of metabolite abundance in primary basal and luminal mouse prostate cells with three technical replicates for each of the three biological replicates. (e) Aconitate to citrate fractional contribution ratio in primary basal and luminal mouse prostate cells fed [U-^{13}C]glucose tracer for 16 hours. (f-g) Percent M2 citrate (f) and percent M3 citrate (g) from [U-^{13}C]glucose in basal and luminal cells. (h) Fold change in glycolytic and TCA cycle enzymes from RNA sequencing of basal and luminal cells from three human prostates.

Figure 2. Basal to luminal differentiation is accompanied by metabolic reprogramming

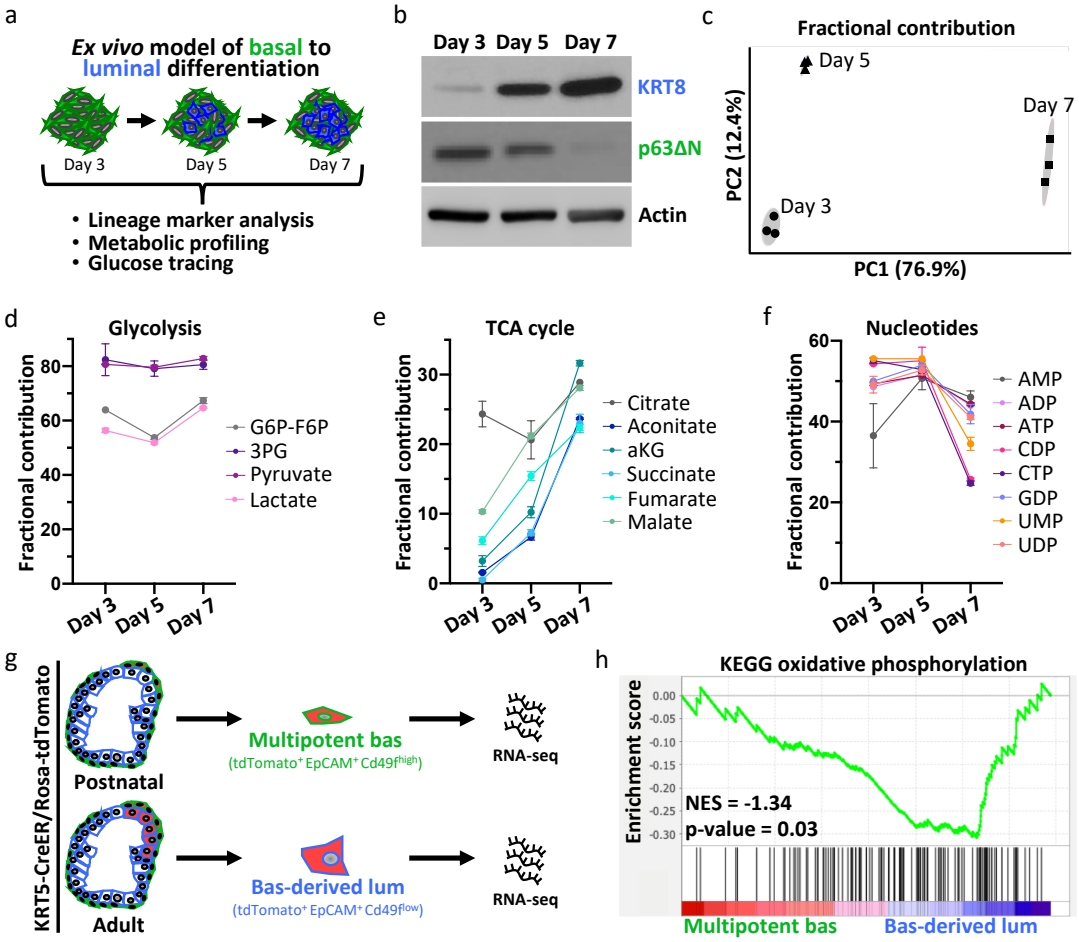

Figure 2. Basal to luminal differentiation is accompanied by metabolic reprogramming. (a) Schematic of lineage marker analysis, metabolic profiling and glucose tracing performed on primary basal-derived mouse organoids three, five and seven days after plating into organoid culture. (b) Western blot analysis of basal marker p63ΔN and luminal marker cytokeratin 8 (KRT8) in basal-derived organoids. (c) Principal component analysis of fractional contribution from [U-^{13}C]glucose metabolic tracing data of basal-derived organoids with three technical replicates per timepoint. Organoids were cultured with [U-^{13}C]glucose 48 hours prior to harvesting metabolites at each timepoint. (d-f) Fractional contribution from [U-^{13}C]glucose to glycolytic (d), TCA cycle (e) and nucleotide intermediates (f) in basal-derived organoids with three technical replicates per timepoint. (g) Schematic of *in vivo* lineage tracing model of basal to luminal differentiation. (h) Gene set enrichment analysis showing positive enrichment of KEGG oxidative phosphorylation in basal-derived luminal cells relative to multipotent basal cells *in vivo*.

Figure 3. Inhibition or knockout of the mitochondrial pyruvate carrier prevents basal to luminal differentiation

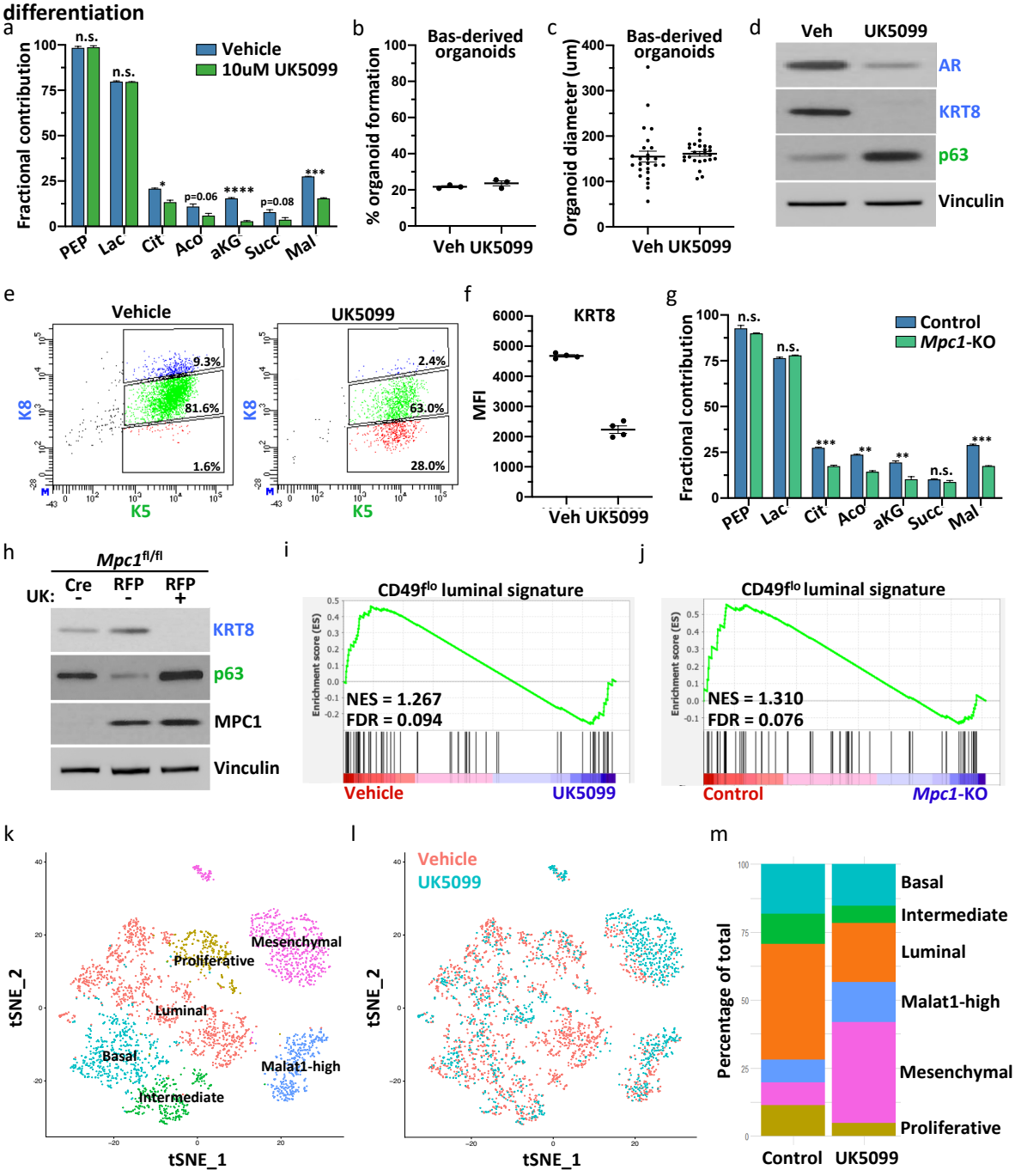

Figure 3. Inhibition or knockout of the mitochondrial pyruvate carrier prevents basal to luminal differentiation. (a) [U-^{13}C]glucose tracer analysis of vehicle- and 10uM UK5099-treated basal-derived organoids seven days after plating. (b-c) Percent organoid formation (b) and organoid diameter (c) of vehicle- and 10uM UK5099-treated basal-derived organoids seven days after plating. (d) Western blot analysis of luminal markers androgen receptor (AR) and cytokeratin 8 (KRT8) and basal marker p63ΔN in vehicle- and 10uM UK5099-treated basal-derived organoids seven days after plating. (e) Intracellular flow cytometry of KRT8 and basal marker cytokeratin 5 (KRT5) in vehicle- and 10uM UK5099-treated basal-derived organoids seven days after plating. (f) Quantification of mean fluorescence intensity (MFI) of KRT8 from panel e. (g) [U-^{13}C]glucose tracer analysis of control and MPC1 knockout basal-derived organoids. (h) Western blot analysis of basal and luminal markers in control, MPC1 knockout, and UK5099-treated basal-derived organoids. (i) GSEA showing enrichment of CD49f low luminal signature in vehicle-treated relative to 10uM UK5099-treated basal-derived organoids. (j) GSEA showing enrichment of CD49f low luminal signature in control relative to MPC1 knockout basal-derived organoids. (k) tSNE plot of scRNA-seq data illustrating distinct cell populations. (l) tSNE plot of vehicle- and 10uM UK5099-treated cells from scRNA-seq data. (m) Quantification of percentage of vehicle- and 10uM UK5099-treated cells in each cluster from scRNA-seq data.

Figure S1.

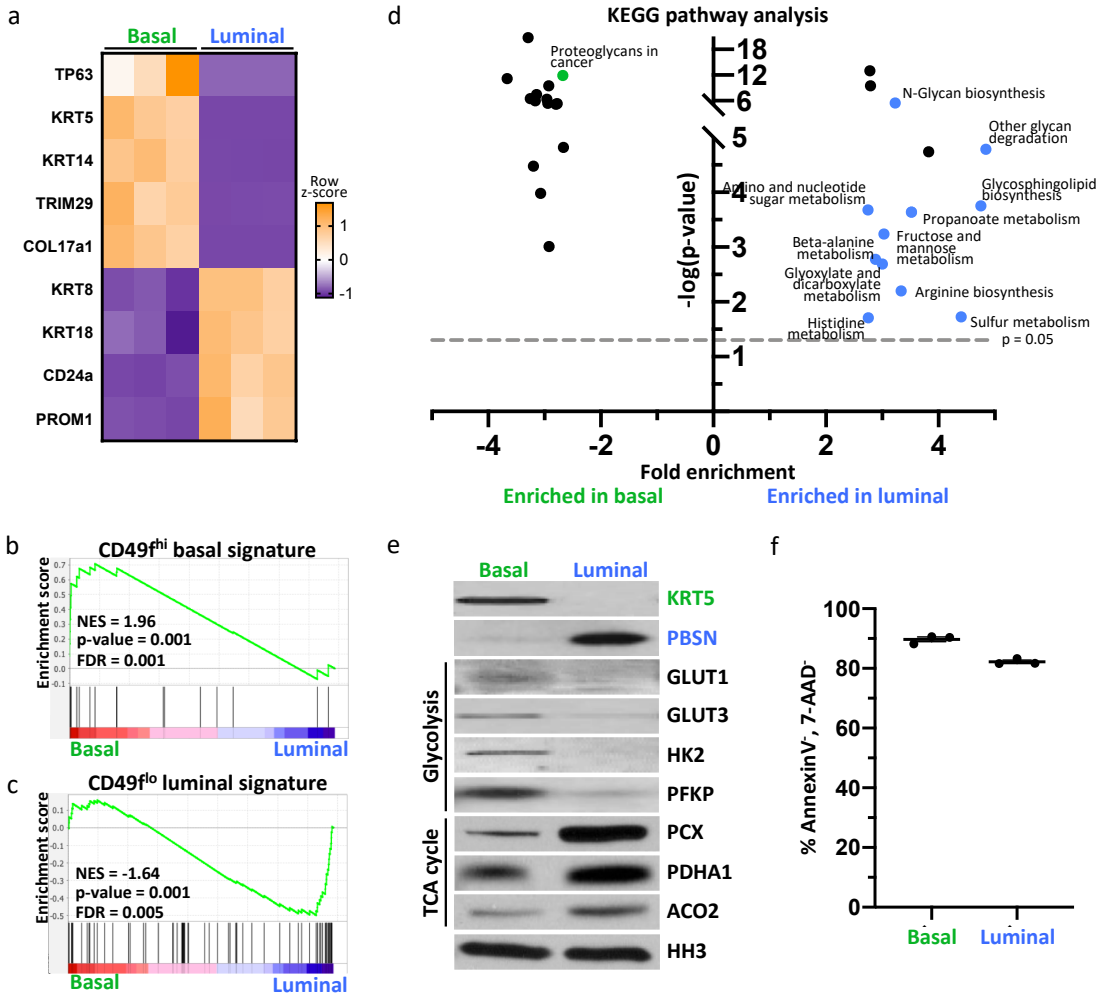
a
Basal
Luminal
TP63
KRT5
KRT14
TRIM29
COL17a1
KRT8
KRT18
CD24a
PROM1
Row z-score
1
0
-1
d
KEGG pathway analysis
Proteoglycans in cancer
N-Glycan biosynthesis
Other glycan degradation
Amino and nucleotide sugar metabolism
Glycosphingolipid biosynthesis
Propanoate metabolism
Fructose and mannose metabolism
Beta-alanine metabolism
Glyoxylate and dicarboxylate metabolism
Arginine biosynthesis
Histidine metabolism
Sulfur metabolism
p = 0.05
-log(p-value)
Fold enrichment
Enriched in basal
Enriched in luminal
b
CD49f^hi basal signature
Enrichment score
NES = 1.96
p-value = 0.001
FDR = 0.001
Basal
Luminal
c
CD49f^lo luminal signature
Enrichment score
NES = -1.64
p-value = 0.001
FDR = 0.005
Basal
Luminal
e
Basal
Luminal
KRT5
PBSN
Glycolysis
GLUT1
GLUT3
HK2
PFKP
TCA cycle
PCX
PDHA1
ACO2
HH3
f
% AnnexinV-, 7-AAD-
Basal
Luminal

Figure S1. (a) Heatmap of select canonical basal and luminal markers from RNA sequencing of primary basal and luminal mouse prostate cells with three biological replicates. (b) Gene set enrichment analysis (GSEA) showing positive enrichment of $CD49f^{high}$ signature in basal cells relative to luminal cells. (c) GSEA showing positive enrichment of $CD49f^{low}$ signature in luminal cells relative to basal cells. (d) Top 30 significantly enriched pathways identified by KEGG pathway analysis on differentially expressed (fold change ≥ 2, p-value < 0.05, FDR < 0.2) genes in basal and luminal cells. Metabolism-related pathways highlighted in green (basal-enriched) and blue (luminal-enriched). (e) Western blot analysis of select glycolytic and TCA cycle enzymes in basal and luminal cells. (f) Percentage of $AnnexinV^-$, $7\text{-}AAD^-$ primary basal and luminal cells after overnight culture.

Figure S2.

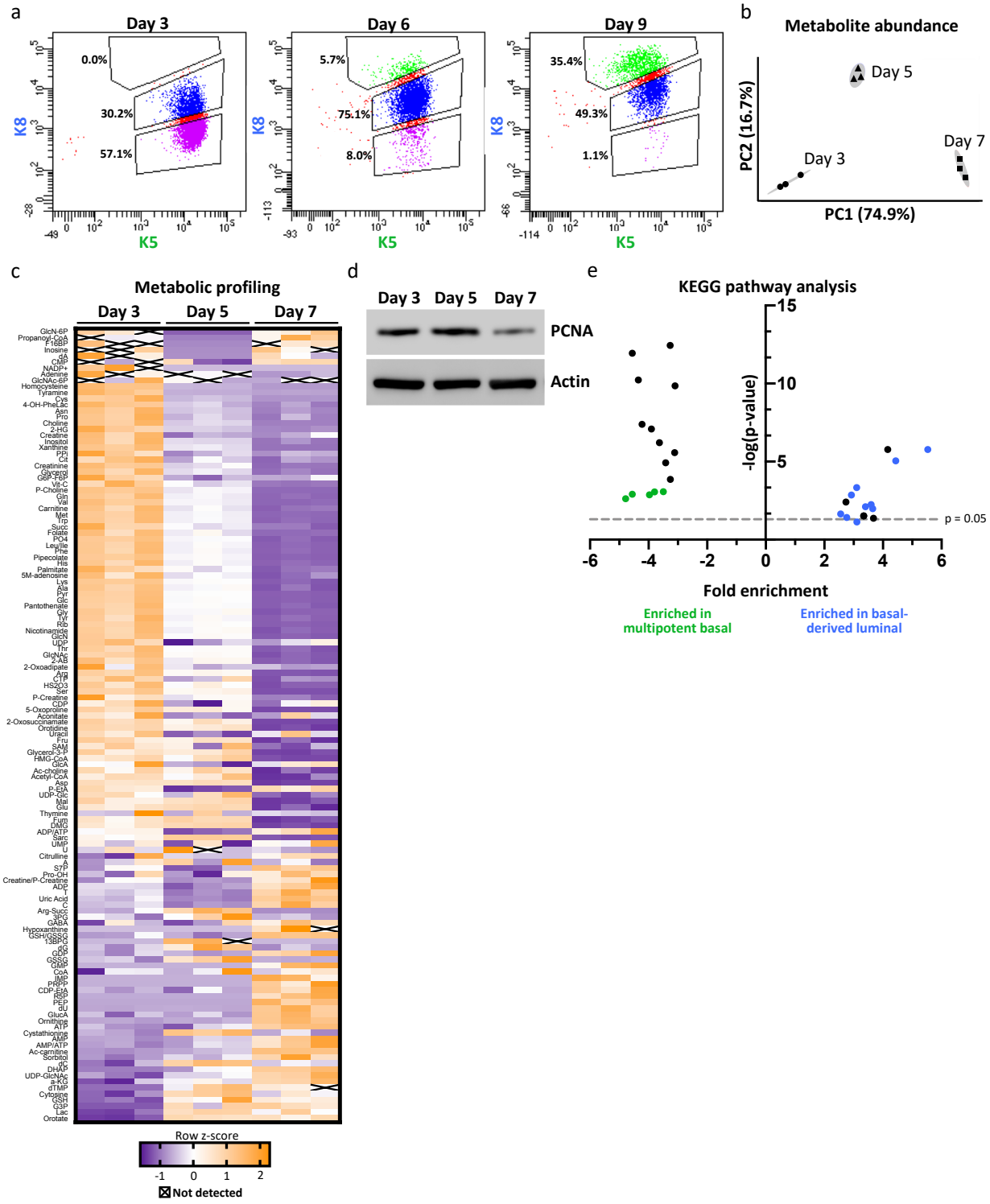
a
Day 3
Day 6
Day 9
0.0%
30.2%
57.1%
5.7%
75.1%
8.0%
35.4%
49.3%
1.1%
K8
K5
b
Metabolite abundance
Day 5
Day 3
Day 7
PC2 (16.7%)
PC1 (74.9%)
c
Metabolic profiling
Day 3
Day 5
Day 7
Row z-score
-1
0
1
2
Not detected
d
Day 3
Day 5
Day 7
PCNA
Actin
e
KEGG pathway analysis
-log(p-value)
15
10
5
p = 0.05
-6
-4
-2
0
2
4
6
Fold enrichment
Enriched in multipotent basal
Enriched in basal-derived luminal

Figure S2. (a) Intracellular flow cytometry analysis of basal marker cytokeratin 5 (KRT5) and luminal marker cytokeratin 8 (KRT8) in primary basal-derived mouse organoids three, six and nine days after plating into organoid culture. (b) Principal component analysis of metabolic profiling data for basal-derived organoids with three technical replicates per timepoint. (c) Heatmap of metabolite abundance in primary basal-derived mouse organoids with three technical replicates for each timepoint. (d) Western blot analysis of proliferation marker PCNA in basal-derived organoids. (e) Top 30 significantly enriched pathways identified by KEGG pathway analysis on differentially expressed (fold change ≥ 2) genes in multipotent basal cells and basal-derived luminal cells. Metabolism-related pathways highlighted in green (multipotent basal-enriched) and blue (basal-derived luminal-enriched).

Figure S3.

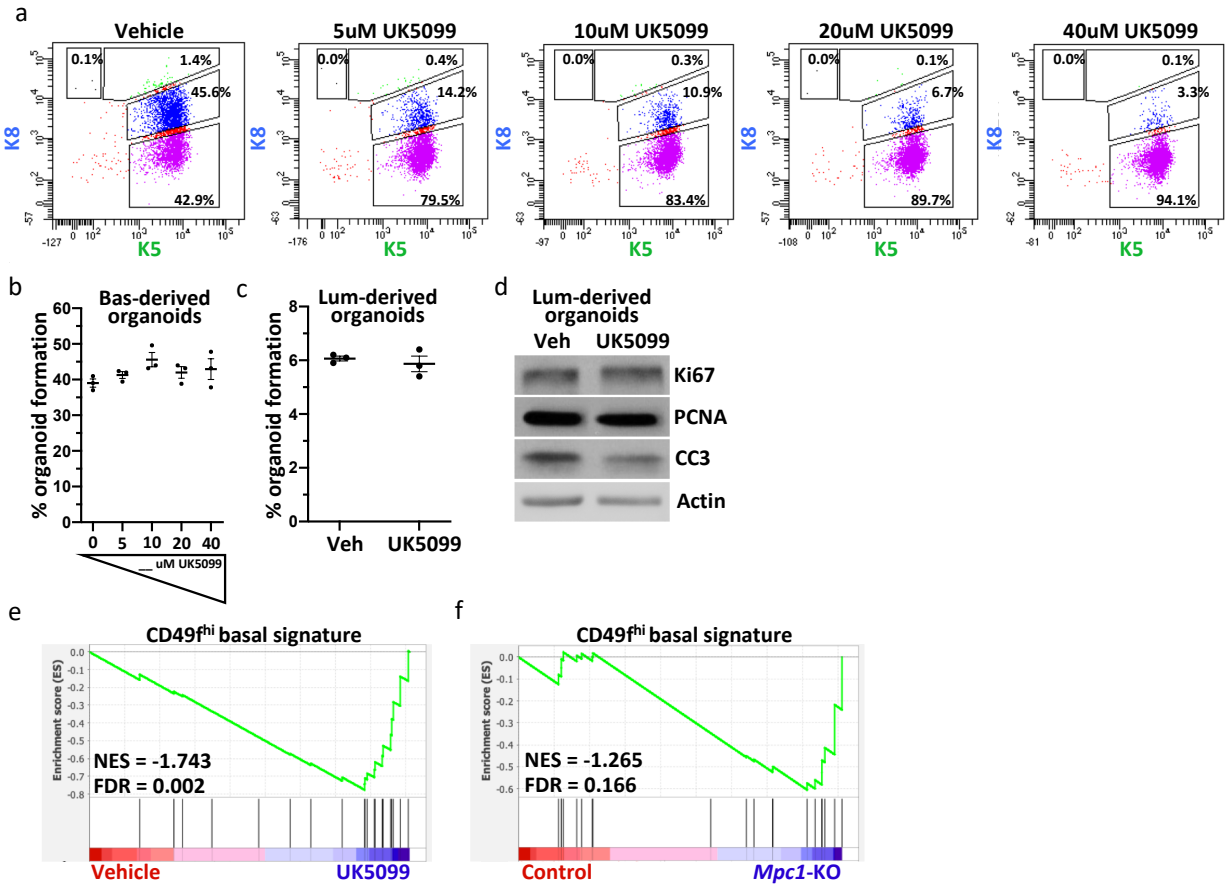
a
Vehicle
5uM UK5099
10uM UK5099
20uM UK5099
40uM UK5099
K8
K5
0.1%
1.4%
45.6%
42.9%
0.0%
0.4%
14.2%
79.5%
0.0%
0.3%
10.9%
83.4%
0.0%
0.1%
6.7%
89.7%
0.0%
0.1%
3.3%
94.1%
b
Bas-derived organoids
% organoid formation
0 5 10 20 40
uM UK5099
c
Lum-derived organoids
% organoid formation
Veh UK5099
d
Lum-derived organoids
Veh UK5099
Ki67
PCNA
CC3
Actin
e
CD49f^hi basal signature
Enrichment score (ES)
NES = -1.743
FDR = 0.002
Vehicle
UK5099
f
CD49f^hi basal signature
Enrichment score (ES)
NES = -1.265
FDR = 0.166
Control
Mpc1-KO

Figure S3. (a) Intracellular flow cytometry of KRT8 and KRT5 in basal-derived organoids treated with 0-40uM UK5099 for seven days. (b) Percent organoid formation of basal-derived organoids treated with 0-40uM UK5099 . (c) Percent organoid formation of vehicle- and 10uM UK5099-treated luminal-derived organoids. (d) Western blot analysis of proliferation markers (Ki67 and PCNA) and apoptosis marker (cleaved caspase-3) in vehicle- and 10uM UK5099-treated luminal-derived organoids seven days after plating. (e) GSEA showing enrichment of CD49f high basal signature in 10uM UK5099-treated relative to vehicle-treated basal-derived organoids. (f) GSEA showing enrichment of CD49f high basal signature in MPC1 knockout relative to control basal-derived organoids.

METHODS

Mouse prostate dissociation to single cells

Using a razor blade, individual mouse prostates were mechanically dissociated in dissociation media comprised of RPMI 1640 (GIBCO) containing 10% fetal bovine serum (Corning), 1x penicillin-streptomycin (GIBCO), 1mg/mL collagenase type I (GIBCO), 1mg/ml dispase (GIBCO), 0.1mg/mL deoxyribonuclease (GIBCO), and 10uM of the p160ROCK inhibitor Y-27632 dihydrochloride (Tocris Bioscience). When chunks were no longer visible, the samples were incubated at 37C on a nutating platform for 1.5h in 10mL of dissociation media. After centrifugation at 800g for 5 min, the pellet was washed with 1x phosphate buffered saline (PBS, GIBCO). The cell pellet was resuspended in 2.7mL of 0.05% Trypsin-EDTA (GIBCO) and incubated at 37C for 5 min. Trypsin was inactivated with 300mL of dissociation media. Cells were further dissociated by pipetting with a P-1000 pipette and an 18G syringe. Cells were passed through a 100um cell strainer (Corning).

Staining and sorting cells from mouse prostate

Dissociated cells were stained with directly conjugated primary antibodies: rat anti-CD49f-PE (BioLegend), rat anti-CD326 (EpCAM)-APC (BioLegend), rat anti-CD31-FITC (BioLegend), rat anti-CD45-FITC (BioLegend), rat anti-Ter119-FITC (BioLegend) and rat anti-ESAM-FITC (BioLegend) for 20 min on ice. Cells were stained in media containing RPMI 1640 (GIBCO), 10% FBS (Corning), 1x penicillin-streptomycin (GIBCO), and 10uM of the p160ROCK inhibitor Y-27632 dihydrochloride (Tocris Bioscience). Sorting was performed on a BD FACS Aria II (BD Biosciences).

RNA-sequencing

RNA was extracted from the cells using the RNeasy Mini Kit (QIAGEN) following the manufactural instruction. Libraries for RNA-Seq were prepared with KAPA Stranded mRNA-Seq Kit (Roche). The workflow consists of mRNA enrichment, cDNA generation, and end repair to generate blunt ends, A-tailing, adaptor ligation and PCR amplification. Different adaptors were used for multiplexing samples in one lane. Sequencing was performed on Illumina HiSeq 3000 for 1x50 run. Sequencing data have been deposited in NCBI's Gene expression Omnibus and can be accessed through GEO Series accession number GSE122367, GSE206555

Primary cell metabolic profiling and nutrient tracing

12-well plates were coated with a 1/80 dilution of reduced-growth factor Matrigel (Corning) in RPMI-1640 (GIBCO) to enhance cell attachment. The 1/80 Matrigel coating was aspirated before primary basal and luminal cells were seeded at a density of 200,000 cells/well and 140,000 cells/well respectively. Cells were cultured overnight in mouse organoid media[27] containing [U-^{13}C]glucose (Cambridge Isotope Laboratories). Prior to metabolite extraction, tracer-containing media was aspirated and cells were washed with cold 150mM ammonium acetate pH 7.3. Metabolite extractions were performed by adding 500ul cold 80% methanol to each well and removing cells using a cell scrapper. The cell suspension was transferred to an Eppendorf tube and 10ul 1mM norvaline (Sigma) was added as an internal standard. Each sample was vortexed for 30 seconds and centrifuged

at 17000g for 5 min at 1C. 420ul of the supernatant was transferred to an ABC vial (Fisher Scientific) and evaporated using an EZ-2Elite evaporator (Genevac). Samples were stored at -80C prior to analysis.

Normalization was performed by resuspending the cell pellet in 300ul lysis solution (0.1M NaCl, 20mM Tris-HCl, 0.1% SDS, 5mM EDTA in distilled water). Samples were syringed with a 25G needle to reduce viscosity and 50ul of each sample was transferred to a 96-well black wall clear bottom tissue culture plate (Corning). 50ul lysis solution was added to one well for a blank reading. 100ul of 5ug/ml Hoechst 33342 (Invitrogen) in distilled water was added to each well and 96-well plates were incubated for 30 minutes in the dark at 37C before measurement of DNA-based florescence using a Tecan Infinite M1000 plate reader with 355nm excitation and 465nm emission. The blank reading was subtracted from each absorbance value to calculate relative cell amount.

Western blot

Primary basal and luminal cells were sorted and immediately lysed in RIPA buffer (50mM Tris-HCl pH 8.0, 150mM NaCl, 1% NP-40, 0.5% Sodium Deoxycholate, 0.1% SDS, Fisher Scientific) containing a cOmplete protease inhibitor cocktail tablet (Roche) and Halt Phosphatase Inhibitor (Fisher Scientific). Each sample was sonicated for 40 sec at 20kHz with a sonic dismembrator (Fisher Scientific) to improve membranous and nuclear protein yield. Samples were run on NuPAGE 4–12% Bis-Tris Gel (Invitrogen) and transferred onto PVDF membranes (Millipore Sigma). Total protein was visualized using SYPRO RUBY protein blot stain (Fisher Scientific) and membranes were blocked in PBS + 0.1% Tween-20 (Fisher Scientific) + 5% milk (Fisher Scientific).

Organoid culture and assays

Primary basal cells from mouse prostate were isolated by fluorescence-activated cell sorting as previously described[28]. Sorted cell populations were plated in a 24-well plate (Corning). Basal cells were plated at a density of 1000 cells/well. Prostate organoids were cultured based on established protocols[27, 29]. Single organoids were imaged on a light microscope and organoid diameter was measured as a readout of organoid size.

Organoid metabolic profiling and nutrient tracing

17.5mM [U-^{13}C]glucose (Cambridge Isotope Laboratories) was added to glucose-free SILAC Advanced DMEM/F-12 Flex Media (Fisher Scientific). Arginine, lysine and alanine were also added back to the SILAC base media at the same concentrations found in Advanced DMEM/F-12 (Fisher Scientific). Organoids were grown in mouse organoid media made with the SILAC base media. Prior to metabolite extraction, tracer-containing media was aspirated. Organoids were repeatedly blasted with cold 150mM ammonium acetate pH 7.3 using a P-1000 pipette until the Matrigel ring was dislodged. The suspension was transferred to an Eppendorf tube and centrifuged at 800g for 5 min at 1C. The supernatant was aspirated and 500ul cold 80% methanol was added to the organoid pellet. 10ul 1mM norvaline (Sigma) was added as an internal standard. Each sample was vortexed for 30 seconds and centrifuged at 17000g for 5 min at 1C. 420ul of the supernatant was transferred to an ABC vial (Fisher Scientific) and evaporated using an EZ-2Elite evaporator (Genevac). Samples were stored at -80C prior to analysis.

Normalization was performed as described in primary cell metabolic profiling and nutrient tracing section above. Proteinase K (Fisher Scientific) was added at a concentration of 500ug/ml to lysis solution to help dissolve organoid pellet.

Intracellular flow cytometry

Dissociated cells from mouse prostate organoids were washed with PBS and fixed in 1ml of 2% paraformaldehyde made from 16% paraformaldehyde (Electron Microscopy Sciences) in PBS for 15 min on ice. Cells were washed with PBS and permeabilized in 1ml of permeabilization buffer (0.1% Saponin (Sigma-Aldrich), 5% FBS (Corning) in PBS) for 15 min at room temperature in the dark. Cells were resuspended in 100 mL of permeabilization buffer and stained with rabbit anti-cytokeratin 5-Alexa Fluor 647 (Abcam) and rabbit anti-cytokeratin 8-Alexa Fluor 488 (Abcam) for 20 min at room temperature in the dark. Cells were washed with permeabilization buffer and resuspended in PBS for analysis on a BD FACS Canto (BD Biosciences).

Chapter 5: Androgen receptor inhibition induces metabolic reprogramming and increased reliance on oxidative mitochondrial metabolism in prostate cancer

Title:
Androgen receptor inhibition induces metabolic reprogramming and increased reliance on oxidative mitochondrial metabolism in prostate cancer

Authors:
Preston D. Crowell[1], Jenna M. Giafaglione[1], Anthony E. Jones[2], Nicholas M. Nunley[3], Takao Hashimoto[3], Amelie M.L. Delcourt[3], Anton Petcherski[4], Matthew J. Bernard[1], Rong Rong Huang[5], Jin-Yih Low[6], Nedas Matulionis[7], Xiangnan Guan[8], Nora M. Navone[9], Joshi J. Alumkal[10], Michael C. Haffner[6,11], Huihui Ye[5], Amina Zoubeidi[12,13], Heather R. Christofk[7,14,15], Orian S. Shirihai[2,4,16], Ajit S. Divakaruni[2], Andrew S. Goldstein[3,14,15,17,18,*]

Affiliations:
[1]Molecular Biology Interdepartmental Program, University of California, Los Angeles, Los Angeles, CA 90095, USA.
[2]Department of Molecular and Medical Pharmacology, University of California, Los Angeles, Los Angeles, CA 90095, USA.
[3]Department of Molecular, Cell, and Developmental Biology, University of California, Los Angeles, Los Angeles, CA 90095, USA.
[4]Division of Endocrinology, Department of Medicine, David Geffen School of Medicine at UCLA, Los Angeles, CA 90095, USA.
[5]Department of Pathology & Laboratory Medicine, UCLA, 10833 Le Conte Ave, Los Angeles, CA, 90095, USA.
[6]Divisions of Human Biology and Clinical Research, Fred Hutchinson Cancer Research Center, Seattle, WA, USA.
[7]Department of Biological Chemistry, David Geffen School of Medicine, University of California, Los Angeles (UCLA), Los Angeles, CA, USA.
[8]Knight Cancer Institute, Oregon Health and Science University, 3303 SW Bond Ave., Portland, OR 97239, USA.
[9]Department of GU Medical Oncology, MD Anderson Cancer Center, Houston, Texas.
[10]Department of Internal Medicine, Rogel Cancer Center, University of Michigan, Ann Arbor, Michigan, USA.
[11]Department of Laboratory Medicine and Pathology, University of Washington, Seattle, WA, USA.
[12]Department of Urologic Sciences, University of British Columbia, Vancouver, British Columbia, Canada.
[13]Vancouver Prostate Centre, Vancouver, British Columbia, Canada.
[14]Jonsson Comprehensive Cancer Center, UCLA, Los Angeles, CA, USA.
[15]Eli and Edythe Broad Stem Cell Research Center, UCLA, Los Angeles, CA, USA.
[16]Department of Clinical Biochemistry, School of Medicine, Ben Gurion University of The Negev, Beer-Sheva, Israel.
[17]Department of Urology, David Geffen School of Medicine, University of California, Los Angeles, Los Angeles, CA 90095, USA.
[18]Molecular Biology Institute, University of California, Los Angeles, Los Angeles, CA 90095, USA.
*Correspondence: agoldstein@mednet.ucla.edu

Lead Contact: Andrew S. Goldstein, agoldstein@mednet.ucla.edu

Abstract:

Prostate cancer cells that survive clinical androgen receptor (AR) blockade mediate disease progression and lethality. Reprogrammed metabolic signaling is one mechanism by which tumor cells can survive treatment. However, how AR inhibition reprograms metabolism, and whether altered metabolism can be exploited to eradicate cells that survive AR blockade, remains unclear. Here, we comprehensively characterized the effect of AR blockade on prostate cancer metabolism using transcriptomics, metabolomics, and bioenergetics approaches. AR inhibition maintains oxidative mitochondrial metabolism and reduces glycolytic signaling, through hexokinase II downregulation and decreased MYC activity. Robust elongation of mitochondria via reduced DRP1 activity supports cell fitness after AR blockade. In addition, AR inhibition enhances sensitivity to complex I inhibitors in several models, suggesting that AR blockade increases reliance on oxidative mitochondrial metabolism. Our study provides an enhanced understanding of how AR inhibition alters metabolic signaling and highlights the potential of therapies that target metabolic vulnerabilities in AR-inhibited cells.

Introduction:

Prostate cancer is the leading cause of cancer-related death in non-smoking males in the United States[1]. Prostate cancer progression from localized to advanced metastatic disease is driven by aberrant androgen receptor activity. Therefore, patients with metastatic prostate cancer are treated with androgen deprivation therapies (ADTs), which dampen AR activity by depleting the levels of circulating androgens, alone or in combination with chemotherapy[2]. Prostate cancer that responds to ADT is termed

castration-sensitive prostate cancer (CSPC). Prostate cancer that recurs after ADT is termed castration-resistant prostate cancer (CRPC)[3]. As AR activation remains critical for the survival and growth of the majority of CRPC cells, CRPC is treated with androgen-receptor pathway inhibitors (ARPIs), including enzalutamide which directly interacts with AR to impair its function[4]. Although ARPIs are initially effective, prolonged ARPI treatment invariably leads to treatment resistance and disease progression, ultimately causing lethality[5]. New approaches are needed to understand how prostate cancer cells survive ADT and/or ARPI treatment in order to target them and prevent or delay disease progression.

Prostate cancer initiation and progression are associated with metabolic reprogramming and several studies suggest that metabolic pathways can be targeted in prostate cancer to impair tumor growth[6-13]. For example, targeting lipogenesis via FASN inhibition or targeting glutamine metabolism via glutaminase inhibition antagonizes CRPC[7,8]. Additionally, CAMKK2 inhibition impairs CSPC and CRPC growth by disrupting autophagy[9,10]. Furthermore, serine biosynthesis activity and lactate export have been targeted to reduce growth in models of neuroendocrine prostate cancer[11,13]. While stimulation of AR signaling has been shown to promote anabolic metabolism, the effect of AR blockade on the metabolic signaling of prostate cancer cells has not been comprehensively defined. Therefore, it is critical to determine how metabolism is reprogrammed in the cells that survive AR inhibition in order to exploit therapy-induced metabolic vulnerabilities to delay or prevent prostate cancer progression.

In this study, we hypothesized that the metabolic requirements and vulnerabilities of AR-driven prostate cancer cells may shift as a result of AR inhibition. We utilized a variety of models and approaches to define how AR blockade alters the metabolic phenotype of prostate cancer cells. AR inhibition reprograms the metabolome in a consistent manner *in vitro* and *in vivo*. Cells that survive AR blockade are able to maintain oxidative mitochondrial metabolism while exhibiting reduced glycolysis driven by HK2 downregulation and decreased MYC activity. Mitochondrial elongation, via reduced DRP1-driven mitochondrial fission, enables AR inhibited cells to better survive AR blockade. We explored whether AR inhibition results in increased reliance on oxidative mitochondrial metabolism and observed enhanced sensitivity to complex I inhibitors after AR blockade. Taken together, our data suggest that AR blockade reprograms cellular metabolism and increases dependence on oxidative mitochondrial metabolism.

Results:

Transcriptomic and metabolomic profiling reveal AR inhibition-induced metabolic reprogramming

To gain insight into how prostate cancer cells survive AR inhibition, we evaluated which pathways are altered after clinical AR blockade using the *Rajan et al* dataset[14] which contains transcriptomics data from 7 patient tumors collected prior to and after androgen deprivation therapy (ADT). 10 of the top 30 significantly altered pathways identified by KEGG PATHWAY analysis were metabolism-related (Fig. 1a). To model transcriptional responses to extended AR inhibition, we treated the 16D CRPC cell line[15] with 10μM enzalutamide for more than two months, termed LTenza for Long-Term enzalutamide-

treatment. Gene Set Enrichment Analysis (GSEA) identified negative enrichment of Hallmark_androgen_response genes in LTenza 16D cells (Supplementary Figure 1a), validating AR inhibition. Transcriptomics analysis revealed that enzalutamide-naïve (vehicle-treated) 16D cells cluster with pre-ADT clinical samples, whereas LTenza 16D cells cluster with post-ADT samples from the *Rajan et al* dataset[14] (Fig. 1b). 16D cells cultured with enzalutamide for up to 48 hours, termed STenza for Short-Term enzalutamide-treatment, clustered in between naïve 16D and LTenza 16D cells (Supplementary Figure 1b). Both STenza and LTenza 16D cells contained increased expression of genes upregulated post-ADT in the *Rajan et al* dataset, with LTenza cells containing the highest expression of such genes (Fig. 1c). Differential expression analysis identified 2074 enzalutamide-upregulated and 1498 enzalutamide-downregulated genes in LTenza 16D cells (Fig. 1d). KEGG PATHWAY analysis on the differentially expressed genes identified 12 metabolism-related pathways among the top 30 significantly altered pathways (Fig. 1e). Taken together, these data provide strong evidence that (1) AR inhibition modulates metabolic gene expression, and (2) enzalutamide treatment of 16D cells models transcriptional responses to clinical AR blockade.

Having identified transcriptional evidence of AR blockade-induced metabolic reprogramming, we asked whether enzalutamide treatment of 16D cells alters the metabolome. NOD SCID IL2Rγ^{null} (NSG) mice bearing subcutaneous 16D tumors were treated with vehicle or enzalutamide for 10 days prior to tumor harvest, metabolite extraction, and metabolic profiling by high performance liquid chromatography mass spectrometry. Enzalutamide-treated tumors exhibited reduced protein expression of PSA,

an AR target, and increased expression of NSE, which is repressed by AR, confirming AR inhibition *in vivo* (Supplementary Figure 1c). Metabolomic profiling of vehicle- and enzalutamide-treated tumors identified 47 enzalutamide-increased and 10 enzalutamide-decreased metabolites (Fig. 1f). We asked whether *in vitro* enzalutamide treatment similarly alters the metabolome by performing metabolic profiling on naïve and LTenza 16D cells. These analyses revealed that metabolic profiles group based on treatment, as naïve 16D cells cluster with vehicle-treated 16D tumors, whereas LTenza 16D cells cluster with enzalutamide-treated 16D tumors (Fig. 1g). In addition, we observed a higher abundance of *in vivo* enzalutamide-enriched metabolites in LTenza 16D cells compared to naïve 16D cells (Fig. 1h). *In vitro* metabolomics identified 32 enzalutamide-increased and 8 enzalutamide-decreased metabolites (Supplementary Figure 1d). To identify metabolic pathways commonly altered *in vivo* and *in vitro*, we performed Metabolite Set Enrichment Analysis (MSEA) on the enzalutamide-increased metabolites from each dataset. Among the commonly enriched KEGG pathways were terms related to lipid metabolism and the tricarboxylic acid cycle (TCA cycle) (Fig. 1i).

AR blockade maintains oxidative phosphorylation and reduces glycolysis

Having identified enzalutamide-induced changes to the metabolome, we explored whether AR inhibition of 16D cells alters bioenergetics by measuring oxygen consumption rate (OCR) and extracellular acidification rate (ECAR) in naïve and LTenza 16D cells[16,17] (Fig. 2a,b). Although enzalutamide treatment did not significantly alter ATP-linked respiration (Fig. 2a,c), FCCP-stimulated respiration was increased in enzalutamide-treated cells (Fig. 2a,d), demonstrating an enhanced maximal capacity for oxidative

mitochondrial metabolism. We then transformed rates of OCR and ECAR into rates of mitochondrial and glycolytic ATP production to quantify the redistribution between oxidative phosphorylation and glycolysis upon enzalutamide treatment[18]. The mitochondrial ATP production rate was not altered in LTenza 16D cells (Fig. 2a,e), whereas the glycolytic ATP production rate was dramatically reduced (Fig. 2b,f). As such, the total ATP production rate in LTenza 16D cells (Fig. 2g) was substantially reduced, and oxidative phosphorylation comprised a greater percentage of the overall ATP supply (Fig. 2h). Consistent with dampened glycolysis, lower steady-state lactate was observed in LTenza 16D cells (Fig. 2i).

As a complementary approach to respirometry, we performed isotope tracing with U-$13C_6$-labeled glucose to confirm a relative shift away from glycolysis and towards oxidative phosphorylation upon enzalutamide treatment. There was less glucose enrichment into lactate in LTenza cells, consistent with reduced glycolysis (Fig. 2j). Unlike the substantial decrease in labeling from glucose into lactate, enrichment into TCA cycle intermediates was largely maintained between naive and long-term enzalutamide-treated cells (Fig. 2k – o). The lone exception was a slight increase in relative flux from glucose into citrate in naïve cells (Fig. 2k), which could be indicative of decreased *de novo* lipogenesis upon AR inhibition[19]. Our data support a model whereby AR inhibition leads to reduced glycolysis but maintenance of oxidative mitochondrial metabolism. Interestingly, similar features have been reported in triple negative breast cancer cells that survive chemotherapy[20], suggesting that LTenza cells may adopt a metabolic phenotype associated with treatment-resistance in other epithelial tumor types.

Impaired MYC activity and downregulation of Hexokinase 2 contribute to AR inhibition-induced metabolic reprogramming

We wondered what mechanisms induced by AR blockade may contribute to the reduction in glycolysis. Transcriptomic analysis identified a trend toward downregulation of glycolytic genes in LTenza 16D cells (Fig. 3a). Among the most downregulated genes were *Hexokinase 2* (*HK2*) and *Lactate Dehydrogenase A* (*LDHA*) (Fig. 3a). Western blot analysis confirmed reduced protein expression of HK2 and LDHA in LTenza 16D cells (Fig. 3b). In addition, week-long enzalutamide-treated subcutaneous 16D tumors exhibited robust downregulation of HK2 and LDHA suggesting consistent enzalutamide-induced downregulation of HK2 and LDHA *in vivo* and *in vitro* (Fig. 3c). We performed immunohistochemistry on tissue sections from 16D tumors and observed relatively uniform HK2 downregulation in enzalutamide-treated tissues (Supplementary Figure 2a). To better understand the *in vivo* regulation of glycolytic enzymes following AR inhibition, we utilized an AR-positive patient-derived xenograft (PDX) model originating from a patient with localized CRPC, termed 180-30[21]. We confirmed reduced PSA and increased NSE expression in 1-week enzalutamide-treated 180-30 tumors (Fig. 3d). Consistent with our findings in the 16D model, enzalutamide-treated 180-30 tumors contained reduced expression of HK2 and LDHA (Fig. 3d).

We next asked whether there is evidence of *HK2* and *LDHA* downregulation in clinical datasets after AR inhibition. Transcriptomics analysis of the *Quigley et al* dataset[22], which contains enzalutamide-naïve and enzalutamide-treated metastatic CRPC biopsies,

revealed significant *HK2* mRNA downregulation and a trend toward reduced *LDHA* levels in the enzalutamide-treated samples (Fig. 3e,f). To investigate whether AR inhibition-induced HK2 and LDHA downregulation is unique to CRPC or if it is broadly associated with AR blockade, we evaluated *HK2* and *LDHA* levels in castration-sensitive tumors before and after ADT using the *Rajan et al* dataset[14]. *HK2* mRNA expression was reduced in all 7 patients post-ADT (Fig. 3g) while *LDHA* expression was reduced in 5 of 7 patients (Fig. 3h). These data suggest that AR inhibition lowers *HK2* and *LDHA* levels across various disease states.

Previous work suggests that AR can regulate select glycolytic genes[9]. We analyzed our previous AR ChIP-seq datasets in 16D cells[23] and did not observe evidence of binding to the *HK2* or *LDHA* loci, suggesting that these glycolytic enzymes are not direct targets of AR in 16D cells. To explore an indirect mechanism of *HK2* and *LDHA* downregulation after AR inhibition, we investigated whether AR blockade alters transcriptional signatures of MYC, a key regulator of glycolysis[24]. GSEA revealed negative enrichment of Hallmark_Myc_targets in LTenza 16D cells (Fig. 3i). Consistent with these findings, we observed negative enrichment of Hallmark_Myc_targets in *Rajan et al* patient samples post-ADT[14] (Fig. 3j). In addition, negative enrichment of Hallmark_Myc_targets was observed after castration in the AR positive LTL331 PDX model[25] (Supplementary Figure 2b).

To determine whether reduced MYC activity mediates reduced HK2 and LDHA expression in AR inhibited cells, we attempted to rescue MYC activity via ectopic MYC

expression in LTenza 16D cells. GSEA revealed positive enrichment of Hallmark_Myc_targets in MYC-transduced LTenza cells compared to RFP-transduced LTenza 16D cells (Supplementary Figure 2c). Furthermore, there was no significant negative enrichment of Hallmark_Myc_targets between MYC-transduced LTenza cells and naïve 16D cells indicating successful rescue of MYC transcriptional activity (Supplementary Figure 2d). Western blot analysis revealed increased expression of HK2 and LDHA in MYC-transduced LTenza cells compared to RFP-transduced LTenza 16D cells. However, HK2 expression remained roughly 50 percent lower in MYC-transduced LTenza cells than in naïve 16D cells (Fig 3k). Targeted bisulfite sequencing identified a statistically significant increase in the mean percentage of methylated CpGs within the transcriptional start site of *HK2* in LTenza 16D cells suggesting that epigenetic alterations may cooperate with reduced MYC activity to antagonize HK2 expression (Supplementary Figure 2e).

Since HK2 is upstream of LDHA and catalyzes the first committed step of glycolysis, we evaluated whether HK2 knockdown (shHK2) in naïve 16D cells is sufficient to reduce glycolytic activity, compared to a scrambled control shRNA (shScr). HK2 knockdown was confirmed by Western blot (Fig. 3l). To broadly measure cellular glycolytic capacity, we measured ECAR after treatment with the ATP synthase inhibitor oligomycin, which will stimulate an increase in glycolysis due to the loss of oxidative phosphorylation. Whereas oligomycin stimulated a 2-fold increase in ECAR of shScr-transduced 16D cells (Fig. 3m), the rate was unchanged in shHK2-transduced 16D cells (Fig. 3n) or LTenza 16D cells (Fig. 3o). Accordingly, shHK2-transduced 16D cells and LTenza 16D cells exhibited

reduced oligomycin-stimulated ECAR compared to shScr-transduced 16D cells (Supplementary Figure 2f). These data establish reduced HK2 as one mechanism contributing to a lower glycolytic capacity in response to AR inhibition.

Enzalutamide induces mitochondrial elongation via reduced DRP1 activity

As mitochondrial dynamics can change in response to cellular and environmental stresses[26], we explored the effect of AR inhibition on mitochondrial morphology. Mitochondria were visualized in naïve and LTenza 16D cells by staining for the mitochondria-associated protein TUFM. Immunofluorescence identified robustly elongated mitochondria in LTenza 16D cells (Fig. 4a). Quantification of mitochondrial elongation and branching was performed by calculating the mitochondrial aspect ratio, which is equal to the ratio of the major axis to the minor axis of an object, and form factor, a value that compensates for irregularity in the shape of an object, respectively[27] (Fig. 4b). LTenza 16D cell mitochondria exhibited a higher aspect ratio (Fig. 4c) and lower form factor (Fig. 4d) compared to naïve cell mitochondria, consistent with mitochondrial elongation and increased branching. Eccentricity, the ratio of the distance between the foci of an ellipse and its major axis length, was used as a secondary approach to quantify mitochondrial elongation. Increased mitochondrial eccentricity was calculated in LTenza 16D cells, confirming mitochondrial elongation (Supplementary Figure 3a). Enzalutamide treatment did not alter mitochondrial size, subtly increased mitochondrial count, and did not alter mitochondrial volume (Supplementary Figure 3b-d). As mitochondrial elongation and branching have been associated with enhanced mitochondrial function in certain

contexts[28], these features may enable cells to compensate for reduced glycolytic activity after AR inhibition.

Mitochondrial morphology is determined by the relative amounts of mitochondrial fission and fusion[29]. Several reports provide evidence that AR may regulate DRP1[30], encoded by the *DNM1L* gene, which mediates mitochondrial fission. We therefore explored whether DRP1 levels are altered in LTenza 16D cells. DRP1 expression was only subtly reduced in LTenza 16D cells (Fig. 4e). As DRP1 phosphorylation at S616 is required for DRP1 activity[31], we hypothesized that LTenza 16D cells may exhibit reduced DRP1-S616 phosphorylation. Indeed, DRP1-S616 phosphorylation was dramatically reduced in LTenza cells compared to naïve 16D cells (Fig. 4e). Enzalutamide-treated 16D tumors contained both reduced total DRP1 expression and reduced DRP1-S616 phosphorylation (Supplementary Figure 3e,f). Furthermore, we observed both reduced total DRP1 expression and reduced DRP1-S616 phosphorylation in 180-30 PDX tumors suggesting that the tumor microenvironment may influence the response of DRP1 expression to AR blockade (Figure 4f). Analysis of 16D AR ChIP-seq data[23] revealed binding to the *DNM1L* locus, suggesting that AR directly regulates DRP1 in this model (Supplementary Figure 3g).

To evaluate the functional role of DRP1, we ectopically expressed a constitutively active DRP1 phosphomimetic[23], DRP1^{S616E}, in naïve and LTenza 16D cells (Fig. 4g). DRP1^{S616E}-transduced LTenza 16D cells contained more fragmented mitochondria than RFP-transduced LTenza 16D cells (Fig. 4h,i). Apoptosis and cell cycle analyses revealed that

whereas naïve 16D cells are relatively insensitive to DRP1^{S616E} expression, DRP1^{S616E}-transduced LTenza cells exhibit increased apoptosis and reduced proliferation compared to RFP-transduced LTenza cells (Fig. 4j,k). These data suggest that elongation of mitochondria may enable LTenza 16D cells to better survive enzalutamide treatment. Our data are consistent with previous reports that mitochondrial elongation can promote tumor cell survival during energetic stress[26,31,32].

AR inhibition enhances sensitivity to complex I inhibitors

As enzalutamide-treated 16D cells generate a greater proportion of ATP from oxidative mitochondrial metabolism and exhibit reduced glycolytic activity and higher respiratory capacity, we hypothesized that these cells may be increasingly sensitive to inhibition of oxidative phosphorylation. To test our hypothesis, we treated naïve and LTenza 16D cells with the highly-specific complex I inhibitor IACS-010759[33] (IACS). Respirometry and U-$13C_6$-glucose tracer analysis were performed to validate the on-target effect of IACS. IACS reduced the ATP-linked respiration of naïve and LTenza 16D cells by roughly 95 percent (Fig. 5a). In addition, IACS treatment significantly reduced M+2 labeling of TCA cycle intermediates from U-$13C_6$-glucose in both naïve and LTenza 16D cells (Supplementary Figure 4a,b). Increased M+3-labeled lactate was observed in both naïve and LTenza 16D cells after IACS treatment indicating that both cell types compensate for reduced complex I activity by increasing glycolysis (Supplementary Figure 4c). Respirometry revealed that while both naïve and LTenza 16D cells increase glycolytic ATP production in response to IACS, naïve cells contain a 2-fold higher IACS-induced glycolytic ATP production rate compared to LTenza 16D cells (Supplementary Figure 4d).

Accordingly, IACS treatment reduced the total ATP production of naïve cells by just 12% compared to a 29% reduction of total ATP production in LTenza 16D cells (Supplementary Figure 4e).

We performed cell cycle analysis to determine the effect of IACS on the proliferation of naïve and LTenza 16D cells and identified robust differential sensitivity (Fig. 5b). Whereas IACS treatment did not alter the proliferation of naïve cells, IACS reduced the proliferation of LTenza 16D cells by roughly 35 percent in just 72 hours (Fig. 5b and Supplementary Figure 4f). Apoptosis analysis revealed that while IACS treatment increased apoptosis in both naïve and LTenza 16D cells, the percentage of apoptotic naïve cells remained far below one percent after 72 hours (Fig. 5c). In contrast, nearly 6% of IACS-treated LTenza cells were apoptotic after the same period (Fig. 5c). Since AR blockade increases sensitivity to complex I inhibition, we wondered if IACS treatment of naïve 16D cells might increase enzalutamide sensitivity. 72hr IACS pretreatment significantly enhanced enzalutamide sensitivity, effectively doubling the growth inhibition caused by enzalutamide (Fig. 5d). These data demonstrate the potential for combining IACS and enzalutamide to reduce prostate cancer cell proliferation regardless of which treatment is initiated first.

We explored whether the clinically viable drug metformin, which has complex I inhibitor activity *in vitro*[34], alters the enzalutamide sensitivity of naïve 16D cells. Reduced ATP-linked respiration in metformin-treated 16D cells was confirmed by respirometry (Supplementary Figure 4g). Cell cycle analysis revealed that, unlike IACS, metformin

alone was sufficient to impair the proliferation of naïve 16D cells (Supplementary Figure 4h). Reduced proliferation in metformin-treated 16D cells was likely caused by known off-target effects[34] as IACS treatment reduced ATP-linked respiration by greater than 95% without altering EdU labeling. Consistent with IACS pretreatment increasing responsiveness to AR inhibition, 72hr metformin pretreatment significantly enhanced the sensitivity of naïve 16D cells to enzalutamide (Supplementary Figure 4i).

To better understand the interaction between AR inhibition and complex I inhibition across various disease states, we explored whether metformin similarly enhances the sensitivity of LNCaP cells to castration. After validating castration-induced suppression of AR target gene expression (Supplementary Figure 5a), and demonstrating that castrated LNCaP cells transcriptionally resemble castrated LTL331 PDX tumors[25] and patient tumors post-ADT[14] (Supplementary Figure 5b-e), we explored whether castrated LNCaP cells exhibit altered metabolic gene expression. GSEA revealed negative enrichment of Hallmark_Myc_targets (Supplementary Figure 5f), and we identified mRNA downregulation of select glycolytic genes including *HK2* and *LDHA* after castration (Supplementary Figure 5g). Western blot analysis confirmed lower HK2 and LDHA levels and identified reduced total DRP1 expression and DRP1-S616 phosphorylation (Supplementary Figure 5h). Consistent with our findings in the 16D model, metformin treatment reduced the growth of LNCaP cells and significantly increased castration sensitivity, from roughly 45 percent to greater than 85 percent (Supplementary Figure 5i,j). These data suggest that AR blockade-induced metabolic changes may be conserved

across various disease states and that complex I inhibition could broadly enhance sensitivity to AR inhibition.

After showing that various complex I inhibitors can synergize with AR blockade *in vitro*, we explored whether enzalutamide treatment of mice bearing 180-30 PDX tumors enhances IACS sensitivity. After one week of treatment with vehicle or enzalutamide *in vivo*, we analyzed IACS sensitivity using *ex vivo* culture. Week-long enzalutamide-treated 180-30 PDX tumors contained reduced protein expression of PSA, HK2, and LDHA (Fig. 5e,f). Cell cycle analysis after *ex vivo* culture of tumor tissue in prostate organoid conditions confirmed reduced proliferation in enzalutamide-treated 180-30 PDX tumors (Fig. 5g). Analysis of IACS sensitivity revealed that enzalutamide-treated samples accounted for 4 of the 5 most IACS-sensitive samples (Fig. 5h). Furthermore, whereas IACS did not alter the growth of vehicle-treated tumor cells in a statistically significant manner (Fig. 5i), IACS significantly reduced proliferation of enzalutamide-treated cells (Fig. 5j).

Discussion:

Therapy-induced metabolic reprogramming has been reported in various cancers where standard of care therapy can synergize with targeting of reprogrammed metabolism to impair treatment-resistance[20,35,36]. In this study, we comprehensively characterized the effect of AR blockade on prostate cancer metabolism. Transcriptomic and metabolomic analyses revealed AR-inhibition-induced changes to metabolic gene expression and metabolite abundance respectively. We identified sustained oxidative mitochondrial

metabolism, including increased maximal respiration, and reduced basal and oligomycin-stimulated glycolysis, after AR inhibition. Mechanistically, decreased MYC activity and HK2 downregulation contributed to reduced glycolytic activity. Interestingly, we observed robust elongation of mitochondria driven by lower DRP1 activity in enzalutamide-treated cells and found that mitochondrial elongation supports cell survival and proliferation after AR blockade. We explored whether AR inhibition increases reliance on oxidative mitochondrial metabolism and observed increased sensitivity to complex I inhibitors after AR blockade. In addition, pre-treatment with complex I inhibitors increased sensitivity to AR inhibition, demonstrating the effectiveness of combined complex I inhibition and AR blockade.

Our study identifies mitochondrial elongation as a potential survival mechanism after AR blockade. Elongation has been shown to protect mitochondria from autophagosomal degradation during nutrient starvation[26,32]. A hyperfused mitochondrial phenotype has been observed in triple negative breast cancer cells that survive chemotherapy[37] and has been shown to enable chemotherapy resistance in gynecological cancers[38]. The functional impact of mitochondrial morphology on metabolic output has proven to be highly context dependent. For example, mitochondrial fission drives increased oxidative mitochondrial metabolism and tumorigenic potential in pancreatic ductal adenocarcinoma cells[39,40] and decreased oxidative mitochondrial metabolism in neuroblastoma cells[41]. Future work is needed to understand how mitochondrial elongation enables prostate cancer cells to better survive AR blockade.

It is critical to consider the window when complex I inhibition could cooperate with AR inhibition to improve patient outcomes. Our functional data suggest that complex I inhibition could be combined with ADT to treat castration-sensitive prostate cancer and/or ARPIs to treat CRPC. These findings are further supported by our observation from clinical datasets that *HK2* downregulation occurs after both ADT treatment of localized castration-sensitive disease, and ARPI treatment of metastatic CRPC. While most prostate tumors initially respond to AR inhibition, they eventually recur in a more aggressive form, driven by the acquisition of additional somatic mutations such as disruption of RB1 and TP53[42,43]. Interestingly, knockdown of *RB1* and *TP53* in LTenza 16D cells was not sufficient to alter enzalutamide-induced metabolic features including reduced MYC activity and enhanced sensitivity to complex I inhibitors despite increased neuroendocrine signatures[44-46] (Supplementary Figure 6). In contrast, in the LTL331 PDX model[25], which relapses as terminally differentiated neuroendocrine prostate cancer after castration, relapsed tumors contained robust enrichment of Hallmark_Myc_targets compared to castrated tumors despite maintenance of low AR activity (Supplementary Figure 7). These data suggest that rescue of AR activity is not necessary to restore MYC signaling and that the effectiveness of combined AR blockade and complex I inhibitor treatment in relapsed ARPI-resistant disease may depend on the tumor phenotype and/or genetic driver. Future work is necessary to determine whether MYC reactivation is broadly associated with relapse, and whether increased MYC activity may contribute to prostate cancer recurrence by restoring glycolytic activity.

Metformin has been explored as a prostate cancer treatment for functions distinct from complex I inhibition. Specifically, metformin has been shown to inhibit the proliferation of prostate cancer cell lines *in vitro* by reducing AR and cyclin D1 levels[47,48]. These effects may explain why naïve 16D cells exhibit sensitivity to metformin, despite lacking sensitivity to IACS, which reduces mitochondrial respiration by greater than 95 percent. In addition, metformin has been shown to synergize with bicalutamide in mouse models by preventing AR blockade-induced hyperinsulinemia, which enhances tumor growth[49]. Accordingly, several observational and clinical trials have been performed and others are ongoing to determine the efficacy of combined metformin treatment and AR blockade[50]. Such trials have thus far been inconclusive regarding metformin use and both recurrence-free survival and overall survival[51]. Importantly, the concentration of metformin required to inhibit complex I activity *in vitro* (1mM) is more than 10 times higher than the maximally-achievable therapeutic concentration (70μM) found in patients[34,52]. Therefore, improved clinically-viable inhibitors of complex I are needed to evaluate the efficacy of combined AR blockade and inhibition of mitochondrial oxidation in patients.

References:

1. Siegel RL, Miller KD, Fuchs HE, Jemal A. Cancer statistics, 2022. *CA Cancer J Clin.* 2022;72(1):7-33.
2. Sayegh N, Swami U, Agarwal N. Recent Advances in the Management of Metastatic Prostate Cancer. *JCO Oncol Pract.* 2022;18(1):45-55.
3. Nakazawa M, Paller C, Kyprianou N. Mechanisms of Therapeutic Resistance in Prostate Cancer. *Curr Oncol Rep.* 2017;19(2):13. PMC5812366
4. Tran C, Ouk S, Clegg NJ, Chen Y, Watson PA, Arora V, Wongvipat J, Smith-Jones PM, Yoo D, Kwon A, Wasielewska T, Welsbie D, Chen CD, Higano CS, Beer TM,

Hung DT, Scher HI, Jung ME, Sawyers CL. Development of a second-generation antiandrogen for treatment of advanced prostate cancer. *Science.* 2009;324(5928):787-790. PMC2981508

5. Schmidt KT, Huitema ADR, Chau CH, Figg WD. Resistance to second-generation androgen receptor antagonists in prostate cancer. *Nat Rev Urol.* 2021;18(4):209-226.
6. Priolo C, Pyne S, Rose J, Regan ER, Zadra G, Photopoulos C, Cacciatore S, Schultz D, Scaglia N, McDunn J, De Marzo AM, Loda M. AKT1 and MYC induce distinctive metabolic fingerprints in human prostate cancer. *Cancer Res.* 2014;74(24):7198-7204. PMC4267915
7. Zadra G, Ribeiro CF, Chetta P, Ho Y, Cacciatore S, Gao X, Syamala S, Bango C, Photopoulos C, Huang Y, Tyekucheva S, Bastos DC, Tchaicha J, Lawney B, Uo T, D'Anello L, Csibi A, Kalekar R, Larimer B, Ellis L, Butler LM, Morrissey C, McGovern K, Palombella VJ, Kutok JL, Mahmood U, Bosari S, Adams J, Peluso S, Dehm SM, Plymate SR, Loda M. Inhibition of de novo lipogenesis targets androgen receptor signaling in castration-resistant prostate cancer. *Proc Natl Acad Sci U S A.* 2019;116(2):631-640. PMC6329966
8. Xu L, Yin Y, Li Y, Chen X, Chang Y, Zhang H, Liu J, Beasley J, McCaw P, Zhang H, Young S, Groth J, Wang Q, Locasale JW, Gao X, Tang DG, Dong X, He Y, George D, Hu H, Huang J. A glutaminase isoform switch drives therapeutic resistance and disease progression of prostate cancer. *Proc Natl Acad Sci U S A.* 2021;118(13). PMC8020804
9. Massie CE, Lynch A, Ramos-Montoya A, Boren J, Stark R, Fazli L, Warren A, Scott H, Madhu B, Sharma N, Bon H, Zecchini V, Smith DM, Denicola GM, Mathews N, Osborne M, Hadfield J, Macarthur S, Adryan B, Lyons SK, Brindle KM, Griffiths J, Gleave ME, Rennie PS, Neal DE, Mills IG. The androgen receptor fuels prostate cancer by regulating central metabolism and biosynthesis. *EMBO J.* 2011;30(13):2719-2733. PMC3155295
10. Lin C, Blessing AM, Pulliam TL, Shi Y, Wilkenfeld SR, Han JJ, Murray MM, Pham AH, Duong K, Brun SN, Shaw RJ, Ittmann MM, Frigo DE. Inhibition of CAMKK2

impairs autophagy and castration-resistant prostate cancer via suppression of AMPK-ULK1 signaling. *Oncogene.* 2021;40(9):1690-1705. PMC7935762

11. Reina-Campos M, Linares JF, Duran A, Cordes T, L'Hermitte A, Badur MG, Bhangoo MS, Thorson PK, Richards A, Rooslid T, Garcia-Olmo DC, Nam-Cha SY, Salinas-Sanchez AS, Eng K, Beltran H, Scott DA, Metallo CM, Moscat J, Diaz-Meco MT. Increased Serine and One-Carbon Pathway Metabolism by PKClambda/iota Deficiency Promotes Neuroendocrine Prostate Cancer. *Cancer Cell.* 2019;35(3):385-400 e389. PMC6424636
12. Bader DA, Hartig SM, Putluri V, Foley C, Hamilton MP, Smith EA, Saha PK, Panigrahi A, Walker C, Zong L, Martini-Stoica H, Chen R, Rajapakshe K, Coarfa C, Sreekumar A, Mitsiades N, Bankson JA, Ittmann MM, O'Malley BW, Putluri N, McGuire SE. Mitochondrial pyruvate import is a metabolic vulnerability in androgen receptor-driven prostate cancer. *Nat Metab.* 2019;1(1):70-85. PMC6563330
13. Choi SYC, Ettinger SL, Lin D, Xue H, Ci X, Nabavi N, Bell RH, Mo F, Gout PW, Fleshner NE, Gleave ME, Collins CC, Wang Y. Targeting MCT4 to reduce lactic acid secretion and glycolysis for treatment of neuroendocrine prostate cancer. *Cancer Med.* 2018. PMC6051138
14. Rajan P, Sudbery IM, Villasevil ME, Mui E, Fleming J, Davis M, Ahmad I, Edwards J, Sansom OJ, Sims D, Ponting CP, Heger A, McMenemin RM, Pedley ID, Leung HY. Next-generation sequencing of advanced prostate cancer treated with androgen-deprivation therapy. *Eur Urol.* 2014;66(1):32-39. PMC4062940
15. Bishop JL, Thaper D, Vahid S, Davies A, Ketola K, Kuruma H, Jama R, Nip KM, Angeles A, Johnson F, Wyatt AW, Fazli L, Gleave ME, Lin D, Rubin MA, Collins CC, Wang Y, Beltran H, Zoubeidi A. The Master Neural Transcription Factor BRN2 Is an Androgen Receptor-Suppressed Driver of Neuroendocrine Differentiation in Prostate Cancer. *Cancer Discov.* 2017;7(1):54-71.
16. Divakaruni AS, Paradyse A, Ferrick DA, Murphy AN, Jastroch M. Analysis and interpretation of microplate-based oxygen consumption and pH data. *Methods Enzymol.* 2014;547:309-354.
17. Jones AE, Sheng L, Acevedo A, Veliova M, Shirihai OS, Stiles L, Divakaruni AS. Forces, fluxes, and fuels: tracking mitochondrial metabolism by integrating

measurements of membrane potential, respiration, and metabolites. *Am J Physiol Cell Physiol.* 2021;320(1):C80-C91. PMC7846976

18. Desousa BR, Kim KKO, Hsieh WY, Jones AE, Swain P, Morrow DH, Ferrick DA, Shirihai OS, Neilson A, Nathanson DA, Rogers GW, Dranka BP, Murphy AN, Affourtit C, Bensinger SJ, Stiles L, Romero N, Divakaruni AS. Calculating ATP production rates from oxidative phosphorylation and glycolysis during cell activation. *bioRxiv.* 2022:2022.2004.2016.488523.
19. Mah CY, Nassar ZD, Swinnen JV, Butler LM. Lipogenic effects of androgen signaling in normal and malignant prostate. *Asian J Urol.* 2020;7(3):258-270. PMC7385522
20. Evans KW, Yuca E, Scott SS, Zhao M, Paez Arango N, Cruz Pico CX, Saridogan T, Shariati M, Class CA, Bristow CA, Vellano CP, Zheng X, Gonzalez-Angulo AM, Su X, Tapia C, Chen K, Akcakanat A, Lim B, Tripathy D, Yap TA, Francesco MED, Draetta GF, Jones P, Heffernan TP, Marszalek JR, Meric-Bernstam F. Oxidative Phosphorylation Is a Metabolic Vulnerability in Chemotherapy-Resistant Triple-Negative Breast Cancer. *Cancer Res.* 2021;81(21):5572-5581. PMC8563442
21. Palanisamy N, Yang J, Shepherd PDA, Li-Ning-Tapia EM, Labanca E, Manyam GC, Ravoori MK, Kundra V, Araujo JC, Efstathiou E, Pisters LL, Wan X, Wang X, Vazquez ES, Aparicio AM, Carskadon SL, Tomlins SA, Kunju LP, Chinnaiyan AM, Broom BM, Logothetis CJ, Troncoso P, Navone NM. The MD Anderson Prostate Cancer Patient-derived Xenograft Series (MDA PCa PDX) Captures the Molecular Landscape of Prostate Cancer and Facilitates Marker-driven Therapy Development. *Clin Cancer Res.* 2020;26(18):4933-4946. PMC7501166
22. Quigley DA, Dang HX, Zhao SG, Lloyd P, Aggarwal R, Alumkal JJ, Foye A, Kothari V, Perry MD, Bailey AM, Playdle D, Barnard TJ, Zhang L, Zhang J, Youngren JF, Cieslik MP, Parolia A, Beer TM, Thomas G, Chi KN, Gleave M, Lack NA, Zoubeidi A, Reiter RE, Rettig MB, Witte O, Ryan CJ, Fong L, Kim W, Friedlander T, Chou J, Li H, Das R, Li H, Moussavi-Baygi R, Goodarzi H, Gilbert LA, Lara PN, Jr., Evans CP, Goldstein TC, Stuart JM, Tomlins SA, Spratt DE, Cheetham RK, Cheng DT, Farh K, Gehring JS, Hakenberg J, Liao A, Febbo PG, Shon J, Sickler B, Batzoglou S, Knudsen KE, He HH, Huang J, Wyatt AW, Dehm SM, Ashworth A, Chinnaiyan

AM, Maher CA, Small EJ, Feng FY. Genomic Hallmarks and Structural Variation in Metastatic Prostate Cancer. *Cell.* 2018;175(3):889.

23. Davies A, Nouruzi S, Ganguli D, Namekawa T, Thaper D, Linder S, Karaoglanoglu F, Omur ME, Kim S, Kobelev M, Kumar S, Sivak O, Bostock C, Bishop J, Hoogstraat M, Talal A, Stelloo S, van der Poel H, Bergman AM, Ahmed M, Fazli L, Huang H, Tilley W, Goodrich D, Feng FY, Gleave M, He HH, Hach F, Zwart W, Beltran H, Selth L, Zoubeidi A. An androgen receptor switch underlies lineage infidelity in treatment-resistant prostate cancer. *Nat Cell Biol.* 2021;23(9):1023-1034. PMC9012003
24. Stine ZE, Walton ZE, Altman BJ, Hsieh AL, Dang CV. MYC, Metabolism, and Cancer. *Cancer Discov.* 2015;5(10):1024-1039. PMC4592441
25. Akamatsu S, Wyatt AW, Lin D, Lysakowski S, Zhang F, Kim S, Tse C, Wang K, Mo F, Haegert A, Brahmbhatt S, Bell R, Adomat H, Kawai Y, Xue H, Dong X, Fazli L, Tsai H, Lotan TL, Kossai M, Mosquera JM, Rubin MA, Beltran H, Zoubeidi A, Wang Y, Gleave ME, Collins CC. The Placental Gene PEG10 Promotes Progression of Neuroendocrine Prostate Cancer. *Cell Rep.* 2015;12(6):922-936.
26. Gomes LC, Di Benedetto G, Scorrano L. During autophagy mitochondria elongate, are spared from degradation and sustain cell viability. *Nat Cell Biol.* 2011;13(5):589-598. PMC3088644
27. Petcherski A, Trudeau KM, Wolf DM, Segawa M, Lee J, Taddeo EP, Deeney JT, Liesa M. Elamipretide Promotes Mitophagosome Formation and Prevents Its Reduction Induced by Nutrient Excess in INS1 beta-cells. *J Mol Biol.* 2018;430(24):4823-4833. PMC6290358
28. Chan DC. Mitochondrial Dynamics and Its Involvement in Disease. *Annu Rev Pathol.* 2020;15:235-259.
29. Mishra P, Chan DC. Metabolic regulation of mitochondrial dynamics. *J Cell Biol.* 2016;212(4):379-387. PMC4754720
30. Lee YG, Nam Y, Shin KJ, Yoon S, Park WS, Joung JY, Seo JK, Jang J, Lee S, Nam D, Caino MC, Suh PG, Chan Chae Y. Androgen-induced expression of DRP1 regulates mitochondrial metabolic reprogramming in prostate cancer. *Cancer Lett.* 2020;471:72-87.

31. Rambold AS, Kostelecky B, Elia N, Lippincott-Schwartz J. Tubular network formation protects mitochondria from autophagosomal degradation during nutrient starvation. *Proc Natl Acad Sci U S A.* 2011;108(25):10190-10195. PMC3121813
32. Li J, Huang Q, Long X, Guo X, Sun X, Jin X, Li Z, Ren T, Yuan P, Huang X, Zhang H, Xing J. Mitochondrial elongation-mediated glucose metabolism reprogramming is essential for tumour cell survival during energy stress. *Oncogene.* 2017;36(34):4901-4912.
33. Molina JR, Sun Y, Protopopova M, Gera S, Bandi M, Bristow C, McAfoos T, Morlacchi P, Ackroyd J, Agip AA, Al-Atrash G, Asara J, Bardenhagen J, Carrillo CC, Carroll C, Chang E, Ciurea S, Cross JB, Czako B, Deem A, Daver N, de Groot JF, Dong JW, Feng N, Gao G, Gay J, Do MG, Greer J, Giuliani V, Han J, Han L, Henry VK, Hirst J, Huang S, Jiang Y, Kang Z, Khor T, Konoplev S, Lin YH, Liu G, Lodi A, Lofton T, Ma H, Mahendra M, Matre P, Mullinax R, Peoples M, Petrocchi A, Rodriguez-Canale J, Serreli R, Shi T, Smith M, Tabe Y, Theroff J, Tiziani S, Xu Q, Zhang Q, Muller F, DePinho RA, Toniatti C, Draetta GF, Heffernan TP, Konopleva M, Jones P, Di Francesco ME, Marszalek JR. An inhibitor of oxidative phosphorylation exploits cancer vulnerability. *Nat Med.* 2018;24(7):1036-1046.
34. He L, Wondisford FE. Metformin action: concentrations matter. *Cell Metab.* 2015;21(2):159-162.
35. Mukhopadhyay S, Goswami D, Adiseshaiah PP, Burgan W, Yi M, Guerin TM, Kozlov SV, Nissley DV, McCormick F. Undermining Glutaminolysis Bolsters Chemotherapy While NRF2 Promotes Chemoresistance in KRAS-Driven Pancreatic Cancers. *Cancer Res.* 2020;80(8):1630-1643. PMC7185043
36. Zhou W, Yao Y, Scott AJ, Wilder-Romans K, Dresser JJ, Werner CK, Sun H, Pratt D, Sajjakulnukit P, Zhao SG, Davis M, Nelson BS, Halbrook CJ, Zhang L, Gatto F, Umemura Y, Walker AK, Kachman M, Sarkaria JN, Xiong J, Morgan MA, Rehemtualla A, Castro MG, Lowenstein P, Chandrasekaran S, Lawrence TS, Lyssiotis CA, Wahl DR. Purine metabolism regulates DNA repair and therapy resistance in glioblastoma. *Nat Commun.* 2020;11(1):3811. PMC7393131
37. Baek ML, Lee J, Pendleton KE, Berner MJ, Goff EB, Tan L, Martinez SA, Wang T, Meyer MD, Lim B, Barrish JP, Porter W, Lorenzi PL, Echeverria GV. Mitochondrial

structure and function adaptation in residual triple negative breast cancer cells surviving chemotherapy treatment. *bioRxiv.* 2022:2022.2002.2025.481996.

38. Kong B, Tsuyoshi H, Orisaka M, Shieh DB, Yoshida Y, Tsang BK. Mitochondrial dynamics regulating chemoresistance in gynecological cancers. *Ann N Y Acad Sci.* 2015;1350:1-16.
39. Courtois S, de Luxan-Delgado B, Penin-Peyta L, Royo-Garcia A, Parejo-Alonso B, Jagust P, Alcala S, Rubiolo JA, Sanchez L, Sainz B, Jr., Heeschen C, Sancho P. Inhibition of Mitochondrial Dynamics Preferentially Targets Pancreatic Cancer Cells with Enhanced Tumorigenic and Invasive Potential. *Cancers (Basel).* 2021;13(4). PMC7914708
40. Yu M, Nguyen ND, Huang Y, Lin D, Fujimoto TN, Molkentine JM, Deorukhkar A, Kang Y, San Lucas FA, Fernandes CJ, Koay EJ, Gupta S, Ying H, Koong AC, Herman JM, Fleming JB, Maitra A, Taniguchi CM. Mitochondrial fusion exploits a therapeutic vulnerability of pancreatic cancer. *JCI Insight.* 2019;5. PMC6777817
41. Hagenbuchner J, Kuznetsov AV, Obexer P, Ausserlechner MJ. BIRC5/Survivin enhances aerobic glycolysis and drug resistance by altered regulation of the mitochondrial fusion/fission machinery. *Oncogene.* 2013;32(40):4748-4757.
42. Ku SY, Rosario S, Wang Y, Mu P, Seshadri M, Goodrich ZW, Goodrich MM, Labbe DP, Gomez EC, Wang J, Long HW, Xu B, Brown M, Loda M, Sawyers CL, Ellis L, Goodrich DW. Rb1 and Trp53 cooperate to suppress prostate cancer lineage plasticity, metastasis, and antiandrogen resistance. *Science.* 2017;355(6320):78-83. PMC5367887
43. Mu P, Zhang Z, Benelli M, Karthaus WR, Hoover E, Chen CC, Wongvipat J, Ku SY, Gao D, Cao Z, Shah N, Adams EJ, Abida W, Watson PA, Prandi D, Huang CH, de Stanchina E, Lowe SW, Ellis L, Beltran H, Rubin MA, Goodrich DW, Demichelis F, Sawyers CL. SOX2 promotes lineage plasticity and antiandrogen resistance in TP53- and RB1-deficient prostate cancer. *Science.* 2017;355(6320):84-88. PMC5247742
44. Guo H, Ci X, Ahmed M, Hua JT, Soares F, Lin D, Puca L, Vosoughi A, Xue H, Li E, Su P, Chen S, Nguyen T, Liang Y, Zhang Y, Xu X, Xu J, Sheahan AV, Ba-Alawi W, Zhang S, Mahamud O, Vellanki RN, Gleave M, Bristow RG, Haibe-Kains B,

Poirier JT, Rudin CM, Tsao MS, Wouters BG, Fazli L, Feng FY, Ellis L, van der Kwast T, Berlin A, Koritzinsky M, Boutros PC, Zoubeidi A, Beltran H, Wang Y, He HH. ONECUT2 is a driver of neuroendocrine prostate cancer. *Nat Commun.* 2019;10(1):278. PMC6336817

45. Aggarwal R, Huang J, Alumkal JJ, Zhang L, Feng FY, Thomas GV, Weinstein AS, Friedl V, Zhang C, Witte ON, Lloyd P, Gleave M, Evans CP, Youngren J, Beer TM, Rettig M, Wong CK, True L, Foye A, Playdle D, Ryan CJ, Lara P, Chi KN, Uzunangelov V, Sokolov A, Newton Y, Beltran H, Demichelis F, Rubin MA, Stuart JM, Small EJ. Clinical and Genomic Characterization of Treatment-Emergent Small-Cell Neuroendocrine Prostate Cancer: A Multi-institutional Prospective Study. *J Clin Oncol.* 2018;36(24):2492-2503. PMC6366813
46. Beltran H, Prandi D, Mosquera JM, Benelli M, Puca L, Cyrta J, Marotz C, Giannopoulou E, Chakravarthi BV, Varambally S, Tomlins SA, Nanus DM, Tagawa ST, Van Allen EM, Elemento O, Sboner A, Garraway LA, Rubin MA, Demichelis F. Divergent clonal evolution of castration-resistant neuroendocrine prostate cancer. *Nat Med.* 2016;22(3):298-305. PMC4777652
47. Demir U, Koehler A, Schneider R, Schweiger S, Klocker H. Metformin anti-tumor effect via disruption of the MID1 translational regulator complex and AR downregulation in prostate cancer cells. *BMC Cancer.* 2014;14:52. PMC3929757
48. Ben Sahra I, Laurent K, Loubat A, Giorgetti-Peraldi S, Colosetti P, Auberger P, Tanti JF, Le Marchand-Brustel Y, Bost F. The antidiabetic drug metformin exerts an antitumoral effect in vitro and in vivo through a decrease of cyclin D1 level. *Oncogene.* 2008;27(25):3576-3586.
49. Colquhoun AJ, Venier NA, Vandersluis AD, Besla R, Sugar LM, Kiss A, Fleshner NE, Pollak M, Klotz LH, Venkateswaran V. Metformin enhances the antiproliferative and apoptotic effect of bicalutamide in prostate cancer. *Prostate Cancer Prostatic Dis.* 2012;15(4):346-352.
50. Nobes JP, Langley SE, Klopper T, Russell-Jones D, Laing RW. A prospective, randomized pilot study evaluating the effects of metformin and lifestyle intervention on patients with prostate cancer receiving androgen deprivation therapy. *BJU Int.* 2012;109(10):1495-1502.

51. Ahn HK, Lee YH, Koo KC. Current Status and Application of Metformin for Prostate Cancer: A Comprehensive Review. *Int J Mol Sci.* 2020;21(22). PMC7698147
52. Hess C, Unger M, Madea B, Stratmann B, Tschoepe D. Range of therapeutic metformin concentrations in clinical blood samples and comparison to a forensic case with death due to lactic acidosis. *Forensic Sci Int.* 2018;286:106-112.

Acknowledgments: P.D.C. and J.M.G. acknowledge the support of the UCLA Eli and Edythe Broad Center of Regenerative Medicine and Stem Cell Research Training Program. P.D.C. is also supported by the NIH grants TL1 DK132768 and U2C DK129496. A.E.J. is supported by the UCLA Tumor Cell Biology Training Grant (NIH T32CA009056). A.S.G. is supported by the National Cancer Institute of the National Institutes of Health under Award Number R01CA237191. The content is solely the responsibility of the authors and does not necessarily represent the official views of the National Institutes of Health. A.M.L.D. is supported by NCI/NIH supplement related to R01CA237191. A.S.G. is also supported by American Cancer Society award RSG-17-068-01-TBG, the UCLA Eli and Edythe Broad Center of Regenerative Medicine and Stem Cell Research Rose Hills Foundation Innovator Grant, the UCLA Jonsson Comprehensive Cancer Center and Eli and Edythe Broad Center of Regenerative Medicine and Stem Cell Research Ablon Scholars Program, the National Center for Advancing Translational Sciences UCLA CTSI Grant UL1TR001881, STOP CANCER, and the UCLA Institute of Urologic Oncology. A.S.G., A.S.D. and O.S.S. are supported by the UCLA Prostate Cancer Specialized Programs of Research Excellence (SPORE) NCI P50 CA092131. J.J.A is supported by the National Cancer Institute award R01CA251245, the Pacific Northwest Prostate Cancer Specialized Programs of Research Excellence (SPORE) NCI P50 CA097186, the NCI Drug Resistance and Sensitivity Network NCI P50 CA186786-07S1, and the

Department of Defense Idea Award (W81XWH-20-1-0405). M.C.H. is supported by the U.S. Department of Defense Prostate Cancer Research Program (W81XWH-20-1-0111, W81XWH-21-1-0229) and Grant 2021184 from the Doris Duke Charitable Foundation. We thank UCLA Technology Center for Genomics & Bioinformatics, UCLA Metabolomics Center, UCLA MCDB/BSCRC Microscopy Core. N.M.N. is supported by NCI U01 CA224044-03. The UCLA Integrated Technologies Core is supported by CURE/P30 DK041301. We thank Michaela Veliova, Thomas Graeber, Linsey Stiles, Matthew Rettig, Brigitte Gomperts, Paul Boutros and other collaborators who provided intellectual support and critical feedback during the course of this project.

Author Contributions:

P.D.C., J.M.G., A.E.J., N.M.N (Nunley), T.H., A.M.L.D., and M.J.B. conducted the experiments. P.D.C., A.E.J., A.S.D and A.S.G. designed the experiments, wrote and edited the manuscript. R.R.H. and H.Y. performed immunohistochemistry and provided pathology expertise and wrote the related methods section. A.P. and O.S.S. performed mitochondrial morphology quantification, provided metabolism expertise, and wrote the related methods section. J.L. and M.C.H. performed the DNA methylation analysis, and wrote the related methods section. N.M. and H.R.C. performed mass spectrometry on in vivo tumor metabolites, provided metabolism expertise and wrote the related methods section. X.G. and J.J.A. provided transformed data from the *Quigley et al* dataset and wrote the related methods section. A.Z. provided ChIP sequencing data, key cell lines, and wrote the related methods section. N.M.N (Navone) provided PDX models. A.S.G. procured funding and supervised the experiments.

Competing Interests Statement:

The authors declare no competing interests.

Figure 1

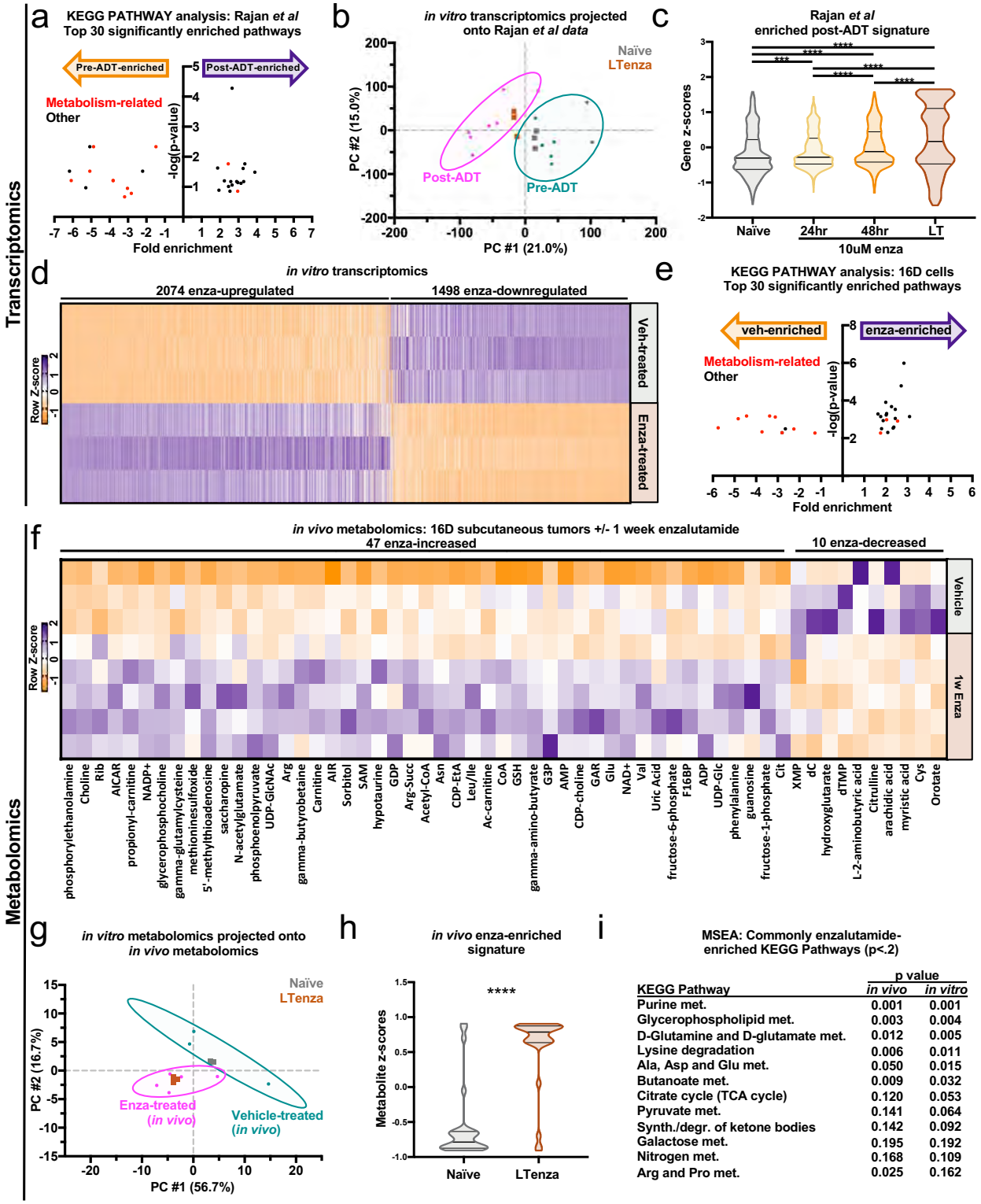

KEGG Pathway	p value *in vivo*	p value *in vitro*
Purine met.	0.001	0.001
Glycerophospholipid met.	0.003	0.004
D-Glutamine and D-glutamate met.	0.012	0.005
Lysine degradation	0.006	0.011
Ala, Asp and Glu met.	0.050	0.015
Butanoate met.	0.009	0.032
Citrate cycle (TCA cycle)	0.120	0.053
Pyruvate met.	0.141	0.064
Synth./degr. of ketone bodies	0.142	0.092
Galactose met.	0.195	0.192
Nitrogen met.	0.168	0.109
Arg and Pro met.	0.025	0.162

Figure 1. Transcriptomic and metabolic profiling identify AR-inhibition-induced metabolic reprogramming. (a) Top 30 significantly enriched pathways identified by KEGG PATHWAY analysis on differentially expressed (fold change ≥ 2, FDR < 0.2) *Rajan et al* pre-androgen deprivation therapy (Pre-ADT) and post-androgen deprivation therapy (Post-ADT) genes. Metabolism-related pathways highlighted in red. (b) Naïve and LTenza 16D transcriptomics data projected onto principle component analysis (PCA) plot of pre-ADT and post-ADT samples from *Rajan et al* data. 95% confidence eclipses for pre- and post-ADT data are shown in cyan and pink respectively. (c) Violin plot indicating gene z-scores of 1023 *Rajan et al* genes enriched post-ADT (fold change ≥ 2, FDR < 0.2) in naïve, 24hr enzalutamide-treated (enza), 48hr enza, and LTenza 16D cells. Data represent mean +/- SEM. (d) Heatmap of differentially expressed genes (fold change ≥ 2, FDR < 0.05) in LTenza 16D cells (Enza-treated) compared to naïve (Veh-treated) 16D cells. (e) Top 30 significantly enriched pathways identified by KEGG PATHWAY analysis on differentially expressed genes (fold change ≥ 2, FDR < 0.05) in naïve and LTenza 16D cells. Metabolism-related pathways highlighted in red. (f) Heatmap of differentially abundant metabolites (fold change ≥ 1.25, FDR < 0.2) in 1-week enzalutamide-treated 16D tumors compared to vehicle-treated 16D tumors. (g) *In vitro* naïve and LTenza 16D metabolomics data projected onto PCA plot of vehicle-treated and enza-treated samples from *in vivo 16D* metabolomics. 95% confidence eclipses for vehicle- and enza-treated *in vivo* data are shown in cyan and pink respectively. (h) Violin plot indicating metabolite z-scores of 47 *in vivo* enza-enriched metabolites (fold change ≥ 1.25, FDR < 0.2) in naïve and LTenza 16D cells. Data represent mean +/- SEM. (i) Metabolite Set Enrichment Analysis (MSEA) on *in vivo* enzalutamide-enriched metabolites (fold change ≥ 1.25, FDR < 0.2) and *in vitro* enzalutamide-enriched metabolites (fold change ≥ 1.25, FDR < 0.05) identifies commonly-enriched KEGG pathways (p<.2). P-values were calculated from an unpaired t-test with Welch's correction (c and h) and a Fisher's Exact Test (i). ***p < 0.001, ****p < 0.0001.

Figure 2

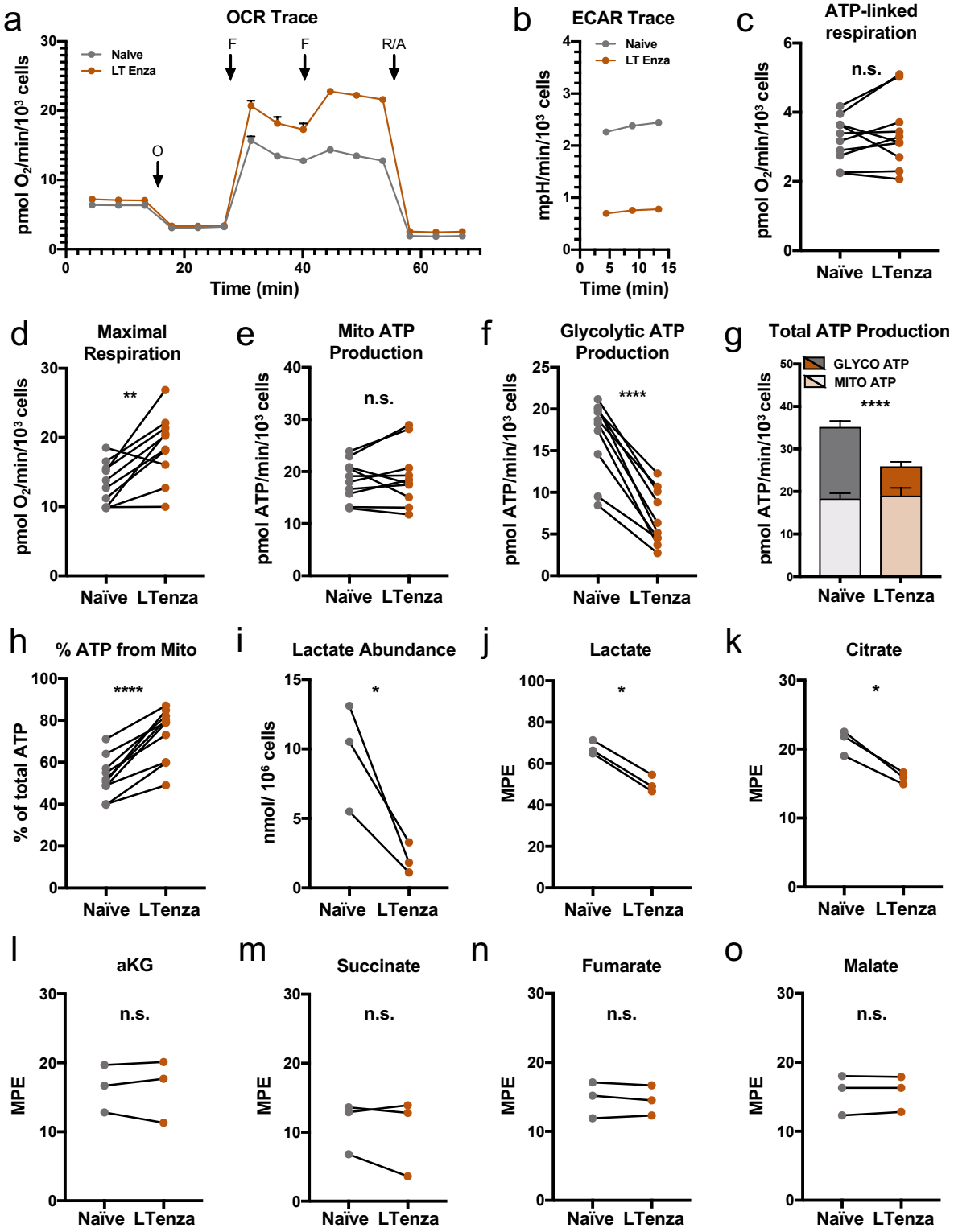
a
OCR Trace
Naive
LT Enza
F
F
R/A
O
pmol O2/min/10³ cells
Time (min)
b
ECAR Trace
Naive
LT Enza
mpH/min/10³ cells
Time (min)
c
ATP-linked respiration
n.s.
pmol O2/min/10³ cells
Naïve LTenza
d
Maximal Respiration
**
pmol O2/min/10³ cells
Naïve LTenza
e
Mito ATP Production
n.s.
pmol ATP/min/10³ cells
Naïve LTenza
f
Glycolytic ATP Production
****
pmol ATP/min/10³ cells
Naïve LTenza
g
Total ATP Production
GLYCO ATP
MITO ATP
****
pmol ATP/min/10³ cells
Naïve LTenza
h
% ATP from Mito
****
% of total ATP
Naïve LTenza
i
Lactate Abundance
*
nmol/ 10⁶ cells
Naïve LTenza
j
Lactate
*
MPE
Naïve LTenza
k
Citrate
*
MPE
Naïve LTenza
l
aKG
n.s.
MPE
Naïve LTenza
m
Succinate
n.s.
MPE
Naïve LTenza
n
Fumarate
n.s.
MPE
Naïve LTenza
o
Malate
n.s.
MPE
Naïve LTenza

Figure 2. AR blockade maintains oxidative mitochondrial metabolism and reduces glycolysis. (a and b) Representative kinetic trace plots of the Oxygen Consumption Rate (OCR) (a) and Extracellular Acidification Rate (ECAR) (b) of naïve and LTenza 16D cells. Treatment with Oligomycin (O), FCCP (F), Rotenone and Antimycin A (R/A) are indicated with arrows. Data represent mean +/- SEM. (c and d) ATP-linked respiration (c) and maximal respiration (d) of naïve and LTenza 16D cells from 10 biological replicate experiments. (e and f) Mitochondrial (Mito) ATP production (e) and glycolytic ATP production (f) of naïve and LTenza 16D cells from 10 biological replicate experiments. (g) Total ATP production as the sum of mitochondrial ATP production (Mito ATP) and glycolytic ATP production (Glyco ATP) of naïve and LTenza 16D cells from 10 biological replicate experiments. Statistics refer to comparison of total ATP levels. Data represent mean + SEM. (h) Percentage of total ATP production from mitochondrial ATP production (% ATP from Mito) of naïve and LTenza 16D cells from 10 biological replicate experiments. (i) Lactate abundance in naïve and LTenza 16D cells from 3 biological replicate experiments. (j - o) Moles percent enrichment (MPE) of U-$13C_6$-labeled glucose in lactate (j), citrate (k), alpha-ketoglutarate (aKG) (l), succinate (m), fumarate (n), and malate (o) in naïve and LTenza 16D cells from 3 biological replicate experiments. P-values were calculated from a ratio paired t-test. *$p < 0.05$, **$p < 0.01$, ****$p < 0.0001$, n.s. = not significant, $p \geq 0.05$.

Figure 3

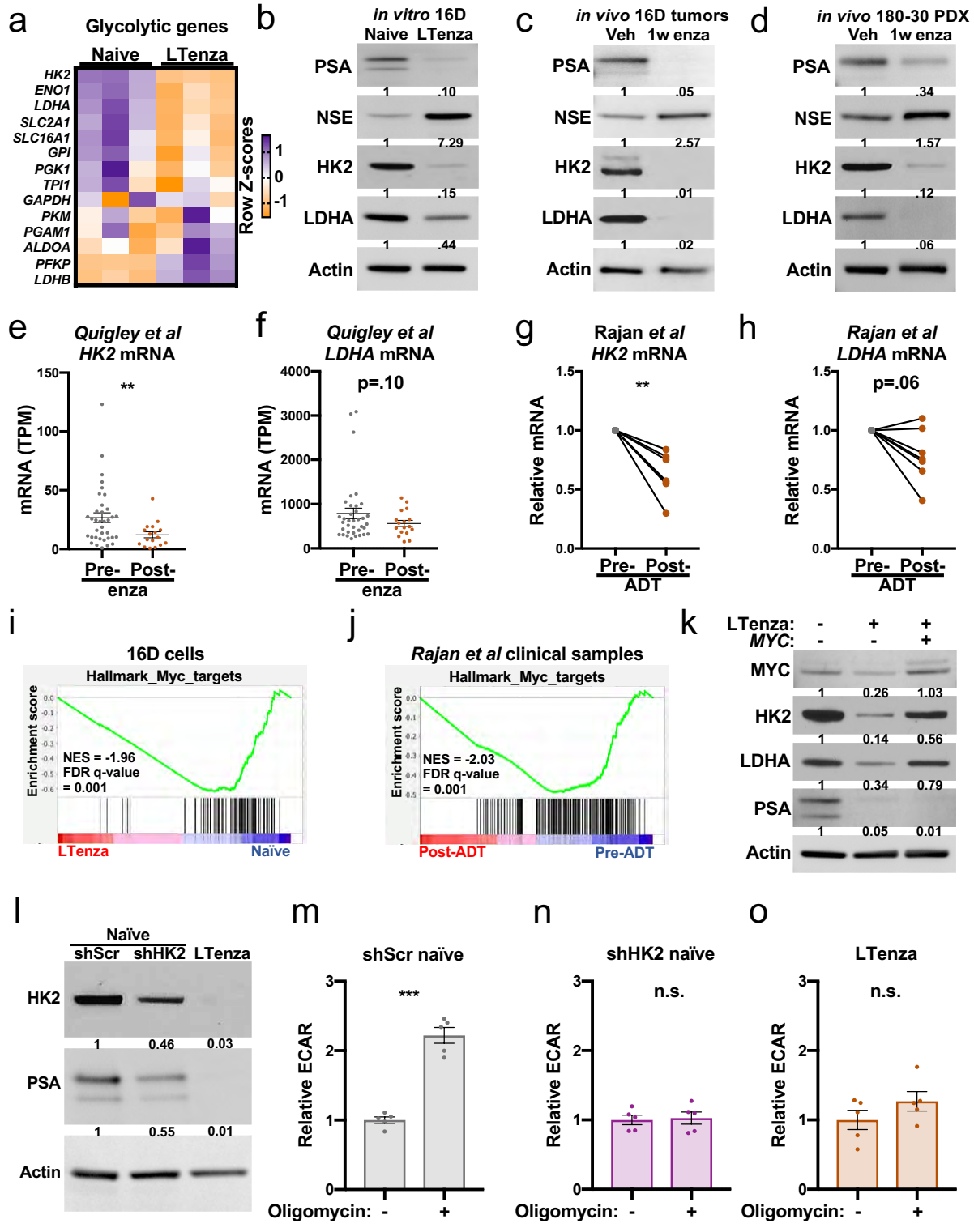
a
Glycolytic genes
Naive
LTenza
HK2
ENO1
LDHA
SLC2A1
SLC16A1
GPI
PGK1
TPI1
GAPDH
PKM
PGAM1
ALDOA
PFKP
LDHB
Row Z-scores
1
0
-1
b
in vitro 16D
Naive LTenza
PSA
NSE
HK2
LDHA
Actin
1 .10
1 7.29
1 .15
1 .44
c
in vivo 16D tumors
Veh 1w enza
PSA
NSE
HK2
LDHA
Actin
1 .05
1 2.57
1 .01
1 .02
d
in vivo 180-30 PDX
Veh 1w enza
PSA
NSE
HK2
LDHA
Actin
1 .34
1 1.57
1 .12
1 .06
e
Quigley et al
HK2 mRNA
mRNA (TPM)
**
Pre- Post-
enza
f
Quigley et al
LDHA mRNA
mRNA (TPM)
p=.10
Pre- Post-
enza
g
Rajan et al
HK2 mRNA
Relative mRNA
**
Pre- Post-
ADT
h
Rajan et al
LDHA mRNA
Relative mRNA
p=.06
Pre- Post-
ADT
i
16D cells
Hallmark_Myc_targets
Enrichment score
NES = -1.96
FDR q-value
= 0.001
LTenza
Naïve
j
Rajan et al clinical samples
Hallmark_Myc_targets
Enrichment score
NES = -2.03
FDR q-value
= 0.001
Post-ADT
Pre-ADT
k
LTenza:
MYC:
MYC
HK2
LDHA
PSA
Actin
1 0.26 1.03
1 0.14 0.56
1 0.34 0.79
1 0.05 0.01
l
Naïve
shScr shHK2 LTenza
HK2
PSA
Actin
1 0.46 0.03
1 0.55 0.01
m
shScr naïve
Relative ECAR
***
Oligomycin:
n
shHK2 naïve
Relative ECAR
n.s.
Oligomycin:
o
LTenza
Relative ECAR
n.s.
Oligomycin:

Figure 3. HK2 downregulation after AR inhibition contributes to reduced glycolytic capacity. (a) Heatmap showing the mRNA expression of glycolytic genes from RNA sequencing of 3 technical replicates of naïve and LTenza 16D cells. (b-d) Western blots indicating the expression of PSA, NSE, HK2, LDHA, and Actin (control) in lysates from naïve and LTenza 16D cells cultured *in vitro* (b), vehicle (veh) and 1-week enzalutamide-treated (1w enza) 16D tumors *in vivo* (c), and veh and 1w enza 180-30 patient derived xenografts *in vivo* (180-30 PDX) (d). (e and f) *HK2* (e) and *LDHA* (f) mRNA expression in unmatched enzalutamide-naïve (Pre-enza) and enzalutamide-treated (Post-enza) metastatic CRPC biopsies from *Quigley et al* dataset. Data represent the mean +/- SEM. (g and h) *HK2* (g) and *LDHA* (h) mRNA expression in matched pre- and post-androgen deprivation therapy (ADT) biopsies from the *Rajan et al* dataset. (i and j) GSEA of Hallmark_Myc_targets in naïve and LTenza 16D cells (i), and *Rajan et al* pre-ADT and post-ADT samples (j) showing normalized enrichment scores (NES) and false discovery rates (FDR). (k) Western blot indicating expression of MYC, HK2, LDHA, PSA, and Actin (control) in naïve (-/-), RFP-transduced LTenza (+/-), and MYC-transduced (+/+) LTenza 16D lysates. (l) Western blot detecting HK2, PSA and Actin (control) in shScr-transduced naïve, shHK2-transduced naïve, and LTenza 16D lysates. (m - o) Relative Extracellular Acidification Rate (ECAR) of shScr-transduced naïve (m), shHK2-transduced naïve (n), and LTenza 16D cells (o) treated +/- Oligomycin. Data represent the mean +/- SEM of 5 technical replicates from a representative experiment (n=2). P-values were calculated from an unpaired t-test with Welch's correction (e, f, m, n, and o) and a ratio paired t-test (g and h). $^{**}p < 0.01$, $^{***}p < 0.001$, n.s. = not significant, $p \geq 0.05$.

Figure 4

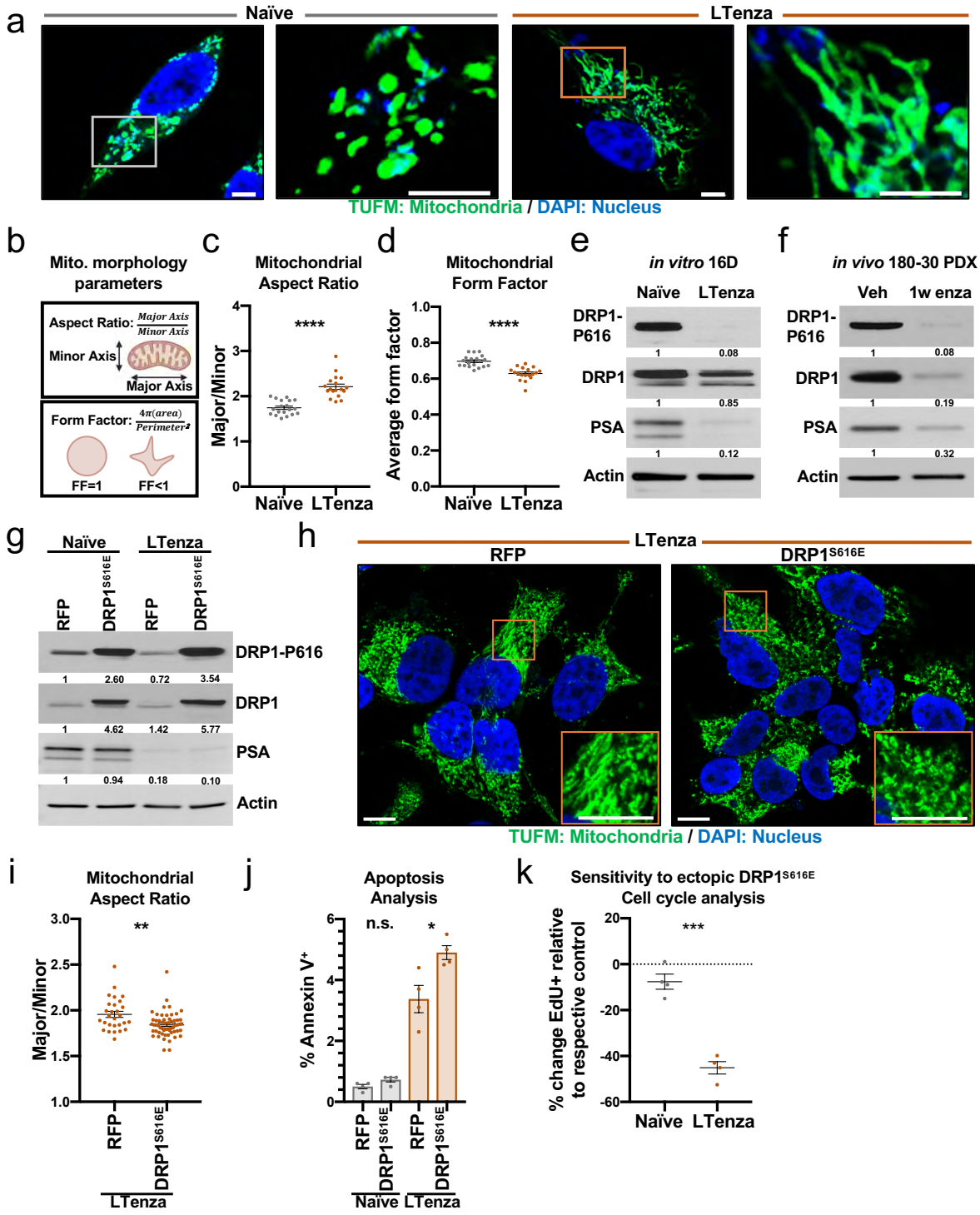
a
Naïve
LTenza
TUFM: Mitochondria / DAPI: Nucleus
b
Mito. morphology parameters
Aspect Ratio: Major Axis / Minor Axis
Minor Axis
Major Axis
Form Factor: 4π(area) / Perimeter²
FF=1
FF<1
c
Mitochondrial Aspect Ratio
Major/Minor
****
Naïve LTenza
d
Mitochondrial Form Factor
Average form factor
****
Naïve LTenza
e
in vitro 16D
Naïve LTenza
DRP1-P616
DRP1
PSA
Actin
f
in vivo 180-30 PDX
Veh 1w enza
DRP1-P616
DRP1
PSA
Actin
g
Naïve LTenza
RFP DRP1S616E RFP DRP1S616E
DRP1-P616
DRP1
PSA
Actin
h
LTenza
RFP
DRP1S616E
TUFM: Mitochondria / DAPI: Nucleus
i
Mitochondrial Aspect Ratio
Major/Minor
**
RFP DRP1S616E
LTenza
j
Apoptosis Analysis
% Annexin V+
n.s.
*
RFP DRP1S616E RFP DRP1S616E
Naïve LTenza
k
Sensitivity to ectopic DRP1S616E
Cell cycle analysis
% change EdU+ relative to respective control
***
Naïve LTenza

Figure 4. AR blockade elongates mitochondria via reduced DRP1 activity. (a) Representative immunofluorescent images of naïve and LTenza 16D cells stained for TUFM (green) and DAPI (blue). Scale bars, 5 μm. (b) Schematic illustrating calculation of aspect ratio and form factor. (c and d) Quantification of mitochondrial aspect ratio (c) and mitochondrial form factor (d) from TUFM stains from 20 images per treatment group. Data represent the mean +/- SEM. (e and f) Western blots detecting DRP1 phosphorylation at S616 (DRP1-P616), DRP1, PSA, and Actin (control) in naïve and LTenza 16D lysates (e), and vehicle (veh) and 1-week enzalutamide-treated (1w enza) 180-30 PDX tumor lysates (f). (g) Western blot indicating DRP1-P616, DRP1, PSA, and Actin (control) expression in lysates from RFP- or $DRP1^{S616E}$-transduced naïve and LTenza 16D cells. (h) Representative immunofluorescent images of RFP- and $DRP1^{S616E}$-transduced LTenza 16D cells stained for TUFM (green) and DAPI (blue). Scale bars, 10 μm. (i) Quantification of mitochondrial aspect ratio from TUFM stains from at least 28 cells per treatment group. Data represent the mean +/- SEM. (j) Apoptosis analysis to identify the percentage of Annexin V-positive cells (% Annexin V^+) in each transduced line after 48 hours of culture. Data represent the mean +/- SEM of 4 technical replicates. (k) Cell cycle analysis to quantify the relative sensitivity of naïve and LTenza 16D cells to ectopic $DRP1^{S616E}$ expression. Data represent the mean +/- SEM of 4 technical replicates from a representative experiment (n=2). P-values were calculated from an unpaired t-test with Welch's correction. *$p < 0.05$, **$p < 0.01$, ***$p < 0.001$, ****$p < 0.0001$, n.s. = not significant, $p \geq 0.05$.

Figure 5

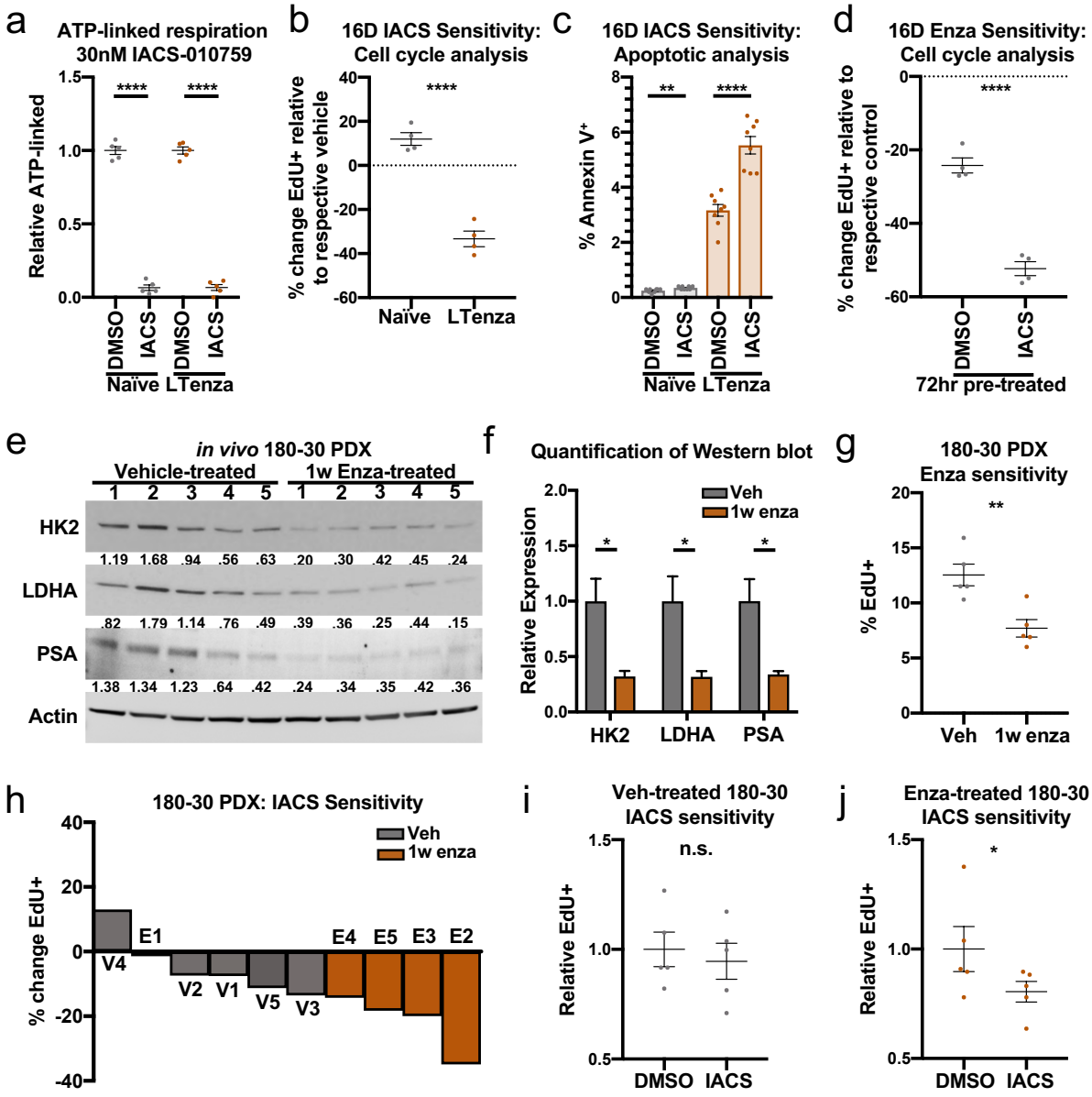
a
ATP-linked respiration
30nM IACS-010759
Relative ATP-linked
DMSO
IACS
Naïve LTenza
b
16D IACS Sensitivity:
Cell cycle analysis
% change EdU+ relative to respective vehicle
Naïve LTenza
c
16D IACS Sensitivity:
Apoptotic analysis
% Annexin V+
Naïve LTenza
d
16D Enza Sensitivity:
Cell cycle analysis
% change EdU+ relative to respective control
72hr pre-treated
e
in vivo 180-30 PDX
Vehicle-treated
1w Enza-treated
HK2
LDHA
PSA
Actin
f
Quantification of Western blot
Relative Expression
Veh
1w enza
HK2
LDHA
PSA
g
180-30 PDX
Enza sensitivity
% EdU+
Veh
1w enza
h
180-30 PDX: IACS Sensitivity
% change EdU+
Veh
1w enza
E1
E2
E3
E4
E5
V1
V2
V3
V4
V5
i
Veh-treated 180-30
IACS sensitivity
n.s.
Relative EdU+
DMSO
IACS
j
Enza-treated 180-30
IACS sensitivity
Relative EdU+
DMSO
IACS

Figure 5. AR blockade enhances sensitivity to complex I inhibition. (a) ATP-linked respiration of naïve and LTenza 16D cells treated with vehicle (DMSO) or 30nM IACS-010759 (IACS) for 24 hrs. Data represent the mean +/- SEM of 5 technical replicates. (b) Cell cycle analysis to quantify the relative sensitivity of naïve and LTenza 16D cells to 30nM IACS. Data represent the mean +/- SEM of 4 technical replicates from a representative experiment (n=3). (c) Apoptosis analysis to identify the percentage of Annexin V-positive cells (% Annexin V^+) in naïve and LTenza 16D cells treated with DMSO or 30nM IACS for 48 hours. Data represent the mean +/- SEM of 8 technical replicates. (d) Cell cycle analysis to quantify the relative sensitivity of DMSO- and 72hr 30nM IACS-treated naïve 16D cells to enzalutamide. Data represent the mean +/- SEM of 4 technical replicates. (e and f) Western blot detecting HK2, LDHA, PSA, and Actin (control) expression in lysates from 5 vehicle-treated and 5 1-week enzalutamide-treated 180-30 PDX tumors (e) and associated quantification (f). Data represent the mean +/- SEM. (g) Cell cycle analysis to quantify the proliferation (% EdU^+) of vehicle-treated (veh) and 1w enza-treated 180-30 tumors after 3-day *ex vivo* culture in organoid conditions. Data represent the mean +/- SEM of 5 tumor samples per treatment group. (h) Waterfall plot indicating the *ex vivo* sensitivity of 180-30 PDX tumor tissue from veh- and 1w enza-treated tumors to 30nM IACS. Data represent the percent change in EdU positivity (% change EdU^+) relative to the respective vehicle. (i and j) Cell cycle analysis of the sensitivity of vehicle-treated (i) or enza-treated (j) 180-30 PDX tumor tissue to *ex vivo* culture +/- 30nM IACS. Data represent the mean +/- SEM of 5 tumor samples per treatment group. P-values were calculated from an unpaired t-test with Welch's correction (a-d, f and g) and a ratio paired t-test (i and j). *$p < 0.05$, **$p < 0.01$, ****$p < 0.0001$, n.s. = not significant, $p \geq 0.05$.

Supplementary Figure 1 (related to Figure 1)

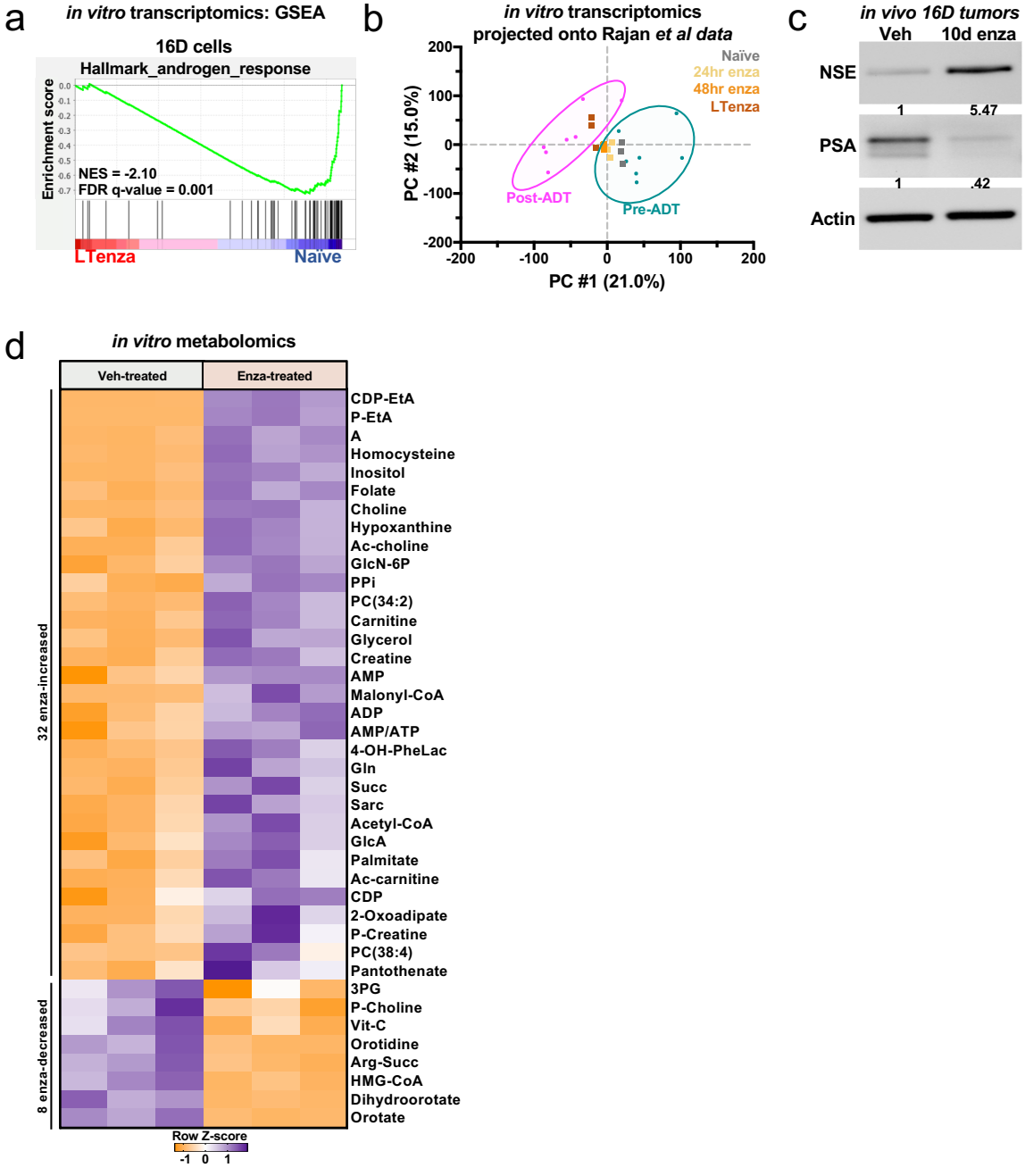

Supplementary Figure 1. Validation of *in vitro* 16D model, *in vivo* enzalutamide delivery and heatmap from *in vitro* metabolomics. (a) Gene Set Enrichment Analysis (GSEA) of Hallmark_androgen_response genes in naïve and LTenza 16D cells showing normalized enrichment score (NES) and false discovery rate (FDR). (b) Naïve, 24hr enzalutamide-treated (enza), 48hr enza, and LTenza 16D transcriptomics data projected onto principle component analysis (PCA) plot of pre-androgen deprivation therapy (pre-ADT) and post-ADT samples from *Rajan et al* data. (c) Western blot analysis of NSE, PSA, and Actin (loading control) in lysates from vehicle-treated (Veh) and 10-day (10d) enzalutamide-treated subcutaneous 16D tumors. (d) Heatmap of differentially abundant metabolites (fold change ≥ 1.25, FDR < 0.05) in LTenza 16D cells (Enza-treated) compared to naïve (Veh-treated) 16D cells.

Supplementary Figure 2 (related to Figure 3)

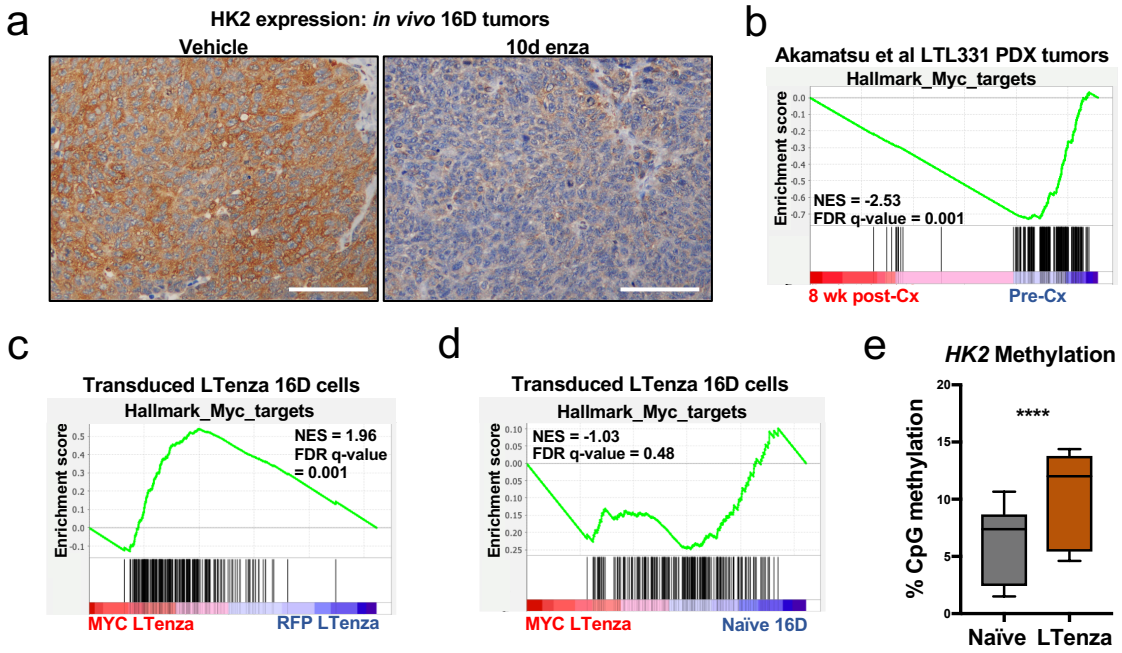

Supplementary Figure 2. Reduced MYC activity and reduced glycolysis through HK2 downregulation in anti-androgen treated cells. (a) 3, 3'-diaminobenzidine staining indicates HK2 expression in representative tissue sections from vehicle- and 10-day enzalutamide-treated (10d enza) 16D tumors. Scale bars, 100μm. (b) GSEA of Hallmark_Myc_targets in pre-castration (pre-Cx) and 8-week post-castration (8 wk post-Cx) LTL331 tumor samples from the *Akamatsu et al* dataset. (c) GSEA of Hallmark_Myc_targets in RFP-transduced LTenza (RFP LTenza) and MYC-transduced LTenza (MYC LTenza) 16D cells. (d) GSEA of Hallmark_Myc_targets in naïve 16D and MYC LTenza 16D cells. (e) Mean percentage of methylated CpGs within the *HK2* locus of naïve and LTenza 16D cells. (f) Oligomycin-stimulated Extracellular Acidification Rate (ECAR) of shScr-transduced naïve, shHK2-transduced naïve, and LTenza 16D cells. Data represent the mean +/- SEM of 5 technical replicates from a representative experiment (n=2). Significance was evaluated (b-d) using normalized enrichment scores (NES) and false discovery rates (FDR). P-values were calculated from an unpaired t-test with Welch's correction (e and f). **$p < 0.01$, ****$p < 0.0001$.

Supplementary Figure 3 (related to Figure 4)

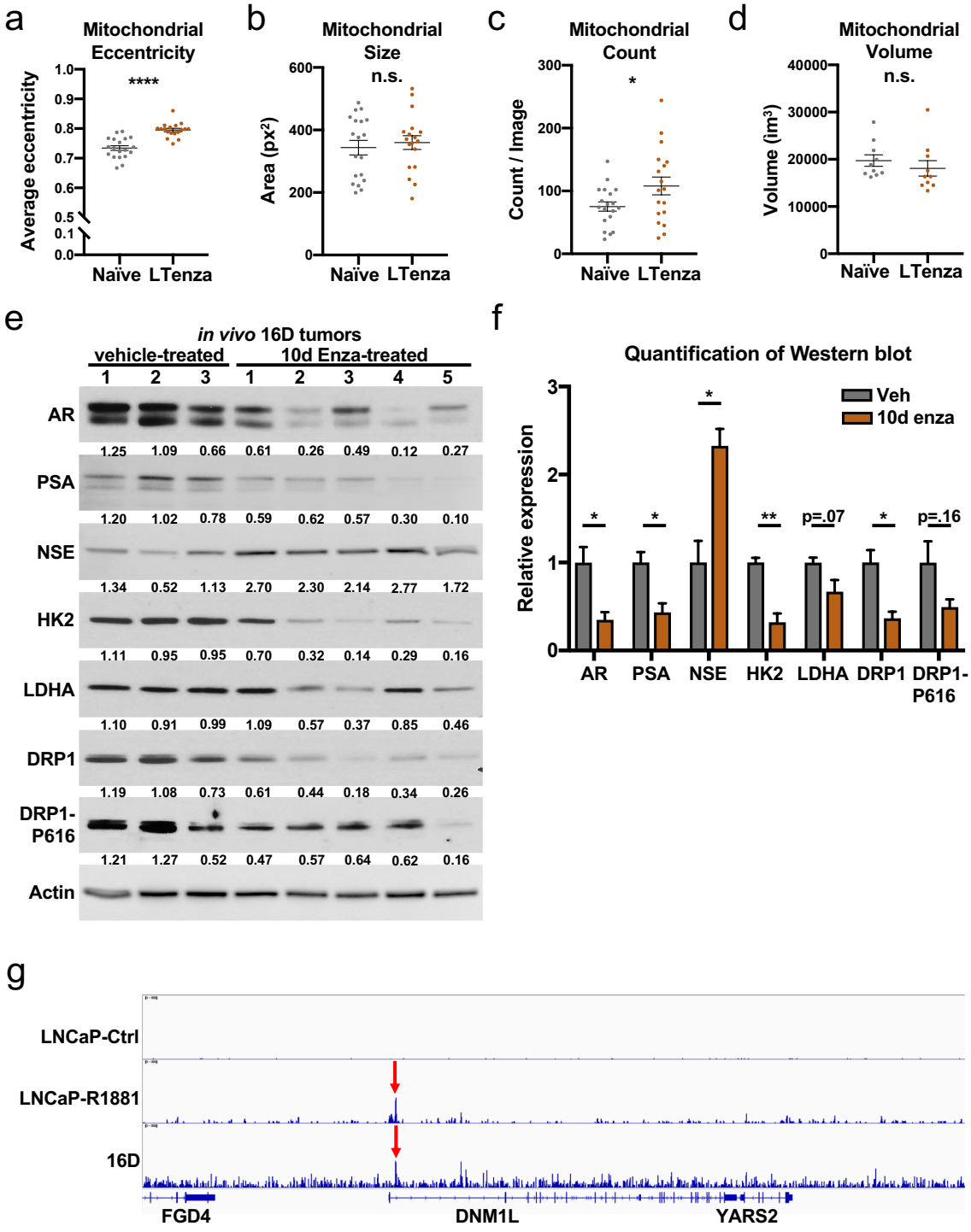

Supplementary Figure 3. Quantification of mitochondrial parameters in naïve and LTenza 16D cells and DRP1 expression in vehicle- and enzalutamide-treated 16D tumors. (a-c) Quantification of mitochondrial eccentricity (a), mitochondrial size (b), and mitochondrial count (c) from TUFM stains from 20 images of naïve or LTenza 16D cells. Data represent the mean +/- SEM. (d) Quantification of the mitochondrial volume of naïve and LTenza 16D cells from 3-dimensional reconstruction of 10 z-stack images per treatment group. Data represent the mean +/- SEM. (e and f) Western blot indicating AR, PSA, NSE, HK2, LDHA, DRP1, DRP1 phosphorylation at S616 (DRP1-P616), and Actin (control) expression in lysates from 3 vehicle-treated and 5 10-day enzalutamide-treated (10d Enza-treated) 16D tumors (e) and associated quantification (f). Data represent the mean +/- SEM. (g) AR binding of LNCaP-Ctrl, LNCaP-R1881 and 16D at the DNM1L genomic locus was analyzed by visualizing AR ChIP-seq bigwig tracks. Red arrow indicates sharp peak called by macs to demonstrate binding of AR. P-values were calculated from an unpaired t-test with Welch's correction. *$p < 0.05$, **$p < 0.01$, ****$p < 0.0001$, n.s. = not significant, $p \geq 0.05$.

Supplementary Figure 4 (related to Figure 5)

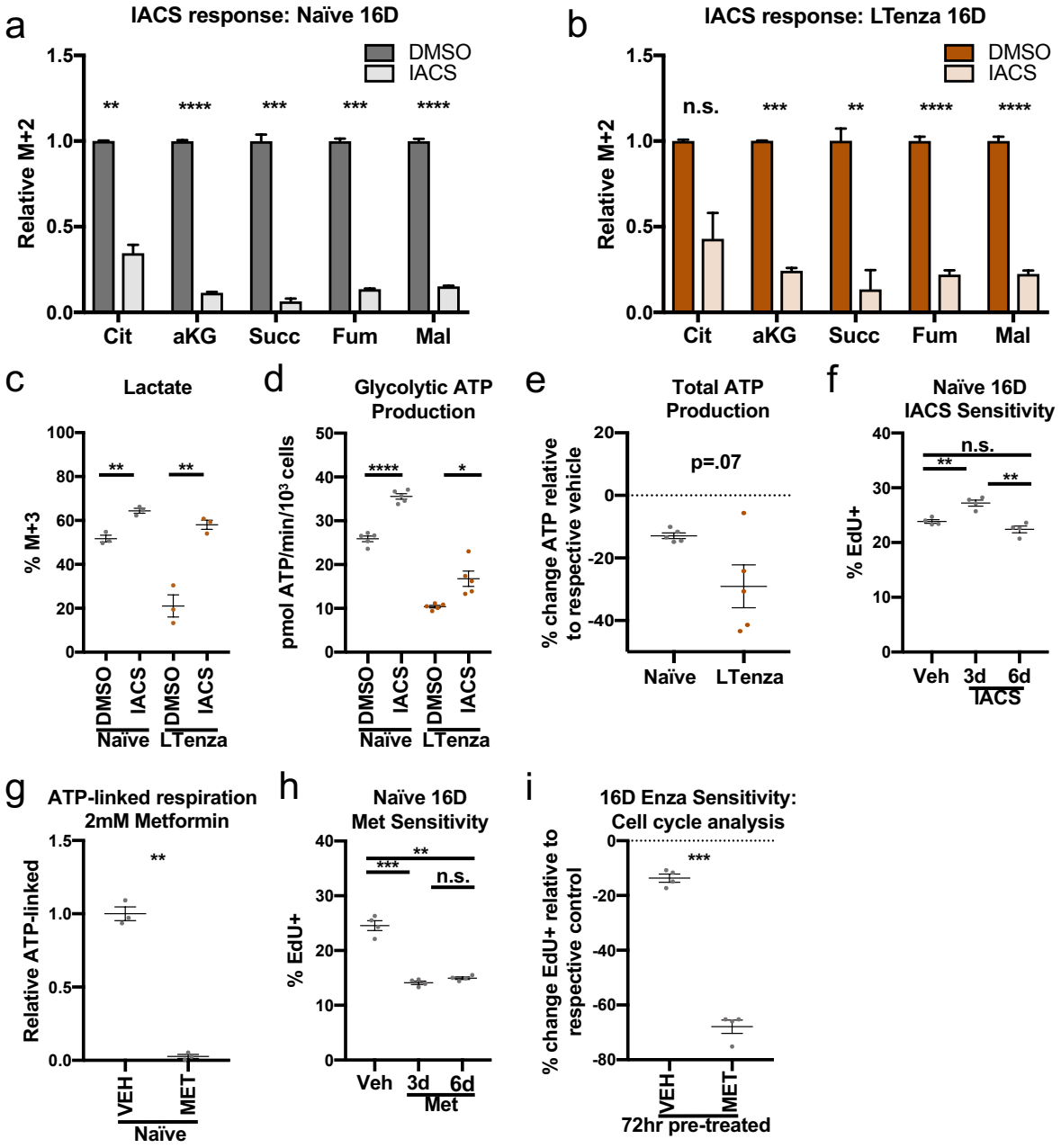

Supplementary Figure 4. Validation of complex I inhibitors and sensitivity of enzalutamide-treated cells to complex I inhibition. (a and b) Relative M+2-labeling of citrate (cit), alpha-ketoglutarate (aKG), succinate (succ), fumarate (fum), and malate after 24hr U-$13C_6$-glucose tracer analysis of DMSO- and 30nM IACS-010759-treated naïve (a) or LTenza 16D cells (b). Data represent the mean +/- SEM of 3 technical replicates. (c) Percentage of M+3-labeled lactate in naïve and LTenza 16D cells treated with DMSO or 30nM IACS for 24 hours. Data represent the mean +/- SEM of 3 technical replicates. (d) Glycolytic ATP production of naïve and LTenza 16D cells treated with DMSO or 30nM IACS for 24 hours. Data represent the mean +/- SEM of 5 technical replicates. (e) Relative sensitivity of the total ATP production of naïve and LTenza 16D cells to 30nM IACS. Data represent the mean +/- SEM of 5 technical replicates. (f) Cell cycle analysis measuring the proliferation (% EdU^+) of vehicle-, 3-day (3d), and 6d 30nM IACS-treated naïve 16D cells. Data represent the mean +/- SEM of 4 technical replicates from a representative experiment (n=3). (g) ATP-linked respiration of naïve 16D cells treated with DMSO or 2mM metformin (Met) for 24 hrs. Data represent the mean +/- SEM of 3 technical replicates. (h) Cell cycle analysis measuring the percentage of EdU^+ cells of vehicle-, 3d, and 6d 2mM Met-treated naïve 16D cells. Data represent the mean +/- SEM of 4 technical replicates. (i) Cell cycle analysis to quantify the relative sensitivity of DMSO- and 72hr 2mM Met-treated naïve 16D cells to enzalutamide. Data represent the mean +/- SEM of 4 technical replicates. P-values were calculated from an unpaired t-test with Welch's correction. *$p < 0.05$, **$p < 0.01$, ***$p < 0.001$, ****$p < 0.0001$, n.s. = not significant, $p \geq 0.05$.

Supplementary Figure 5 (related to Figure 5)

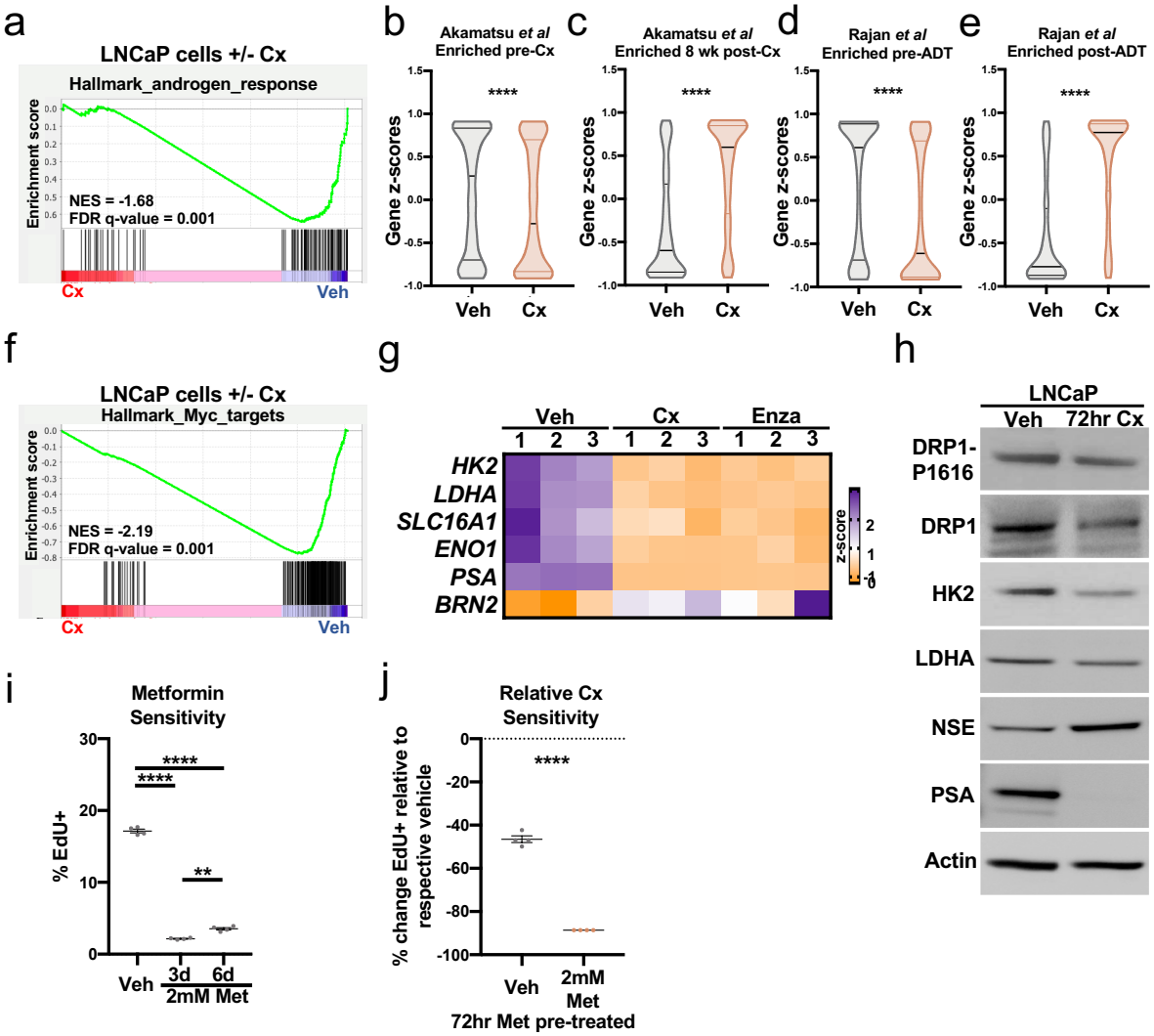

Supplementary Figure 5. AR inhibition-induced metabolic hallmarks are observed in LNCaP cells after castration. (a) GSEA of Hallmark_androgen_response genes in control (veh) and 72-hour castrated (Cx) LNCaP cells showing normalized enrichment score (NES) and false discovery rate (FDR). (b and c) Violin plots indicating gene z-scores of *Akamatsu et al* genes enriched pre-Cx (fold change ≥ 3, row mean > 1, 2710 genes) (b), or 8 weeks post-Cx (fold change ≥ 3, row mean > 1, 3371 genes) (c) in veh and 72-hour Cx LNCaP cells. Data represent mean +/- SEM. (d and e) Violin plots indicating gene z-scores of *Rajan et al* genes enriched pre-ADT (fold change ≥ 2, FDR < 0.2, 911 genes) (d) or post-ADT (fold change ≥ 2, FDR < 0.2, 1023 genes) (e) in veh and 72-hour Cx LNCaP cells. Data represent mean +/- SEM. (f) GSEA of Hallmark_Myc_targets genes in veh and 72-hour Cx LNCaP cells showing NES and FDR. (g) Heatmap showing the mRNA expression of select glycolytic genes from RNA sequencing of 3 technical replicates of veh, 72-hour Cx, and 72-hour enzalutamide-treated (enza) LNCaP cells. (h) Western blot detecting DRP1 phosphorylation at S616 (DRP1-P616), DRP1, HK2, LDHA, NSE, PSA, and Actin (control) in veh and 72-hour Cx LNCaP lysates. (i) Cell cycle analysis measuring the % EdU^+ cells of veh, 3-day (3d), and 6d 2mM metformin-treated (Met) LNCaP cells. Data represent the mean +/- SEM of 4 technical replicates. (j) Cell cycle analysis to quantify the relative sensitivity of veh and 72hr Met LNCaP cells to castration. Data represent the mean +/- SEM of 4 technical replicates. P-values were calculated from an unpaired t-test with Welch's correction. **p < 0.01, ****p < 0.0001.

Supplementary Figure 6

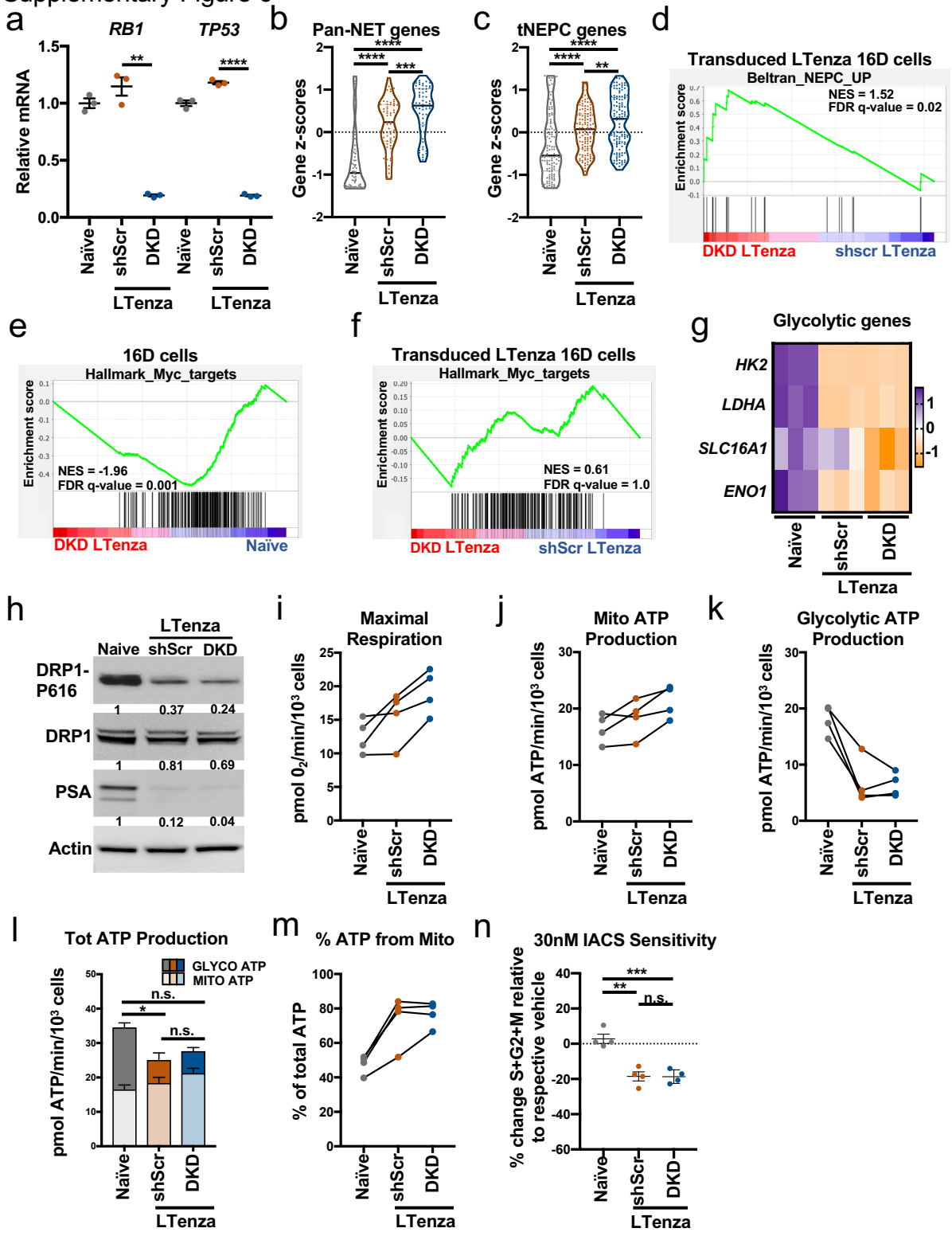

Supplementary Figure 6. AR inhibition-induced metabolic hallmarks are retained in enzalutamide-treated 16D cells after knockdown of *RB1* and *TP53*. (a) mRNA expression of *RB1* and *TP53* in naïve, shScr-transduced (shScr) LTenza, and shRB1_shTP53-transduced (DKD) LTenza 16D cells. Data represent the mean +/- SEM of 3 technical replicates. (b and c) Violin plots indicating gene z-scores of Pan-neuroendocrine tumor (Pan-NET) associated genes defined by *Guo et al* (b) and treatment-emergent small-cell neuroendocrine prostate cancer (tNEPC) associated genes (fold change ≥ 1.5, 330 genes) from the *Aggarwal et al* dataset (c) in naïve, shScr LTenza, and DKD LTenza 16D cells. Data represent mean +/- SEM. (d) GSEA of Beltran_NEPC_UP genes in DKD LTenza and shScr LTenza 16D cells. (e and f) GSEA of Hallmark_Myc_targets in DKD LTenza and naïve 16D cells (e), or DKD LTenza and shScr LTenza 16D cells (f). (g) Heatmap of select glycolytic genes from 3 technical replicates per line. (h) Western blot detecting DRP1 phosphorylation at S616 (DRP1-P616), DRP1, PSA, and Actin (control) in naïve, shScr LTenza, and DKD LTenza 16D lysates. (i-k) Maximal respiration (i), mitochondrial (Mito) ATP production (j), and glycolytic ATP production (k) in naïve, shScr LTenza, and DKD LTenza 16D cells from 4 biological replicate experiments. (l) Total ATP production, represented as the sum of mitochondrial ATP production (Mito ATP) and glycolytic ATP production (Glyco ATP), of naïve, shScr LTenza, and DKD LTenza 16D cells from 4 biological replicate experiments. Statistics refer to comparison of total ATP levels. Data represent mean +/- SEM. (m) Percentage of total ATP production from mitochondrial ATP production (% ATP from Mito) of naïve, shScr LTenza, and DKD LTenza 16D cells from 4 biological replicate experiments. (n) Relative sensitivity of the proliferation of naïve, shScr LTenza, and DKD LTenza 16D cells to 72-hour treatment with 30nM IACS. Significance was evaluated (d-f) using normalized enrichment scores (NES) and false discovery rates (FDR). P-values were calculated from an unpaired t-test with Welch's correction (a-c, l and n). *$p < 0.05$, **$p < 0.01$, ***$p < 0.001$, ****$p < 0.0001$, n.s. = not significant, $p \geq 0.05$.

Supplementary Figure 7

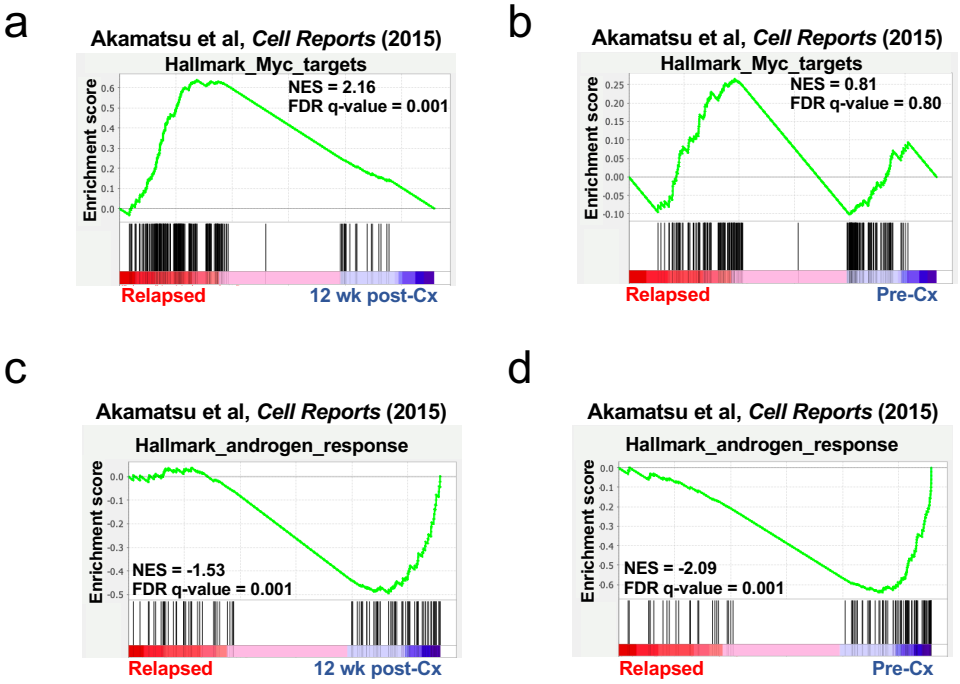

Supplementary Figure 7. MYC target gene expression is restored in LTL331 model of relapsed castration-resistant prostate cancer despite maintenance of low AR activity. (a and b) GSEA of Hallmark_Myc_targets in relapsed and 12-week post-castration (12 wk post-Cx) LTL331 tumor samples (a) and relapsed and pre-castration (Pre-Cx) samples (b) from the *Akamatsu et al* dataset. (c and d) GSEA of Hallmark_androgen_response genes in relapsed and 12 wk post-Cx LTL331 tumor samples (c) and relapsed and pre-Cx samples (d) from the *Akamatsu et al* dataset. Significance was evaluated (a-d) using normalized enrichment scores (NES) and false discovery rates (FDR).

MATERIALS AND METHODS

13C isotope tracing

Naïve and LTenza 16D cells were plated in 6-well dishes at 225,000 and 350,000 cells/well respectively. After 24 hours, cells were washed and cultured in a base RPMI supplemented with 10 mM uniformly labeled 13C6-glucose (Cambridge Isotope Laboratories), 10% (v/v) FBS, 2 mM glutamine, 100 units/mL penicillin, and 100 µg/mL streptomycin.

24 hours after the addition of U-$13C_6$-glucose, cells were harvested and extracted for GC/MS analysis using established methods[1]. Briefly, cell plates were placed on ice and quickly washed with ice-cold 0.9% (w/v) NaCl. Cells were immediately treated with 500 µL of ice-cold MeOH and 200 µL water containing 1 µg of the internal standard norvaline. Cells were then scraped and placed in 1.5 mL centrifuge tubes kept on ice. Next, 500 µL of chloroform was added, after which samples were vortexed for 1 min and then spun at 10,000*g* for 5 min at 4C. The aqueous layer was transferred to a GC/MS sample vial and dried overnight using a refrigerated CentriVap.

Once dry, samples were resuspended in 20 µL of 2% (w/v) methoxyamine in pyridine and incubated at 37C for 45 minutes. This was followed by addition of 20 µL of MTBSTFA + 1% TBDMSCl (Ntert-Butyldimethylsilyl-N-methyltrifluoroacetamide with 1% tertButyldimethylchlorosilane), mixing, and incubation for an additional 45 minutes at 37C. Samples were run as previously described[1], and analyzed using Agilent MassHunter software. Stable isotope tracing data was corrected for natural abundance of heavy isotopes with FluxFix software using a reference set of unlabeled metabolite standards[2].

Animal work

All animal work was performed using IACUC approved protocols under the supervision of veterinarians from the Division of Laboratory Animal Medicine at UCLA. 7 million 16D cells were implanted subcutaneously with 100 µl Matrigel (Corning) into NSG mice to form primary tumors. Primary tumors were harvested, minced, and re-implanted (20 - 80 mg of minced tumor tissue with 100ul Matrigel per mouse) into NSG mice. 16D tumor-bearing mice were treated by oral gavage with 10 mg/kg/day of enzalutamide in the vehicle (1% carboxymethyl cellulose, 0.5% Tween 80, and 5% dimethylsulfoxide) or the vehicle only, with a two-days-on/one-day-off schedule. Tumors were collected after 10 days of treatment and prepared for histology, protein extraction, and metabolite extraction. 180-30 PDX tumors were maintained by serial implantation of 20 - 80 mg of minced tumor tissue. Treatment with vehicle or enzalutamide was initiated one week after implantation and performed using the approach described above. Tumors were collected after 7 days of treatment and prepared for protein extraction and *ex vivo* organoid culture.

Apoptosis analysis

Cells were seeded at 40 percent confluence and cultured in 6-well dishes for 48 hours prior to apoptosis analysis. No media changes were performed to preserve all material. Cell culture media and wash media were collected and pooled with quenched trypsin-containing media containing cells and apoptosis analysis was performed using an

apoptosis detection kit (BioLegend, 640922) according to the provided protocol. Flow cytometry was performed to quantify the percentage of annexin V^+ cells. In experiments using transduced lines, analysis was restricted to the transduced cells which were identified via flow cytometry by analyzing RFP florescence.

Bioenergetic assays

Oxygen consumption and extracellular acidification rates were measured using an Agilent Seahorse XF96 or XF^e96 Analyzer. Briefly, 16D prostate cancer cells were plated at 40,000 cells/well in XF96 plates for 24 hours. At the time of experiment, tissue culture growth medium was replaced with assay medium consisting of unbuffered DMEM (Sigma, 5030) supplemented with 10mM glucose, 2mM pyruvate, 2mM glutamine, and 5mM HEPES. Respiration was measured at baseline and in response to acute treatment with 2 μM oligomycin, FCCP (two sequential pulses of 500nM), and 0.2μM rotenone with 1 μM antimycin A. All respiratory parameters were calculated as previously described in[3]. Where indicated, cells were treated with 5μM UK5099, 5μM etomoxir, or 1μM CB-839 15 minutes prior to recording the initial measurements.

Rates of ATP produced from oxidative phosphorylation and glycolysis were calculated as previously described[4]. Mitochondrial ATP production rates were determined by stoichiometric conversion of the ATP-linked respiration rate, and glycolytic ATP production rates were measured by correcting rates of extracellular acidification for the scaling factor of the microplate sensor coverage and confounding respiratory acidification. Where indicated, cells were treated with 2 μM oligomycin 15 minutes prior to recording the initial measurements.

Cell cycle analysis

Cells were seeded at 30 percent confluence and cultured in 6-well dishes for 72 hours prior to cell cycle analysis. Media changes were performed 48 hours after plating. After 72 hours of culture, cell cycle analysis was performed using a 5-ethynyl-2'-deoxyuridine-based (EdU) kit (ThermoFisher, C10635) according to the specified protocol. EdU labeling was performed for 2 hours in LNCaP and 16D cells, and for 5 hours in 180-30 PDX organoids. For experiments that contained small molecule inhibitors, fresh inhibitor(s) were adding during each media change. PDX 180-30 organoids were dissociated after EdU labeling prior to fixation for cell cycle analysis. In select experiments, the 1ug/ml Hoechst 33342 DNA stain (ThermoFisher, 62249) was added prior to flow cytometry analysis to identify G2 and M phase cells. Flow cytometry analysis identified the percentage of EdU-positive and/or Hoechst-positive cells. For experiments with transduced lines, analysis was restricted to the RFP-positive transduced cells.

Cell lines, lentiviral transductions, and cloning of knockdown vectors

Cell lines were routinely tested for mycoplasma and authentication by short tandem repeat analysis (Laragen). Tissue culture plates were coated with 0.01% (v/v) Poly-L-Lysine (Sigma, P4832) diluted 1/20 in distilled water and washed with PBS to enhance cell attachment. 16D and LNCaP cells were cultured in RPMI base media (Gibco) + 10% FBS (v/v) + 100 units/mL penicillin, and 100 μg/mL streptomycin. Enzalutamide treatment was performed by adding 10uM enzalutamide (Selleck Chemicals, S1250) every 48

hours. For LNCaP castration experiments, LNCaP cells were grown in RPMI base media + 10% CSS (v/v) (Sigma, F6765) + 100 units/mL penicillin, and 100 µg/mL streptomycin +/- 0.5nM DHT (Sigma) and fresh media was provided every 48 hours.

For lentiviral transductions, cells were seeded at 30-50% confluence. Transductions were performed 24-48 hours after seeding with 8ug/ml Polybrene (Fisher, NC0663391). Flow cytometry-based cell sorting was performed at least 72 hours after transduction to isolate color-tagged transduced cells.

MYC virus was produced using a plasmid vector FU-MYC-CRW[5]. Plasmid vectors for shHK2, and DRP1S616E were obtained from VectorBuilder. The target sequence for HK2 is TGACGACAGCATCATTGTTAA. shScramble (FU-shScr-CRW) and shRB1-shTP53 (FU-shTP35-shRB1-CRW) vectors were cloned as follows. First, the pBSPacI shuttle vector was made by inserting an adaptor oligonucleotide AG220: 5'-AATTCTTTAATTAAAG-3' at the EcoRI site of pBluescript II KS(+) (Stratagene). The pPass1 shuttle was cloned as follows. Annealed oligonucleotides AG232: 5'-CCTTAATTAAGCGATCGCACTGGGTACCTGGGCC-3' and AG233: 5'-CAGGTACCCAGTGCGATCGCTTAATTAAGGGTAC-3' were inserted between KpnI and ApaI sites of pBluescript II KS(+). Then, annealed oligonucleotides AG234: 5'-CTTAATTAAACTGGGGAGCTCCGC-3' and AG235: 5'-GGAGCTCCCCAGTTTAATTAAGAGCT-3' were inserted between SacI and SacII sites. This creates a PacI-AsiSI-[Multiple cloning sites]-PacI cassette. Annealed oligonucleotides AG218: 5'-GACGATGATTAATTAA-3', and AG220 (above) were ligated with KfiI-EcoRI fragment of shp53 pLO1 pure (Addgene) and inserted into PacI site in pBSPacI (pBSPacI-shTP53). PacI fragment of pBSPacI-shTP53 was then inserted into the AsiSI site in pPassI (pPass1-shTP53). The PacI-PacI fragment of FU-shRB1-AR-CGW was blunted and digested with HindIII creating a HindIII-blunt fragment of H1-shRB1 cassette. This cassette was inserted between HindIII and EcoRV sites in pPass1-shTP53 (pPass1-shTP53-shRB1). PacI fragment of pPass1-shTP53-shRB1 was then inserted into the PacI site of FU-CRW (FU-shTP53-shRB1-CRW). The U6-Scramble cassette was made by ligating annealed oligonucleotides AG227: 5'-CACCGAATTCTTCCATAGAGCTCGTCAAGAGCGAGCTCTATGGAAGAATTC-3' and AG228: 5'-AAAAGAATTCTTCCATAGAGCTCGCTCTTGACGAGCTCTATGGAAGAATTC-3' in pENTR/U6 vector (Invitrogen). Then, the BamHI-XbaI fragment was purified and inserted between BamHI and XbaI sites in pBSPacI (pBSPacI-shScr21A). The PacI fragment from pBSPacI-shScr21A was inserted at the PacI site in FU-CRW (FU-shScr-CRW). Concentrated viral aliquots were produced either by VectorBuilder or UCLA Integrated Molecular Technologies Core.

ChIP sequencing

AR ChIP-seq bigwig files were generated using deeptools program suite[6]. AR binding profiles of LNCaP-Ctrl, LNCaP-R1881[7], 16D[8] samples at genomic loci (namely LDHA, HK2 and DNM1L) were analyzed by visualizing AR ChIP-seq bigwig tracks using IGV[9].

DNA methylation analysis

Bisulfite sequencing was carried out as described previously[10]. In brief, genomic DNA was bisulfite converted using the EZ DNA methylation kit (Zymo Research, Orange, CA, USA) and amplified using primers specific to the promoter of HK2 (F-5′-AGTTGAGTTTTAGTGATTTTGTGGT -3′, R-5′-AACTTACCTTCTACACTTAATCATAATTAA -3). All PCR reactions were carried out in 40 µl volume containing 20 ng of bisulfite converted DNA, 1 × Platinum Taqbuffer (Invitrogen), 1.5 U Platinum Taq (Life Technologies), 250 µM each dNTPs, 1.5 mM MgCl2, 0.25 µg/µl bovine serum albumin, 2 µl dimethyl sulfoxide, 400 nM forward primer, and 400 nM reverse primer. Cycling conditions were 95C for 3 min, 36 cycles of 95C for 30 s, 55C for 30 s, and 72C for 30 s, followed by a 7 min extension step at 72C. PCR products were gel purified after electrophoresis on a 2% agarose gel. Amplicons were sequenced to an average coverage of 27,380x using established amplicon sequencing protocols (Azenta). Raw bisulfite amplicon sequencing fastq reads were first trimmed using Trim Galore version 0.6.6 and then aligned to UCSC hg19 reference genome using Bismark version 0.23.0[11]. Bismark was further used to deduplicate the alignments and extract methylation call files which report the percentage of methylated cytosines for each CpG dinucleotide.

Immunohistochemistry

16D tumor tissue from vehicle- and 10-day enzalutamide-treated mice was fixed with 4% paraformaldehyde in PBS for 6-8 hours and processed for paraffin sections. Tumor samples were color inked and formalin-fixed paraffin embedded. 3- to 4-µm thick sections were placed on charged slides for immunohistochemical staining that was carried out on Dako's Automated AS48Link Autostainer in SPORE Pathology Core laboratory at UCLA. Positive and negative control slides were pretreated with Heat Induced Epitope Retrieval (HIER) in Dako PT Link using the Envision FLEX Target Retrieval solution at low pH (6.0), and incubated at 97C for 15 minutes. Primary Rabbit anti-Human HK2 monoclonal antibody (Cell Signaling, 28675), clone C64G5, was added at a 1:600 dilution and incubated for 60 minutes at room temperature. Sections were then incubated for 5 minutes with the EnVision Flex+ Rabbit linker (Agilent, SM805) prior to a 5-minute treatment with the Polymer Flex/HRP (Agilent, SM802) reagent. Negative control slides received the Flex Rabbit Negative Control Immunoglobulin fraction (Agilent, IR600) instead of primary antibody. Slides were developed in Envision Flex DAB+Chromogen and counterstained with Mayer's hematoxylin.

***In vivo* metabolomics**

After tumor dissection, a maximum of 30mg of tissue was weighed, snap frozen, and stored at -80C until metabolite extraction. To extract metabolites, weighed tumor tissue was added to a bead tube (Fisher) containing 1ml 80% methanol plus 10mM potassium trifluoromethanesulfonate (TMSO) internal standard on ice. Samples were homogenized for 1 minute at max speed on a bead homogenizer (Fisher). Bead tubes were spun at 17000g at 4C for 10 minutes. The supernatant was transferred to an Eppendorf tube and spun at 17000g at 4C for 10 minutes. A volume of extraction equivalent to 3mg of tumor tissue was transferred to an ABC vial (Fisher). All volumes were normalized to 500ul with 80% methanol containing TMSO internal standard. 80% MeOH was evaporated from the

ABC vials using the EZ-2Elite evaporator (Genevac) and samples were stored at -80°C until analysis.

Dried metabolites were reconstituted in 100 µL of a 50% acetonitrile (ACN) 50% dH20 solution. Samples were vortexed and spun down for 10 min at 17,000g. 70 µL of the supernatant was then transferred to HPLC glass vials. 10 µL of these metabolite solutions were injected per analysis. Samples were run on a Vanquish (Thermo Scientific) UHPLC system with mobile phase A (20mM ammonium carbonate, pH 9.7) and mobile phase B (100% ACN) at a flow rate of 150 µL/min on a SeQuant ZIC-pHILIC Polymeric column (2.1 × 150 mm 5 µm, EMD Millipore) at 35°C. Separation was achieved with a linear gradient from 20% A to 80% A in 20 min followed by a linear gradient from 80% A to 20% A from 20 min to 20.5 min. 20% A was then held from 20.5 min to 28 min. The UHPLC was coupled to a Q-Exactive (Thermo Scientific) mass analyzer running in polarity switching mode with spray-voltage=3.2kV, sheath-gas=40, aux-gas=15, sweep-gas=1, aux-gas-temp=350°C, and capillary-temp=275°C. For both polarities mass scan settings were kept at full-scan-range=(70-1000), ms1-resolution=70,000, max-injection-time=250ms, and AGC-target=1E6. MS2 data was also collected from the top three most abundant singly-charged ions in each scan with normalized-collision-energy=35. Each of the resulting ".RAW" files was then centroided and converted into two ".mzXML" files (one for positive scans and one for negative scans) using msconvert from ProteoWizard[12]. These ".mzXML" files were imported into the MZmine 2 software package[13]. Ion chromatograms were generated from MS1 spectra via the built-in Automated Data Analysis Pipeline (ADAP) chromatogram module[14] and peaks were detected via the ADAP wavelets algorithm. Peaks were aligned across all samples via the Random sample consensus aligner module, gap-filled, and assigned identities using an exact mass MS1(+/-15ppm) and retention time RT (+/-0.5min) search of our in-house MS1-RT database. Peak boundaries and identifications were then further refined by manual curation. Peaks were quantified by area under the curve integration and exported as CSV files. If stable isotope tracing was used in the experiment, the peak areas were additionally processed via the R package AccuCor[15] to correct for natural isotope abundance. Peak areas for each sample were normalized by the measured area of the internal standard trifluoromethanesulfonate (present in the extraction buffer) and by the number of cells present in the extracted well.

***In vitro* metabolomic profiling**

Cells were seeded at 30 percent confluence and cultured in 6-well dishes for 72 hours prior to metabolite extractions. Media was aspirated and cells were washed with cold 150mM ammonium acetate pH 7.3. Metabolite extractions were performed by adding 500ul of cold 80% methanol containing 2nM Norvaline (Sigma) as an internal standard per well. Cells were removed using a cell scraper before transferring cell suspensions to 1.5ml Eppendorf tubes. Samples were vortexed for 30 seconds and spun at 4C for 5 minutes at maximum speed to pellet the insoluble fraction before 420ul of the soluble fraction was transferred to ABC vials (Fisher). 80% MeOH was evaporated from the ABC vials using the EZ-2Elite evaporator (Genevac) and samples were stored at -80°C until analysis.

Dried metabolites were resuspended in 50% ACN:water and 1/10th was loaded onto a Luna 3um NH2 100A (150 × 2.0 mm) column (Phenomenex). The chromatographic separation was performed on a Vanquish Flex (Thermo Scientific) with mobile phases A (5 mM NH4AcO pH 9.9) and B (ACN) and a flow rate of 200 µl/min. A linear gradient from 15% A to 95% A over 18 min was followed by 9 min isocratic flow at 95% A and reequilibration to 15% A. Metabolites were detection with a Thermo Scientific Q Exactive mass spectrometer run with polarity switching (+3.5 kV/− 3.5 kV) in full scan mode with an m/z range of 70-975 and 70.000 resolution. TraceFinder 4.1 (Thermo Scientific) was used to quantify the targeted metabolites by area under the curve using expected retention time and accurate mass measurements (< 5 ppm).

Normalization was performed by resuspending the insoluble fraction in 300ul of lysis solution (0.1M NaCl, 20mM Tris-HCl, 0.1% SDS, 5mM EDTA in distilled water) and proceeding with DNA measurement. Samples were syringed with a 25G needle to reduce viscosity and 50ul of each sample was transferred to a 96-well black wall clear bottom tissue culture plate (Corning). 50ul lysis solution was added to one well for a blank reading. 100ul of 5ug/ml Hoechst 33342 (Invitrogen) in distilled water was added to each well and 96-well plates were incubated for 30 minutes in the dark at 37C before measurement of DNA-based florescence using a Tecan Infinite M1000 plate reader with 355nm excitation and 465nm emission. The blank reading was subtracted from each absorbance value to calculate relative cell amount.

Organoid culture

Using a razor blade, individual tumors were mechanically dissociated in dissociation media comprised of RPMI-1640 containing 10% (v/v) fetal bovine serum, 100 units/mL penicillin, and 100 µg/mL streptomycin, 1mg/mL collagenase type I, 1mg/ml dispase, 0.1mg/mL deoxyribonuclease, and 10uM of the p160ROCK inhibitor Y-27632 dihydrochloride (Tocris Bioscience). When chunks were no longer visible, the samples were incubated at 37C on a nutating platform for 45 minutes in 10mL of dissociation media. After centrifugation at 800g for 5 min, the pellet was washed with 1x phosphate buffered saline. The cell pellet was resuspended in human organoid media[16] and passed through a 100um cell strainer. Growth factor reduced Matrigel (Corning) was added to the cell suspension at a final concentration of 75% before plating into rings in 24-well plates. After Matrigel rings solidified at 37C for 1 hour, 500ul human organoid media was added to each well. Each vehicle- and enzalutamide-treated sample was cultured +/- 30nM IACS-010759 (ChemieTek) for 72 hours.

RNA sequencing

RNA was extracted from samples using the RNeasy Mini Kit (QIAGEN). Library preparation was performed using the KAPA Stranded mRNA-Seq Kit (Roche). The workflow consists of mRNA enrichment, cDNA generation, and end repair to generate blunt ends, A-tailing, adaptor ligation, and PCR amplification. Different adaptors were used for multiplexing samples in one lane. The Illumina HiSeq 3000 was used to perform sequencing for 1x50 run.

Visualization of mitochondria

Cells were cultured in μ-Slide Well (Ibidi) and fixed with 4% PSA/PBS for 2 minutes. After washing with PBS, cells were stained with anti-TUFM (Atlas Antibodies, AMAb90966) followed by Alexa Fluor 488-conjugated anti-mouse IgG (H+L) (Invitrogen, A11001) and 4',6-diamidino-2-phenylindole (DAPI) (Sigma, D8417). Signals were visualized using Zeiss LSM 880 confocal scanning microscope with Airyscan with 100x oil immersion objectives.

Western blot

Cells were lysed in RIPA buffer (50mM Tris-HCL pH8.0, 150nM NaCl, 1% NP-40, 0.5% Sodium Deoxycholate, 0.1% SDS) containing a phosphatase inhibitor cocktail (Halt, 78428) and a protease inhibitor cocktail (Millipore Sigma, 11697498001). Sonication was performed with a sonic dismembrator (Fisher, FB120) to improve membranous and nuclear protein yield. For extraction of protein lysate from tumor samples, tumors were minced with a razor blade prior to transfer to pre-filled bead mill tubes (Fisher, 15-340-153) and resuspension in the lysis solution described above. Homogenization was performed for 2 minutes at max intensity using a Bead Mill 4 homogenizer (Fisher, 15-340-164). Samples were run on NuPAGE 4%-12% Bis-Tris Gels (Fisher, NP0335) and protein was transferred to PVDF transfer membranes (Fisher, IPV00010). Total protein was visualized using the SYPRO RUBY protein blot stain (Fisher, S11791) and membranes were blocked in PBS +.1% Tween-20 (Fisher, BP337-500) + 5% milk (Fisher, BC9121673). Proteins were probed with primary antibodies followed by chromophore-conjugated anti-mouse (Invitrogen, A21235) or anti-rabbit secondary antibodies (Invitrogen, A21244) or HRP-conjugated anti-mouse (Thermo, 31430) or anti-rabbit secondary antibodies (Thermo, 31463) and detected via florescence or HRP chemiluminescence respectively. Primary antibodies used were beta-Actin (Invitrogen, MA1-140), Androgen Receptor (Cell Signaling, 5153S), Hexokinase II (Cell Signaling, 28675), DRP1 (Cell Signaling, 5391S), Phospho-DRP1 (Ser616) (Cell Signaling, 3455S), Anti-LDH-A (MilliporeSigma, MABC150), Recombinant-Anti-c-MYC (Abcam, ab32072), NSE (Proteintech, 66150-1-Ig), and PSA/KLK3 (Cell Signaling, 5877).

QUANTIFICATION AND STATISTICAL ANALYSIS

Metabolomics analysis

For projection plots, principal component analysis (PCA) was performed with the scikit-learn, NumPy, pandas, and Matplotlib libraries in Python. Feature selection was done based on shared features between differing datasets. Count/abundance matrices were sorted along their respective feature-axis to ensure features were listed in the same order. After performing z-score scaling, the coordinates from the *in vitro* samples were merged onto a PCA plot with the values from *in vivo* samples. 95% confidence ellipses were generated from PCA-transformed coordinates using a script from Matplotlib (https://github.com/Nick-Nunley/PCA-for-AR-induced-metabolic-reprogramming-in-CRPCa). Heatmaps were generated by plotting row z-scores in GraphPad Prism Version 7. To generate the average z-score plot, an *in vivo* enza-enriched metabolite signature was defined. Row z-scores of *in vivo* enza-enriched metabolites were calculated from *the in vitro* metabolomics dataset. Row z-scores from three technical replicates from a

representative experiment (n=3) were averaged and represented on a dot plot. MSEA was generated using Metaboanalyst 5.0[17] (https://www.metaboanalyst.ca/MetaboAnalyst/home.xhtml).

Mitochondrial content and morphology

Mitochondrial elongation was expressed as aspect ratio (long axis/short axis ratio) and eccentricity, calculated as the ratio of the distance between the foci of an ellipse and its major axis length. Branching was expressed as form factor ($(4\pi(\text{area}))/\text{Perimeter}^2$). Mitochondrial parameters were determined from mitochondrial TUFM staining. Image analysis was performed using ImageJ v1.53c and CellProfiler v2.0[18]. For mitochondrial volume quantification, z-stack images were processed with Imaris software (Oxford Instruments) to identify TUFM-positive regions and calculate TUFM-positive volume.

RNA sequencing analysis

KEGG pathway analysis was performed using DAVID Bioinformatics[19,20]. GSEA was performed as described previously using GSEA_4.0.3 software[21,22]. Projection plots were generated as described for metabolomics analysis. After performing z-score scaling, the coordinates from the *in vitro* 16D enzalutamide time-course RNA-sequencing data were merged onto a PCA plot with the values from the *Rajan et al* dataset. 95% confidence ellipses were generated as described for metabolomics analysis. Average z-score plots and heatmaps were generated as described for metabolomics analysis.

In the *Quigley et al* dataset, there were 63 enzalutamide-naive and 36 enzalutamide-resistant patients whose tumor underwent RNA-seq[23]. Alignment to hg38-decoy reference was performed using STAR aligner (version 2.5.0b) with per-gene counts quantification on the basis of Illumina RNA-seq alignment app Version 1.1.0[24].

Western blot quantification

Western blots were quantified using ImageJ software. Background values were subtracted from the mean gray value for each band. Each band was normalized to its respective loading control.

DATA AND CODE AVAILABILITY

The data discussed in this publication have been deposited in NCBI's Gene Expression Omnibus and are accessible through GEO Series accession numbers GSE202885, GSE202755, and GSE202897.

MATERIALS AND METHODS REFERENCES

1. Cordes T, Metallo CM. Quantifying Intermediary Metabolism and Lipogenesis in Cultured Mammalian Cells Using Stable Isotope Tracing and Mass Spectrometry. *Methods Mol Biol.* 2019;1978:219-241.
2. Trefely S, Ashwell P, Snyder NW. FluxFix: automatic isotopologue normalization for metabolic tracer analysis. *BMC Bioinformatics.* 2016;17(1):485. PMC5123363

3. Divakaruni AS, Paradyse A, Ferrick DA, Murphy AN, Jastroch M. Analysis and interpretation of microplate-based oxygen consumption and pH data. *Methods Enzymol.* 2014;547:309-354.
4. Desousa BR, Kim KKO, Hsieh WY, Jones AE, Swain P, Morrow DH, Ferrick DA, Shirihai OS, Neilson A, Nathanson DA, Rogers GW, Dranka BP, Murphy AN, Affourtit C, Bensinger SJ, Stiles L, Romero N, Divakaruni AS. Calculating ATP production rates from oxidative phosphorylation and glycolysis during cell activation. *bioRxiv.* 2022:2022.2004.2016.488523.
5. Stoyanova T, Cooper AR, Drake JM, Liu X, Armstrong AJ, Pienta KJ, Zhang H, Kohn DB, Huang J, Witte ON, Goldstein AS. Prostate cancer originating in basal cells progresses to adenocarcinoma propagated by luminal-like cells. *Proc Natl Acad Sci U S A.* 2013;110(50):20111-20116. PMC3864278
6. Ramirez F, Ryan DP, Gruning B, Bhardwaj V, Kilpert F, Richter AS, Heyne S, Dundar F, Manke T. deepTools2: a next generation web server for deep-sequencing data analysis. *Nucleic Acids Res.* 2016;44(W1):W160-165. PMC4987876
7. Zhang A, Zhao JC, Kim J, Fong KW, Yang YA, Chakravarti D, Mo YY, Yu J. LncRNA HOTAIR Enhances the Androgen-Receptor-Mediated Transcriptional Program and Drives Castration-Resistant Prostate Cancer. *Cell Rep.* 2015;13(1):209-221. PMC4757469
8. Davies A, Nouruzi S, Ganguli D, Namekawa T, Thaper D, Linder S, Karaoglanoglu F, Omur ME, Kim S, Kobelev M, Kumar S, Sivak O, Bostock C, Bishop J, Hoogstraat M, Talal A, Stelloo S, van der Poel H, Bergman AM, Ahmed M, Fazli L, Huang H, Tilley W, Goodrich D, Feng FY, Gleave M, He HH, Hach F, Zwart W, Beltran H, Selth L, Zoubeidi A. An androgen receptor switch underlies lineage infidelity in treatment-resistant prostate cancer. *Nat Cell Biol.* 2021;23(9):1023-1034. PMC9012003
9. Robinson JT, Thorvaldsdottir H, Winckler W, Guttman M, Lander ES, Getz G, Mesirov JP. Integrative genomics viewer. *Nat Biotechnol.* 2011;29(1):24-26. PMC3346182
10. Yegnasubramanian S, Lin X, Haffner MC, DeMarzo AM, Nelson WG. Combination of methylated-DNA precipitation and methylation-sensitive restriction enzymes (COMPARE-MS) for the rapid, sensitive and quantitative detection of DNA methylation. *Nucleic Acids Res.* 2006;34(3):e19. PMC1363782
11. Krueger F, Andrews SR. Bismark: a flexible aligner and methylation caller for Bisulfite-Seq applications. *Bioinformatics.* 2011;27(11):1571-1572. PMC3102221
12. Chambers MC, Maclean B, Burke R, Amodei D, Ruderman DL, Neumann S, Gatto L, Fischer B, Pratt B, Egertson J, Hoff K, Kessner D, Tasman N, Shulman N, Frewen B, Baker TA, Brusniak MY, Paulse C, Creasy D, Flashner L, Kani K, Moulding C, Seymour SL, Nuwaysir LM, Lefebvre B, Kuhlmann F, Roark J, Rainer P, Detlev S, Hemenway T, Huhmer A, Langridge J, Connolly B, Chadick T, Holly K, Eckels J, Deutsch EW, Moritz RL, Katz JE, Agus DB, MacCoss M, Tabb DL, Mallick P. A cross-platform toolkit for mass spectrometry and proteomics. *Nat Biotechnol.* 2012;30(10):918-920. PMC3471674

13. Pluskal T, Castillo S, Villar-Briones A, Oresic M. MZmine 2: modular framework for processing, visualizing, and analyzing mass spectrometry-based molecular profile data. *BMC Bioinformatics.* 2010;11:395. PMC2918584
14. Myers OD, Sumner SJ, Li S, Barnes S, Du X. One Step Forward for Reducing False Positive and False Negative Compound Identifications from Mass Spectrometry Metabolomics Data: New Algorithms for Constructing Extracted Ion Chromatograms and Detecting Chromatographic Peaks. *Anal Chem.* 2017;89(17):8696-8703.
15. Su X, Lu W, Rabinowitz JD. Metabolite Spectral Accuracy on Orbitraps. *Anal Chem.* 2017;89(11):5940-5948. PMC5748891
16. Drost J, Karthaus WR, Gao D, Driehuis E, Sawyers CL, Chen Y, Clevers H. Organoid culture systems for prostate epithelial and cancer tissue. *Nat Protoc.* 2016;11(2):347-358. PMC4793718
17. Pang Z, Chong J, Zhou G, de Lima Morais DA, Chang L, Barrette M, Gauthier C, Jacques PE, Li S, Xia J. MetaboAnalyst 5.0: narrowing the gap between raw spectra and functional insights. *Nucleic Acids Res.* 2021;49(W1):W388-W396. PMC8265181
18. Kamentsky L, Jones TR, Fraser A, Bray MA, Logan DJ, Madden KL, Ljosa V, Rueden C, Eliceiri KW, Carpenter AE. Improved structure, function and compatibility for CellProfiler: modular high-throughput image analysis software. *Bioinformatics.* 2011;27(8):1179-1180. PMC3072555
19. Jacobs PP, Geysens S, Vervecken W, Contreras R, Callewaert N. Engineering complex-type N-glycosylation in Pichia pastoris using GlycoSwitch technology. *Nat Protoc.* 2009;4(1):58-70.
20. Huang da W, Sherman BT, Lempicki RA. Bioinformatics enrichment tools: paths toward the comprehensive functional analysis of large gene lists. *Nucleic Acids Res.* 2009;37(1):1-13. PMC2615629
21. Subramanian A, Tamayo P, Mootha VK, Mukherjee S, Ebert BL, Gillette MA, Paulovich A, Pomeroy SL, Golub TR, Lander ES, Mesirov JP. Gene set enrichment analysis: a knowledge-based approach for interpreting genome-wide expression profiles. *Proc Natl Acad Sci U S A.* 2005;102(43):15545-15550. PMC1239896
22. Mootha VK, Lindgren CM, Eriksson KF, Subramanian A, Sihag S, Lehar J, Puigserver P, Carlsson E, Ridderstrale M, Laurila E, Houstis N, Daly MJ, Patterson N, Mesirov JP, Golub TR, Tamayo P, Spiegelman B, Lander ES, Hirschhorn JN, Altshuler D, Groop LC. PGC-1alpha-responsive genes involved in oxidative phosphorylation are coordinately downregulated in human diabetes. *Nat Genet.* 2003;34(3):267-273.
23. Quigley DA, Dang HX, Zhao SG, Lloyd P, Aggarwal R, Alumkal JJ, Foye A, Kothari V, Perry MD, Bailey AM, Playdle D, Barnard TJ, Zhang L, Zhang J, Youngren JF, Cieslik MP, Parolia A, Beer TM, Thomas G, Chi KN, Gleave M, Lack NA, Zoubeidi A, Reiter RE, Rettig MB, Witte O, Ryan CJ, Fong L, Kim W, Friedlander T, Chou J, Li H, Das R, Li H, Moussavi-Baygi R, Goodarzi H, Gilbert LA, Lara PN, Jr., Evans CP, Goldstein TC, Stuart JM, Tomlins SA, Spratt DE, Cheetham RK, Cheng DT, Farh K, Gehring JS, Hakenberg J, Liao A, Febbo PG, Shon J, Sickler B, Batzoglou S, Knudsen KE, He HH, Huang J, Wyatt AW, Dehm SM, Ashworth A, Chinnaiyan

AM, Maher CA, Small EJ, Feng FY. Genomic Hallmarks and Structural Variation in Metastatic Prostate Cancer. *Cell.* 2018;174(3):758-769 e759. PMC6425931

24. Dobin A, Davis CA, Schlesinger F, Drenkow J, Zaleski C, Jha S, Batut P, Chaisson M, Gingeras TR. STAR: ultrafast universal RNA-seq aligner. *Bioinformatics.* 2013;29(1):15-21. PMC3530905

Chapter 6: Conclusion

Prostate cancer is among the most common causes of cancer-related death[1]. Understanding mechanisms of prostate cancer initiation, progression, and treatment resistance is required to reduce mortality from the disease. The work presented in this thesis represents our efforts to (1) understand how age-related changes to prostate epithelial cells increase susceptibility to prostate cancer initiation, (2) define how metabolism regulates lineage transitions, which drive progression to therapy-resistant disease, and (3) identify treatment-induced metabolic alterations that can be targeted to eradicate the cells that survive treatment.

Aging and progenitor activity

Whereas aging in many tissues is associated with atrophy and a decline in stem/progenitor cell function, aging in the prostate is associated with growth-related diseases such as benign prostatic hyperplasia and prostate cancer[2,3]. Prior to our work, the effects of aging on the gene expression and progenitor activity of prostate epithelial cells were poorly defined. In chapter 2, I described our effort to identify key age-related phenotypes in the mouse and human prostate. We found that *ex vivo* progenitor activity of mouse basal and luminal prostate epithelial cells is maintained during aging. We explored the mechanism by which aged luminal cells form larger organoids and identified an age-related expansion of progenitor-enriched luminal cells in the mouse prostate that is conserved in human prostate. Single cell RNA sequencing by several groups has since confirmed that mouse Trop2+ progenitor-enriched luminal cells cluster separately from other luminal subsets[4-6]. As progenitor-enriched luminal cells in both human and mouse

exhibit greater susceptibility to transformation, our data provide one mechanism by which aging could increase risk for prostatic disease[4,7].

The mechanism by which progenitor-enriched luminal cells are expanded during aging remains unclear. Within the luminal compartment, we observed a higher proliferation rate in Trop2+ luminal cells than Trop2- luminal cells. One possibility is that Trop2+ luminal cells may be expanded during aging due to a sustained proliferative advantage within this subset throughout life. Alternatively, Trop2+ luminal cells may be expanded due to asymmetric cell division from multipotent basal cells. Progenitor-enriched luminal cells share several markers with basal cells including Trop2 and PSCA. Lineage tracing of multipotent basal cells could reveal if basal to luminal differentiation contributes to Trop2+ luminal cell expansion.

The impact of age-related changes to the microenvironment on the prostate epithelium remains poorly defined. As older mice are heavier and contain more prostate-associated adipose tissue, we explored whether adult mice fed a high fat diet replicate the prostate aging phenotype. Prostates from mice fed a high fat diet for 3 months did not contain an expansion of Trop2+ luminal cells. Using flow and mass cytometry approaches, we identified an age-related increase in lymphocytes. Whether aging-associated lymphocyte infiltration favors Trop2+ luminal cell expansion remains unclear. Depletion of lymphocytes could help to uncover the role of these cells in the expansion of progenitor-enriched luminal cells. Understanding how progenitor-enriched luminal cells are

expanded during aging could enable us to explore whether preventing the expansion of these cells reduces the incidence of prostatic disease.

Aging and metabolic reprogramming

Aging in various tissues is associated with metabolic reprogramming, which can contribute to cancer initiation[8]. In chapter 3, I described our preliminary work to uncover age-related changes to prostate metabolism. We transcriptionally profiled stromal, basal, Trop2+ luminal, and Trop2- luminal cells isolated from adult and old mouse prostate. Hypoxia-related signaling, glutathione metabolism, and antioxidant response were enriched in all aged prostatic lineages suggesting that a common age-related metabolic signature may be shared by distinct cell types in the old prostate.

Future work will seek to identify key regulators of age-related changes to metabolic gene expression. The transcription factors that mediate age-related changes to metabolic gene expression remain unclear. As NRF2 regulates the cellular response to oxidative stress, increased NRF2 activity could promote increased glutathione and antioxidant gene expression in the old mouse prostate[9]. Using NRF2 knockout mice, we will explore the role of NRF2 in facilitating age-related changes to metabolic gene expression. Importantly, how age-related changes to the prostate microenvironment alter the metabolic signaling of distinct prostate cell types remains poorly understood. As aging is associated with chronic inflammation, we will explore if inflammation-induced changes to the microenvironment influence the metabolism of aged prostate cell types using immune cell-specific depletion approaches[10-12]. Whether age-related changes to metabolic gene

expression aid age-related maintenance of progenitor activity, perhaps by protecting cells from oxidative stress, remains unclear. Identifying key regulators of age-related changes to metabolic gene expression will enable us to investigate if interfering with age-related altered gene expression influences progenitor activity and/or susceptibility to prostatic disease.

Metabolic regulation of cell fate

Basal to luminal differentiation occurs during development, tissue regeneration, and prostate cancer initiation from basal cells[13-18]. In addition, loss of luminal identity drives treatment resistance in metastatic CRPC[19-21]. Recent studies have characterized epigenetic regulation of prostate epithelial lineage identity, yet defining upstream metabolic regulation of lineage identity has been challenging due to an incomplete understanding of cell type-specific metabolic features[19,22,23]. In chapter 4, I described our effort to delineate prostate cell type-specific metabolic signatures and investigate metabolic regulation of prostate epithelial lineage identity. Using metabolic profiling and isotope-labeled nutrient tracer analysis we identified prostate epithelial cell type-specific metabolic features, including enrichment of glycolytic activity in basal cells. We defined metabolic changes associated with basal to luminal differentiation in the *ex vivo* prostate organoid model and found that luminal differentiation in prostate organoids is associated with increased glucose oxidation. Our findings were corroborated *in vivo* using lineage tracing approaches in combination with RNA sequencing. We explored the effect of interfering with MPC activity using genetic and pharmacological approaches and found that MPC inhibition reduces luminal differentiation in both benign and prostate cancer

organoids. Intracellular lactate accumulation may mediate MPC inhibition-induced reduced luminal differentiation. Our results implicate upstream metabolic signaling in regulation of prostate epithelial lineage identity.

It remains unclear how MPC inhibition alters the epigenome to reduce luminal differentiation, and whether altering metabolism to promote luminal differentiation in treatment-resistant prostate cancer that exhibits loss of luminal features would be sufficient to restore sensitivity to anti-androgen therapies. Future studies will be necessary to define MPC inhibition-induced changes to the epigenome using a number of approaches including ATAC sequencing, ChIP sequencing, and bisulfite sequencing. In addition, future studies will explore whether MPC overexpression in non-luminal treatment-resistant prostate cancer organoids promotes reacquisition of luminal features and enhances sensitivity to AR blockade. As treatment-resistant disease accounts for the vast majority of prostate cancer-related death, uncovering new strategies to target treatment-resistant prostate cancer cells is of utmost importance.

Therapy-induced metabolic reprogramming in cancer

Rewiring of metabolic signaling occurs in many tissues during cancer initiation and progression, and can contribute to therapy resistance[24]. Studies from several groups provide evidence of metabolic reprogramming in prostate cancer, yet the effect of AR blockade on prostate cancer metabolism had not been well defined[25-32]. In addition, whether altered metabolism in cells that survive AR inhibition could be targeted to prevent disease progression was previously unclear. In chapter 5, I described our effort to

determine how AR blockade alters prostate cancer cell metabolism. We found that AR inhibition maintains oxidative mitochondrial metabolism and reduces glycolytic activity and capacity, via decreased MYC activity and HK2 downregulation. Mitochondrial elongation supports cellular fitness after AR blockade. In addition, AR inhibition increases the sensitivity of prostate cancer cells to complex I inhibitors, suggesting that AR blockade increases reliance on oxidative mitochondrial metabolism. Our findings identify altered metabolic signaling as a resistance mechanism and provide an example of how therapy-induced altered metabolism can be targeted to eradicate the cells that survive AR inhibition.

Our finding that mitochondrial elongation supports cell survival after AR blockade is consistent with findings in breast and gynecological cancers where mitochondrial elongation enabled chemotherapy resistance[33,34]. Interestingly, elongation has been shown to protect mitochondria from autophagosomal degradation induced by nutrient deprivation[35,36]. Importantly, the functional consequence of mitochondrial activity on metabolic output is highly context dependent. For example, mitochondrial fragmentation drives increased oxidative metabolism and accelerates cancer progression in pancreatic cancer models, whereas fragmentation reduces oxidative metabolism in neuroblastoma cells[37-39]. Future work will seek to define the mechanism by which elongation of mitochondria supports cell fitness after AR inhibition.

It is important to consider when combining complex I inhibition with AR blockade could improve patient outcomes. Our data support combining complex I inhibitors with ADT in

CSPC or ARPIs to treat CRPC. It remains unclear whether lineage transitions that support ARPI resistance alter ARPI-induced metabolic phenotypes including increased complex I sensitivity. Among the most common causes of ARPI-induced lineage plasticity is disruption of *RB1* and *TP53*[19,20]. We found that knockdown of *RB1* and *TP53* in LTenza 16D cells was not sufficient to alter MYC activity or sensitivity to complex I inhibitors. However, in the LTL331 patient-derived xenograft model, where relapsed tumors contain neural features, relapsed tumors contain enrichment for MYC targets despite retaining low AR activity. These data suggest that the effectiveness of combined AR blockade and complex I inhibition to treat relapsed prostate cancer may depend on tumor phenotype and/or the genetic driver. Future work is needed to determine whether restored MYC activity enables prostate cancer recurrence, perhaps through restored glycolytic signaling.

Several observational studies and clinical trials have been performed to explore the efficacy of combined complex I inhibition via metformin treatment and AR inhibition with inconclusive results regarding both recurrence-free survival and overall outcome[40,41]. Importantly, metformin has known off-target effects, and does not reach concentrations in plasma of patients sufficient to inhibit complex I activity[42,43]. Therefore, improved clinically-viable inhibitors of oxidative metabolism are needed to test whether AR blockade can synergize with metabolic drugs to improve patient outcomes.

References

1. Siegel RL, Miller KD, Fuchs HE, Jemal A. Cancer statistics, 2022. *CA Cancer J Clin.* 2022;72(1):7-33.
2. Roehrborn CG. Benign prostatic hyperplasia: an overview. *Rev Urol.* 2005;7 Suppl 9:S3-S14. PMC1477638
3. Lopez-Otin C, Blasco MA, Partridge L, Serrano M, Kroemer G. The hallmarks of aging. *Cell.* 2013;153(6):1194-1217. PMC3836174
4. Guo W, Li L, He J, Liu Z, Han M, Li F, Xia X, Zhang X, Zhu Y, Wei Y, Li Y, Aji R, Dai H, Wei H, Li C, Chen Y, Chen L, Gao D. Single-cell transcriptomics identifies a distinct luminal progenitor cell type in distal prostate invagination tips. *Nat Genet.* 2020;52(9):908-918. PMC8383310
5. Crowley L, Cambuli F, Aparicio L, Shibata M, Robinson BD, Xuan S, Li W, Hibshoosh H, Loda M, Rabadan R, Shen MM. A single-cell atlas of the mouse and human prostate reveals heterogeneity and conservation of epithelial progenitors. *Elife.* 2020;9. PMC7529463
6. Karthaus WR, Hofree M, Choi D, Linton EL, Turkekul M, Bejnood A, Carver B, Gopalan A, Abida W, Laudone V, Biton M, Chaudhary O, Xu T, Masilionis I, Manova K, Mazutis L, Pe'er D, Regev A, Sawyers CL. Regenerative potential of prostate luminal cells revealed by single-cell analysis. *Science.* 2020;368(6490):497-505. PMC7313621
7. Liu X, Grogan TR, Hieronymus H, Hashimoto T, Mottahedeh J, Cheng D, Zhang L, Huang K, Stoyanova T, Park JW, Shkhyan RO, Nowroozizadeh B, Rettig MB, Sawyers CL, Elashoff D, Horvath S, Huang J, Witte ON, Goldstein AS. Low CD38 Identifies Progenitor-like Inflammation-Associated Luminal Cells that Can Initiate Human Prostate Cancer and Predict Poor Outcome. *Cell Rep.* 2016;17(10):2596-2606. PMC5367888
8. Ren R, Ocampo A, Liu GH, Izpisua Belmonte JC. Regulation of Stem Cell Aging by Metabolism and Epigenetics. *Cell Metab.* 2017;26(3):460-474.
9. Ma Q. Role of nrf2 in oxidative stress and toxicity. *Annu Rev Pharmacol Toxicol.* 2013;53:401-426. PMC4680839
10. Gurel B, Lucia MS, Thompson IM, Jr., Goodman PJ, Tangen CM, Kristal AR, Parnes HL, Hoque A, Lippman SM, Sutcliffe S, Peskoe SB, Drake CG, Nelson WG, De Marzo AM, Platz EA. Chronic inflammation in benign prostate tissue is associated with high-grade prostate cancer in the placebo arm of the prostate cancer prevention trial. *Cancer Epidemiol Biomarkers Prev.* 2014;23(5):847-856. PMC4012292
11. Sfanos KS, De Marzo AM. Prostate cancer and inflammation: the evidence. *Histopathology.* 2012;60(1):199-215. PMC4029103
12. Shafique K, Proctor MJ, McMillan DC, Qureshi K, Leung H, Morrison DS. Systemic inflammation and survival of patients with prostate cancer: evidence from the Glasgow Inflammation Outcome Study. *Prostate Cancer Prostatic Dis.* 2012;15(2):195-201.
13. Choi N, Zhang B, Zhang L, Ittmann M, Xin L. Adult murine prostate basal and luminal cells are self-sustained lineages that can both serve as targets for prostate cancer initiation. *Cancer Cell.* 2012;21(2):253-265. PMC3285423

14. Ousset M, Van Keymeulen A, Bouvencourt G, Sharma N, Achouri Y, Simons BD, Blanpain C. Multipotent and unipotent progenitors contribute to prostate postnatal development. *Nat Cell Biol.* 2012;14(11):1131-1138.
15. Wang J, Zhu HH, Chu M, Liu Y, Zhang C, Liu G, Yang X, Yang R, Gao WQ. Symmetrical and asymmetrical division analysis provides evidence for a hierarchy of prostate epithelial cell lineages. *Nat Commun.* 2014;5:4758.
16. Wang ZA, Mitrofanova A, Bergren SK, Abate-Shen C, Cardiff RD, Califano A, Shen MM. Lineage analysis of basal epithelial cells reveals their unexpected plasticity and supports a cell-of-origin model for prostate cancer heterogeneity. *Nat Cell Biol.* 2013;15(3):274-283. PMC3743266
17. Kwon OJ, Zhang B, Zhang L, Xin L. High fat diet promotes prostatic basal-to-luminal differentiation and accelerates initiation of prostate epithelial hyperplasia originated from basal cells. *Stem Cell Res.* 2016;16(3):682-691.
18. Kwon OJ, Zhang L, Ittmann MM, Xin L. Prostatic inflammation enhances basal-to-luminal differentiation and accelerates initiation of prostate cancer with a basal cell origin. *Proc Natl Acad Sci U S A.* 2014;111(5):E592-600. PMC3918789
19. Ku SY, Rosario S, Wang Y, Mu P, Seshadri M, Goodrich ZW, Goodrich MM, Labbe DP, Gomez EC, Wang J, Long HW, Xu B, Brown M, Loda M, Sawyers CL, Ellis L, Goodrich DW. Rb1 and Trp53 cooperate to suppress prostate cancer lineage plasticity, metastasis, and antiandrogen resistance. *Science.* 2017;355(6320):78-83. PMC5367887
20. Mu P, Zhang Z, Benelli M, Karthaus WR, Hoover E, Chen CC, Wongvipat J, Ku SY, Gao D, Cao Z, Shah N, Adams EJ, Abida W, Watson PA, Prandi D, Huang CH, de Stanchina E, Lowe SW, Ellis L, Beltran H, Rubin MA, Goodrich DW, Demichelis F, Sawyers CL. SOX2 promotes lineage plasticity and antiandrogen resistance in TP53- and RB1-deficient prostate cancer. *Science.* 2017;355(6320):84-88. PMC5247742
21. Schmidt KT, Huitema ADR, Chau CH, Figg WD. Resistance to second-generation androgen receptor antagonists in prostate cancer. *Nat Rev Urol.* 2021;18(4):209-226.
22. Dardenne E, Beltran H, Benelli M, Gayvert K, Berger A, Puca L, Cyrta J, Sboner A, Noorzad Z, MacDonald T, Cheung C, Yuen KS, Gao D, Chen Y, Eilers M, Mosquera JM, Robinson BD, Elemento O, Rubin MA, Demichelis F, Rickman DS. N-Myc Induces an EZH2-Mediated Transcriptional Program Driving Neuroendocrine Prostate Cancer. *Cancer Cell.* 2016;30(4):563-577. PMC5540451
23. Davies A, Nouruzi S, Ganguli D, Namekawa T, Thaper D, Linder S, Karaoglanoglu F, Omur ME, Kim S, Kobelev M, Kumar S, Sivak O, Bostock C, Bishop J, Hoogstraat M, Talal A, Stelloo S, van der Poel H, Bergman AM, Ahmed M, Fazli L, Huang H, Tilley W, Goodrich D, Feng FY, Gleave M, He HH, Hach F, Zwart W, Beltran H, Selth L, Zoubeidi A. An androgen receptor switch underlies lineage infidelity in treatment-resistant prostate cancer. *Nat Cell Biol.* 2021;23(9):1023-1034. PMC9012003
24. DeBerardinis RJ, Chandel NS. Fundamentals of cancer metabolism. *Sci Adv.* 2016;2(5):e1600200. PMC4928883
25. Priolo C, Pyne S, Rose J, Regan ER, Zadra G, Photopoulos C, Cacciatore S, Schultz D, Scaglia N, McDunn J, De Marzo AM, Loda M. AKT1 and MYC induce

distinctive metabolic fingerprints in human prostate cancer. *Cancer Res.* 2014;74(24):7198-7204. PMC4267915
26. Zadra G, Ribeiro CF, Chetta P, Ho Y, Cacciatore S, Gao X, Syamala S, Bango C, Photopoulos C, Huang Y, Tyekucheva S, Bastos DC, Tchaicha J, Lawney B, Uo T, D'Anello L, Csibi A, Kalekar R, Larimer B, Ellis L, Butler LM, Morrissey C, McGovern K, Palombella VJ, Kutok JL, Mahmood U, Bosari S, Adams J, Peluso S, Dehm SM, Plymate SR, Loda M. Inhibition of de novo lipogenesis targets androgen receptor signaling in castration-resistant prostate cancer. *Proc Natl Acad Sci U S A.* 2019;116(2):631-640. PMC6329966
27. Reina-Campos M, Linares JF, Duran A, Cordes T, L'Hermitte A, Badur MG, Bhangoo MS, Thorson PK, Richards A, Rooslid T, Garcia-Olmo DC, Nam-Cha SY, Salinas-Sanchez AS, Eng K, Beltran H, Scott DA, Metallo CM, Moscat J, Diaz-Meco MT. Increased Serine and One-Carbon Pathway Metabolism by PKClambda/iota Deficiency Promotes Neuroendocrine Prostate Cancer. *Cancer Cell.* 2019;35(3):385-400 e389. PMC6424636
28. Bader DA, Hartig SM, Putluri V, Foley C, Hamilton MP, Smith EA, Saha PK, Panigrahi A, Walker C, Zong L, Martini-Stoica H, Chen R, Rajapakshe K, Coarfa C, Sreekumar A, Mitsiades N, Bankson JA, Ittmann MM, O'Malley BW, Putluri N, McGuire SE. Mitochondrial pyruvate import is a metabolic vulnerability in androgen receptor-driven prostate cancer. *Nat Metab.* 2019;1(1):70-85. PMC6563330
29. Choi SYC, Ettinger SL, Lin D, Xue H, Ci X, Nabavi N, Bell RH, Mo F, Gout PW, Fleshner NE, Gleave ME, Collins CC, Wang Y. Targeting MCT4 to reduce lactic acid secretion and glycolysis for treatment of neuroendocrine prostate cancer. *Cancer Med.* 2018. PMC6051138
30. Zhang J, Mao S, Guo Y, Wu Y, Yao X, Huang Y. Inhibition of GLS suppresses proliferation and promotes apoptosis in prostate cancer. *Biosci Rep.* 2019;39(6). PMC6591571
31. Lin C, Blessing AM, Pulliam TL, Shi Y, Wilkenfeld SR, Han JJ, Murray MM, Pham AH, Duong K, Brun SN, Shaw RJ, Ittmann MM, Frigo DE. Inhibition of CAMKK2 impairs autophagy and castration-resistant prostate cancer via suppression of AMPK-ULK1 signaling. *Oncogene.* 2021;40(9):1690-1705. PMC7935762
32. Massie CE, Lynch A, Ramos-Montoya A, Boren J, Stark R, Fazli L, Warren A, Scott H, Madhu B, Sharma N, Bon H, Zecchini V, Smith DM, Denicola GM, Mathews N, Osborne M, Hadfield J, Macarthur S, Adryan B, Lyons SK, Brindle KM, Griffiths J, Gleave ME, Rennie PS, Neal DE, Mills IG. The androgen receptor fuels prostate cancer by regulating central metabolism and biosynthesis. *EMBO J.* 2011;30(13):2719-2733. PMC3155295
33. Baek ML, Lee J, Pendleton KE, Berner MJ, Goff EB, Tan L, Martinez SA, Wang T, Meyer MD, Lim B, Barrish JP, Porter W, Lorenzi PL, Echeverria GV. Mitochondrial structure and function adaptation in residual triple negative breast cancer cells surviving chemotherapy treatment. *bioRxiv.* 2022:2022.2002.2025.481996.
34. Kong B, Tsuyoshi H, Orisaka M, Shieh DB, Yoshida Y, Tsang BK. Mitochondrial dynamics regulating chemoresistance in gynecological cancers. *Ann N Y Acad Sci.* 2015;1350:1-16.

35. Rambold AS, Kostelecky B, Elia N, Lippincott-Schwartz J. Tubular network formation protects mitochondria from autophagosomal degradation during nutrient starvation. *Proc Natl Acad Sci U S A.* 2011;108(25):10190-10195. PMC3121813
36. Li J, Huang Q, Long X, Guo X, Sun X, Jin X, Li Z, Ren T, Yuan P, Huang X, Zhang H, Xing J. Mitochondrial elongation-mediated glucose metabolism reprogramming is essential for tumour cell survival during energy stress. *Oncogene.* 2017;36(34):4901-4912.
37. Courtois S, de Luxan-Delgado B, Penin-Peyta L, Royo-Garcia A, Parejo-Alonso B, Jagust P, Alcala S, Rubiolo JA, Sanchez L, Sainz B, Jr., Heeschen C, Sancho P. Inhibition of Mitochondrial Dynamics Preferentially Targets Pancreatic Cancer Cells with Enhanced Tumorigenic and Invasive Potential. *Cancers (Basel).* 2021;13(4). PMC7914708
38. Yu M, Nguyen ND, Huang Y, Lin D, Fujimoto TN, Molkentine JM, Deorukhkar A, Kang Y, San Lucas FA, Fernandes CJ, Koay EJ, Gupta S, Ying H, Koong AC, Herman JM, Fleming JB, Maitra A, Taniguchi CM. Mitochondrial fusion exploits a therapeutic vulnerability of pancreatic cancer. *JCI Insight.* 2019;5. PMC6777817
39. Hagenbuchner J, Kuznetsov AV, Obexer P, Ausserlechner MJ. BIRC5/Survivin enhances aerobic glycolysis and drug resistance by altered regulation of the mitochondrial fusion/fission machinery. *Oncogene.* 2013;32(40):4748-4757.
40. Nobes JP, Langley SE, Klopper T, Russell-Jones D, Laing RW. A prospective, randomized pilot study evaluating the effects of metformin and lifestyle intervention on patients with prostate cancer receiving androgen deprivation therapy. *BJU Int.* 2012;109(10):1495-1502.
41. Ahn HK, Lee YH, Koo KC. Current Status and Application of Metformin for Prostate Cancer: A Comprehensive Review. *Int J Mol Sci.* 2020;21(22). PMC7698147
42. He L, Wondisford FE. Metformin action: concentrations matter. *Cell Metab.* 2015;21(2):159-162.
43. Hess C, Unger M, Madea B, Stratmann B, Tschoepe D. Range of therapeutic metformin concentrations in clinical blood samples and comparison to a forensic case with death due to lactic acidosis. *Forensic Sci Int.* 2018;286:106-112.